Northumbria University
NEWCASTLE

Design and Development of Dual-Polarised Photovoltaic Solar Antennae for Ku-band SatComs.

Farhat Emhemed Nashad

A thesis submitted in partial fulfilment of the requirements of the University of Northumbria at Newcastle for the degree of

Doctor of Philosophy

Research undertaken in the Faculty of Engineering and Environment

April/2019

Abstract

The aim of this thesis is to review the state-of-the-art of transparent patch antennae and to develop design techniques for the experimental development of dual-band, dual-polarised compact transparent patch antennae integrated with solar cells for Ku-band satellite applications. It can be specifically used for Fixed-Satellite-Services (FSS) operating over the frequency range from 11.7 GHz to 12.22 GHz (downlink) and 14.0 GHz to 14.5 GHz (uplink) bands.

The research reported in this thesis demonstrated a suspended meshed patch antennae serves as a basic building-block element for a Ku-band dual-polarised transparent array antennae for long distance communications. The results are shown that the use of a suspended patch above a printed radiating patch and ground plane (all transparent) provides dual-band operation for the uplink and downlink. In this work, firstly, a compact low-profile linearly polarised meshed element has been designed, and simulated in CST Microwave Studio electromagnetic simulation software. The photovoltaic antennae element was then fabricated and measured. The comparison between the experimental results and simulation by CST demonstrates good agreement between predicted and practical measurements. The developed antennae element achieved the overall broad bandwidth of more than 1GHz (500 MHz in each of the uplink and downlink bands), and the nominal element gain is 6.055 dBi (downlink) and 7.61 dBi (uplink). A good compromise between the RF performance and the transparency is also obtained with optical transparency of 84% and negligible degradation of the RF performance.

The design is then extended to develop a Ku-band photovoltaic antennae element for dual-polarised operation This element could be used for frequency re-use in Ku-band satellite downlink and uplink communications in order to double capacity. In addition, the simulation of a 2 x2 sub-array of dual polarised transparent antennae elements (using the experimentally measured performance of the single dual-polarised element) is presented. It has yielded a narrow beam with increased gain of 13 dBi and a cross-polar discrimination of greater than 30 dB is demonstrated, which is a requirement for frequency re-use operation. Hence, the dual-polarised 4-element sub-array described herein could be utilised as the primary building block for a 2D SatCom phased array antennae. In order to meet the full requirements of Ku-band SatCom communications employing frequency re-use which essentially doubles the achievable capacity, i.e. two data channels can use the same frequency bands simultaneously using the two orthogonal polarisations with high cross-polar isolation. Using these new designs providing new knowledge in the field of photovoltaic communication antennae at high frequencies, and bridge the associated drawbacks with the current PV antennae.

Table of Contents

Abstract I
List of Figures VI
List of Tables X
Glossary of symbols XI
Glossary of Acronyms XIII
Acknowledgements XIV
Declaration XV
Chapter 1 Introduction 1
1.1 Background 1
1.1.1 Historical Review of Patch Antennae 1
1.1.2 Photovoltaic Solar Cells and Microwave Communication Antennae 2
1.2 Problem Statement 3
1.3 Research Motivations and Aims 4
1.4 Original Contribution 5
1.5 Thesis Outline 7
Chapter 2 Antennae Theory 9
2.1 Introduction 9
2.2 Antennae 9
2.2.1 Antennae parameters 10
2.2.1.1 Radiation pattern 10
2.2.1.2 Beamwidth 11
2.2.1.3 Input impedance 12
2.2.1.4 Scattering Parameters (S-parameters) 14
2.2.1.5 Return loss (RL) 16
2.2.1.6 Bandwidth 16
2.2.1.7 Gain, Directivity and Efficiency 17
2.2.1.8 Polarisation 18
2.2.2 Choice of Antennae Type with Respect to Solar Cell Photovoltaic Integration 20
2.2.3 Microstrip Patch Antennae Theory 20
2.2.3.1 Feed Antennae Techniques 22
2.2.3.1.1 Coaxial probe feed 23
2.2.3.1.2 Microstrip Feed line 24
2.2.3.1.3 Proximity-coupled feed 25
2.2.3.1.4 Aperture coupled feed 26

2.2.3.2 Analysis Methods for Microstrip Patch Antennae 27
2.2.3.2.1 Transmission Line Model 27
2.2.3.2.2 Cavity Model Patch Antennae 31
2.2.3.2.3 Multipart Network Model 34
2.2.3.2.3.1 Z-parameters of n-port network 37
2.3 Summary 38
Chapter 3 Literature Review 39
3.1 Antennae and Solar Cells Main Integration Techniques 39
3.2 Literature Review 39
Chapter 4 Photovoltaic (PV) Solar Cell 55
4.1 Introduction 55
4.2 Photovoltaics 55
4.3 Structure of a Crystal Silicon Solar Cell 56
4.4 Characteristics of a solar cell 57
4.4.1 Open Circuit Voltage (V_{OC}) 58
4.4.2 Short Circuit Current (ISC) 59
4.4.3 PV Cell IV-Curve 60
4.5 Solar Cell Efficiency and Losses 60
4.6 Connection of Solar Cells 64
4.6.1 Series Connection 64
4.6.2 Parallel Connection 65
4.7 Summary 66
Chapter 5 Analysis of Slots Loaded Patch Antennae Using Segmentation Model 67
5.1 Introduction 67
5.2 Basic Theory of Slot loaded Microstrip Patch Antennae 67
5.3 Applied the Green's Function to Square Patch Antennae 68
5.4 Solid Square Patch Antennae CST Model 70
5.5 Segmentation Technique for Slots loaded Patch Antennae 72
5.6 Application of Segmentation to Patch Antennae with Square Slots 73
5.6.1 Square Patch with Single Slot 73
5.6.2 Square Patch with Multi-Slots Slot 78
5.7 Modelling of Slots loaded Patch Antennae Using CST Microwave Studio 81
5.8 Results and Discussion 82
5.9 Summary 83

Chapter 6 Design and Development of ku-band Combined Solar Antennae for SatCom. ……85
6.1 Introduction 85
6.2 Methodology and Design Process 85
6.3 Ku-band Suspended Meshed Patch Antennae Integrated with PV Solar Cell 88
6.3.1 Single Meshed patch antennae design 88
6.3.2 Selection of an appropriate Substrate Material for The Proposed Transparent Patch Antennae 89
6.3.3 Dual-band Enhancement for the Proposed Transparent Antennae 91
6.3.4 Design and Fabrication of Ku-band Suspended Meshed Patch Antennae Element ……..…..91
6.4 Analysing and Discussion of Simulation and Measurement Results 97
6.4.1 Effect of variation of the grid widths and lengths on the RF S_{11} antennae performance 97
6.4.2 Impedance Characteristics 99
6.4.3 Current Distribution 100
6.4.4 Effect of Solar Cell on the Antennae Performance 101
6.4.5 Radiation Pattern and Gain 104
6.5 Solar Cell Performance Characteristics Measurement Respect to Integration with Meshing Patch Antennae 111
6.6 Transparency Improvement of Ku-band Suspended Transparent Patch Solar Antennae ……114
6.6.1 Introduction 114
6.6.2 Ku-band Suspended Transparent ITO conductor Patch Antennae 115
6.6.3 Suspended Meshed Patch Antennae Design 117
6.6.4 Transparency Improvement Using ITO Transparent Parasitic Conductor Element ……...117
6.6.5 Results and Discussion 119
6.7 Chapter Summary 121
Chapter 7 Dual-band, Dual-polarised Combined Solar Antennae for Ku-band Frequency Re-use. 124
7.1 Introduction 124
7.2 Dual-Polarized Single Element Design 124
7.2.1 Simulation and Measurement Results 125

7.3 Design of dual-polarised Subarray Antennae to Achieve Extremely Low Cross-polar Levels 129
7.3.1 Introduction 129
7.3.2 2x2 Sub-Array Dual-Polarized Antennae Model 129
7.3.3 Results and Discussion 131
7.4 Summary 135
Chapter 8 Conclusion and Future Work 136
8.1 Conclusion 136
8.2 Future work 139
References 140
List of Publications 156
APPENDIX 3A 157
APPENDIX: 3B 159
APPENDIX: 3C 160

List of Figures

Figure 1.1: Independent solar power system for remote area communication system……..3
Figure 1.2: Research roadmap and the original contributions ……...6
Figure 2.1: Antennae Radiation Pattern Parameters……...……...11
Figure 2.2: Beam-width of an antennae……..12
Figure 2.3: Antennae in transmitting mode……..……13
Figure 2.4: Antennae in receiving mode…….…….……14
Figure 2.5: Two-port network……..15
Figure 2.6: Types of Polarisation; (a) linear polarisation, (b) Circular polarisation, (c) Elliptical polarisation…….……...…….……...19
Figure 2.7: Dual-fed patch antennae arrangement……..20
Figure 2.8: Patch Antennae……....21
Figure 2.9: Microstrip Antennae shapes…….21
Figure 2.10: Classified of antennae feeding techniques……..22
Figure 2.11: Coaxial Probe Fed Patch Antennae…....23
Figure 2.12: Equivalent circuit for coaxial probe fed patch antennae……..23
Figure 2.13: (a) Microstrip line feed patch antennae, (b) Inset microstrip line fed……..24
Figure 2.14: Proximity coupled feed…….……25
Figure 2.15: Equivalent circuit for Proximity coupled feed patch antennae……25
Figure 2.16: Aperture coupled feed……...26
Figure 2.17: Equivalent circuit for aperture coupled feed patch antennae……..26
Figure 2.18: Transmission line model of the patch antennae……..27
Figure 2.19: Equivalent circuit for a microstrip- radiating element……...28
Figure 2.20: Physical and effective lengths of a rectangular microstrip patch……...29
Figure 2.21: Microstrip line and Electric Fringing Fields…….....30
Figure 2.22: Cavity model of a patch antennae…….……..31
Figure 2.23: Cavity model with boundaries for a patch by 2D-wave equation……32
Figure 2.24: Types of modes on the patch antennae……..…..…33
Figure 2.25: Voltage and current distributions and field configuration TM modes of the patch (a) TM_{01}, (b) TM_{02} ……...…….34
Figure 2.26: Multi-Port Network Model of Rectangular patch……..…...35
Figure 2.27: Planar structure with current source……..36
Figure 2.28: port *i* and port *j* are located at planar circuit……..37

Figure 4.1: Basic structure of a crystalline silicon solar cell……..... 55
Figure 4.2. Equivalent circuit model of a PV cell……..……57
Figure 4.3: Equivalent circuit of open-circuit termination an ideal solar cell model……....58
Figure 4.4: Equivalent circuit of short-circuit termination an ideal solar cell model…….59
Figure 4.5: I-V curve characteristics in the dark and under illumination……..……60
Figure 4.6: I-V maximum power curve……...……..61
Figure 4.7: Fill Factor (FF) and maximum Power form an I-V curve……..…..62
Figure 4.8: Series connection module of solar cells……..……64
Figure 4.9: Total I-V curve for N solar cells in series module…….……..65
Figure 4.10: Parallel connection of solar cells in a module……65
Figure 4.11: Total I-V curve for M solar cells in parallel module……..……66
Figure 5.1: Patch current flow for (a) single slot (b) double slots…….67
Figure 5.2: Single Square Patch Antennae…….68
Figure 5.3: Two ports i and j at the same point on x-axis……..….69
Figure 5.4: Sold patch square patch antennae CST model...……...….70
Figure 5.5: The input impedance of square patch antennae (a) real and (b) imaginary…….71
Figure 5.6: Basic segmentation method (a) a simple complete circuit (b) adding patch segments……...……72
Figure 5.7: Basic de-segmentation method (a) a complete circuit (b) subtracting patch segment……...……..73
Figure 5.8: Square patch antennae loaded with single square slot at 3 GHz……...74
Figure 5.9: Patch decomposed into segments……..……..74
Figure 5.10: Combining of α_1 and β_1 segments……..…74
Figure 5.11: Complete structure (γ segment) of single square slot patch…….……..75
Figure 5.12: Real and imaginary part of the slot square patch antennae by Segmentation approach……...….76
Figure 5.13: Square patch antennae with single square slot ……..76
Figure 5.14: (a) Real and (b) imaginary input impedance of patch antennae with square slot.....77
Figure5.15:Square patch antennae loaded with Square slots at 11.95 GHz……..78
Figure 5.16: Decomposition the patch into a number of segments……..……79
Figure 5.17: Ports of α1 and β1 segments…….79
Figure 5.18: Synthesis of γ segments into final structure…….……..80

Figure 5.19: Final γ segment of patch design……81
Figure 5.20: The CST slot patch model……..…81
Figure 5.21: Input impedance of slots loaded square patch antennae with (a) Real and (b) imaginary……..82
Figure 6.1: Flow chart shows the design process for the proposed sub-array antennae… 87
Figure 6.2: Square single meshed patch antennae excited by microstrip line at resonant frequency of 11.95 GHz (downlink)…….88
Figure 6.3: Reflection coefficient S_{11} (dB) of the single meshed square patch antennae…...89
Figure 6.4: Effect of substrate properties on S_{11}-response, a) Glass Pyrex substrate, b) Plexiglas substrate……..……..90
Figure 6.5: Suspended meshed patch antennae integrated with solar cell: (a) overall view in CST Microwave Studio; (b) side view. Dimensions: *W1*=6 mm, *W2*=15 mm, *wt* =0.5 mm, *L1*=6 mm, *L2*=18 mm, *h1*=2 mm, *h2*=1.5 mm, *h3*=2 mm, *h4*=3 mm……..……92
Figure 6.6: The suspended solid patch antennae integrated with solar cell…….……93
Figure 6.7: S_{11} response of the reference solid suspended patch antennae design……...94
Figure 6.8: The effect of the meshing on the S_{11} simulated result of the antennae with and without meshing……..….94
Figure 6.9: The effect of the reduction in proposed antennae dimensions on the S_{11} simulated reflection coefficient……95
Figure 6.10: A photograph of fabricated proposed meshed patch Antennae: (a) perspective side view (b) front view, (c) fabricated antennae under measurement……..….96
Figure 6.11: S_{11}-parameters of Simulated and practical meshed suspended patch……97
Figure 6.12: Meshed suspended solar patch antennae with varying meshing line widths (a) line width of 0.3 mm (optical transparency = 87%), (b) line width of 0.5 mm (optical transparency = 84%)……..…….…….98
Figure 6.13: Effect of variation of the grid line width on the S_{11}-parameter……..…98
Figure 6.14: Z-parameters (a) Real, and (b) Imaginary parts of the meshed patch antennae with varying meshing line widths……...100
Figure 6.15: Current distribution across the suspended meshed Patch at (a) 11.95 GHz, (b) 14.25 GHz bands……..…….……..101
Figure 6.16: Proposed suspended meshed patch antennae (a) with solar cell (b) without solar cell and cover glass (with only meshed ground plane)……102
Figure 6.17: Simulated S_{11}- parameters of suspended meshed antennae with and without solar cell…….……102

Figure 6.18: Simulated radiation patterns of the meshed antennae with and without solar cell: (a) H-plane downlink / with and without solar cells, (b) H-plane uplink / with and without the solar cells, (c) E-plane downlink / with and without solar cells, (d) E-plane uplink / with and without the solar cells……..….103
Figure 6.19: Antennae far-field measurement for the meshed suspended proposed antennae in the anechoic chamber……..……104
Figure 6.20: Simulated and measured results of far-field radiation patterns: (a) *H*-plane downlink, (b) *H*-plane uplink, (c) *E*-plane downlink, (d) *E*-plane uplink for suspended transparent patch antennae……...…….106
Figure 6.21: 3D-patterns: (a) H-plane downlink, (b) H-plane up link radiation patterns, (c) E-plane down-link, (d) E-plane up link……...…108
Figure 6.22: Simulated total radiation efficiency and realized gain at (a) down-link, (b) up-link resonance frequency……109
Figure 6.23. Polycrystalline solar cell DC characteristics measurement; (a) flood Light Solar Simulator (normal incidence) (b) from oblique angle (c) without any antennae integrated above…….112
Figure 6.24: light meter….....112
Figure 6.25: ITO suspended antennae integrated with solar cell Overall view……..….115
Figure 6.26: Simulated results for transparent ITO patch Antennae (a) S_{11}-parameter (dB) radiation patterns; (b) down-link at11.95 GHz, and (c) uplink at14.25 GHz……..…116
Figure 6.27: Single suspended meshed patch antennae integrated with solar cell: perspective view in CST Microwave Studio……..117
Figure 6.28: Meshed antennae with ITO suspended patch…….….118
Figure 6.29: Simulated results of ITO suspended meshed antennae: (a) S_{11}- parameters, radiation patterns; (b) down-link at 11.95 GHz, and (c) uplink at 14.25 GHz…….119
Figure 6.30: Simulated S_{11}-parameters of ITO suspended patch, suspended meshed patch, and ITO suspended meshed antennae……..120
Figure 7.1: Dual-polarised suspended meshed patch antennae with a poly-Si solar cell: (a) design in CST Microwave Studio; (b) side view; (c) fabricated prototype antennae……125
Figure 7.2: Simulated and measured reflection coefficients of the dual-polarised solar patch antennae (a) S_{11}, (b) S_{22}…….126
Figure 7.3: cross-polarisation isolation level……..127
Figure 7.4: Simulated E-plane and H-plane far-field radiation patterns (a) antennae fed through port1 (b) antennae fed through port 2……..….128

Figure 7.5: Configuration of the 2 × 2 sub-array dual-Polarized antennae……130
Figure 7.6: Simulated E-plane and H-plane far-field radiation of patterns 2 × 2 element sub-array……....131
Figure 7.7: Simulated S_{11} reflection coefficients (S_{11} port 1 – S_{11} port 8)……...133
Figure 7.8: Simulated 3D far-field radiation pattern of the 2 x 2 sub-array solar antennae, at (a) 11.95 GHz downlink, (b) 14.25 GHz uplink…….……134

List of Tables

Table 2.1: Coaxial Probe Fed advantages and disadvantages ……...……..23
Table 2.2: Microstrip line feed advantages and disadvantages……..24
Table 2.3: Proximity-coupled feed advantages and disadvantages……..…….25
Table 2.4: Aperture coupled feed advantages and disadvantages……..26
Table 4.1: Recorded of solar cells efficiencies……..63
Table 5.1: Impedance characteristic of square patch antennae obtained by the theoretical model and CST simulated results…….….71
Table 5.2: Input Impedance of square single slot patch antennae obtained by the theoretical model and CST simulation……...….77
Table 5.3: Impedances characteristic of slots loaded square patch antennae obtained by the theoretical model and CST simulated results……83
Table: 6.1. Performance results for the proposed antennae over the uplink and downlink frequency bands…….…….110
Table 6.2: Solar cell performance characteristics……..……..113
Table 6.3: Summary of simulation results for three antennae over resonance frequencies bands……...120

Glossary of symbols

Symbol	Definitions
ε_r	Relative Dielectric constant
ε_0	Permittivity of free space
t	Thickness of Microstrip line
L	Length antennae
W	Width antennae
L_{eff}	Effective patch length
W_{eff}	Effective patch width
ε_{reff}	Effective permittivity
λ	Wavelength
λ_0	Free space wavelength
λ_{reff}	Effective wavelength
h	Substrate thickness
f	Frequency
Zo	Characteristic impedance of patch antennae
Z_{in}	Input impedance
Δf	The frequency difference
Zt	Impedance transformers
S_{11}	Reflection coefficient (port 1)
S_{12}	Transmission coefficient (from port 2 to port 1)
S_{21}	Transmission coefficient (from port 1 to port 2)
S_{22}	Reflection coefficient (port 2)
μ_o	Permeability of free space
μ	Relative permeability
c	Speed of light (= 3 x 108 m/s)
V_p	Phase velocity
$D_{(\theta, \phi)}$	Angular directivity
D_{max}	Maximum directivity
$G_{(\theta, \phi)}$	Angular gain
GR	Gain of the Antennae Under Test
G_{max}	Maximum gain
G_T	Gain of the reference antennae
L_{Cable}	Cable loss
e_c	Conductance efficiency
e_{cd}	Radiation efficiency
e_d	Dielectric efficiency
et	Total efficiency
λ_g	Guide wavelength in the dielectric
Rs	Surface resistance

Qt	Total quality factor of the antennae
Q_c	Q factor of the antennae due to conduction loss
Q_d	Q factor of the antennae due to dielectric loss
Q_r	Q factor of the antennae due to radiation loss
Q_{sw}	Q factor due to surface wave loss
tanδ	Dielectric loss tangent
Y	Admittance
G	Conductance
k	The wave number
k_0	The wave number in free space
J_1	The Bessel function of the first kind of order
a, b	Patch dimensions with extension length.
B	Capacitance due to fringing fields
Gr	Radiation conductance
D	Antennae directivity
C	Capacitance
E	Electric field strength
e	Electronic charge
I	Current
I_D	Diode current
I_{MP}	Cell current at the maximum power point
I_{ph}	Photo generated current
Is	Saturation current
V_{MP}	Cell voltage at the maximum power point
V_{oc}	Open-circuit voltage
P_{in}	Total input solar power
P_{MP}	Solar maximum power
η	Solar efficiency
P_R	Power received by the AUT
R	Distance between the AUT and the receiving antennae
q	Electric charge of an electron
Si	Silicon
Cp	Patch antennae boundary
m,n	Integers relating to mode numbers

Glossary of Acronyms

RF	Radio Frequency
ITO	Indium Tin Oxide
FTO	Florid Tin Oxide
WiMAX	Worldwide Interoperability for Microwave Access
WLAN	Wireless Local Area Network
UMTS	Universal Mobile Telecommunication System
GSM	Global System for Mobile Communications
LTE	Long-Term Evaluation
BW	Bandwidth
UWB	Ultra Wide Band
VSWR	Voltage Standing Wave Ratio
dB	Decibel
Co-pol	Co-polarisation
Cross-pol	Cross-polarisation
FBW	Fractional Bandwidth
FTB	Front- to- back
GHz	Gigahertz
MHz	Megahertz
EM	Electromagnetic
LHCP	Left-hand Circular Polarisation
RHCP	Right-hand Circular Polarisation
LP	Linear Polarisation
MPA	Microstrip Patch Antennae
PIFA	Planar Inverted-F Antennae
MIC	Microwave Integrated Circuit
MMIC	Monolithic Microwave Integrated Circuit
VNA	Vector Network Analyser
a-Si	amorphous silicon
Poly-Si	Polycrystalline Silicon
Mono-Si	Monocrystalline Silicon
PV	Photovoltaics
TM	Transverse Magnetic
dBi	Decibel isotropic
DC	Direct Current
FF	Fill Factor
AUT	Antennae Under Test

Acknowledgements

I would like to express my heartfelt gratitude to my supervisors, namely; Dr. Michael Elsdon, Prof. Stephen Foti, and Prof. David Smith for their tremendous support, inspiring comments and experience guidance through the course of my PhD research.

I am deeply grateful to my parents and all of my brothers and sisters for their continuous support, encouragement. My deepest gratitude goes to my dearest wife, who has persistently accompanied me in completing this journey, I am grateful for her immense patience and support and encouragement during my research.

Finally, I would like to thank the Libyan Ministry of Higher Education and Scientific Research for supporting me during my study.

Declaration

I declare that the work contained in this thesis has not been submitted for any other award and that it is all my own work. I also confirm that this work fully acknowledges opinions, ideas and contributions from the work of others.

Any ethical clearance for the research presented in this thesis has been approved. Approval has been sought and granted by the Faculty Ethics Committee on 28/01/2015.

I declare that the Word Count of this Thesis is 35,322 words.

Name: Farhat Emhemed Nashad

Signature:

Date: 14/11/2018

Chapter 1 Introduction

1.1 Background

1.1.1 Historical Review of Patch Antennae

The history and concept of planar antennae dates back to 1953, when radiated microstrip geometries were first contemplated by Dechamps, in the USA [1-3]. In 1955, the initial part for a microstrip aerial flat element entitled ‘‘Flat aerial for ultra-high frequencies’’ by Gutton and Baissinot was given a patent in France [4]. Shortly thereafter, Lewin carried out investigations of radiation from stripline discontinuities [5]. None of the previous patented proposed microstrip configurations were called ‘microstrip patch antennae’, as they are known nowadays. The term ‘microstrip’ referred to a microstrip transmission line. From the mid- to-late 1960s, further research for the basic element of the microstrip patch antennae was carried out by Kaloi. Later, in 1969, the ability of rectangular and circular microstrip resonators to radiate efficiently was noted by Denlinger [6], in work which described the electromagnetic radiation mechanism of a rectangular microstrip resonator, which is attributed to the discontinuities at each end of a truncated microstrip transmission line. Later in the same year, Watkins described the resonant modes (fields and currents) of circular microstrip geometries [7].

Subsequently, the first implementation of the practical microstrip antennae applications were to wait until the 1970s [8, 9]. Early in that decade, the first practical microstrip-radiating element of a conducting patch was conceived by Byron [10], with specified dimensions of a half wavelength width and several wavelengths’ length, separated from the layer of the ground plane by a dielectric substrate. It was fed by coaxial connectors at the radiating edge and used as ‘a new Flush Mounted Antennae Element for Phased Array Applications’. Shortly thereafter, Munson [11] patented another practical microstrip patch element. His designs were developed and resulted in low-profile antennae structures that could be used in some applications on flush-mounted antennae systems: for instance, in space rockets. Also, Howell designed basic rectangular and circular patch elements in 1972 [12]. The design consisted of a low-profile planar resonating element, separated by a length of very thin dielectric substrate from the ground plane. During the 1980s and 1990s, patch antennae, due to their obvious advantages and use of new substrate materials, were given considerable attention. Since then, many studies have concentrated on microstrip antennae, which became

the subject of a special issue of the IEEE [3]. In addition, a large number of books have been published. Recent years have seen continued fast development of microstrip patch antennae, which are now considered one of the most common types of antennae, and have been extensively used for civilian and military applications, such as radars, military and commercial applications, including satellites, mobile communications, television broadcasting, ultra-wideband communication systems, biomedicine, the automotive industry and spacecraft. Moreover, they have potential for further future developments to miniaturise metamaterial and integrated PV solar cell microstrip antennae.

1.1.2 Photovoltaic Solar Cells and Microwave Communication Antennae

Photovoltaic (PV) solar cells have been known for more than 150 years, with the study of photo-electricity stretching back to the mid-1800s and to the industrial revolution. In 1839, Edmund Becquerel, a French scientist [13], discovered the photovoltaic effect on an electrode in a conductive solution where voltage and electric current in the material were created upon exposure to light. Over 100 years later, in 1941, solar cells were developed when Russell Ohl patented a solar cell "Light sensitive device". During the 1950s, solar cell wafers were achieved, and in 1954, the first practical silicon solar cell of DC power was developed at Bell Laboratories in the USA [14]. It was for space activities, and specifically, to power spacecraft communications systems. Over subsequent years, solar cells were improved dramatically basedon growinginterest in applications for terrestrial co mmunications: i.e. antennae or for industrial purposes.

For either satellite SATCOM stations or terrestrial communication sites, wireless communication technologies have evolved rapidly over, and demands on communications services require higher data rates over long distances [15]. Today's satellite communications have advantages over other communication technologies for remote area applications, and provide good solutions, such as constant connectivity, redundancy and back-up services for remote locations. In a number of applications in places where access to the electric power grid is not easily obtainable, communication systems with uninterruptible power source capabilities are required to provide long-term and continuous communication services. PV solar cell panels can serve as a viable power source for these communication terminals in rural, remote areas, such as remote base stations, remote homes, caravans, and villages in developing countries. In addition, they can be used at off-grid remote industrial locations for Supervisory Control and Data Acquisition (SCADA) remote fixed sites, which are used for

gas and oil cathodic protection monitoring points, along pipelines, as well as for different facility substations of remote sites of automatic monitoring weather stations [15, 16]. In any of the previously mentioned applications, the collected data information is transmitted to and received, from a satellite via one- or two-way wireless communication systems. In these systems, the antennae is a key component, and recent years have witnessed growing interest and an increasing need to provide compact, lightweight, high-gain broadband antennae for good performance long distance wireless communication systems [16].

1.2 Problem Statement

At no-power wireless communication locations, the microwave antennae and solar PV cells ideally work independently of each other in order to avoid any electromagnetic or thermal interference [17-24]. This stand-alone arrangement has an effect on the size, weight and surface area [25], which must be sufficiently large, and this increases in project components, in addition to increase of overall power consumption due to peripheral cables and terminals, hence, making the project more costly and uneconomical. Moreover, these types of autonomous systems are not suitable for today's modern, compact, low-profile broadband communication applications. The Figure 1.1 illustrates an independently solar cell panel powered remote antennae communication systems.

Figure1.1: Independent solar power system for remote area communication system [26, 27]

Such autonomous systems present challenges and drawbacks in full integrating topologies of microwave antennae performance and PV technology on the same surface along with their different configuring techniques. Therefore, the proposed solution will be addressed in detail within this thesis in the subsequent chapters.

1.3 Research Motivations and Aims

There are several main motivations for integrating antennae with solar cells for remote area applications:

- Self-powered integrated systems for remote area wireless communications.
- A cost-effective system for rural or remote sites, with the integration of antennae elements and solar PV cells on the same surface can improve economic viability. Therefore, the relatively lower cost of this technology is another advantage in comparison to other autonomous systems.
- No significant work has been carried out into the design of integrated solar wider dual-band antennae in remote areas to achieve good characteristics for long distance communications, such as earth-space satellite communications. Most works in the literature have focused on the combination of solar PV cells and antennae operating in relatively low frequency bands and exhibiting narrow bandwidths.
- Most solar integrated antennae have linear polarisation or circular polarisation performance. Therefore, these cannot be developed and employed for dual polarisation compact array applications.
- A technology is sought that could be used for most applications of both satellite and terrestrial systems at remote locations.

Considering the discussion in the foregoing, the aims of this research are as follows:

- To propose and demonstrate a prototype dual-band, dual-polarised transparent patch antennae which provides a good performance trade-off between RF antennae performance and solar cell illumination efficiency, and which can be developed into two-dimensional fully dual-polarised PV array transparent patch antennae.
- Perform a literature survey and rigorous investigation on integration techniques for the efficient co-location of RF antennae elements and photovoltaic cells.
- To investigate of antennae type and antennae geometry for efficient integration of dual- polarised microwave antennae with photovoltaic solar cells.

- Present and undertake theoretical analytical model that can be applied to propose slot loaded compact patch antennae design to determine the performance.
- To investigate direct coupling signal feeding technique for RF antennae elements which is compatible with good illumination efficiency operation of the solar panels.
- To realise the compact configuration using direct illumination geometries of a small-antennae.
- To identify the optimum integrated RF antennae and solar cell configuration from the above and to:
    - Propose new dual-linear polarised transparent solar patch antennae for frequency re-use of Ku-band down link and uplink satellite communications.
    - Design, Develop and Simulate.
    - Construct and demonstrate a prototype antennae.

1.4 Original Contribution

The original contributions to the world of knowledge from this research are summarised in the following:

- Proposed broad dual-band (Downlink, Uplink) integrated photovoltaic solar compact transparent patch antenna element (Bandwidth enhancement) for remote areas, which provides a good performance trade-off between the performance of RF antenna and solar cell. It covers the frequency bands ranging from 11.7 - 12.22 GHz (downlink) and 14.0 - 14.5 GHz (uplink) allocated by the ITU to Regions 1 and 2.
- New proposed of dual-polarised photovoltaic transparent patch antenna for frequency re-use in Ku-band satellite downlink and uplink communications, serves as a basic building-block element, which can be developed and employing into two-dimensional dual-polarised PV array patch antennas.
- Proposed a sub-array of dual-polarised transparent antenna elements, with narrow beam and improved gain more than 13 dBi and a cross-polar discrimination of greater than 30 dB, which is a requirement for frequency re-use operation, and has the potential to be developed to meet the full requirements of a Ku-band solar 2D-phased array antenna to achieve a high gain and good characteristics for long distance communications.
- A rigorous investigation of the integration techniques from the perspective of both RF antenna and PV solar cell. The results of this study provide a new knowledge and

design methodology for future high frequency/ millimeter-wave photovoltaic antenna configurations.

The block diagram of the overall research roadmap and the original contributions of this thesis is illustrated in Figure 1.3.

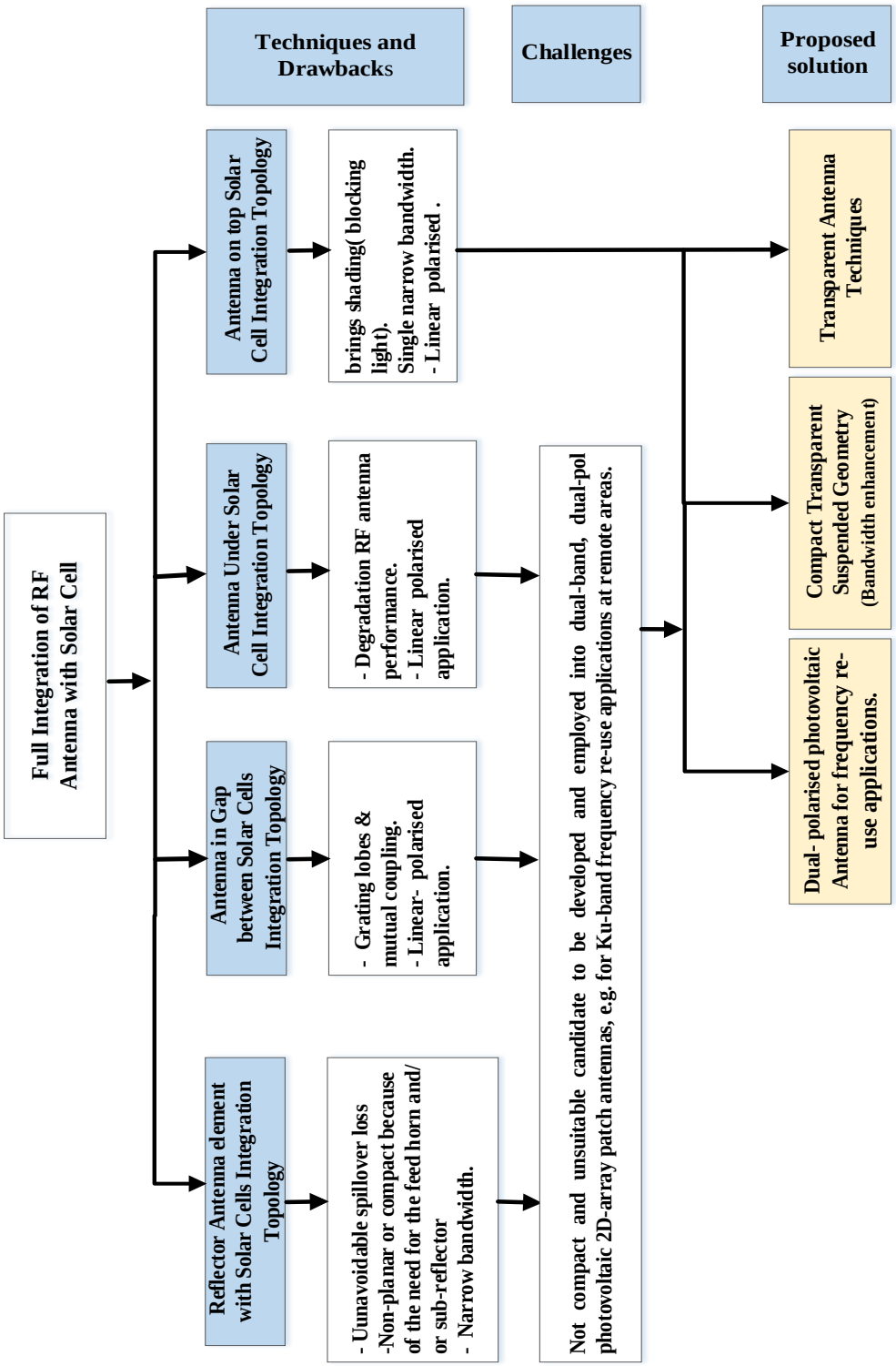

Figure 1.2: Block diagram of the research roadmap and the original contributions

1.5 Thesis Outline

Chapter 1: A brief information about the historical review of the development of microstrip patch antennae and photovoltaic solar cells are given, in addition, the problem statement is introduced. Following this introductory, the research motivation and aims for combined of microwave antennae with photovoltaics are outlines and introduced. After that, a rigorous literature review including previous researches and various integration techniques of microwave antennae with PV is performed. The research methodology for the thesis are described and the flowchart diagram and the roadmap are illustrated.

Chapter 2: In this chapter, antennae types and its main characteristic parameters such as radiation pattern, beam width, directivity, input impedance, bandwidth, gain, efficiency, polarisation purity and Dual-polarisation are explained. The selection of antennae type with respect to solar cell is described. Then, the fundamental theory of microstrip patch antennae (MPAs), including structures, the advantages and disadvantages, feeding techniques are Introduced. The present analysis methods including, transmission line model, cavity model, co-planar multi-port network with the design equations, which are used for analysing the MPAs are reviewed and explained in detail. Investigation into the most a suitable modelling approach for analysing complex geometries is presented.

Chapter 3: This chapter involves the analysis of a simple square geometry patch using the Green's function approach to determine an input impedance. The relevant basic theory of slot-loaded patch is explained. This followed by theoretical analysis of the slots loaded on a microstrip patch antennae by using a modelling technique. The most often suggested technique is the segmentation approach in conjunction with multiport network modelling (MNM) that can be applied for patch antennae with irregular structures. This approach gives flexibility in modelling such complicated structures to determine the input impedance characteristic. The results obtained from the mathematical are demonstrated, compared with CST simulations, and discussed.

Chapter 4: Gives a background on photovoltaics and solar cells. It provides the functions and an understanding of photovoltaics and crystalline silicon solar cells operation. The most common types of crystalline silicon solar cells structures are introduced, with their advantages and disadvantages. This chapter also covers the basic theory and models of solar cell PV simple modelling using an equivalent electrical circuit. Then, the I-V characterization of the main parameters is presented and illustrated, followed by a

description of efficiency and outlines of loss factors for these solar cells. It presents also the structure connection of crystalline silicon solar cells into a module structure.

Chapter 5: This chapter includes the design of a dual band dual frequency transparent patch antennae integrated with a solar cell, which is the use of solar antennae integration topology of the solar cell beneath the antennae element. A proposed technique using a suspended transparent element is implemented. This solar antennae is used to achieve broadband performance with good transparency for the Ku-band desired applications in remote areas. Investigation is performed on the selection of an appropriate substrate material for the proposed transparent antennae. The proposed antennae is fabricated and tested, and then rigorous investigations into the effect of the solar integration on the RF antennae performance are carried out. The simulation and practical results are compared and discussed. The solar cell performance is also determined with respect to the combination with the antennae. Moreover, in this chapter, a bandwidth enhancement proposed approach is implemented for the previous antennae design that is developed in overall transparency, using transparent patch with ITO conductive material, instead of meshed elements.

Chapter 6: Provides new proposed design of dual-polarised, dual-band suspended transparent patch antennae integrated with solar cells for Ku-band frequency re-use, are designed and demonstrated, which can be developed and employed into two-dimensional fully PV array patch antennae. This design is modelled and fabricated, the obtained results are demonstrated and discussed. In this chapter, also an arrangement of 2×2, sub-array dual-polarised transparent patch antennae is presented with good port isolation.

Chapter 7: The conclusions of the study and suggestions for future work are presented.

Chapter 2 Antennae Theory

2.1 Introduction

In this chapter, an antennae theory is given before embarking on the design of the proposed dual-band, dual-polarised transparent antennae, for frequency re-use in Ku-band SATCOM. Firstly, in this chapter, critical performance parameters for the antennae are described. This chapter also describes the theory of microstrip patch antennae, followed by their main advantages and disadvantages: also, a description of feed techniques is given. Then, the most popular analytical methods for rectangular or square microstrip patch antennae are discussed.

2.2 Antennae

There are numerous definitions of the antennae and these are similar in meaning in general, as in [28-31]. There are also a number of varieties of antennae available in the communication environment and each one has its own specifications and application. An antennae's radiating element can be of different shapes and sizes. The most commonly used can be classified as:

- Wire antennae: this kind of antennae can be seen everywhere, for example on buildings, ships, automobiles and aircraft. It takes different shapes such as a dipole, helix and loop, short dipole antennae, half-wave dipole, monopole antennae, folded dipole antennae, and cloverleaf antennae.
- Aperture or slot antennae[32]: this kind of antennae is more familiar today than the wire antennae, and slot antennae are very useful for spacecraft and aircraft applications, because "they can be very conveniently flush–mounted on the skin of an aircraft or spacecraft. Also, they can be covered with a direct material to protect them from hazardous conditions of the environment" [33].
- Microstrip antennae or printed patch antennae: this kind of antennae is used commonly for government and commercial applications. They consist of a metallic patch on a ground substrate.
- Array antennae: this kind of antennae consists of more than one element, because some applications require radiation characteristics, which may not be achieved by a single element [34].

- Reflector Antennae: these antennae are used over a long distance. Therefore, to transmit or receive signals that have to travel millions of miles, a reflector antennae should be used.
- Lens Antennae: the spherically radiated microwave energy can be converted into a plane wave (in a given direction) by using a point source (open end of the waveguide) with a collimating lens. A collimating lens forces all radial segments of the spherical wave front into parallel paths [35].
- Other Antennae such as NFC Antennae, Fractal Antennae and Wearable Antennae.

Microwave antennae are a very important device, which have many benefits in wireless communication systems. Planar antennae are finding increasing popularity due to the advantages in their size, minimal cost and ease of fabrication process: especially for microstrip antennae. Due to their low profile characteristics, these have come to be in demand in modern mobile and advanced wireless systems [36, 37]. The microstrip antennae will be presented and addressed in this thesis.

2.2.1 Antennae parameters

There are some important parameters, which can be used to gauge the performance of an antennae, and the critical parameters are explained in the subsections below.

2.2.1.1 Radiation pattern

The radiation pattern of any antennae is defined as the mathematical functions of a graphical representation of the far-field radiation properties of the antennae as a function of space coordinates. It is specified by the elevation angle and the azimuth angle. When the distance between the transmitter and the receiver is bigger than or equal to $2D^2/\lambda$, the far field-region is considered where D is the largest dimension of the antennae and λ is the wavelength. The antennae radiates in a linearly polarised manner, with the electric field lying in the same direction as the patch length. Figure 2.1 shows an antennae radiation pattern: the two common types of antennae radiation pattern are [38]:

- Power Pattern – the square of the magnitude weight of the electric $|E^2|$ or magnetic field $|H^2|$ in the far field and mostly expressed in decibels (dB) or given on a logarithmic scale.
- Field Pattern - magnitude of the electric $|E|$ or magnetic field $|H|$.

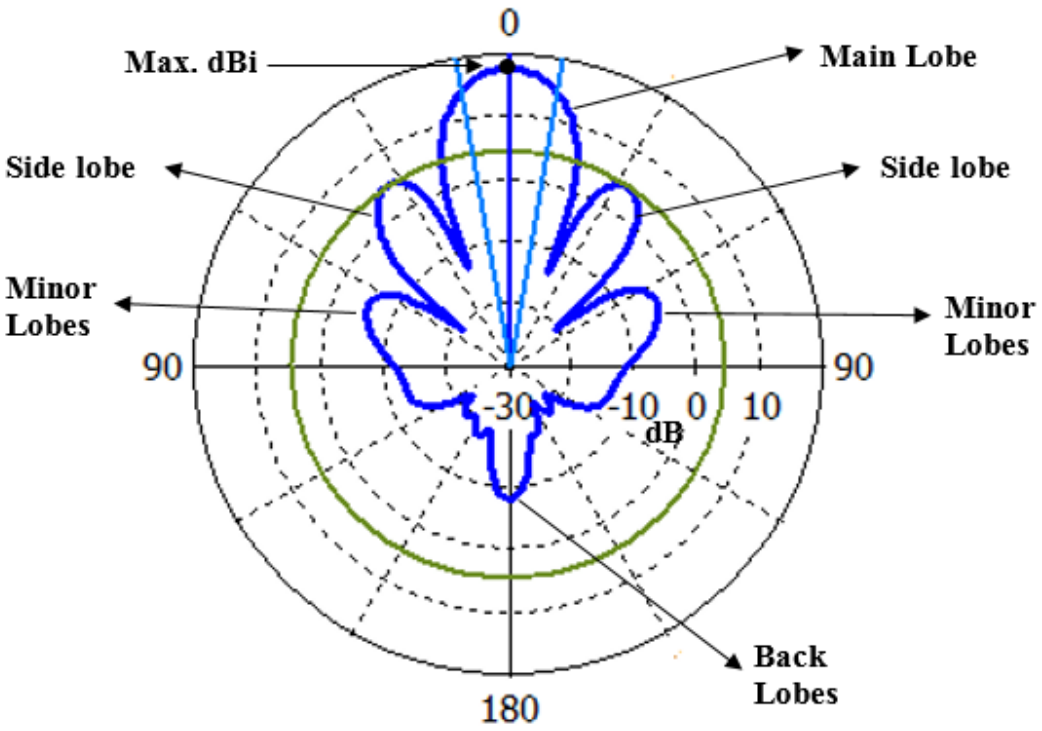

Figure 2.1: Antennae radiation pattern parameters

Figure 2.1 illustrates an antennae radiation pattern with the parts of the pattern, termed lobes, classified as follows:

- Main lobe or major lobe: the radiation lobe in the desired direction of maximum radiation.
- Minor lobe: radiation lobe in undesired directions. Side lobes are the largest of the minor lobes.
- Back lobe: The radiation lobe that is inverse to the main lobe.

The front-to-back ratio (FBR) is the ratio of power gain in the maximum peak gain direction, to the power gain in the direction of the opposite-side turned 180◦ relative to the main gain direction.

2.2.1.2 Beamwidth

The beam width is another important characteristic parameter in antennae applications, which is defined in each plane as the angle between the points of the half-power (-3dB) of the main pattern lobe of the antennae, as illustrated in Figure 2.2. The antennae beam-width is usually expressed by degrees.

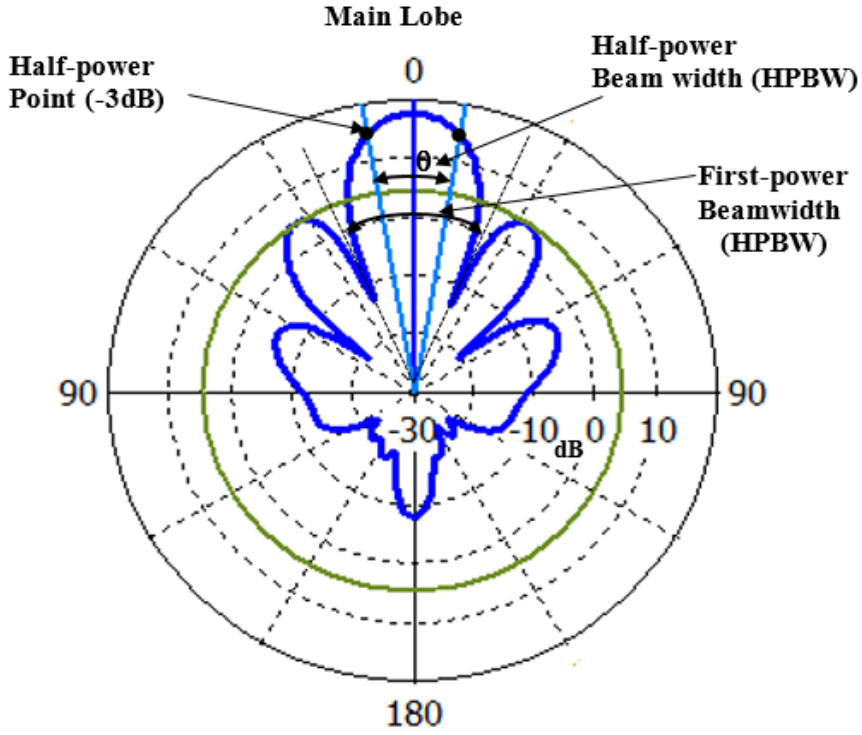

Figure 2.2: Beam-width of an antennae

The beam-width can be called half-power beam-width (HPBW), which is the angular width of the main beam at the half-power points where the power drops to one-half (-3 dB) below its maximum beam value, or the first null beam width (FNBW), which is the angular width between the first nulls on either side of the main beam. The most commonly used beam-width in practical terms is HPBW, if no other information is obtained. The beam-width can be also used as a compromise between the side lobe level and the beam-width itself; as the side lobe increases, the beam-width decreases and vice versa [38].

2.2.1.3 Input impedance

The input impedance of an antennae is defined as the ratio of the voltage appearing across the connector of the input port to the current at the same terminal point. Alternatively, the input impedance is determined by the ratio of the components of the electric field to magnetic fields at that point. Hence, it can be written as:

$$Z_A = R_A + jX_A \tag{2.1}$$

where, Z_A, is the antennae impedance at the input port terminal, R_A is the antennae resistance, and X_A the antennae reactance. The power stored in the near electric field of the antennae is represented by the imaginary part, X_A of the input impedance. Figure 2.3 shows dipole antennae in transmitting mode.

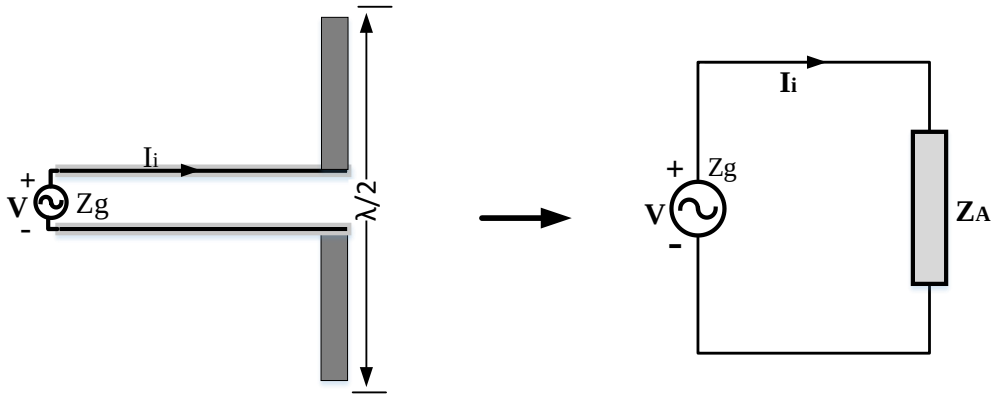

Antenna element

(a) (b)

Figure 2.3: Antennae in transmitting mode

The resistive part, R_A consists of two components; radiation resistance (R_r) and loss resistance (R_L), as given in Equation (2.2)

$$R_A = R_R + R_L \tag{2.2}$$

If an antennae is connected to a signal generator with internal impedance for feeding the antennae as illustrated in Figure 2.3 (a) in a transmitting mode.

$$Z_g = R_g + jX_g \tag{2.3}$$

In Equation (2.3), R_g = resistance of generator impedance, and X_g = reactance of generator impedance. In Figure. 2.3 (b), the current I_g that flows in the circuit, as shown in the equivalent circuit model, can be calculated as [39]:

$$I_i = \frac{V_g}{Z_t} = \frac{V_g}{Z_g + Z_A} \tag{2.4}$$

where, *Vg* is the peak voltage of the generator. The total power supplied to the antennae, which is distributed between the signal source and the load, can be given as:

$$P_T = P_A + P_G \tag{2.5}$$

$$P_T = \frac{1}{2}|I_i|^2 R_A + \frac{1}{2}|I_i|^2 R_G \tag{2.6}$$

In order to transfer full power to the dipole antennae, as in Figure 2.3, the input impedance of the antennae and the signal generator internal impedance need to be conjugate matched.

$$R_A = R_G \tag{2.7}$$

$$X_A = -X_G \tag{2.8}$$

The maximum transmitted power transferred from the excitation supply to the dipole antennae can be given as follows [39]:

$$P = \frac{|V_g|^2}{4}\left[\frac{1}{R_r + R_L}\right] \tag{2.9}$$

Radiation resistance *Rr* can be calculated from the power radiated as:

$$P_{rad} = \frac{1}{2}|I_g|^2 R_r \tag{2.10}$$

Power loss is represented as heat in the antennae, and can be given as:

$$P_{loss} = \frac{1}{2}|I_g|^2 R_L \tag{2.11}$$

For a receiving antennae similar to the antennae in transmitting mode, the receiving mode is shown in Figure 2.4. If the antennae is under conjugate impedance matching, half of the total maximum power is transferred to the load, and the other half is reradiated through R_r and dissipated as heat through R_L.

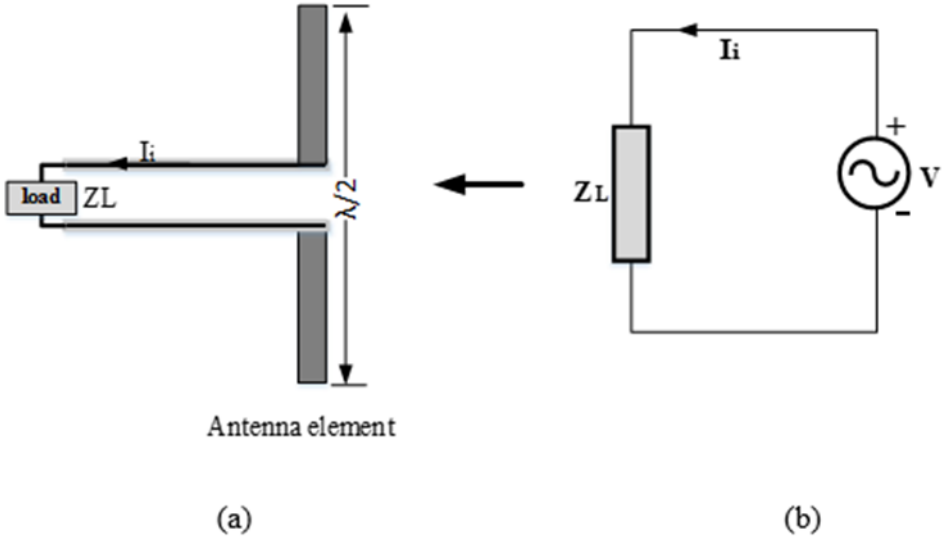

Figure 2.4: Antennae in receiving mode

2.2.1.4 Scattering Parameters (S-parameters)

At high frequencies, when circuit elements have to be characterised, scattering parameters are used to represent the transmission line or microstrip line as two-port networks, as shown in Figure 2.5. The transmission line serves to separate forward and backward travelling waves. The two-port characterisation of networks at high frequencies is based on incident

and reflected waves rather than voltage or current. The equivalent voltages V_r are incident voltage waves travelling along the transmission line to forward port "1", and the equivalent voltages V are reflected voltage waves travelling away from port "n" [40].

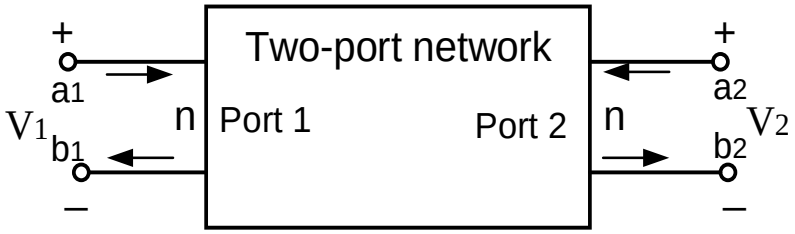

Figure 2.5: Two-port network

The scattering-parameters of the two-ports are defined as:

$$b_1 = S_{11}a_1 + S_{12}a_2 \tag{2.12}$$

$$b_2 = S_{21}a_1 + S_{22}a_2 \tag{2.13}$$

The relationship between the S-parameter and the reflected incident power can be given in matrix form as:

$$\begin{bmatrix} b_1 \\ b_2 \end{bmatrix} = \begin{bmatrix} S_{11} & S_{12} \\ S_{21} & S_{22} \end{bmatrix} \begin{bmatrix} a_1 \\ a_2 \end{bmatrix} \tag{2.14}$$

To find S_{11} the output line of the two-ports network is matched, $Z_L = Zo$, the load cannot reflect power: $a_2 = 0$, so that S_{11} can be found from the following equation [41]:

$$b_1 = S_{11}a_1 + S_{12}a_2 \tag{2.15}$$

$$S_{11} = \frac{b_1}{a_1} \quad , \quad a_2 = 0 \tag{2.16}$$

$$S_{22} = \frac{b_2}{a_2} \quad , \quad a_1 = 0 \tag{2.17}$$

By matching the input and the output, the remaining parameters are as follows:

$$S_{21} = \frac{b_2}{a_1} , \; a_2 = 0 \tag{2.18}$$

$$S_{12} = \frac{b_1}{a_2} , \; a_1 = 0 \tag{2.19}$$

where, S_{11} = is the input reflection coefficient at port1, with $a_2 = 0$

S_{22} = is the output reflection coefficient at port2, with $a_1 = 0$

S_{21}= is the forward transfer coefficient (port1 to port2)

S_{12} = is the reverse transfer coefficient (port2 to port1)

The reflection coefficient for an impedance "*Z*" loading a transmission line is [40]:

$$\Gamma = \frac{Z - Zo}{Z + Zo} \tag{2.20}$$

Therefore;

$$S_{11} = \frac{Z_{in} - Z_o}{Z_{in} + Z_o} \tag{2.21}$$

And,

$$S_{22} = \frac{Z_{out} - Z_o}{Z_{out} + Z_o} \tag{2.22}$$

2.2.1.5 Return loss (RL)

The return loss (R_L) is a parameter which indicates the amount of power that is "lost "to the load and does not return as a reflection, waves are reflected, leading to the formation of standing waves when the transmitter and antennae impedance do not match. Hence, the *RL* is a parameter similar to the VSWR, indicating how well the transmitter and antennae are matched. *RL* is given in [40] as:

$$R_L = -20 \log_{10} |\Gamma| \tag{2.23}$$

For perfect matching between the transmitter and the antennae, $\Gamma = 0$, and $R_L = \infty$ which means that no power would be reflected back.

2.2.1.6 Bandwidth

Bandwidth (*BW*) can be defined as the frequency range on both sides of the centre frequency of the antennae where the critical characteristic parameters over the desired band of operation are very close in behaviour to those, which are obtained at the centre frequency. Simply, the relation is inverse between the *BW* and its quality factor (*Q*), and can be given as follows [42]:

$$BW = \frac{1}{Q} \tag{2.24}$$

where the impedance bandwidth of the microstrip antennae increasing, when the quality factor (*Q*) is decreased [9]. The bandwidth is normally defined in terms of VSWR as:

$$BW = \frac{VSWR - 1}{Q\sqrt{VSWR}} \tag{2.25}$$

where, VSWR is the Voltage Standing Wave Ratio, and defined in terms of the input reflection coefficient (Γ) as:

$$VSWR = \frac{1+|\Gamma|}{1-|\Gamma|} \tag{2.26}$$

The bandwidth of an antennae is normally determined by its fractional bandwidth (*FBW*), and can be defined as the ratio of the upper to lower frequencies of band operation, and can be given by [33]:

$$FBW = \frac{f_U - f_L}{f_C} \tag{2.27}$$

where f_H, upper frequency, f_L, lower frequency, f_C , centre frequency.

2.2.1.7 Gain, Directivity and Efficiency

Simply, the gain of an antennae is related to the antennae directivity, which is defined by the ratio of the power radiated by the antennae element to that power radiated by an isotropic radiator, which are fed with the same input signal. The gain of an antennae can be expressed as [33, 39]:

$$Gain = \frac{Radiation\ intensity}{Total\ input\ power} = 4\pi \frac{U(\theta, \emptyset)}{P_{in}} \tag{2.28}$$

where P_{in}: total input power, U_θ : radiation intensity in E_θ field. U_φ: radiation intensity in E_φ field. Normally, the antennae's gain is measured by taking into account the directivity (*D*) and the efficiency (*e*) of the antennae. Normally, the overall antennae efficiency is derived as:

$$e_o = e_r e_c e_d \tag{2.29}$$

where, e_0 = total efficiency, e_r = reflection efficiency, e_c = conduction efficiency, e_d = dielectric efficiency.

The relation between antennae's gain and directivity includes another parameter, which describes the total antennae radiation efficiency is given by:

$$G = e_0 . D \tag{2.30}$$

The maximum gain related to the directivity D $(_{\theta, \varphi})$ for the orthogonal θ and φ weights of an antennae can be re-expressed as:

$$G_{(\theta, \varphi)} = e_o . D_{(\theta, \varphi)} \tag{2.31}$$

2.2.1.8 Polarisation

Polarisation is one of the most important properties of a wireless antennae, and can be defined as the orientation of the electric field vector of an electromagnetic wave relative to the antennae propagation [33]. The antennae's polarisation normally refers to the polarisation of the electric field vector of the radiation wave; in other words, the direction of the electric field references to the earth's surface. The most popular types of polarisation are: linear polarisation, which includes horizontal or vertical; and circular polarisation, which includes right and left hand circular polarisations, as shown in Figure 2.6. The electric field vector of a linearly polarised wave is back and forth along a propagation line, whilst in a circularly polarised wave, the electric field vector can be constant in length but rotates around a circular path. A right hand circular polarised (*RHCP*) wave rotates counter-clockwise, whereas in a left hand circular polarized (*LHCP*) wave rotates clockwise [39]. For an antennae to have linear polarisation for instance, electric field (*E*), which has a single component can be represented in terms of two-orthogonal linearly polarised components as:

$$Ex = Ex_0 \cos(\omega t - \beta z) \tag{2.32}$$

And,

$$E_y = E_{y0} \cos(\omega t - \beta_Z + \delta) \tag{2.33}$$

where, β_z is the phase shift of '*E'* propagation in the direction of radiation, δ, phase difference between these components.

Dual-polarisation Antennae for dual feeds can provide benefits in specific communication systems, such as satellite communications. In SatCom communications, dual polarized antennae provide two communication channels for two polarisations; both horizontal and vertical, which either generate transmit or receive radio signal waves simultaneously [43, 44]. For a square patch element, the easiest way to excite dual-polarisation is to feed the patch at two adjacent sides to excite two orthogonal TMo modes. The use of a dual-polarized antennae is more suitable than two antennae operating separately when the available space is limited. The fundamental configuration of a dual-feed polarised antennae is shown in Figure 2.7.

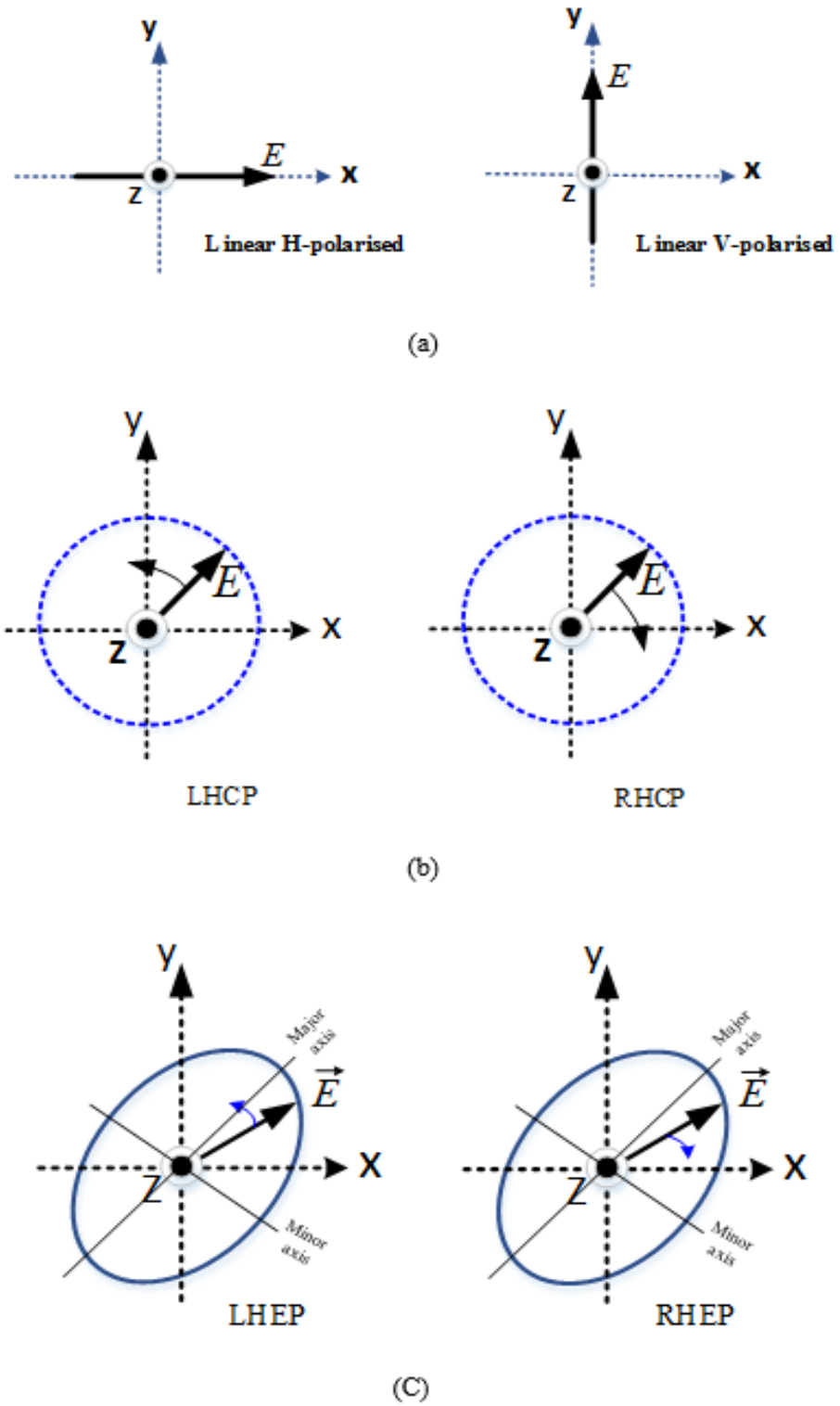

Figure 2.6: Types of Polarisation; (a) linear polarisation, (b) Circular polarisation, (c) Elliptical polarisation

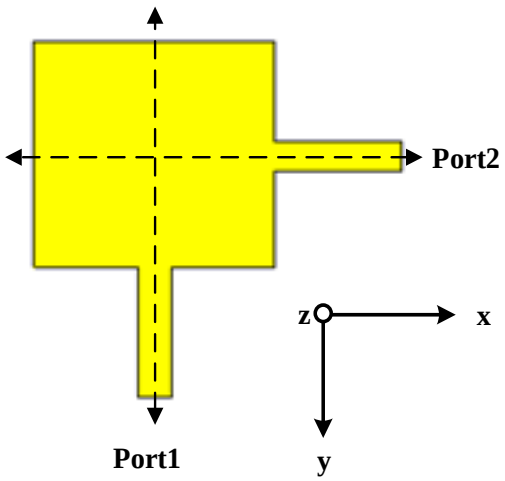

Figure 2.7: Dual-fed patch antennae arrangement

2.2.2 Choice of Antennae Type with Respect to Solar Cell Photovoltaic Integration

For comparison purposes, one of the requirements of this research is to explain some common microwave antennae, as mentioned in Section 2.2, in detail with respect to their integration with solar cells. This was addressed in the literature review in section 1.5. However, in this thesis, printed microwave patch antennae are chosen from among all these types of antennae. This is due to their advantages of planar, lightweight and low profile geometries, and in addition is due to their suitability to be employed in SATCOM communication systems [45]. Therefore, this thesis focuses on the analysis and rigorous investigation of microwave planar dual-fed patch antennae integrated with photovoltaic solar cells. In view of this, a detailed explanation of the microstrip patch antennae is carried out in the sections that follow.

2.2.3 Microstrip Patch Antennae Theory

A microstrip antennae (also known as a printed antennae), which fabricate from microstrip techniques and are a restively new technology and widely used in various applications; especially in wireless communications such as digital broadcasting and mobile radio. The patch antennae element is the most type of microstrip antennae. Basically, most microstrip patch antennae consist of a radiating patch above a dielectric substrate, on the lower surface is a ground plane [33], as shown in Figure 2.8. In general, the patch element is made of conducting materials and may take any shape. Normally, the radiating patch is printed on a

dielectric substrate as can be seen in Figure 2.8, a microstrip patch antennae normally has a lightweight radiating element with a thin slice.

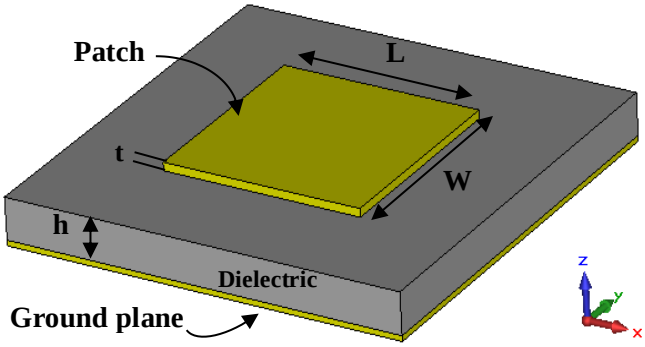

Figure 2.8: patch antennae

This can be expressed as "*t*" which is the patch thickness such that; $t << \lambda o$ (where λo is the free-space wavelength). The dielectric substrate on top of a ground plane with height (h) is usually between $0.003\ \lambda o < h \geq 0.05\ \lambda o$, with a preferable dielectric constant (εr) range of $2.2 < \varepsilon r < 12$. The radiating element can be rectangular, square, triangular, circular, elliptical or any other shape [33], as illustrated in Figure 2.9.

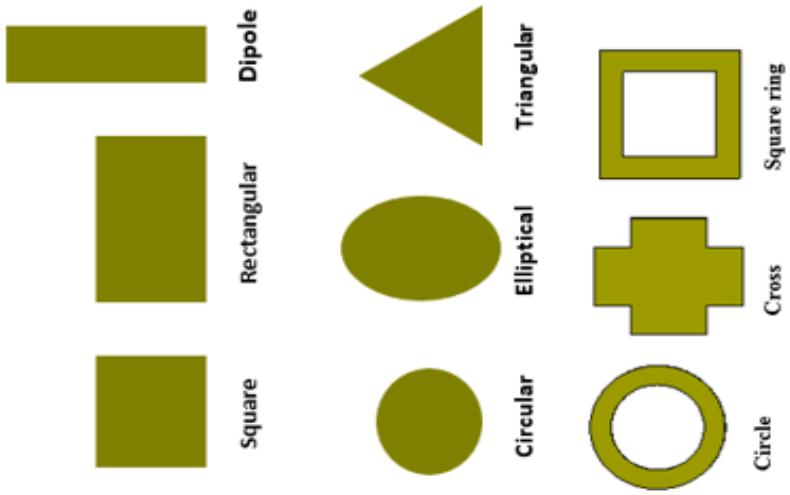

Figure 2.9 Microstrip Antennae shapes

Basically, a microstrip patch antennae radiates due to the fringing fields, which are created between the radiator patch edge and the ground plane through a substrate. Normally, thick substrates provide large bandwidth, yet produce less efficiency. In the process of designing a patch antennae, substrates, which are thick and have a low dielectric constant, are most desirable in terms of providing better efficiency and a large bandwidth: however, they lead to increases in antennae size, and are thus expensive. Meanwhile, using thin substrates with

a higher dielectric constant allows a smaller antennae size to be used [37]. Hence, compromise is required between antennae dimensions and RF performance.

The main advantages of microstrip antennae compared to conventional antennae are [2, 36]:

- Low fabrication costs.
- Simplicity of manufacture.
- Conformable.
- Lightweight and low profile.
- Both linear and circular polarisations are easily achieved.
- Capabilities to be integrated with microwave integrated circuits.
- Matching networks and feed lines can be fabricated on the same substrate with the antennae.

However, microstrip patch antennae suffer from some drawbacks, and are as follows [2]:

- Narrow bandwidth.
- Lower Gain.
- Low efficiency and low power.
- Surface wave excitation and high Q factor.
- Poor polarisation.
- Unipolar radiation characteristic.

2.2.3.1 Feed Antennae Techniques

Microstrip patch antennae can be fed by various techniques: the most common feeding techniques used are; the coaxial probe, microstrip line edge feed, aperture coupling and proximity coupling. These feeding techniques, with their advantages and disadvantages, are classified in Figure 2.10, and are described below.

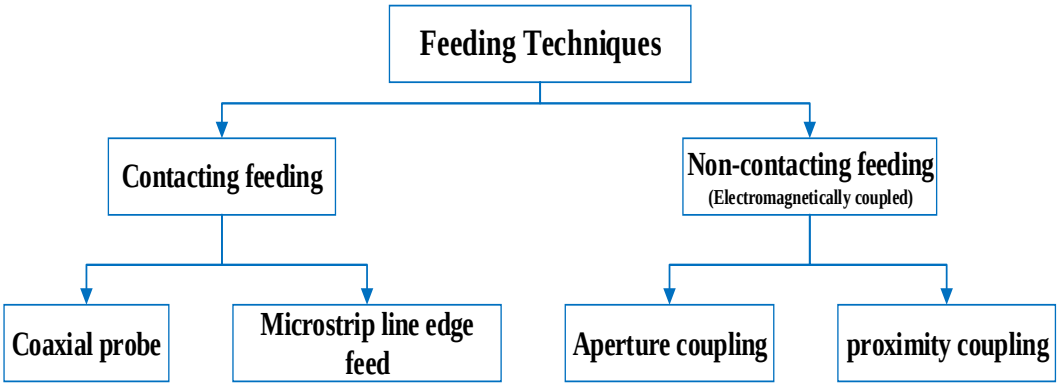

Figure 2.10: Classified of antennae feeding techniques

2.2.3.1.1 Coaxial probe feed

A coaxial probe feed is the most common technique used for the feeding of patch antennae. As can be seen in Figure 2.11, the pin conductor of the coaxial probe is connected to the patch radiating element through the substrate, and the outer conductor is connected to the ground plane [37].

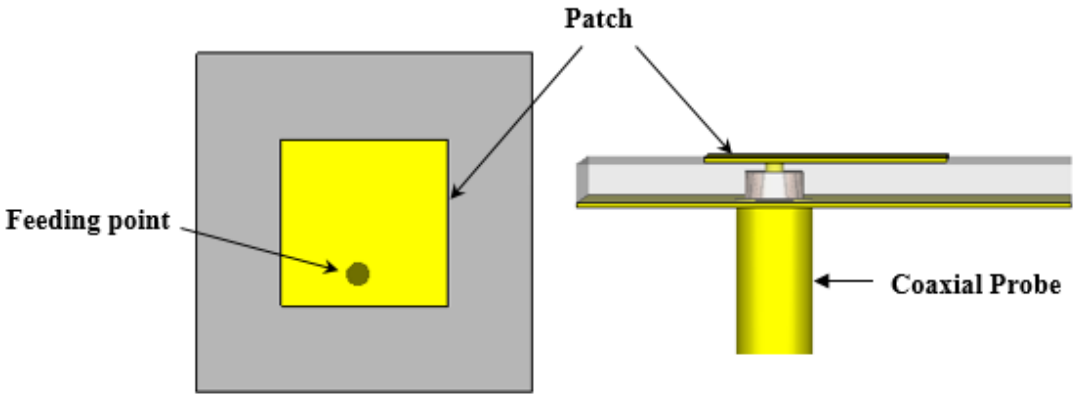

Figure 2.11: Coaxial probe fed patch Antennae

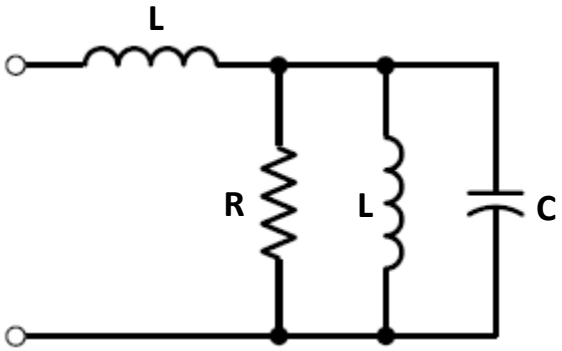

Figure 2.12: Equivalent circuit for coaxial probe fed patch antennae

Table 2.1: Coaxial Probe Fed advantages and disadvantages

Advantages	Disadvantages
➢ Easy to fabricate. ➢ Low spurious feed radiation. ➢ Different value of input impedance obtainable by choosing feed location.	➢ Difficult to model, especially for thick substrates. ➢ Narrow bandwidth. ➢ Cross-polarised radiation due to inherent asymmetries.

2.2.3.1.2 Microstrip Feed line

There are two types of microstrip line edge methods to feed a patch antennae. In the first type, the antennae is fed through a microstrip line at the edge, as shown in Figure 2.13 (a). With this type of feeding, an impedance transformation is needed to match the source impedance of 50 Ω, as the impedance at the edge of the patch is high. The other type is an inset microstrip line feed, in which it is required to run a 50 Ω microstrip feed line to the edge of the patch and create an inset inside the patch in order to find the same impedance point to match, as illustrated in Figure 2.13 (b).

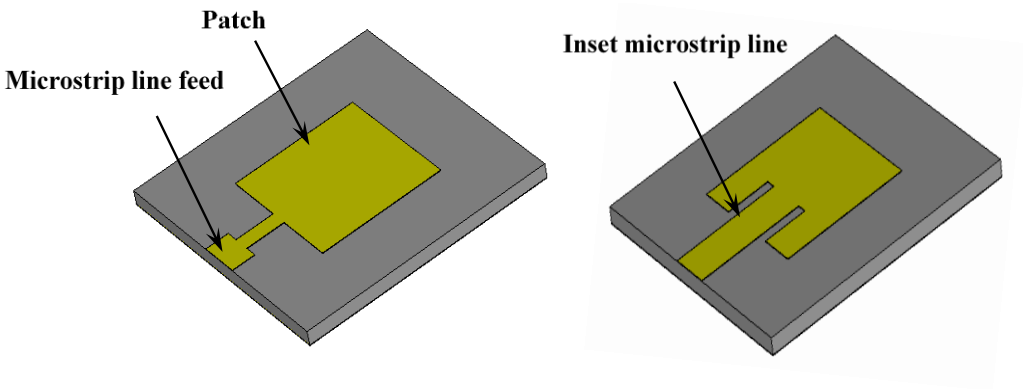

(a) (b)

Figure 2.13: (a) Microstrip line feed patch antennae, (b) Inset microstrip line fed

Table 2.2: Microstrip line feed advantages and disadvantages

Advantages	Disadvantages
➢ Easy to fabricate. ➢ Simple to match. ➢ Rather simple to model.	➢ Surface waves and spurious feed radiation for thick substrates. ➢ Cross-polarised radiation due to inherent asymmetries.

In most microstrip end fed antennae, the feed line impedance (50 ohm) is always the same as the radiation resistance at the edge of the patch, which is usually a few hundred ohms, depending on the patch dimensions and the substrate used. As a result, this input mismatch affects the antennae's performance due to that no total power would be transferred. For this reason, a quarter wave transformer is implemented on the feed network, this improves the performance of the antennae, as there is less reflection [46]. Therefore, the quarter wave transformer is used for matching the patch antennae to the 50-Ohm transmission line. The following expression can be used [47]:

$$Zo = \sqrt{Zin \cdot 50} \tag{2.34}$$

where, Z_0, transmission line impedance and Z_{in}, patch edge input impedance.

2.2.3.1.3 Proximity-coupled feed

The proximity-coupled feed, as illustrated in Figure 2.14, has two layers of a substrate with a_microstrip feed line on the top surface of lower substrate, and with a ground plane on the lower surface. The patch is printed on the top of the upper substrate. The proximity-coupled feed has advantages and disadvantages, as summarised in Table 2.3.

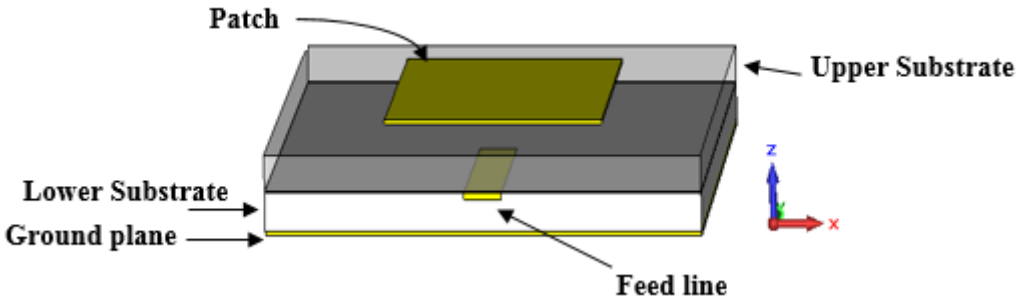

Figure 2.14: Proximity coupled feed

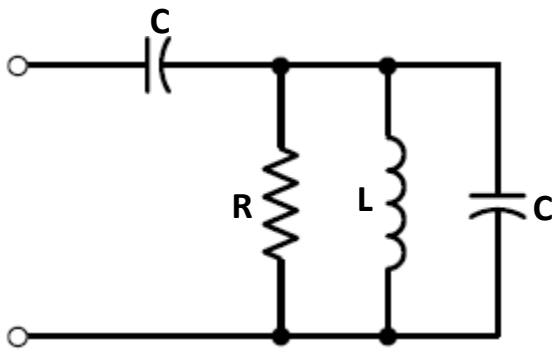

Figure 2.15: Equivalent circuit for Proximity coupled feed patch antennae

Table 2.3: Proximity-coupled feed advantages and disadvantages

Advantages	Disadvantages
➢ Large bandwidth. ➢ Easy to model. ➢ Low spurious feed radiation.	➢ Difficult to fabricate. ➢ No low profile; multilayers antennae.

2.2.3.1.4 Aperture coupled feed

The aperture coupled feed comprises two substrates separated by a layer of ground plane, with the feed line on the bottom side of the lower substrate. The patch on the upper substrate is excited by the feed line through a slot in the ground plane, as shown in Figure 2.16. The advantages and disadvantages of this method are summarized in Table 2.4.

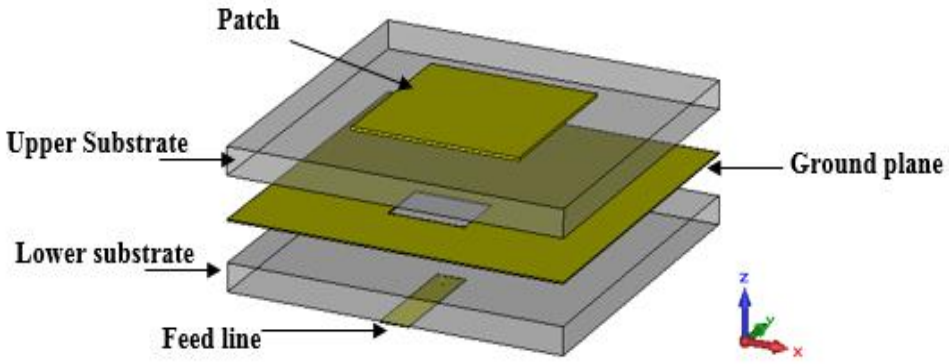

Figure 2.16: Aperture coupled feed

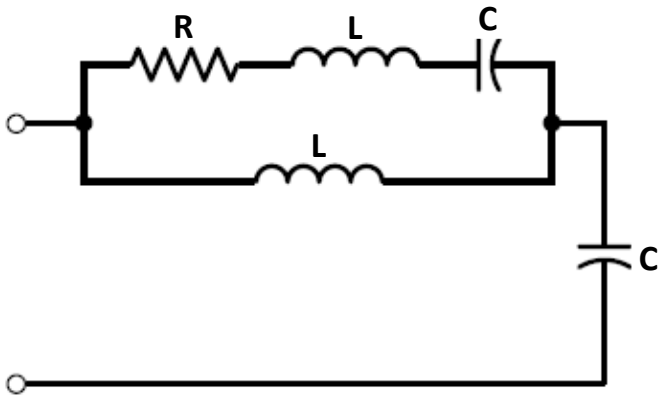

Fig. 2.17: Equivalent circuit for aperture coupled feed patch antennae

Table 2.4: Aperture coupled feed advantages and disadvantages

Advantages	Disadvantages
➢ Independent optimisation of the feed mechanism and the radiating element. ➢ Easy to model. ➢ Moderate spurious feed radiation.	➢ Costly and complex. ➢ Narrow bandwidth. ➢ More space underground plane required.

2.2.3.2 Analysis Methods for Microstrip Patch Antennae

A patch antennae element can be analysed by many methods. The most commonly used are; the transmission line model, cavity model, full wave model [37] and Coplanar Multiport Network Model. The transmission line model has advantages due to the simplicity of analysing and designing a patch antennae; especially in the design of rectangular patch elements, where the obtained results are feasible for most engineering purposes. The other types are complicated however, but can be used for irregular geometries. For instance, a patch loaded with slots changes the structure of the patch antennae. Thus, present changes in modelling and characteristics performance of the antennae. Therefore, a review of the different modelling techniques is presented within this chapter, in order to ascertain which provides the most suitable approach for modelling slotted patch structures.

2.2.3.2.1 Transmission Line Model

By using this model the microstrip antennae is represented by two slots at the edges of the width (*W*), separated normally by a transmission line with a length of *λ/2*, as shown in Figure 2.18.

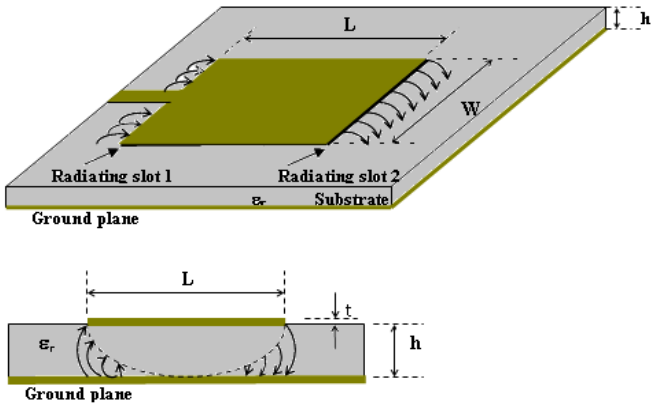

Figure 2.18: Transmission line model of the patch antennae

The microstrip antennae is fed by a microstrip line, and the fields on the microstrip line are faced with change in width causing them to spread out, hence, the fringing field is created at this edge. Another fringing field is created again at the other end of the patch, due to the patch acting as another transmission line, causing fields to propagate to the other edge at the end of the microstrip line. The stored energy in these fringing fields act as capacitors to the ground plane [48]. The equivalent circuit for a microstrip- radiating element is shown in Figure 2.19.

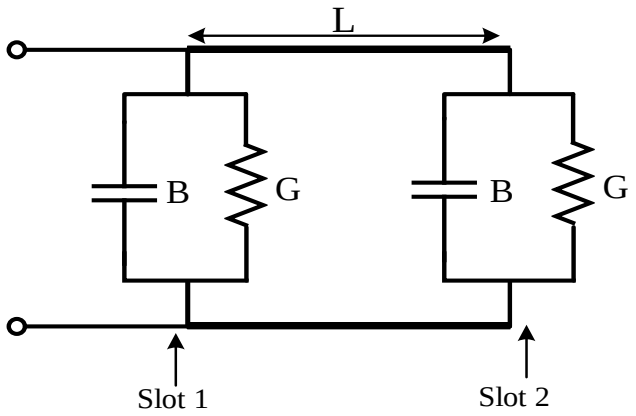

Figure 2.19: Equivalent circuit for a microstrip- radiating element

As illustrated in Figure 2.20, the radiation of the antennae is modelled by two parallel equivalent admittance (*Y)* slots on both edges of the patch, separated by a half wavelength transmission line. To improve the accuracy of the model, the effect of mutual coupling between the radiation edges and total losses (copper and dielectric) of the microstrip line between the *R*-*C* loads needs to be included, due to the patch antennae being much wider than the microstrip transmission line. The radiation which is created by the fringing field is represented by a conductance (*G*) that represents power loss due to radiation, in parallel with a capacitance (*B*), separated by a transmission line of length *L* (usually $L \cong \lambda/2$) which determines the resonant frequency [33, 49], while (*W*) determines the admittance (*Y*). It can be said that the fringing effects along the length of the patch make the fields at the edges of the patch undergo fringing. Hence, the electrical length of the patch looks wider than the physical length, which is extended on each edge by the incremental length of ΔL, as illustrated in Figure 2.20. These alterations in physical dimensions influence the resonant frequency of the patch antennae [33]. The expression for the extended incremental ΔL is given by:

$$\Delta L = \frac{\left(\varepsilon_r + 0.3\right)\left(\frac{W}{h} + 0.264\right)}{\left(\varepsilon_r + 0.258\right)\left(\frac{W}{h} + 0.8\right)} \tag{2.35}$$

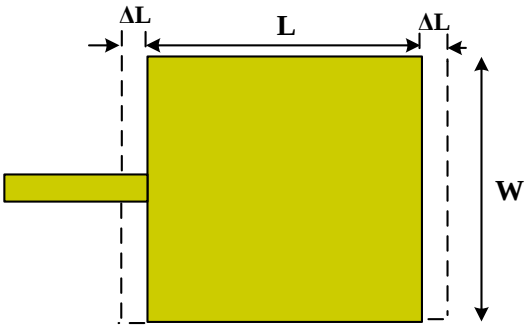

Figure 2.20: Physical and effective lengths of a rectangular microstrip patch

There are also some important parameters, which need to be calculated and obtained before determining the main patch dimensions mathematically, which are the length and the width. On such parameter is the effective dielectric constant (ε_{eff}), which can be interpreted as the dielectric constant of the homogenous medium that replaces the air and the dielectric region of the microstrip transmission line. The effective dielectric constant (ε_{reff}) for the microstrip line can be expressed by the following equation:

$$\varepsilon_{reff} = \frac{\varepsilon_r + 1}{2} + \frac{\varepsilon_r - 1}{2}\left(1 + 12\frac{h}{W}\right) \quad \text{for} \quad \frac{W}{h} \leq 1 \tag{2.36}$$

Since the length of the patch has been extended at both sides by ΔL, the effective length (L_{eff}), of the patch can be given as:

$$Leff = \frac{1}{2f\left(\sqrt{\varepsilon_{reff}}\right)\left(\sqrt{\mu_o \varepsilon_o}\right)} \tag{2.37}$$

$$L_{eff} = L + 2\Delta L \tag{2.38}$$

Therefore, the expression of actual length (L) and width (W) of the microstrip patch are given as follows:

$$L = \frac{1}{2f\left(\sqrt{\varepsilon_{reff}}\right)\left(\sqrt{\mu_o \varepsilon_o}\right)} - (2\Delta L) \tag{2.39}$$

$$W = \frac{c}{2f\sqrt{\frac{2}{\varepsilon r + 1}}} \tag{2.40}$$

where, c: speed of light, f: design frequency, ε_r Dielectric constant of the substrate.

The transmission line is a conducting line used to transmit signal energy between two points. Transmission lines take many forms in practice and have many applications as they traverse the countryside carrying electric power and signals. Figure 2.21, shows the physical construction of a microstrip line, together with fringing fields.

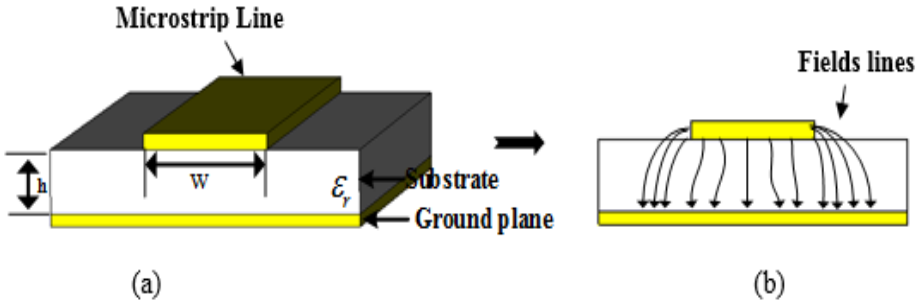

Figure 2.21: Microstrip line and Electric Fringing Fields

The formula for obtaining the width of the 50-ohm transmission line can be given by the following equation [50]:

$$W := Weff + \frac{t}{\pi}\cdot\left(1 + \ln\left(\frac{2h}{t}\right)\right) \tag{2.41}$$

where W_{eff}, is the effective conductor width, t, conductor thickness.

There are different types of losses are associated with microstrip line. These losses introduces attenuation on the transmission line, and identified as; the conductor loss, dielectric loss and the radiation loss. They can be represented by the antennae Q factors where the conductor quality factor (Q_c), which is due to conductor loss, is given by [46, 51]:

$$Qc := h\sqrt{\left(\mu_0\right)\cdot fr\cdot \sigma c} \tag{2.43}$$

where, σ_c, is the conductivity of the metal, h, is substrate height. The dielectric quality factor (Q_d), can be expressed as:

$$Qd := \frac{1}{\tan\delta} \tag{2.44}$$

where, $tan\ \delta$, is the loss tangent of the dielectric material. The radiation quality factor (Q_r), is given by:

$$Qr := \frac{\pi}{4(Gr\cdot Zo)} \tag{2.45}$$

where Z_0 is the characteristic impedance of the patch, and G_r is the radiation conductance, and the expressions [49] are shown in Appendix *A*. Normally, for thin substrates, the surfaces wave quality factor (Q_{sw}) that due to loss surfaces wave is very small and can be neglected. Thus, the total quality factor (Q_t) [29] is expressed as:

$$Qt := \left(\frac{1}{Qd} + \frac{1}{Qc} + \frac{1}{Qr}\right)^{-1} \tag{2.46}$$

2.2.3.2.2 Cavity Model Patch Antennae

Although the transmission-line model is simple and applicable for rectangular patch shapes, as mentioned in Section 2.2.3.2.1, it suffers from numerous disadvantages, such as the fact that the fringing factor must be empirically determined, field variations along the radiating edges are ignored and the patch antennae is presented as a wide microstrip transmission line, which is based on assumption. However, if the patch has irregular geometry (e.g. is loaded with slots), this changes the patch structure, and hence affects the antennae parameters, which means that the assumption is no longer appropriate. Consequently, the transmission line model is not the most effective technique. Such disadvantages can be overcome by the model expansion (cavity model) analysis technique, in which the patch is viewed as a thin TM-mode cavity with magnetic walls.

The cavity model can be employed in order to determine the field configurations inside the patch antennae [29, 52]. The sides of the patch structure can be represented as a dielectric-loaded cavity with electric walls above and below, and a magnetic wall along the perimeter of the patch at the sides, as demonstrated in Figure 2.22. The patch boundary is extended in order to take into account the patch fringing fields. This should result in a more accurate formulation to determine antennae parameters such as input impedance and resonant frequency in comparison to the transmission line method [46].

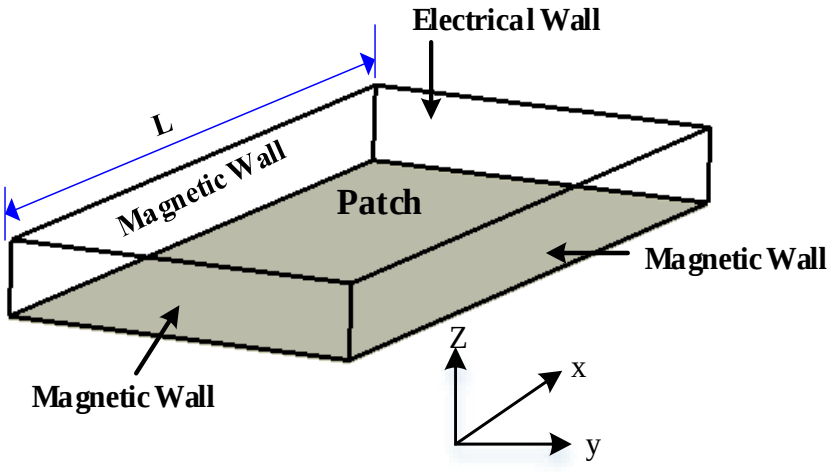

Figure 2.22: Cavity model of a patch antennae

This model assumes that the electric field tangential component is purely to the slots, which are formed between the top and back walls (the radiating patch and the ground plane) with four surrounding sides (patch edges), and is equal to zero ($E_\tau = 0$). The fields within the cavity can be obtained by using Helmholtz's homogeneous wave equation under the

boundary condition. The wave equation with second order partial differential equation (*P.D.E*), which is called the two-dimensional wave equation, is as follows:

$$\nabla^2 E + k^2 E = 0 \tag{2.47}$$

where, *k* is called wave number in the dielectric and is given by:

$$K^2{}_{m,n} = \left(\frac{m\pi}{a}\right)^2 + \left(\frac{n\pi}{b}\right)^2 \tag{2.48}$$

where, m and n are integers relating to mode numbers.

By returning to the (*P.D.E*) of the spatial dependence in Equation (2.47), the two wave equation that has two characteristics can be rewritten as follows:

$$\frac{\partial^2 E_z}{\partial x^2} + \frac{\partial^2 E_z}{\partial y^2} + K^2 E_z = 0 \tag{2.49}$$

The perimeter walls of the patch subject to boundary condition are:

$$\frac{\partial^2 E}{\partial x^2} = 0 \quad , \quad \frac{\partial^2 E}{\partial y^2} = 0 \tag{2.50}$$

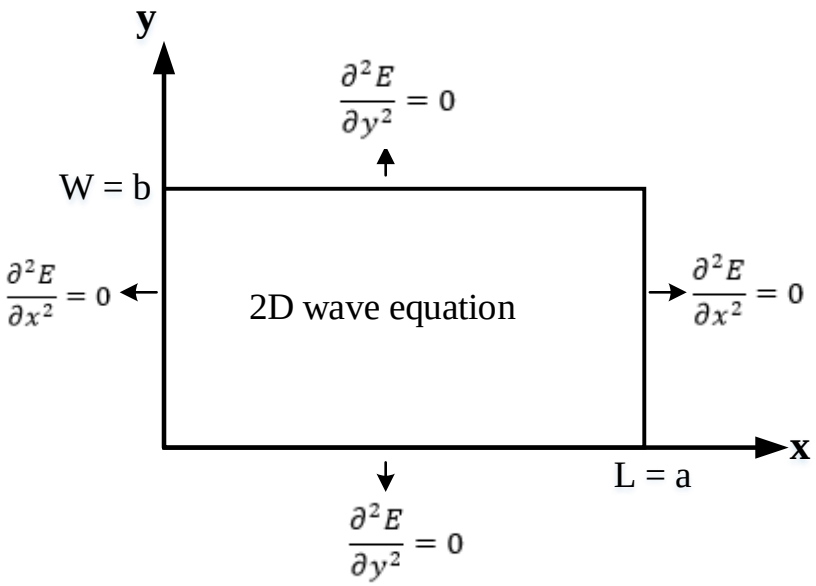

Figure 2.23: Cavity model with boundaries for a patch by 2D-wave equation

The solution given above in Equation (2.49), if under the boundary conditions as illustrated in Figure 2.23, this can lead to Eigen functions, which is as follows:

$$\phi_{m,n}(x,y) = k_{m,n} \cos\left(\frac{m\pi x}{a}\right)\cos\left(\frac{n\pi y}{b}\right)_{m,\, n = 0,\, 1,\, 2\ldots} \tag{2.51}$$

Although microstrip patch antennae are designed to operate at a single frequency, they can also be resonated at more than one frequency by their nature. Normally, all the harmonic modes have a fixed ratio with the fundamental frequency. Theoretically, the following equation can be used in order to calculate the resonant frequency of a patch antennae, which is expressed as [53]:

$$f_{r(m,n)} = \frac{c}{2\pi\sqrt{\varepsilon_{reff}}}\sqrt{\left(\frac{m\pi}{a}\right)^2 + \left(\frac{n\pi}{b}\right)^2} \tag{2.52}$$

The patch antennae's mode can be examined by using the voltage distribution on the radiating patch. Figure 2.24 shows the different types of modes on the patch antennae [29], as TM-modes.

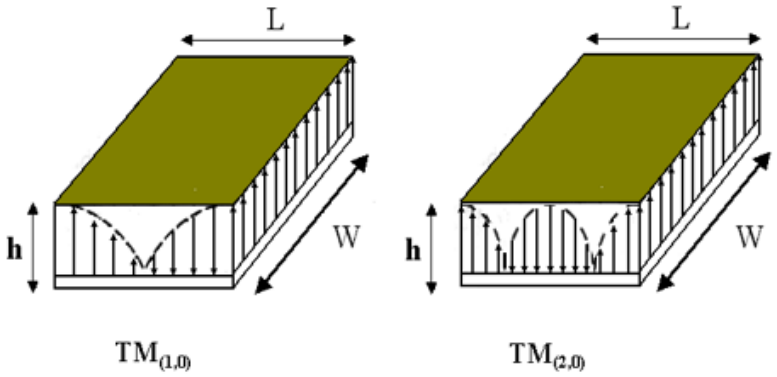

Fig. 2.24: Types of modes on the patch antennae

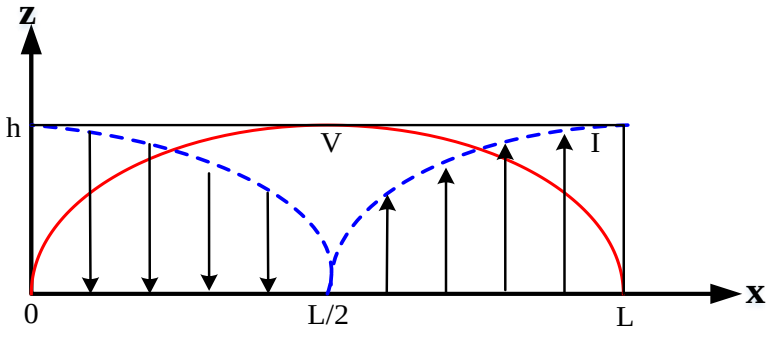

(a)

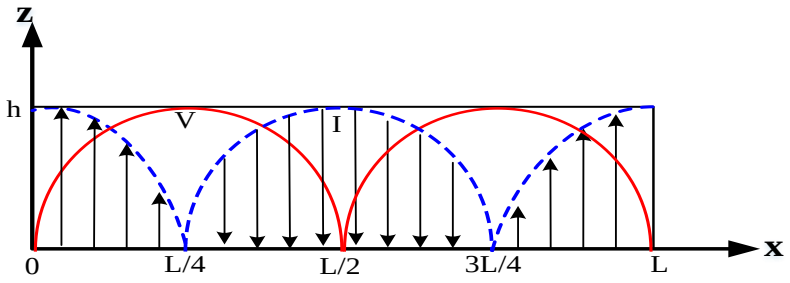

(b)

Figure 2.25: Voltage and current distributions and field configuration TM modes of the patch (a) TM_{01} (b) TM_{02}

The cavity model offers some advantages compared to the transmission line model. However, this cavity model is applicable only for patch antennae that having specific geometries such as rectangular, circular, triangular where the wave equation can be solved by separation of variables. As result of the above, it can be said that neither of the transmission line model or the cavity model that have been applied for a rectangular patch within this chapter, could be applied directly to model a patch with irregular geometric shape, particularly for slotted patch geometry, in order to determine the overall input impedance and electrical-field distributions. In view of this, none of the above analytical methods offer a suitable solution for the slot-modified patch antennae due to the presence of complex geometries. Therefore, this suggests the need for a different method to be employed, such as:

- The Coplanar Multiport Network Model with Segmentation:
  - Generalisation of cavity model
  - Suitable for irregular geometries

Hence, it is ascertained that the most suitable approach for complicated patch geometries, is the Multiport Network Model (MNM).

2.2.3.2.3 Multipart Network Model

The multipart network model approach can be considered as a generalization or an extension of the cavity model [54-60]. In this chapter, the use of the Coplanar Multiport Network Model for the analysis of antennae with a square-shaped patch is presented in order to determine antennae performance, such as in input impedance. In this model, the antennae is modelled as a multi-port network. The patch is analysed as a two-dimensional planar network with *n*-ports located along the edges, as shown in Figure 2.26, an analysis of multiport-network model of patch antennae.

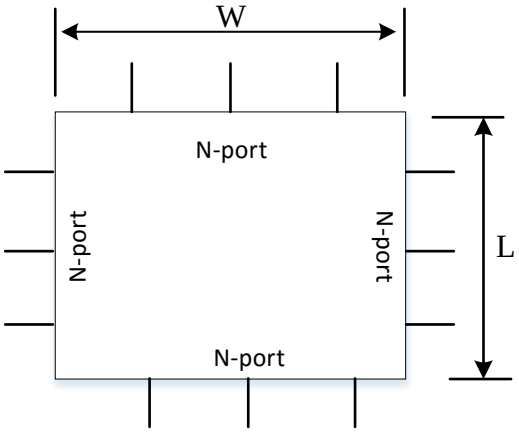

Figure 2.26: Multi-Port Network Model of Rectangular patch

For a rectangular patch excited with current source, consider the following two-dimensional wave equation with an inhomogeneous boundary (non-homogeneous Helmholtz equation) to describe the fields inside a planar patch antennae supplied by a current source, in Figure (2.26) [36, 61]:

$$\left(\frac{\partial^2}{\partial x^2}+\frac{\partial^2}{\partial y^2}+k^2\right)\phi(x,y)=f(x_0,y_0) \tag{2.53}$$

where: $$\phi(x,y)=E_Z(x,y)\,, \tag{2.54}$$

And, $$k^2=\omega^2\mu_0\varepsilon_0\varepsilon_r(1-j\delta), \tag{2.55}$$

k, wavenumber in the dielectric medium, δ is the loss tangent of patch.

This is related to the Maxwell's equations that have [62]:

$$\frac{\partial^2}{\partial x^2}+\frac{\partial^2}{\partial y^2}=\nabla^2 E_z=-j\omega\mu_0 J \tag{2.56}$$

So, that means: $$f(x_0,y_0)=-j\omega\mu_0 J_z(x,y) \tag{2.57}$$

Since the boundary condition along the patch periphery (C_p) is:

$$\frac{\partial E_Z}{\partial n}=0 \qquad \text{on } (C_p) \tag{2.58}$$

when an ideal electric current source (J_s) is injected at the source points (x_0,y_0) of the patch, the forcing function in Eq. (2.62) becomes:

$$f(x_0,y_0)=-j\omega\mu h\delta(x,y-x_0,y_0) \tag{2.59}$$

Thus, the equation (2.53) can be rewritten as:

$$\left(\frac{\partial^2}{\partial x^2}+\frac{\partial^2}{\partial y^2}+k^2\right)\phi(x,y)=-j\omega\mu_0 h\delta(x,y-x_0,y_0) \tag{2.60}$$

where, (x_0, y_0) is the monitoring point, and h is the substrate thickness.

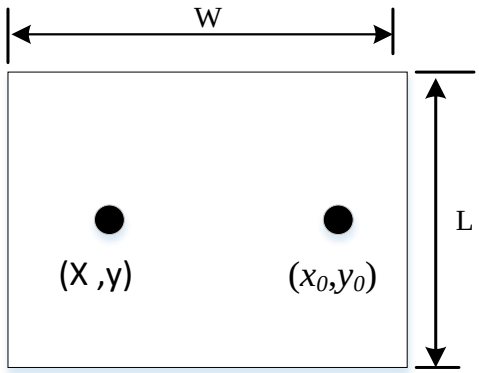

Figure 2.27: Planar structure with current source

when the shape of the patch is a simple geometry as shown in Figure 2.27 (for example; rectangular, circular, triangular). In order to determine input impedance (*Zi*) of a patch antennae related to the RF voltage (*Vi*) at any excitation port point for current source (*Ji*), the Green's function technique can be applied [61].

Two-dimensional green's functions in terms of eigenfunction expansions: The use of *2D* Green's functions method enables the solution of a differential equation containing an inhomogeneous term (an arbitrary source term) to be related to an integral operator containing the source to find the Green's function [36, 63, 64]. Variations of this approach enable us to solve some inhomogeneous boundary problems in terms of the Green's function for the corresponding homogeneous boundary. The Green's function can be expanded in terms of the following set of orthonormal eigenfunctions as:

$$G(x,y;x_0,y_0)=\sum_{m=1}^{\infty}\sum_{n=1}^{\infty}A_{mn}\phi_{mn}(x,y) \tag{2.61}$$

Substituting the Equation (2.61) into Equation (2.60), which was derived as in Appendix (*3C*), and this gives:

$$\sum_{m=1}^{\infty}\sum_{n=1}^{\infty}A_{mn}\phi_{mn}(x,y)=-j\varpi\mu_0 h\delta(x,y-x_0,y_0) \tag{2.62}$$

$$G(x,y;x_0,y_0) = -j\omega\mu_0 h \frac{\phi_{mn}*(x_0,y_0)\phi_{mn}(x,y)}{k_m^{\,2}+k_n^{\,2}-k^2} \tag{2.63}$$

To find the solution to a rectangular patch loaded with n-ports, as shown in Figure 2.27, the voltage for two-dimensional patch, at any point (x, y) due to a current source at (x_0,y_0) can be defined as:

$$V(x,y) = \iint_{D_p} G(x,y;x_0,y_0).Js(x_0,y_0)dx_0dy_0 \tag{2.64}$$

where D_p is the region inside the planar circuit, and G is the 2-dimensional Green's Function of the rectangular patch. If the source and observation points are on the periphery of the patch, the voltage was derived as in Appendix (3C), and is given by:

$$V_i = \frac{1}{W_i}\sum_j \frac{I_j}{W_j}\int_{Wi}\int_{Wj} G(x,y;x_0,y_0)dW_i dW_j \tag{2.65}$$

2.2.3.2.3.1 Z-parameters of n-port network

There are different expressions for the Z-parameter of Multi-Port Network Model, which is coupled between the ports on the patch segment [65, 66]. These expressions depending on the position of the ports and the patch orientation. The expression of Z-parameters with both ports located at the same points on x-axis can be used for the planar circuit illustrated in Figure 2.28.

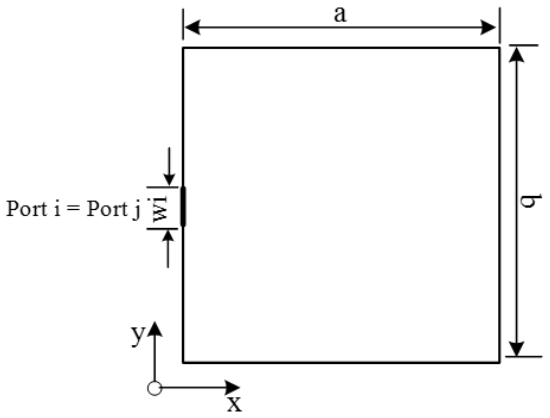

Figure 2.28: port i and port j are located at planar circuit

By considering $Z_{ij,}$ of port i and port j are located at the same point and side, for instance, on x-axis, thus, ($Z_{ij} = Z_{ji} = Z_{ii} = Z_{jj}$). The derivations are shown in Appendix (3C), and the Z-parameter is given by [36]:

$$Z_{ij} = \frac{V_i}{I_j}\Big|_{I_i=0} = \frac{1}{W_i W_j}\int_{Wi}\int_{Wj} G(x, y; x_0, y_0) dW_i dW_j = Z_{ji} \tag{2.66}$$

By Substituting Eq. (2.66) to (2.63), this gives:

$$Z_{ij} = \frac{j\omega\mu_0 h}{abW_i W_j}\int_{Wi}\int_{Wj}\sum_{m=0}^{\infty}\sum_{n=0}^{\infty}\sigma_m\sigma_n \frac{\cos(k_{xm}x_i)\cos(k_{yn}y_i)\cos(k_{xm}x_j)\cos(k_{yn}y_j)\ \ dW_i dW_j}{k_{xm}^{\ 2} + k_{yn}^{\ 2} - k^2} \tag{2.67}$$

where a and b are the length and the width of the rectangle patch with extension length, respectively. h is the height of the substrate, the points (x_i, y_i) and (x_j, y_j) describe the locations of ports i and j, $k = \sqrt{\omega^2 \mu\varepsilon_0\varepsilon_r(1-j\delta)}$, δ = loss of the dielectric, and $\sigma_m = 1(m = 0),\ 2(m \neq 0),\ \sigma_n = 1(n = 0),\ 2(n \neq 0)$. [36, 67].

2.3 Summary

In this chapter, a number of antennae types and their main characteristic parameters such as radiation pattern, beam width, directivity, input impedance, bandwidth, gain, efficiency, polarisation purity and dual-polarisation were explained. The selection of antennae type with respect to solar cell was described. Then, the fundamental theory of microstrip patch antennae (MPAs), including structures, the advantages and disadvantages, feeding techniques were Introduced. The most analysis methods including, transmission line model, cavity model, co-planar multi-port network with the design equations, which are used for analysing the MPAs were reviewed and explained in detail. Investigation into the most a suitable modelling approach for analysing complex geometries was presented. To this end, it was found that the most appropriate approach for complicated patch geometries is the Multiport Network Model (MNM).

Chapter 3 Literature Review

3.1 Antennae and Solar Cells Main Integration Techniques

The main integration topology techniques for microwave antennae and solar cells are outlined as:

- Using the solar cells as ground plane of an antennae. (Transparency techniques, such as meshing RF radiating element or ITO conductive materials are applied).
- A technique which is suggested an antennae is placed under solar cells
- The use of solar cells as an RF radiating element or stacked element.
- Integrated slot antennae or another antennae in the gap between solar cells.
- Other combination technique as applied for non-planar array antennae, e.g. Reflect array & Yagi-Uda.

These integration topologies will be addressed in detail in the next section, which is the literature review.

3.2 Literature Review

The past few years have witnessed a rapidly growing interest in the integration of microwave antennae and the PV solar panel, in addition to its function as a power source, can be integrated with microwave antennae. This integration of antennae and PV technology on the same surface could lead to the development of self-powered integrated systems that can be configured by a variety of design techniques and can help to reduce weight and peripheral expense (minimize operational costs) of the system [68-70]. Hence, this represents a cost-effective system due to the possibility of integrated production [71, 72]. Furthermore, this technology could be used for satellite and terrestrial systems. In relevant studies, various researches have been carried out on the integration of microwave antennae and solar PV cells. The first combined PV solar printed patch antennae was proposed by [73], and integrated solar cells with antennae have since been developed recently with dramatic success, in order to achieve a good photovoltaic antennae performance and a compromise between RF performance and transparency [71,

74]. For the full integration technique, various PV topologies have been studied and reported by various researchers, including:

The use of solar cells as a ground plane (a patch antennae is used on top of the solar cells) or as an extra element integrated with the existing ground plane.

The microwave antennae for this sort of integration, due to the impermeable structure of the radiating element. For instance, a microstrip copper patch arrangement brings shading upon the integrated solar cell and accordingly might essentially reduce solar efficiency. The design in [75] is an inset-feed patch antennae integrated on top of solar cell cover glass, and the study investigates the effect of solar cells on the gain performance of the antennae. It was reported that this approach is valid for an operating frequency of 5 GHz. However, this antennae uses a conventional non-transparent copper element (solid patch), and thereby decreases solar efficiency unless there is meshing of the radiating element upon the solar cells. In addition, the analysis concentrated only on the gain pattern with respect to the thickness of the solar cell cover glass. On the other hand, it was used to operate at a relatively single low frequency, and no results were shown concerning the reflection coefficient or impedance bandwidth. In addition, measurement of the effects of the antennae, which obstructs the incident light on solar cell performance, was not carried out or and demonstrated. Moreover, these issues make the set-up inappropriate for the design of broadband dual-polarised array antennae systems. It was demonstrated in [76] that the proposed inset-fed patch antennae combined with a solar cell has a two-orientation status for solar cells. In the case of the solar cell, top grid conductors are parallel to the antennae radiating element surface current flow, with a bandwidth of 3.11% at a resonance frequency of 2.19 GHz and offers maximum gain of 1.23 dBi. If the solar cell top grid lines are perpendicular to the surface current flow direction, the antennae yields a measured bandwidth of 3.13% at a level of -10 dB and resonates at a lower frequency of 2.168 GHz, with a maximum gain of 1.05 dBi. It was found that the measured solar cell efficiency was approximately 12.3%. In a similar design to [76] an inset-fed microstrip patch integrated with a polycrystalline solar cell was proposed in [77]. Also, two configurations were performed with the Ag-top contact fingers and bus bars of the solar cell orientation perpendicular and parallel to the surface feed current direction. It was reported low measured impedance bandwidths of 2.98% and 2.8%, maximum gains of 2.75 dBi and 0.46 dBi, respectively. Therefore, these designs are not suitable for broadband communication systems. It was also noted that both antennae cannot be operated for dual-polarisation applications, due to having linear-polarisation, and cannot be employed for full

arrays that need specific element spacing without avoiding cut solar cells. In [78], a single inset-fed patch integrated on the cover glass of triple junction solar cells was designed for CubeSat to operate at a frequency of 4.9 GHz. The proposed antennae was placed and examined on top of two types of cover glasses, which are AF32 glass and Plexiglas, to be investigated with and without a solar cell. It was demonstrated that the patch without a solar cell provides a measured gain of 6.1 dBi, whilst it yielded a gain reduction when the solar cell was used, with a value of 2.37 dBi (a difference in gain of 2 and 3 dB between them was observed). In [79], it is reported that an investigation was carried out into a proximity-coupled square microstrip antennae with integrated PV from the back, in which four different possible positions of poly-crystalline solar cells (front-contact orientation) with respect to patch position were examined and compared. The results show that the proposed proximity-coupled patch antennae integrated with solar cells as a ground plane led to slight RF improvement in bandwidth and gain compared to PEC antennae. The maximum values were observed when the configuration ''A'' was performed, in which the top grid-contacts are perpendicular to the microstrip feed patch, with the solar cell's back aluminium layer in contact with an FR4 substrate back. This configuration yielded an impedance bandwidth of 117 MHz (4.29 %) compared to 86 MHz (3.5%) for a PEC antennae, and gains were measured as 5.2 dBi and 4.0 dBi respectively. In spite of this, in both prototypes, the antennae still has a single narrow bandwidth and operates at low resonance frequency. In addition, the investigations did not include any solar cell measurements. In [80] a metal plate quarter-wave shorted suspended patch integrated with a poly-Si solar cell operating as an RF ground plane was proposed for Universal Mobile Telecommunications System (UMTS) base stations. In this design, the suspended radiating shorting wall metal plate antennae was shorted to the silver top grid electrodes of the solar cell with the microstrip feed line, which was printed on an FR4 substrate, and then placed upon the solar cell. Two configurations similar to [81] of parallel and perpendicular cell top contact orientations were carried out. It is reported that with parallel grid orientation, the metal plate solar antennae resonated at 2.08 GHz with an impedance bandwidth of 16.6% at -10 dB, whilst it resonated at 2.064 GHz for an impedance bandwidth of 14.5% with perpendicular top contact orientation. The maximum measured gains achieved were 3.9 dBi and 4 dBi, respectively. For the solar antennae in [82], the integration topology was similar to [80], but the proposed geometry was a printed dipole element with a length of a half-wavelength, printed on a piece of FR4 substrate. This was suspended above a poly-Si silicon solar cell, which operated as a reflector for the antennae, and as an RF ground plane for the 50 Ω microstrip feed line printed on a separate

FR4 substrate. In order to feed the dipole, the feed line was connected to a balun in a balanced manner through the arm. The orientation of the solar cell top contact electrodes was performed in two positions; parallel and perpendicular to the surface current direction of the printed dipole element, respectively. It is stated that the antennae resonated at the centre frequency of 2.339 GHz, at -10 dB impedance bandwidth of 15.8% when the dipole element with the parallel cell top contact electrode orientation was used. Meanwhile, with the perpendicular cell top contact electrode orientation, it resonated at a centre frequency, which was 2.3484 GHz, with an impedance bandwidth of 13.1%. The solar dipole antennae design in both configurations gave a maximum gain of 8.75dBi. In [83], a design of an integration of quarter-wave shorted trapezoidal metal plate antennae with a poly-Si solar cell operating as an RF ground plane was performed. This proposed PV solar antennae comprised a suspended trapezoidal metal plate-radiating element, with a width of 48 mm, a base width of 25 mm and a side length of 21.4 mm, and was placed above the solar cell bus bars, with h =10 mm. The trapezoidal metal plate element was shorted in the two corners to solar cell silver DC bus bars similar to [80]. Thus, this gives the antennae the advantage of operating in a quarter-wavelength mode. It was also fed through a 50Ω microstrip feed line printed on an FR4 substrate upon the solar cell surface, and for good isolation between the DC solar cell and RF functions, two RF blocking inductors were used. It was reported that the antennae operated at a single frequency band of 1.957 GHz, and offered an impedance bandwidth of 15.2% with a gain of 4.5 dBi. However, a reduction of 3.46% in solar cell efficiency was reported due to the shadowing of the radiating metal element and its feeding line. For the same solar antennae integration topologies in [80, 82, 83] although they have low profile radiating elements integrated with solar cell, they have similar drawbacks, such as the fact that the radiating elements above the solar cell are solid elements, and thereby obstruct light incidence, preventing them from being applicable for fully transparent patch antennae applications. In order to address this problem, different transparency techniques have been proposed, such as applying a meshing technique to the patch antennae design or using conductive transparent materials. In [84, 85], it is reported that locating the solar cells beneath the antennae elements reduces solar efficiency, but can improve RF performance. However, a compromise between RF performance and optical transparency can be achieved. In [84], an antennae design is demonstrated which includes two types of meshed patch antennae prototypes; wire and ink mesh. In both of these, the meshed radiating patch element was attached on the top of the solar cells, which operated as an RF ground plane for the antennae. The wire mesh solar patch antennae offered a radiation directivity of 8.2 dB, and

an antennae optical transparency of 93%. For this type of prototype antennae, the effect of the meshing technique on solar cell performance was not reported. The ink meshed prototype antennae operated at a single frequency of 2.61 GHz, and offered a measured directivity of 8.4 dB, while for the obtained antennae element optical transparency was 61%. The proposed solar antennae in [85] presents a transparent patch antennae suspended on the top of a polycrystalline silicon solar cell, which operates across the frequency band of 2.38-2.59 GHz (with a bandwidth of 8.46%), and can be used for 2.4/2.5 GHz WLAN and WiMAX applications. The optical transmittance of the patch was calculated as 95%, and offered a maximum gain of 7.1 dB, with a narrow single bandwidth. In [86] although, the antennae consisted of an array of two meshed transparent radiating patch elements, which differs from previous designs, and covered a multiband to operate at multiple frequency bands for GSM 900/1800/1900, UMTS 1900, 3.5 GHz band WiMAX and C-band applications. In addition, it offered various good gain values across the multiple bands respectively. Nevertheless, this antennae still operates at a relatively low frequency range, and is also not suitable to be incorporated into 2-deminstional dual-polarised array antennae.

Another technique is using a solar cell as a truncated ground plane, and the design presented in [87] of a transparent meshed circular monopole offered a wide bandwidth over a wide frequency range and high transparency. It covered a frequency range of 2.33-10.8 GHz for UWB applications, with an average gain of 4.1 dBi. It was demonstrated that the proposed antennae provided optical transparency of 91%, and produced output DC power of 65.5 mW with a measured solar efficiency of 13.1%. However, this design exhibits a bi-directional radiation pattern due to the truncated ground plane (just beneath the feed line) and is therefore not suitable for SATCOM applications: especially those that require dual-polarized operation and directional radiation.

Different types of transparent materials were used as a single patch antennae element on top of z solar cell: there have been many reported designs of transparent antennae using conductive materials, such as Fluorine Tin Oxide (FTO), Indium Tin Oxide (ITO), AgHT-4 film and IZTO. A number of researchers in [88-91] have reported trade-offs between optical transparency and antennae efficiency. It has been found that transparent conductive antennae could be used due to a reasonable trade-off between light transparency with a minimum visible light transmission of 75-90%, and RF conductivity. However, generally, conductive films of this sort typically show losses and their efficiency is found to be only approximately between 30-50%, as in [88], operating at a single frequency band (with an impedance bandwidth of 4.3% at -10 dB) and a maximum gain of 3.96 dBi. Moreover, most studies

have been conducted for narrow bandwidths at lower operating frequencies rather than high frequencies. Other research has achieved improved radiation efficiencies in the range of 60-80 % operating at high frequencies, as in [92, 93]. The cost of transparent conductive materials is rather expensive, and a higher thickness of substrate (multi-layers) was required.

Use of solar cells as an RF radiating element.

It was demonstrated in [94] that this antennae has an impedance bandwidth of 8%, over a frequency band of 2.753-2.983 GHz and a maximum gain of 5.5 dBi at a single operating frequency of 2.75 GHz. Hence, it is not suitable for applications that need multi-resonance bands. In addition, the antennae radiating element was excited by an RF feed line though a slot in the centre of the FR4 ground plane. Both the feed line and DC collecting lines were integrated on the rear side. This necessitates multi-layers or bottom-layers attached to a ground plane, which is a complicated structure. Therefore, this antennae is not appropriate for modern compact low-profile communication systems and array antennae. In [95] a solar cell replaced the radiating patch element of the antennae to receive and transmit signals, in addition to its function of DC generation. The results showed that the solar antennae had a dual-band frequency, which resonated at 5.77 GHz and 6.18 GHz, with an achieved gain of 1.59dBi and a directivity of 6.12dBi at 6.18 GHz. It is noted that low peak gain and linear polarisation were reported. The proposed solar antennae design in [96] has a suspended solar cell patch operating as radiating element antennae, which provides tri-band operation at different frequencies of 2.4, 2.8 and 3.45 GHz. This is useful for the frequency band of 2.3/2.5 GHz band WiMAX and 2.4 GHz band WLAN networks (with an impedance bandwidth of 9.58%), and the second frequency band of 2.76-2.89 GHz (a bandwidth of 4.64%) for lower WMAX applications. The third resonance band of 3.3-3.58 GHz (a bandwidth of 8.1%) was used for the middle-band WiMAX, occupying 3.3/3.5 GHz frequency. The design shown in [97] is similar to the solar antennae design techniques in [94-96], but with a different form (a windmill shape) of solar cell as the RF radiating element. This proposed solar antennae was designed to operate at a resonance frequency of 13.17 GHz for the Ku band SATCOM application, offering a 10 MHz bandwidth and a good gain value of 8.6 dBi, with a directivity of 8.65 dB. It was indicated that the radiation pattern had a single right lobe and linear polarisation. It can be noted that this solar antennae exhibited a narrow bandwidth, and would be difficult to develop into an array antennae. In contrast to the above single designs [94-97], in [98] demonstrated 2x2 solar antennae array elements covering a frequency band of 2.3-2.75 GHz, offering a wide bandwidth of about 18.36% and a gain of 12.2 dBi. In such designs, to produce current from the solar cells, conductive DC

connection lines are required between the cell terminals and the DC load. However, if good isolation is not implemented, these connections can significantly affect the RF antennae's performance. Thereby, this makes such antennae designs difficult to apply for fully high gain patch broadband array antennae, and especially if an arrangement of 2-dimensional planar array antennae is required, such as Ku-band or Ka-band array antennae.

Use of solar cells as a stacked patch element of an RF radiating patch or attached to an existing RF radiating element.

The study in [99], presents a low-profile quad-band solar PIFA that can be employed for self-powered low-power applications such as GSM 1800, 2.4 GHz band WLAN and 2.3/3.3/5.8 GHz band WiMAX networks. The radiating PIFA element was loaded with W-L shaped multi-slots and stacked with a polycrystalline silicon (poly-Si) solar cell to operate at different centre frequencies of 1.8, 2.4, 3.4, and 5.8GHz. It offered multi measured impedance bandwidths over of GSM 1800 (1.71–1.88 GHz), 2.4 GHz band WLAN (2.4–2.484 GHz), with 16.7%, 9.16%, 7.65%, and 3.45% across 10 dB, respectively. The measured gain values of 2.3, 4.7, 7.1 and 5.8 of the proposed solar PIFA with the cell were achieved at the centre frequencies respectively. By contrast, a slight decrease in gain at 1.8 GHz was observed. By using this stacked poly-Si solar cell as a parasitic element for the radiating PIFA element, a solar efficiency of 14.5% and producing output DC power value of 44 mW were obtained. In [100], a suspended shaped multiple-L slot loaded microstrip patch antennae stacked with a polycrystalline silicon (poly-Si) solar cell was performed. The fabricated solar patch antennae had overall dimensions of L1 = 90 x W1 = 60 mm. The S11 response of the proposed patch antennae with the stacked poly-Si solar cell was investigated. The results indicated that due to the presence of the stacked poly-Si solar cell in the proposed design, which operated as a parasitic patch element, the design showed good enhancement at the resonance bands. It provided the full desired coverage for communication networks of 2.4/5.2 GHz band WLAN and 2.5/3.3/5.8 GHz band WiMAX, with measured gain values of 8.49 dBi, 7.11 dBi, 9.4 dBi and 8.48 dBi, respectively. The measured gains are high in comparison to conventional microstrip patch antennae. The achieved solar performance efficiency was 10%. Consequently, this proposed solar patch antennae is suitable for low-profile multiband resonance bands. Similarly in [101, 102], patch antennae were placed under solar cells to obtain compatibility between antennae and solar cells. In both, the usefulness of locating the solar cells above the antennae elements minimises the blockage of direct solar radiation and maximises solar cell efficiency. For the proposed antennae in [101],

the polycrystalline silicon solar cell stacked Z-double L-slot has quad-band PIFA radiation characteristics, which operates over the frequency bands of 1.75-1.82 GHz, 2.38-2.61 GHz, 3.26-3.53 GHz and 4.66-4.83 GHz for GSM, WLAN and WiMAX networks (with impedance bandwidths of 3.91%, 9.38%, 7.94% and 3.58%). The design achieved far-field radiation pattern gains of 2.1, 6.4, 7.6 and 5.5 dBi, respectively. It also demonstrated a measured solar cell efficiency of 13.9%, producing output DC power of 34 mW. Moreover, the proposed two parallel element array design for long-range communication systems was investigated. It was found that the radiation characteristics were significantly affected due to the coupling. In [102], a wideband solar cell antennae was proposed with a metamaterial technique used for 5 GHZ Wi-Fi communication. The design comprised a slotted patch element stacked with a solar cell above the patch, and the ground plane was etched with multiple complimentary split ring resonators (CSRR). The results show that an impedance bandwidth of 1 GHz was yielded at 5.6 GHz, with a directive gain of 7.73 dBi was achieved across the Wi-Fi desired range. In addition, an antennae size reduction of up to 25% was obtained. However, in these designs [102], due to the requirements of the DC output wire connections to the terminals of the solar cell, these bring a considerable effect on RF performance also prevent such antennae from being applicable to dual-polarised operation for array antennae.

The solar design antennae in [100-102] have the same advantage as the stacked solar cell in operating without any light-blocking occurring from the antennae RF components, where the ground plane of the cell acts as a stacked element for the radiating patch, thereby ensuring optimal solar cell efficiency performance. Nevertheless, due to the need to collect the generated output current of the solar cells by the DC output connections, the connections overlap each other over element feeding lines, and hence, significantly affects the RF performance of the antennae. Additionally, such designs require a complicated decoupling circuit for isolation. Moreover, they exhibit narrow bandwidths in relatively low frequency bands. In [103, 104], a dual-band dipole feeding antennae stacked with a 10-Watt, 72-cell unmodified commercial PV panel was presented. This proposed solar antennae exhibited dual-band frequencies operating at 1.185 GHz and 3.55 GHz (covering the WiMAX band), and offers antennae gains of 17.3 and 6.6 dBi respectively. Despite the fact that a high antennae gain of 17.3dBi was achieved using a Fabry-Pe´rot (FP) cavity mechanism, this mostly brought high-sided lobes and mutual coupling, which affects the radiation pattern: especially if high gain, high frequency array antennae are required. In [105], similar idea was presented to [103], but using different a microwave radiator of reactance elements for a

lower frequency for A GSM 900MHz / DCS 1800 MHZ dual-band. The solar antennae reported in [106] differs from [100-104], and it was demonstrated that it provides a slant ±45° dual-polarized operation for frequency diversity communication systems, and good DC/RF isolation. However, it was shown that it operates at a low frequency band and results in a narrow bandwidth. In addition, it is not suitable to for application within dual-pole solar array antennae due to needing stacked solar cell output connections that overlap each other, which affect RF performance, and also due to the inclusion of a complex DC/RF isolation circuit.

Other works were reported in relevant literature for solar cells attached to the top of antennae [107]: the proposed solar antennae demonstrated in [108] comprised a printed short-circuited multiband radiating element with a capacitive coupled-fed strip line. The antennae composed of two separate ground planes with eight series solar cells connected in between two ground planes. The PV cells were placed upon an FR4 substrate with an inverted-L metal strip printed on the back, which was coupled to the solar cells. The first ground plane was attached to the antennae-radiating element. The reason for using this ground plane was to enable the proposed antennae to operate at a frequency range of 1.63-2.77 GHz, which covers applications of GSM 1800/1900, UMTS and LTE 2300/2500. By exciting the inverted-L metal strip, which is between the ground planes, this makes the solar cells work as an additional ground plane in addition to the first and second ground planes, and therefore, the size of the overall ground plane was extended. This configuration enabled the proposed antennae to achieve multi-band operation. This makes it suitable for the applications operating at 660-990 MHz and 1.63-2.77 GHz covering LTE 700 and GSM 850/900. In addition to GSM 1800/1900, UMTS and LTE 2300/2500. However, no far-field radiation pattern and solar cell measurements were carried out. Also, the antennae configuration would lead to complicated fabrication, and makes it unsuitable for applications required for array antennae in particular. In [109], the broadband monopole radiating antennae element was printed on flexible PET substrate for energy harvesting. The solar cell was attached to the top of the antennae, and one of its terminals was connected to the DC output line and the other to the conductor of the monopole antennae element. Good RF and electrical DC energy performance was reported, but this type of topology integration and antennae geometry are not applicable for incorporation into an array antennae design.

The integration in [110] of a low profile scalable arbitrary-sized solar omnidirectional antennae was presented. This scalable topology consisted of three layers; the solar cell (top layer) was attached to the top of the first RF ground plane (second layer), and in between

these was a dielectric FR4 board. This board was used to prevent the solar cell from coming into contact with the first RF ground plane. Meanwhile, to isolate the solar cell from the RF feeding network (third layer), the first RF ground plane was used. The function of the RF feeding network (third layer) was to carry the RF signal to be divided equally through four feed lines branching from the centre of the design to radiate from the four slots located symmetrically at the antennae edges. The antennae provided an omnidirectional radiation pattern for 2.4-GHz autonomous integrated wireless sensor node application. It was reported that the proposed solar antennae presented a narrow impedance bandwidth with 2.1% and a low gain of 0 dBi in free-space conditions. In view of this, it can be said that the solar antennae integration described in [110] differs from the previous designs in [108, 109], but has similar hindrances in terms of being developed for specific applications, such as one-directional dual-polarised operation or solar array antennae. In [111], a 927 MHz printed folded-slot antennae powered by two thin amorphous silicon solar cells through an oscillator was proposed for applications of wireless energy harvesting. Flexible thin-film solar cells powered the oscillator circuit, which included a low noise micro-power regulator, various parasitic circuit elements and an HJFET transistor. All of these parts were placed upon the CPW ground plane, and the folded-slot antennae printed on Arlon 25N substrate. It was shown that this proposed folded-slot antennae operated at a low frequency band of 800 MHz-1.1GHz, and demonstrated wide H-plane and E-plane co-pol far-field radiation patterns, although, no gain values were reported. In addition, in terms of suitability for compact solar array antennae, the proposed antennae structure remains impracticable.

In [112], a meta-surface circularly polarized (CP) solar patch antennae was presented, which consisted of a slotted circular radiating patch situated vertically underneath the gap distance between the 4 × 4 array solar cells (with an overall dimension of 40mm × 40 mm), while the ground plane was at the bottom. This type of arrangement introduces direct sunlight illumination (direct insolation) to the solar cell without any light blockage. The proposed antennae had good performance, offering a -10 dB impedance bandwidth of 5.98–7.05 GHz. It showed good broadside across the operational frequency, with maximum gain in the range of 6.9-9.0 dBi. It was also demonstrated that it had a right-hand CP with an axial ratio (AR) of under 3 dB, and radiation efficiency of more than 85% was obtained. However, the proposed solar antennae cannot be a candidate for array antennae applications, which need to be ideally specified by equal inter-element spacing between antennae array elements. In this case, it requires cutting slots vertically along the solar cell to allow the antennae to propagate into free space. Hence, this would damage the homogenous structure of the cell.

It should also be noted here that the antennae has CP-polarisation, and therefore cannot be employed for dual linear-polarisation services. The proposed design in [113] is similar to the integration topology of solar antennae demonstrated in [112], the single patch broadband circularly polarized (CP) meta-surface solar antennae was sandwiched between 4 × 4 square meta-surface solar cells at the top and the ground plane at the bottom. It differed in that the radiating element was composed of a square patch loaded with a diagonal slot and operating at a frequency range of 2.28–2.75 GHz. Although, this integration topology also allowed the sunlight to fully illuminate the solar cells of 100 %, and yielded a wideband (19.1%) at –10 dB of bandwidth, with a good broadside gain range of 7.3–8.5 dBi. It has similar issues to [112], which make it unsuitable for incorporating into array antennae. In addition, it is designed for a single, relatively low frequency.

In [114] PV solar cells were combined with a slot structure antennae for GPS applications. The design consisted of three layers, in which a solar cell was placed on the top and underneath in the middle layer was a metallic ground plane loaded with a cross-slot (aperture) in the cell-spacing, fed by a microstrip feedline on the rear side. The bottom layer was responsible for reducing the feeding network RF radiation to the solar cell. However, this proposed solar cell antennae operates for low frequency bands of the GSM 900 and GSM 1800 bands. Also, in this paper, neither simulation nor measured results for RF performance (such as impedance bandwidth and gain) or solar cells were demonstrated. Moreover, due to the requirement for the solar array antennae to be specified with small inter-element spacing between any adjacent antennae elements, this single slot solar antennae configuration cannot be employed for array antennae. In this case, cutting a slot in the cells spacing would be required, and because of this, damages the structure of the cell, and hence has the potential to significantly affect overall cell performance and reduce solar efficiency. In [115], a UWB dipole antennae integrated with thin-layer solar cell was demonstrated for a frequency range from 1 to 12 GHz, which was capable of solar energy harvesting. This dipole antennae had bow-tie shaped elements, and each arm was extended with a square patch integrated with a sloping edge copper tab, where the solar cell attached to the top of both square patches. Then these parts together was printed upon an FR4 substrate, and a DC/RF isolation circuit on the back. It was indicated that far-field radiation patterns at higher range frequencies within UWB were different compared to conventional planar bow-tie antennae far-field radiation patterns. This might be attributed to the front finger contacts of the solar cell. However, this proposed dipole antennae has linear polarisation, due to the polarisation characteristics typical for most dipole antennae. In [116],

a planar array antennae was designed to be used for downlink communication for CubeSat a 3,000-km altitude circular orbit. The photovoltaic cell array and antennae were installed into a deployable satellite structure, on the front and backside layers of the printed circuit board (PCB). The proposed antennae working at downlink central frequency of 2.4 GHz, and offers a bandwidth (BW) of 500 kHz, with receiving and transmitting antennae gains of 70 dBi and 5 dBi, respectively. Wearable aperture-coupled shorted solar patch antennae in [117] to cover a frequency range of 902-928 MHz ISM band for remote tracking and monitoring applications. The antennae radiating patch was made from a copper coated nylon fabric with an H-shaped slot, and printed on a flexible polyurethane foam substrate, and a 50Ω coupling microstrip feed line was placed underneath the patch. In this proposed design, two parallel flexible a-Si solar cells were used, each one producing a maximum output DC power of 48mW, and were then attached to the radiating patch. It was demonstrated that the proposed solar antennae yielded a measured impedance bandwidth of 64 MHz, and achieved a low gain of 1.6 dBi. Another wearable solar antennae was designed in [118], with a different SIW technology using pure copper polyester Taffeta with a cavity, and covered an operation frequency band of 2.4–2.4835GHz (ISM band), and a 2.5–2.69 GHz (4G LTE band). The design provides dual-band, high radiation efficiency of 89%, and gain of about 5.0 dBi. Despite this [118] showed wideband and radiation efficiency. The solar antennae in [117, 118] have a low operating frequency and are not applicable for wideband applications where adequate gain is required, and in addition were designed to be employed on the chest of a human body.

In [119], 2 x4 SOLANT array printed patch elements were combined with amorphous Si-solar cells supplying a monolithic microwave integrated circuit (MMIC) amplifier was proposed. This solar antennae operated at 4GHz for a C-band satellite application, and comprised an array of microstrip patches attached to the upper substrate (Epoxy) and on top of a foam layer. These patches were energised through aperture in the ground plane by microstrip RF feeding network underneath including of Wilkinson power divider. The solar cells were attached to the radiating elements in order to feed the MMIC amplifier that is used on the feedline to produce a maximum gain of 20 dB. It was observed that the proposed solar antennae worked at a centre frequency of 3.95 GHz, and offered an impedance bandwidth of about 600 MHz, which is 15%. The achieved gain was 13 dBi in passive mode, while with the MMIC amplifier, this was 30 dBi in active mode. For the solar measurements, the obtained maximum output DC power was 252 mW. In this solar antennae design, if a full 2D-array solar antennae is required, in this case the solar cells would be difficult to make

compatible in spacing with radiating inter-element spacing, thus producing undesirable side lobes and affecting the mutual coupling.

Other integration technique for integrating planar microwave antennae and solar cells.

These antennae types can be integrated with solar cell panels, and different polarisation configurations can be obtained. In solar antennae designs in which radiation is achieved through cutting a slot in the solar cells, as in [120, 121], this could damage the structure of solar cell, which already has a homogeneous structure for perfect performance. Hence, this would significantly reduce efficiency. The design shown in [122] consisted of a cross-slot in the ground plane supplied through a feed line at 45°. This provided two orthogonal propagation modes at the operating resonance frequency. Hence, this allows the solar antennae to have circular polarisation by exciting modes with the same amplitude and opposite phase. The results demonstrated that an axial ratio (AR) was obtained under 3 dB over the frequency band of 3.82-3.94 GHz (with an impedance band of 3%, at -10 dB), and a gain in the range of 9.7-11.6 dBi was achieved. In terms of solar measurements, no results were reported in the study. The proposed antennae in [123] was developed from a single element in [122], into a linear 6 x 1 cross-slot array. A good measured gain was reported, of 11.6 dBi at 3.80 GHz. However, the design still showed a limited impedance bandwidth of about 500 MHz. In addition, it is not suitable for a set of two-dimensional solar array antennae. In [124], a solar slot antennae was presented, which was integrated with a-Si solar cells and attached to the antennae ground plane, which included a slot sourced through a microstrip feed line. It was reported that a high cross-polarisation level with -12 dB was observed, and the antennae resonated at a single frequency of 4.14 GHz, with a measured gain of 3.15 dBi. The reported measured solar efficiency was about of 5.6%-6%, although the solar measurement conditions were not explained. A low-gain UHF solar cross-slot antennae was proposed in [125, 126], and designed for space vehicle applications, with an overall square dimension of 33 cm, consisting of four sub-patches with a square dimension of 15.2cm. Each one was short-circuited at a single edge to the ground plane. Radiation can be created through the slots at the non-short-circuited edges of the sub-patches. It could be observed that the design resulted in circular polarisation and exhibited a narrow impedance bandwidth of 40 MHz at -10 dB, offering a maximum gain of 4.5 dBi.

The slot solar antennae proposed in [127] was constructed by cutting a linear slot on the solar cell, which was fed by a microstrip. Water was employed as a reconfigurable and transparency dielectric loading material for the antennae line under the solar cell. The

proposed antennae has a wide continuous tuning frequency range of 450-1000 MHz, by changing the water level. The radiation efficiency of the proposed water loaded slot antennae varied between 60% and 96%, relevant to the tuning of the antennae frequency range, with a moderate gain of 5dBi. Nevertheless, for the same reasons as in [124-126], the slot solar cell antennae demonstrated narrow bandwidth (at -10 dB impedance bandwidth) and operated at a low frequency range. In addition, the antennae configuration was not compatible for array solar antennae, because of the slots cut in the cell, whereas for the array antennae, it is necessary to determine inter-space distances along x and y coordinates between elements. As indicated in [128], this cavity-backed slot antennae was performed by etching half wavelength slots in the spaces between ultra-triple junction solar cells to create a radiating element. In this design, three solar prototyped antennae were fabricated using PCB, each one to offer a polarisation type: the first prototype was circularly polarised; the second was linearly polarised; and the third was a dual band linearly polarised antennae array. Two substrates made of Polyimide were used, the upper one for the slot elements, and the lower for the feeding network, where a 50-ohm microstrip line was divided by a tee junction into two lines of 100-ohm. It was reported that the antennae frequency design was 2.64 GHz, and the obtained maximum power was 3.6 watts. Despite that, this integration topology did not affect solar cell performance, no radiation patterns, gains and S-11 parameters were demonstrated. In [129], the design was extended from the cavity-backed slot design in [128], and was composed of eleven apertures on the top of the metallic surface of the upper Roger's Duroid 5880 substrate, and peeling off the lower substrate. The feed line was branched, with each 25-ohm divided into two 50-ohm lines, and printed on the top surface of the second substrate by exciting the cavity at selective points. As a result, different types of polarisation can be achieved at 2.4 GHz, such as left-handed circular polarisation (LHCP) when excited at the lower point and right-handed circular polarisation (RHCP) when excited by the upper, in addition to linear polarisations (LP) at 2.4 GHz and 1.9 GHz. The results show that the axial ratio (AR) from LP ports exceeded 20 dB, and the simulated 3-dB (AR) bandwidth was 40 MHz, with gains of 8.2 dB and 8.46 dB for CP and LP respectively. The antennae in [128, 129] have drawbacks due to their narrow bandwidth, which prevents such designs from being used in wideband communication applications. The solar antennae proposed in [130] has two configurations of linearly polarised slot antennae; a linear or square slot antennae integrated on the glass of the solar cell was presented. This can be used for communication systems of GSM/UMTS (1710–2170 MHz) and WiMAX (3300–3800 MHz) frequency band. Both slot antennae were etched on a low-cost substrate

between adjacent solar cells, without being obstructed by the cells, and excited by microstrip feed lines on the rear side of the panel. It was shown that the linear slot antennae yielded a frequency band for GSM/UMTS with a -10 dB impedance bandwidth of 24%. Meanwhile, the square slot covered a frequency band of 3300–3800 MHz WiMAX.

Furthermore, in view of above, these alternative designs (either slots or dipole antennae types in the gap of the solar cell) such as [131, 132] to achieve simultaneous operation of integrated antennae arrays and solar cells utilizing slots or dipoles solar cells cannot be obtained where Ku-band antennae arrays require small inter-element spacing to avoid grating lobes. Such small inter-element spacing using dipoles or slots between solar cells would dictate a very small cell size and limit design flexibility, especially for array configuration. Hence, for Ku-Band operation, a good performance and transparent antennae array element is desired.

Other Photovoltaic combination techniques for non-planar antennae, such as reflect array and Yagi-Uda.

In [133], a Yagi-Uda antennae for a CubeSat platform consisting of six linear elements was integrated with solar cells. In this proposed Yagi-Uda antennae, the solar cells were placed between the reflector elements. The antennae has an impedance bandwidth of 53 MHz and a maximum gain of 11.5 dBi. The results and discussion have not included any solar performance measurements. The solar parabolic reflector antennae in [134] was designed to be composed of two parabolic circular shaped silicon solar panels with a diameter of 60 cm, connected in parallel. The first silicon solar panel, with a bottom DC contact layer to collect the generated current, at the same time, worked as a parabolic reflector fed by horn. This antennae can be used for household reception of digital TV signals operating in a satellite Ku-band downlink frequency band of 10.90-12.75 GHz. It offered an average gain of 32.8 dB with a narrow beam width of about 2.6% over the desired frequency band. This bandwidth is limited for broadband two-way applications and the antennae is not a good candidate for dual-polarised downlink and uplink operation bands. However, reflect-array antennae have drawbacks of their narrow bandwidth and losses in the system. The losses include spill over, cross-polarisation, blocking and non-uniform illumination, but the main loss that is unavoidable is spill over loss. Therefore, a number of design techniques have been used in order to minimize spill over losses. One of these techniques that use a reflect-array sub reflector or a flat reflect-array sub-reflector with a main parabolic/flat reflector antennae, to provide a very large equivalent focal distance and thus illuminate efficiently the main reflector and reduce the spill-over. Nevertheless, these lead to an increase in weight

and cost. In addition to the inefficiencies associated with these losses, the reflect-array solution [68, 134-136] is not completely planar, and the presence of a feed horn shades the solar cells. Moreover, such antennae typically exhibit narrow bandwidths and work at lower operating frequencies rather than high frequencies and high losses. There have been, likewise, some investigations of such antennae made from different reflect transparent materials. There have also been some PV antennae combinations used for high frequency applications such as earth to satellite communications and vice-versa. These solar antennae apply transparent conductive materials such as ITO or AgHT-4 films, utilized as reflective elements for reflect-array antennae integrated with solar cells. As in [137], a transparent reflect array of 392 elements operating at 26 GHz was designed to mitigate overall losses by using subwavelength elements and extra-wide rectangular ITO reflect array patches, which exhibited a 272° phase range. It provided a beam at 20° and a measured peak gain of 22.2 dBi. It was demonstrated that there was not good matching in the reflection coefficient however, and the design still had narrow bandwidth. The proposed solar reflect antennae in [138-144], despite the fact that these have a planar geometry. However, similar to those designs in [68, 134-136] the general framework is not appropriate for lightweight and non-compact integrated solar antennae, due to the necessity of a feed horn and its accessories, which must be located away from the array.

Chapter 4 Photovoltaic (PV) Solar Cell

4.1 Introduction

Within this thesis, in relation to integrate of microwave antennae with crystalline silicon solar cells techniques. In this chapter, in section 4.2 is to provide the functions and an understanding of photovoltaics and crystalline silicon solar cells, and PV simple modelling using an equivalent electrical circuit. In section 4.3, the most common types of crystalline silicon solar cells structures are introduced with their advantages and disadvantages. Then, in section 4.4 and 4.5, the I-V characterisation of the main parameters is presented and illustrated, followed by a description of efficiency and outlines of loss factors of these solar cells. Section 4.6 presents the structure connection of crystalline silicon solar cells into a module structure.

4.2 Photovoltaics

A PV solar cell, is an electrical device that converts the sunlight directly into electricity by semiconductors photovoltaic effect, which is based on a physical incident [145, 146]. The basic structure of a crystalline silicon solar cell is demonstrated in Figure 4.1.

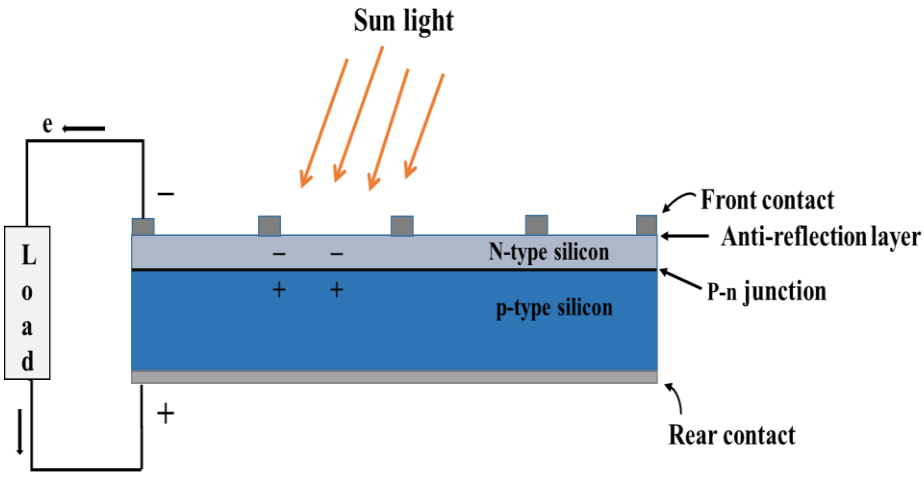

Figure 4.1: Basic structure of a crystalline silicon solar cell

The PV cell has electrical contact fingers on top surface and rear-back contact on bottom to capture the electrons, when the PV cell is illuminated by a light source, an electrical DC power generates and delivers to the load, as shown in Figure 4.1. A PV cell consists of two

layers; p-type silicon layer and n-type silicon, and the area between the two different regions of crystals, is called a p-n junction. The electrons flow out of the p-type side to n-type, because of the electric field at the sides of junction. These electrons carrying a current and go through the external connection wires to the load in the electrical power form. Then back to the p-side through the rear-back contact of the cell, in which they recombine and fill again the holes that are vacancies, then continuing generating a flow of electricity. On the other hand, there is an electric field causes a current flow (conventional current) in the opposite direction of the electrons [145, 147].

4.3 Structure of a Crystal Silicon Solar Cell

There are the different types of solar cells due to the crystalline silicon is the most common type of solar cells. Therefore, in this thesis, the integration of such type of crystalline silicon solar cells with microwave patch antennae are presented and investigated.
The integration of microwave antennae with crystalline silicon solar cells are presented and investigated. Crystalline Silicon PV solar cells can be classified into two main types of crystalline silicon (c-Si) and can be defined and described briefly as follows:

- Monocrystalline silicon (Mono-Si) solar cells: are called "single crystalline" and are made from pure type of silicon where there is seed crystal to grow, typically is produced by common method is the Czochralski process. Mono-crystalline silicon solar cells more efficient than polycrystalline silicon solar cells and most other types of cells. Their efficiencies in percentage have been reported in the range of 13-26.7 ± 0.5 %. However, they take more time in production process and more expensive, compared to the casting of polycrystalline, due to the lattice perfection.

- Polycrystalline silicon or (multicrystalline silicon multi-Si) solar cells: consist of a number of multiple small materials of silicon crystals or crystallites with high purity hence, this gives the name of ‘poly’. They have a blue colure and speckled appearance. For polycrystalline silicon solar cells the Czochralski process are not required and no seed crystals to be grew up. The production process that are used, called ‘casting process’ or solidification process where the molten silicon is carefully cooled down and cast into a square ingot, which then multi-grain sliced into thin silicon wafers. Polysilicon cells are the most common type used in photovoltaics and

are less expensive, but also less efficient than monocrystalline silicon, with typical efficiencies of about between 12-22.4%, due to the lower purity. It has another disadvantage, which is lower heat tolerance [148, 149].

4.4 Characteristics of a solar cell

When no illumination occurred, a PV cell operates as an ideal single semiconductor diode in parallel with a current source, where a diode current, ID flows from the p- side to the n-side of the p-n junction. As shown below in Figure 4.2, a PV solar cell model can be represented by an electrical equivalent circuit. When PV cell under changing illumination, a current is generated by photons, which is often denoted as (photocurrent, Iph). A constant output value depends on constant of illumination intensity of light and temperature. The electrical equivalent circuit is also needed to understand the behaviour of I-V curve characteristics, which will be demonstrated within this chapter. The equivalent circuit model of a simple PV solar cell is illustrated in Figure 4.2.

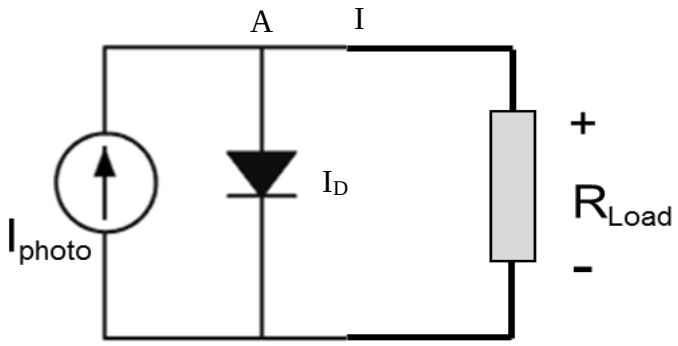

Figure 4.2. Equivalent circuit model of a PV cell.

From an electric component theory perspective, the rules of Kirchhoff's current law can be applied to an ideal PV equivalent circuit and how respond to a load, in order to analyse and determine solar cell distributed currents. The cell current can be obtained as shown below if Kirchhoff's current law is applied to the circuit Node (*A*).

$$I = I_D + I_{ph} \tag{4.1}$$

where, I: is the output current of the solar cell, I_{ph}: is the photo-generated current, I_D: is the diode current. The diode current I_D is given by the Shockley's diode formula:

$$I_D = I_o \left[exp \frac{qV}{KT} - 1 \right] \tag{4.2}$$

Replacing I_D of the equation (4.1) by the equation (4.2) this gives:

$$I = I_L - I_o \left[exp \frac{q(V)}{nKT} - 1 \right] \tag{4.3}$$

where: I_0: "dark saturation current" q: charge of an electron (1.602×10-19 C), V: applied voltage across the diode, *n*: ideal factor, k: Boltzmann's constant (1.381×10-23 *J/K*), *T* : cell working temperature I_L : light generated current.

In order to determine an overall output power of a polycrystalline solar cell characteristics measurement when integrated with microwave patch antennae. There are several important key parameters need to be performed and measured such as: open-circuit voltage (V_{OC}), short-circuit current (*Isc*), the fill factor (*FF*) and efficiency, which are discussed in the following sections.

4.4.1 Open Circuit Voltage (V_{OC})

The open-circuit voltage, V_{OC}: is the maximum voltage available at an open-circuit terminals of an ideal solar cell without any load connected, and this occurs at zero current [150]. Its equivalent circuit model is demonstrated in Figure 4.3.

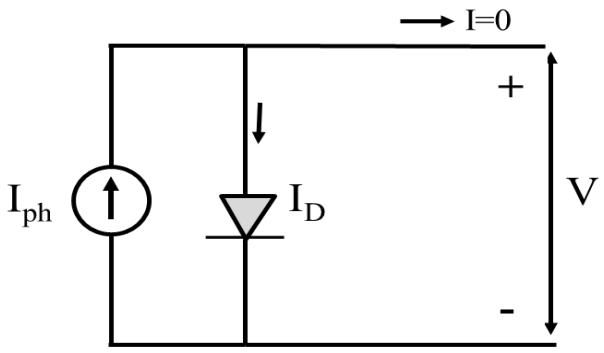

Figure 4.3: Equivalent circuit of open-circuit termination an ideal solar cell model.

By assuming the output current, zero the V_{oc} can be derived as follows:

$$I = I_L - I_0 (e^{qV/kT} - 1) \tag{4.4}$$

$$I_{ph} = qAG\,(L_h + L_e) \tag{4.5}$$

where: *q:* is the electric charge, *A* is the cross-sectional area, *G:* is the generation rate and (L_h , L_e) are the diffusion length of the hole and electron.

As at the open-circuit termination, the cell current is equal to zero, can be expressed by:

$$I = \left\{ I_o \left[exp \frac{qV}{KT} - 1 \right] - I_{ph} \right\} = 0 \tag{4.6}$$

If the current of the cell is equal to zero, hence, a point of output power is $P = I\,x\,V = 0$, at $I = 0 \rightarrow V = V_{oc,}$ the open-circuit voltage can be given as:

$$V_{oc} = \frac{KT}{q} ln(\frac{I_{ph}}{I_o} + 1) \cong \frac{KT}{q} ln(\frac{I_{ph}}{I_o}) \tag{4.7}$$

4.4.2 Short Circuit Current (ISC)

The short circuit current of an ideal solar cell is the maximum current value of a cell as the terminals are connected (short circuit, SC condition) with zero resistance load, when the voltage equals zero. Simplified equivalent circuit model for short circuit current (I_{SC}), is illustrated in Figure 4.4. Note that I_{SC} is directly proportional to the available sunlight, therefore the short-circuit current is the maximum current, which may be produced from the solar cell.

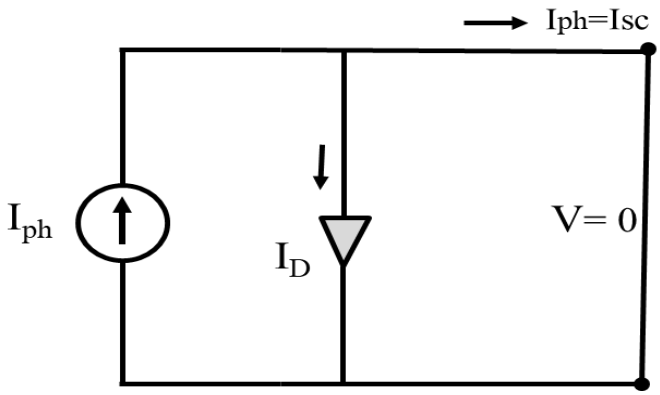

Figure 4.4: Equivalent circuit of short-circuit termination an ideal solar cell model.

In this situation, the voltage across the diode model is equal to zero, $I_D = 0$, this means that the resulted cell current is equal to photocurrent. Consequently, this leads to $I_{ph} = I_{sc}$, which is the maximum current, may be delivered from a solar cell into circuit. From the simplified equivalent circuit above in Figure 4.4, short-circuit current can be found as follows:

$$I_{sc} = \left\{ I_o \left[exp \frac{qV}{KT} - 1 \right] - I_{ph} \right\}_{V=0} \tag{4.8}$$

By Substituting $V = 0$, in equation (4.8) thus, the short current can be determined as:

$$I_{SC} = I_{ph} = -qAG\,(L_h + L_e) \tag{4.9}$$

4.4.3 PV Cell IV-Curve

The most commonly used method for testing solar cells is to perform an IV characteristics curve. An I-V characteristics behaviour of a crystalline silicon solar cell in the dark and under illumination is demonstrated in Figure 4.5. As illustrated in section 4.5, the equivalent circuit model of an ideal crystalline silicon solar cell in Figure 4.2, which includes two elements, behaves such as a diode and a photocurrent source [151].

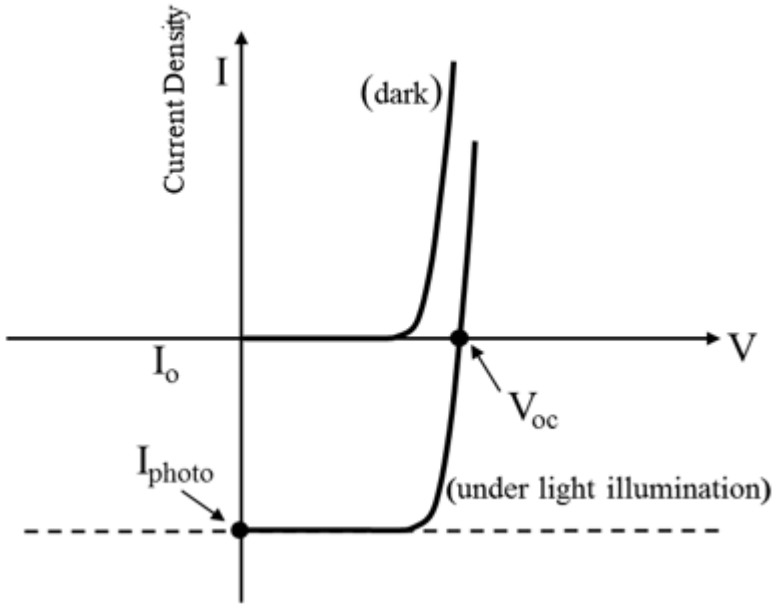

Figure 4.5: I-V curve characteristics in the dark and under illumination

As shown in Figure 4.5, a general solar cell VI characteristic relationship for a PV cell when there is no illumination (dark) and under illuminated (light). The no light plot is just represented a diode curve, as operates in the first and third quadrants. While, the under light curve includes the dark current, in addition to a short-circuit current (I_{SC}), which appears in the fourth quadrant. The cell current is shifted to the fourth quadrant by an amount of current, due to flow against the conventional direction of a forward diode current. It means that a crystalline silicon solar cell has negative current ($-I$) and positive voltage ($+V$), when under illumination it works as an active element and generates an electrical power.

4.5 Solar Cell Efficiency and Losses

Efficiency (η) is the most commonly parameter that used to determine the performance of a photovoltaic solar cell, which can be defined as the percentage ratio of electrical power output generated from the solar cell to the total incoming power. There are two important

parameters are very needed in order to measure the overall efficiency of a solar cell, which are the maximum power and the fill factor [27] and can be defined as:

- Maximum power: Pm
- Fill factor (*FF*)

A maximum power is a power value (peak point) of a solar cell**,** which can be obtained at the maximum point of power (P_m) in the current and voltage (*I-V*) curve. In this chapter PV cell, *IV*-curves are transferred to the first quadrant for easy to understand, as shown in Figure 4.6, and the maximum power can be written by:

$$P_m = I_m \, x \, V_m \tag{4.10}$$

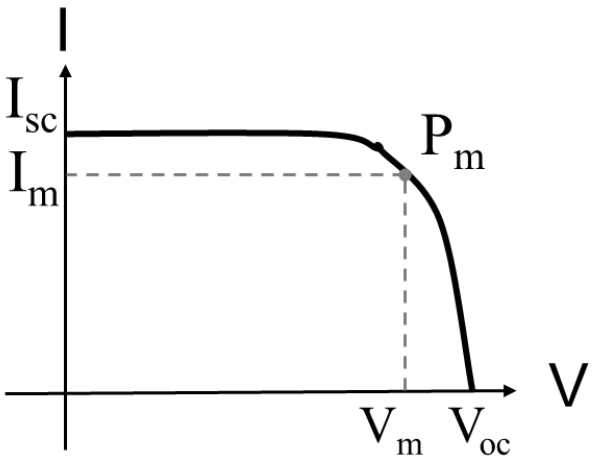

Figure 4.6: I-V maximum power curve

As can be seen in Figure 4.6 above, solar cell *I-V* plot of current is usually shown on positive y –axis. The produced current and voltage values represents the power output in each point of the *IV*-curve. A PV solar cell can be characterised by a maximum power point, the output power of a solar cell increases as voltage rises until reaches a maximum (P_m) value when $V_{mp} \times I_{mp}$ is maximum value and then decreases again. It is known that the output power that is obtained from a solar cell is always DC power.

The Fill Factor (*FF*): is defined as a parameter that based on the ratio of the maximum actual power (P_{MAX}) from the solar cell to the maximum ideal (theoretical) power, determined by the open circuit voltage (V_{OC}) and short circuit current (*Isc*) maximum points [150, 151]. The *FF* can also be described graphically by the largest rectangle area that is fitted under the *I-V* curve.

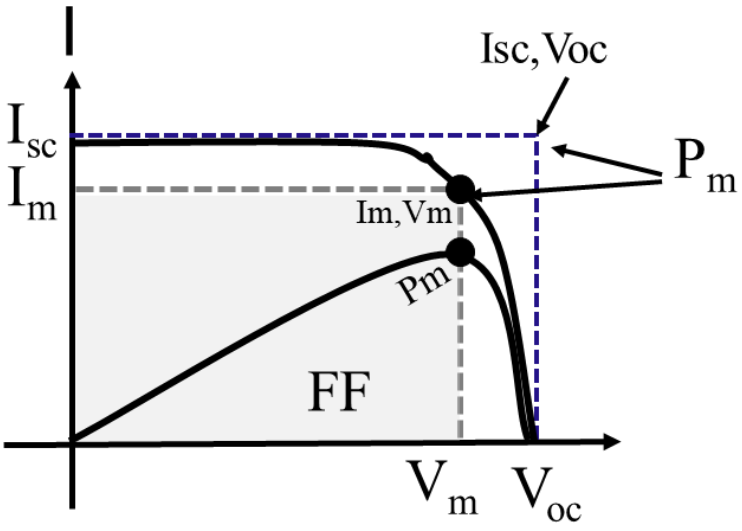

Figure 4.7: - Fill Factor (FF) and maximum Power form an I-V curve

As can be seen in Figure 4.7, showing short-circuit current (*Isc*) and open-circuit voltage (V_{oc}) points, as well as the maximum power (P_{MP}) point at (V_{mp}, I_{mp}). Hence, the *FF* can be obtained in terms of those maximum powers, as follows:

$$FF = \frac{Max\ power\ \ from\ real\ cell}{Max\ power\ \ from\ ideal\ cell} = \frac{V_m I_m}{V_{oc} I_{sc}} \tag{4.11}$$

Thus, from equation (4.11) the fill factor can be re-expressed and given as:

$$FF = \frac{P_{MP}}{V_{OC}\, I_{SC}} \tag{4.12}$$

Therefore, from equation (4.12), P_{MP} can be expressed as:

$$P_{MP} = V_{OC} I_{SC} FF \tag{4.13}$$

Thus, incoming total solar cell power (P_{in}) is equal to:

$$P_{in} = P_{il} A \tag{4.14}$$

where, P_{il} is the total solar illuminating incident light measured standard in W/m^2, and A is the total solar cell surface area. The typical solar cell efficiency based on FF can then be given by the following equation [150, 151]:

$$\eta = \frac{P_{MP}}{P_{in}} = \frac{V_{OC}\, I_{SC} FF}{P_{in}} \tag{4.15}$$

The table 4.1 below shows one of the best records of solar cells efficiencies have been reported for different photovoltaic types, obtained from (values courtesy of the National Renewable Energy Laboratory, Golden, CO). Under conditions of light intensity and room temperature of (1000 W/m^2, 25 ^{0}C) [152].

Table 4.1: Recorded of solar cells efficiencies

Solar Cell Type	**Highest Efficiency (Research)**
Monocrystalline silicon (mono-Si)	26.7 ± 0.5 %
Polycrystalline silicon (multi-Si)	22.3 ± 0.4%
Amorphous silicon (a-Si)	11.9 ± 0.3%
Monocrystalline gallium arsenide (GaAs)1	29.1 ± 0.6%
Cadmium telluride (CdTe)	21%±0.4%
Copper indium gallium selenide (CIGS)	22.9 ± 0.5%
Dye-sensitised (DSSC)	11.9%±0.5%
Organic (OSC)	11.2%±0.3%
Perovskite (PSC)	20.9%±0.7%

There are some main loss factors effect a solar cell overall energy efficiency of crystalline silicon, can be divided into following categories:

- Optical losses
    - Shading by the top contact
    - Reflection from the top surface
    - Reflection from the rear surface
- Losses due to quantization of energy in photons
- Recombination Losses
- Resistive losses

The main above losses will not be addressed in detail due to the solar cells is not the main subject of this thesis.

4.6 Connection of Solar Cells

Photovoltaic module that uses cells with polycrystalline cells are connected in series or parallel offer improved efficiency due to its reliability and ensure reliable long-term performance. Modules of crystalline silicon solar cells can be connected to series and/or in parallel as follows in two different configurations:

4.6.1 Series Connection

In series connection, identical crystalline silicon solar cells can be connected in series configuration, which connect end to end or chained together. In this case, the current, which generates from first cell is the same common current flowing through the other series cells, and produce an additive output voltage [153].

A module of *N* similar crystalline silicon solar cells connected in series is shown in Figure 4.8.

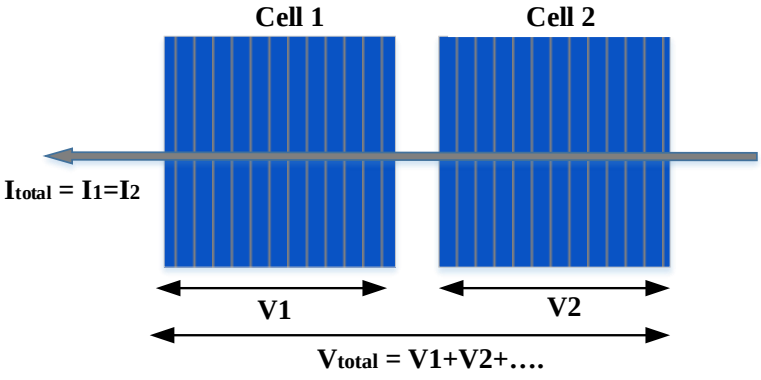

Figure 4.8: Series connection module of solar cells

Supposing that the solar cells are identical in electrical characteristics, the total voltage is equal to the open-circuit voltage of the individual cell module (*Voc*) multiplied by the number (*N*) of cells. The total amount of open-circuit voltage ($V_{max\ OC}$) can be written by:

$$V_{max\ OC} = V_{OC} \times N \tag{4.16}$$

The IV curve of the PV cells module connected in series is the same as the individual cell, except that the amount of current and voltage are increased, as demonstrated in Figure 4.9.

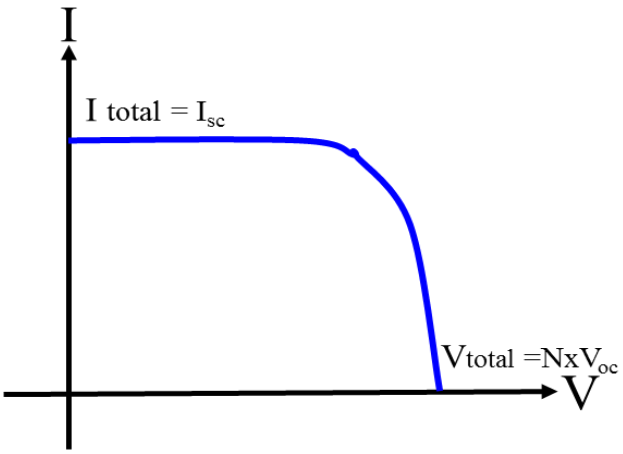

Figure 4.9: Total I-V curve for N solar cells in series module

4.6.2 Parallel Connection

In parallel connections, similar crystalline silicon solar cells connected side by side to each other in parallel configuration, as illustrated in Figure 4.10. In this type of connection, the currents take multiple paths where the current is not the same at all terminal points and then added together. Whereas, the voltage that is produced across all the cells terminals is the same, and collected at a common voltage across line [153]. The following figure 4.10 illustrates (*N*) identical crystalline silicon solar cells in parallel configuration module.

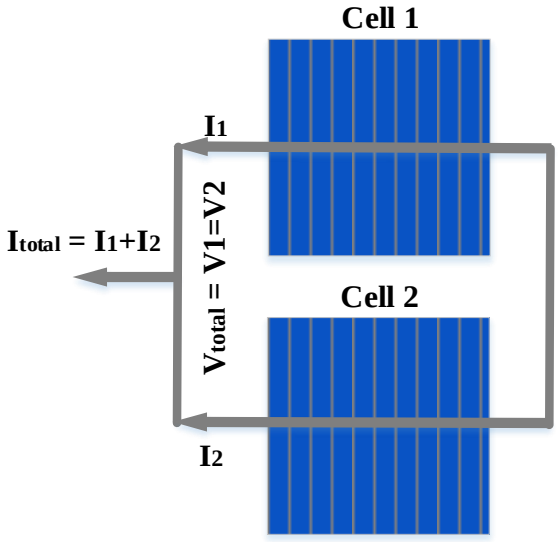

Figure 4.10: Parallel connection of solar cells in a module

The total short-circuit current of crystalline silicon solar cells in parallel module can be simply given as:

$$I_{max\,SC} = I_{SC} \times M \tag{4.17}$$

where, M is the number of cells in parallel. The IV curve of the PV cells module connected in parallel is shown in Figure 4.11.

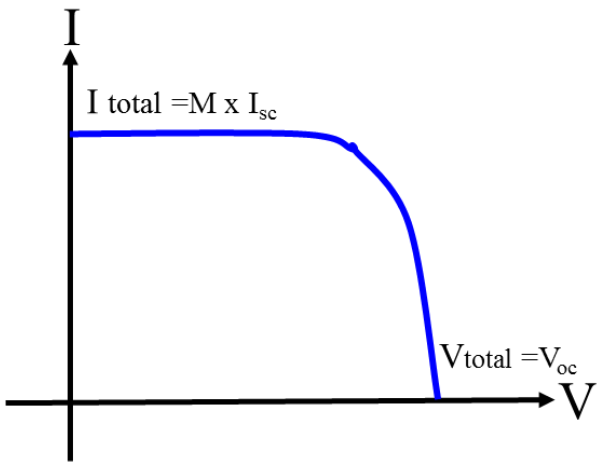

Figure 4.11: Total I-V curve for M solar cells in parallel module

By the way, both modules of the series and the parallel connections can be configured together in order to result a wide variety of maximum ratings of output power.

4.7 Summary

In this chapter a background on photovoltaics and solar cells was given. The functions and an understanding of photovoltaics and crystalline silicon solar cells operation were presented. The most common types of crystalline silicon solar cells structures were introduced, in addition to their advantages and disadvantages. This chapter also covered the basic theory and models of solar cell PV simple modelling using an equivalent electrical circuit. Then, the I-V characterization of the main parameters was presented and illustrated, followed by a description of efficiency and outlines of loss factors for these solar cells. It presented also the structure connection of crystalline silicon solar cells into a module structure.

Chapter 5 Analysis of Slots Loaded Patch Antennae Using Segmentation Model

5.1 Introduction

This chapter involves the analysis of slots loaded on a square patch to determine input impedance. Firstly, the analysis of the antennae will begin by using the Green's function approach for a simple geometry patch, before starting with the use of the segmentation approach, which is the most often-suggested method for irregular geometries. This is followed by the basic theory of slot loaded microstrip patch, which is explained briefly in Section 2.4. Then, the obtained impedance responses of the antennae will be compared with the simulated results of the CST Microwave Studio and analysed.

5.2 Basic Theory of Slot loaded Microstrip Patch Antennae

In order to provide a better understanding about the effect of the slot on microstrip patch antennae characteristics before start designing any slotted patch antennae. Therefore, a basic theory of slot loaded patch antennae is briefly introduced. A slot patch antennae can be defined as a patch with a slit cut out in the flat copper patch, this can be seen in Figure 5.1 (a) and (b), which shows the current flow of an antennae with one slot and two slots.

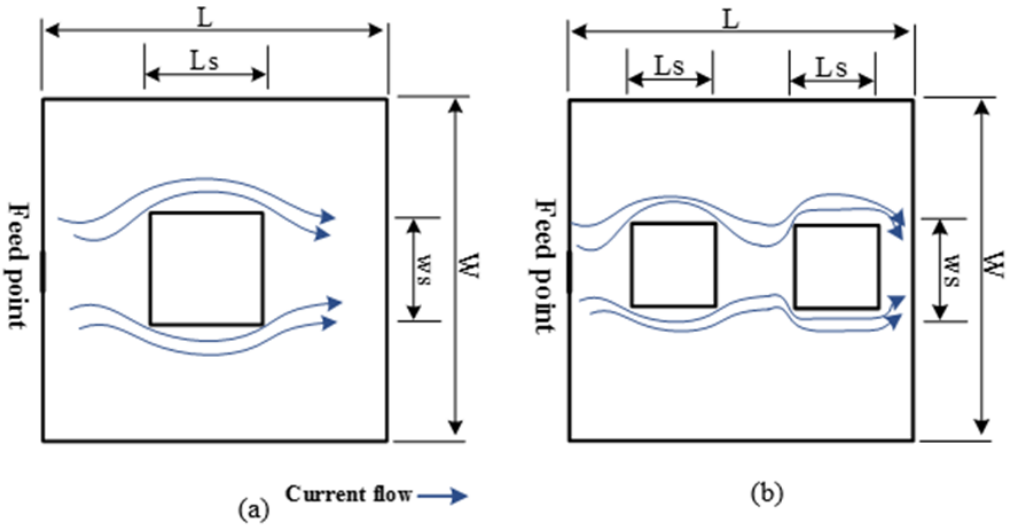

Figure 5.1: Patch current flow for (a) single slot (b) double slots

Normally, in a patch antennae, the current flows from one edge to another edge in a straight path. Essentially, a slot is used in order to reduce the desired frequency to a lower position where frequency is inversely proportional to patch effective length. In many applications, the slot reduces the fundamental and the third harmonic, which is achieved by applying a slot at a certain position on the patch. A single slot would cause a decrease in $TM_{1,0}$ mode and two slots would cause a decrease in $TM_{2,0}$ mode. In general, the slot is loaded by looking at the surface current density distribution on the patch antennae, in which the slot is located in the middle of the patch to reduce the $TM_{1,0}$ mode, and at both the edges for $TM_{3,0}$ mode. The reason the slot is located in the middle for $TM_{1,0}$ mode, and at both edges for the $TM_{3,0}$ mode is that the current density is high in those locations [154-156]. By inserting the slots in the patch where the current density distribution is very high, the radiation from the slots changes the field distribution. However, theoretically, the length of the current flow increases if a slot is placed on its path. This can be seen clearly in Figure 5.1 (a) and (b), and causes decrease in frequency due to the fact that the frequency is controlled by the length of the patch antennae. Therefore, by using this method, a compact antennae can be achieved because the dimensions of the patch antennae with slots would be smaller than the original patch antennae (without slots), although both the patches operate at the same frequency.

5.3 Applied the Green's Function to Square Patch Antennae

The available formulation (Equation 2.67) in the previous chapter, which is based on the Green's function approach. This is used in order to determine the overall input impedance characteristics of a square patch antennae shown in Figure 5.2.

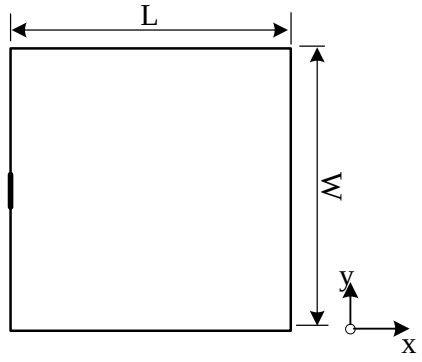

Figure 5.2: Single Square Patch Antennae

The patch antennae, which will be performed in this chapter and next subsequent chapters in this thesis is designed to operate at 3 GHz, and 11.95 GHz printed on substrate, each with relative permittivity (ε_r) = 2.33, and (ε_r) = 2.59, respectively. The width and length of the patch antennae have been made the same, $L = W$ to be applicable later for linear dual-polarised operation. With reference to the Figure B.1, presented in Appendix 3C of both ports are located to be at the same point on the x-axis, is used.

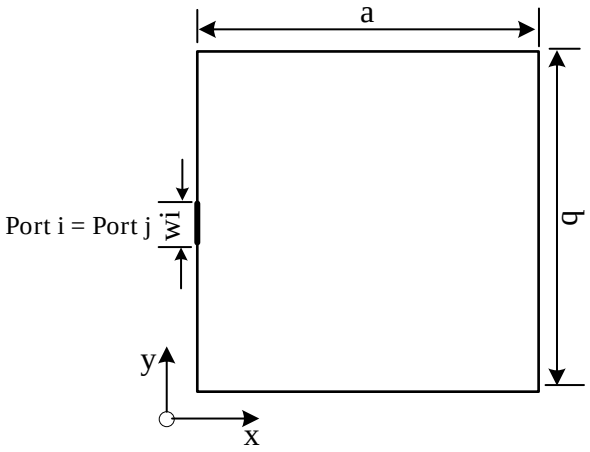

Figure 5.3: Two ports i and j at the same point on x-axis

where, Port i is located at: $x_i, y_i \pm \frac{W_i}{2}$, and Port j is located at: $x_j, y_j \pm \frac{W_j}{2}$

From equation (2.67), the mathematical solution for the formula becomes as follows:

$$Z(f) := \left(\frac{i\cdot 2\cdot\pi\cdot f\cdot\mu_0\cdot h}{a\cdot b\cdot w\cdot w}\right)\cdot\left[\sum_{m=0}^{\infty}\left[\sum_{n=0}^{\infty}\left[\sigma(m)\,\sigma(n)\left(\frac{2\sin\left(ky_n\cdot\frac{w}{2}\right)}{ky_n}\right)^2\cdot\frac{\cos(k(m)\cdot x1)\cdot\cos(k(m)\cdot x2)\cdot\cos\left(ky_n\cdot y1\right)\cdot\cos\left(ky_n\cdot y2\right)}{\left[\left(kx_m\right)^2+\left(ky_n\right)^2-(k(f))^2\right]}\right]+\sigma(m)\,w^2\cdot\left[\frac{\cos(k(m)\cdot x1)\cdot\cos\left(kx_m\cdot x2\right)}{\left[\left(kx_m\right)^2-(k(f))^2\right]}\right]\right]\right] \tag{5.1}$$

The patch dimensions a and b in the above equations include line extensions ΔL, which is given by Equation (2.35) in Chapter 2, to account for fringing fields. Thus, the extended dimensions can be given as:

$$a = L + \Delta L, \quad \text{and} \quad b = W + \Delta L \tag{5.2}$$

The wavenumbers of antennae resonant modes are given by:

$$k_{xm} = \frac{m\pi}{a} \tag{5.3}$$

$$k_{yn} = \frac{n\pi}{b} \tag{5.4}$$

$$k(f) := \sqrt{(2\pi f)^2 \mu_0 \varepsilon o \cdot \varepsilon r \left(1 - \frac{i}{Qt}\right)} \tag{5.5}$$

where, Q_t: is total Q factor of the patch antennae using the equations given in chapter 2. The calculations were conducted using the equations given previously, and are shown in Appendix (*3A*) using Mathcad software. The upper limit on summation were taken to be $m = n = 15$, which was found to give good convergence in results. The theoretical real and imaginary parts for the input impedance against frequency of the sold square patch are shown and compared with CST, in section 5.4.

5.4 Solid Square Patch Antennae CST Model

In order to compare with the theoretical calculation, in this section, a design of 3 GHz square patch with a RT5870 substrate with permittivity 2.33 is modeled and simulated. Using CST Microwave Studio as shown in Figure 5.4.

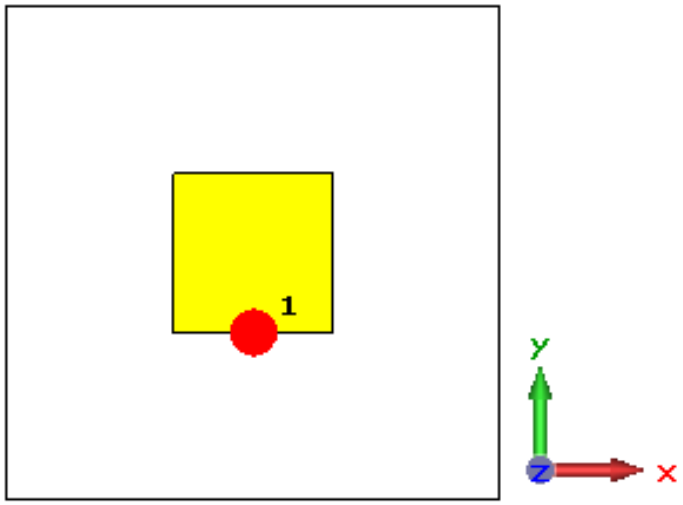

Figure. 5.4: Sold patch square patch antennae CST model

The input impedance (real and imaginary parts) responses are also demonstrated in Figure 5.5. A comparison was conducted of the theoretical and simulated results, and is provided in Table 3.1.

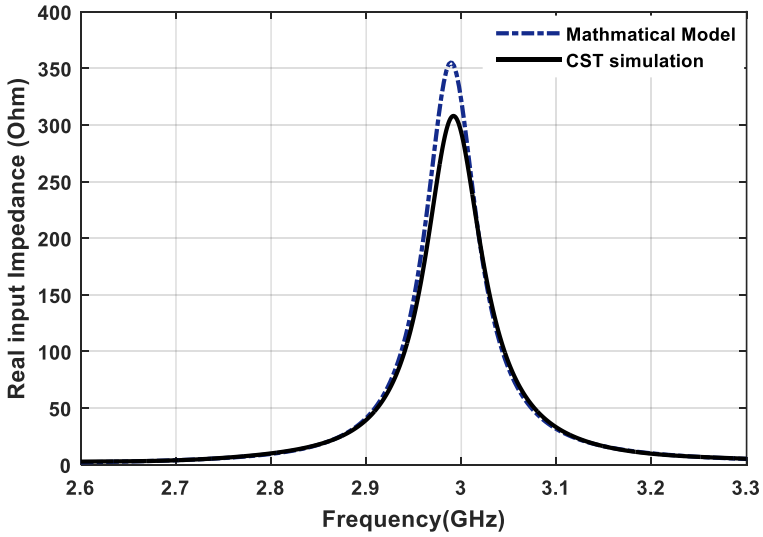

(a)

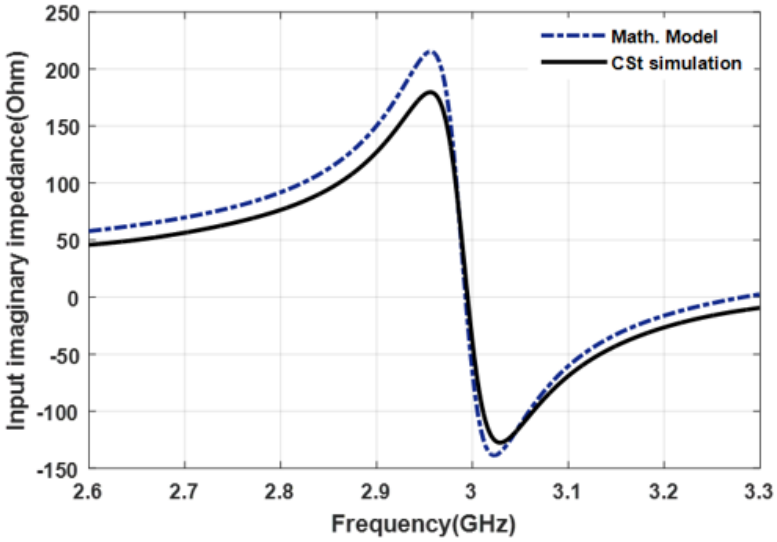

(b)

Figure 5.5: The input impedance of square patch antennae (a) Real parts (solid line CST, dashed line Math. Model), (b) imaginary parts (solid line CST, dashed line Math. Model)

Table 5.1: Impedance characteristic of square patch antennae obtained by the theoretical model and CST simulated results

Modelling	**Centre frequency (GHz)**	**Input impedance Z_{in} (Ω)**
Theoretical	2.984	355.02
CST Simulation	2.993	307.47

It can be seen from the results in Table 5.1 that there is a good agreement between the theoretical and CST simulated results. The theoretical impedance value is slightly higher, with 48 Ohm, which could be due to the theoretical approximation model. However, this offset value is acceptable.

5.5 Segmentation Technique for Slots loaded Patch Antennae

For non-simple geometries where it may be difficult to apply the Green's Function techniques directly, a different approach can be adopted based upon Segmentation [62, 157-161], and De-segmentation [36, 162-165] techniques. The Segmentation approach is based upon breaking up a complex geometrical shape into a small number of simple geometric shapes for which Greens Functions can be readily determined. These simple shapes can be combined to produce more complicated geometries as shown below in Figure 5.6.

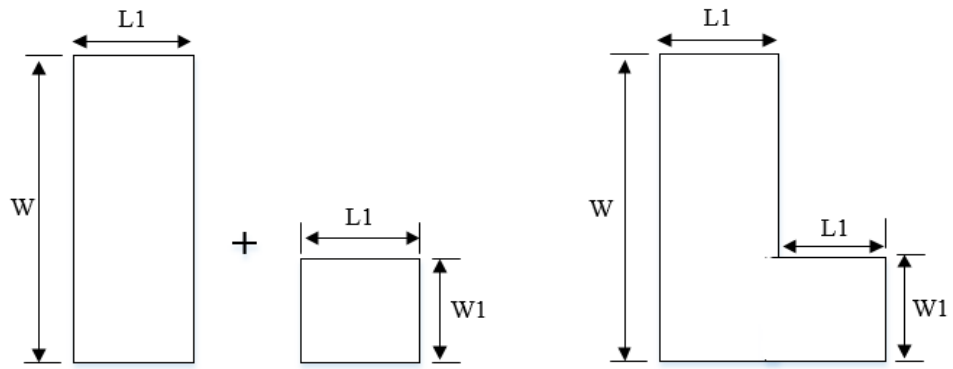

(a) (b)

Figure 5.6: Basic segmentation method (a) a simple complete circuit (b) adding patch segments

Similarly, the De-segmentation technique involves subtracting simple small geometric shapes from a larger shape to produce the required geometry as demonstrated below in Figure 5.7.

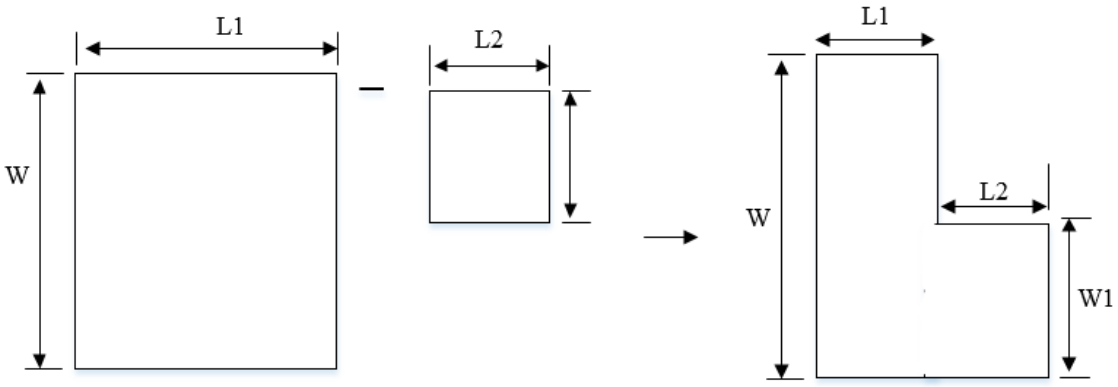

(a) (b)

Figure 5.7: Basic de-segmentation method (a) a complete circuit (b) subtracting patch segment

Threfore, for slots loaded patch antennae, which will be analysed in this chapter, the segmentation approach is selected due to the most appropriate approach for the analysis of such structures. The expression model of Z-parameters is then employed, which was derived directly from Green's Functions in chapter 2. This approach only works with external ports and hence, cannot simply use De-segmentation to subtract a square element from the middle of the solid patch.

5.6 Application of Segmentation to Patch Antennae with Square Slots

5.6.1 Square Patch with Single Slot

A geometry of a square patch antennae with single square slot is shown in Figure 5.8. The segmentation approach is used to analyse this structure, and the model is implemented using Matlab. The results will then be compared with those obtained using CST model. In this modelling approach, there are main process stages, which need to be followed:

- Decomposition of the patch element into a number of regular segments.
- An impedance matrix for each developed segment is determined.
- Synthesis of the segments of the entire structure.

In the first step, the structures of the entire slot-loaded patch are decomposed into several segments, as can be shown in Figure 5.9, in order to make them available for the Green's functions model. Then it is possible to start to determine the impedance matrix of the γ_1

segment, which can be determined by synthesising number of βs and α_1 segments, as in Figure 5.10.

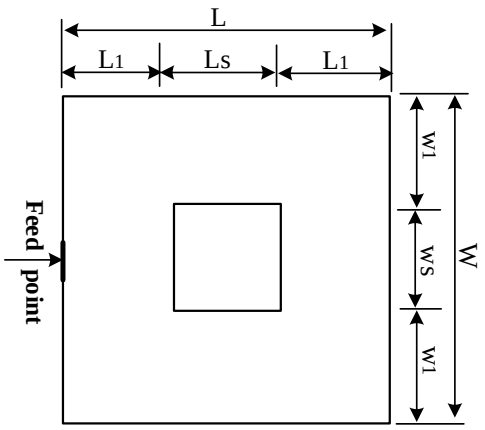

L = W = 30 mm, $l_1 = w_1 = 2$mm, $l_s = w_s = 10$mm, $\varepsilon_r = 2.33$, h = 1.57mm

Figure 5.8: Square patch antennae loaded with single square slot at 3 GHz

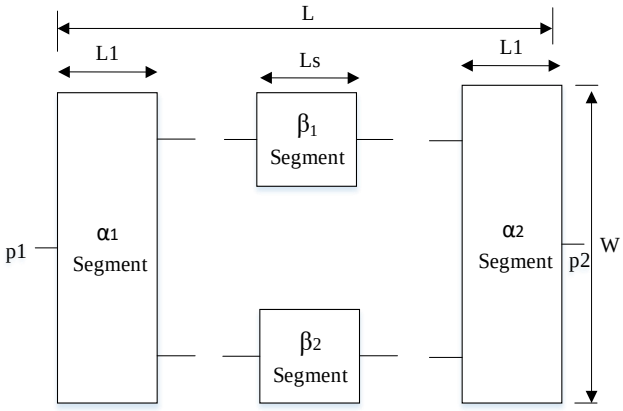

Figure 5.9: Patch decomposed into segments

As can be seen in Figure 5.9, the patch has symmetry segments block of βs, thus the number of computations operation can be reduced by determining one impedance Z-matrix of βs.

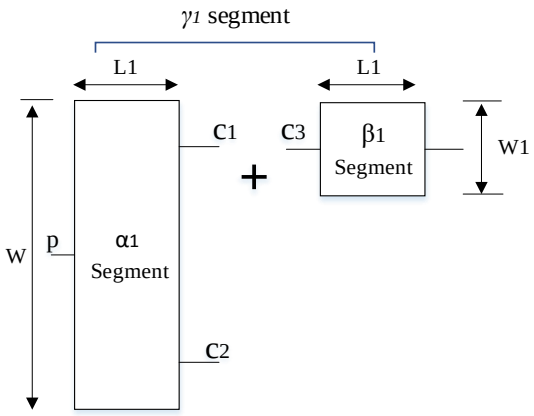

Figure 5.10: Combining of α_1 and β_1 segments

The β_1 segments are then synthesised to α_1 segment until having completed γ_1 segment. The c-ports are represented the internal connections between the connected segments, and the p-ports are external connections for non-joint segment, as illustrated in Figure 3.10. To obtain the impedance matrix for the unit cell, segments α or β can be determined as matrix form:

Z_α represents the Z-matrix of α segment and is given by:

$$Z_\alpha = \begin{bmatrix} Z_{pp} & Z_{pc1} & Z_{pc2} \\ Z_{c1c1} & Z_{c1c2} & Z_{c1p} \\ Z_{c2c2} & Z_{c2c1} & Z_{c2p} \end{bmatrix} \tag{5.6}$$

$$Z_\beta = \begin{bmatrix} Z_{c3c3} & Z_{c3c4} \\ Z_{c4c3} & Z_{c4c4} \end{bmatrix} \tag{5.7}$$

The same process for the β_2 segment and α_2 segment are synthesised to α_1, one by one until the whole structure of γ segment to be completed as shown in Figure 5.11, the final network impedance matrix for the final structure is then given by:

$$Z_p = \begin{bmatrix} Z_{p11} & Z_{p12} \\ Z_{p2p1} & Z_{p22} \end{bmatrix} \tag{5.8}$$

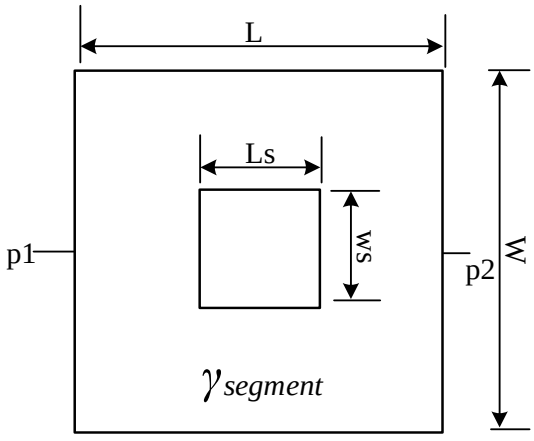

Figure 5.11: Complete structure (γ segment) of single square slot patch

Figure 5.12 shows the response of the real and imaginary part of the slot patch antennae input impedance versus frequency by Segmentation approach.

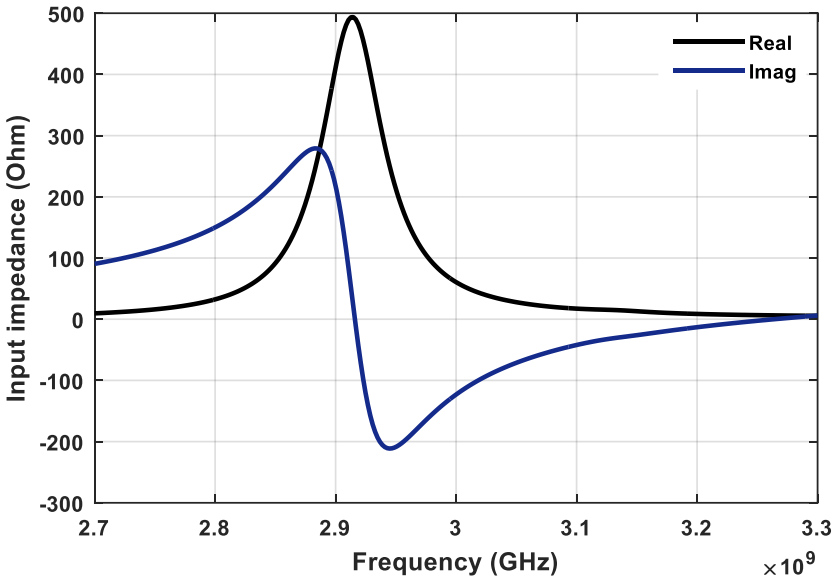

Figure 5.12: Real and imaginary part of the slot square patch antennae by Segmentation approach.

For comparison and more demonstration, the single slot antennae is designed, modelled and simulated at 3 GHz in CST, as shown in Figure 5.13

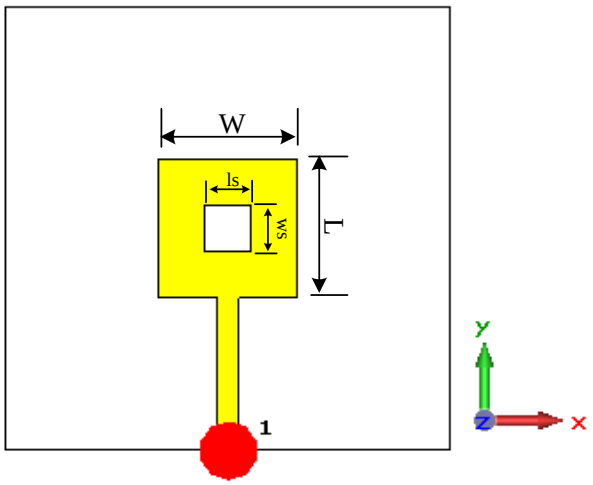

L = W = 30 mm, l_s = w_s = 10 mm, ε_r = 2.33, h = 1.57mm

Figure 5.13: Square patch antennae with single square slot

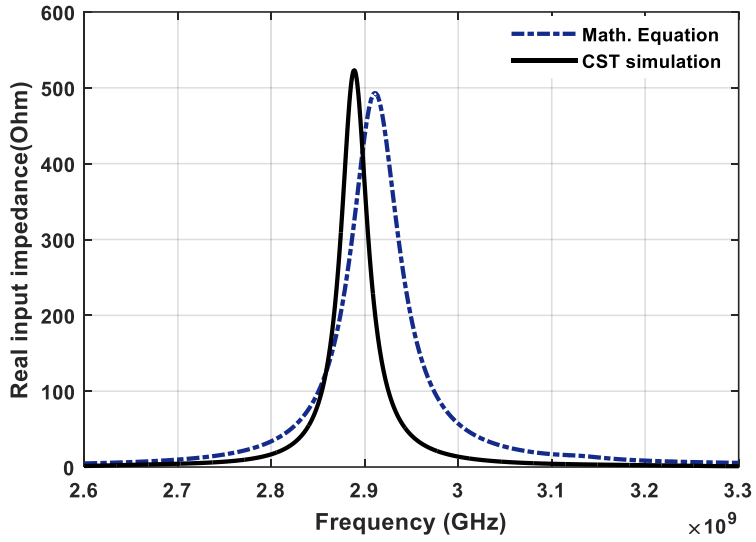

(a)

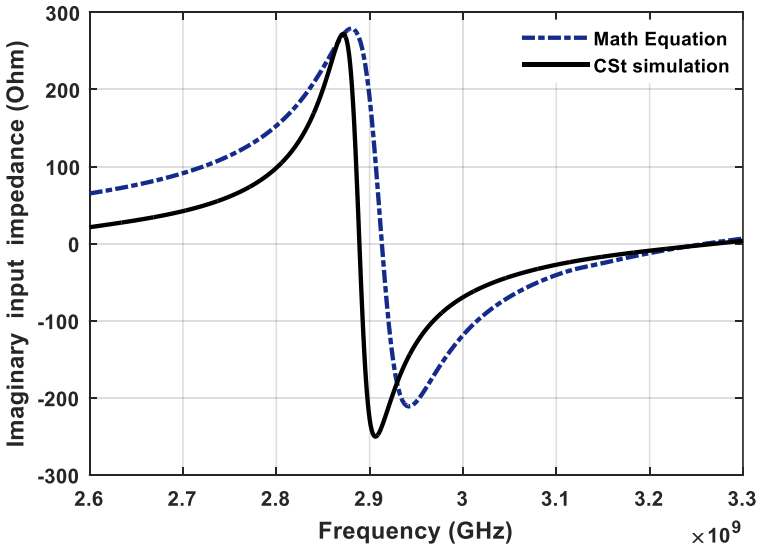

(b)

Figure 5.14: (a) Real parts (solid line CST, dashed line Math. Model) and (b) imaginary parts (solid line CST, dashed line Math. Model) input impedance of square slot patch antennae.

Table 5.2: Input Impedance of square single slot patch antennae obtained by the theoretical model and CST simulation

Modelling	**Centre frequency (GHz)**	**Input impedance Z_{in} (Ω)**
Theoretical	2.91	494.1
CST Simulation	2.88	520.2

As can be seen from table 5.2 that a good agreement between the theoretical and CST simulated results is demonstrated with only about of 1% frequency shift. Also, there is only a small offset-impedance, which the theoretical value is slightly lower by about of 26 Ohms. This could be due to the approximate of the theoretical model. It can be stated that the results having proved that the segmentation technique works well for the single slot case.

5.6.2 Square Patch with Multi-Slots Slot

To examine the segmentation method on to the more complicated geometry such as patch antennae with multi-slots. In this section, 4 x 4 array of slots loaded square patch as shown in Figure 5.15 is analysed and demonstrated.

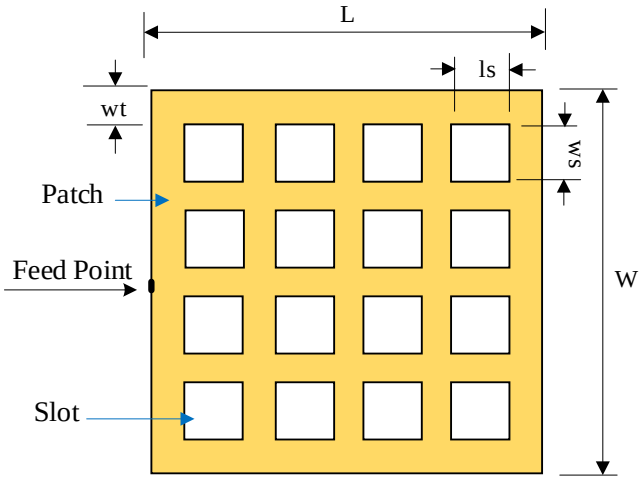

L = W = 6 mm, $l_s = w_s = 0.92$ mm, $w_t = 0.5$mm, $\varepsilon_r = 2.59$, h = 1.5mm

Figure 5.15: Square patch antennae loaded with Square slots at 11.95 GHz

The procedures of the entire process, which were carried out for single slot square patch in Subsection 5.6.1, will be repeated again in this Section. By breaking up the complex geometrical shape in Figure 5.15 into a small number of simple geometric shapes to be available for the Green's functions model. Therefore, the impedance matrix of the γ_s segment can be determined by synthesising α_s and number of β_s segments.

As can be shown in Figure 5.16, due to the symmetry of some segments of the patch e.g. β_{1s}, the number of computations can be reduced by determining one impedance Z-matrix of β_1, using Equation (5.1), and is then duplicated to others in a similar manner. Next then, the β_1 segments are synthesised to α segment one by one till be completed as γ_1 segment, as illustrated in Figure 5.17.

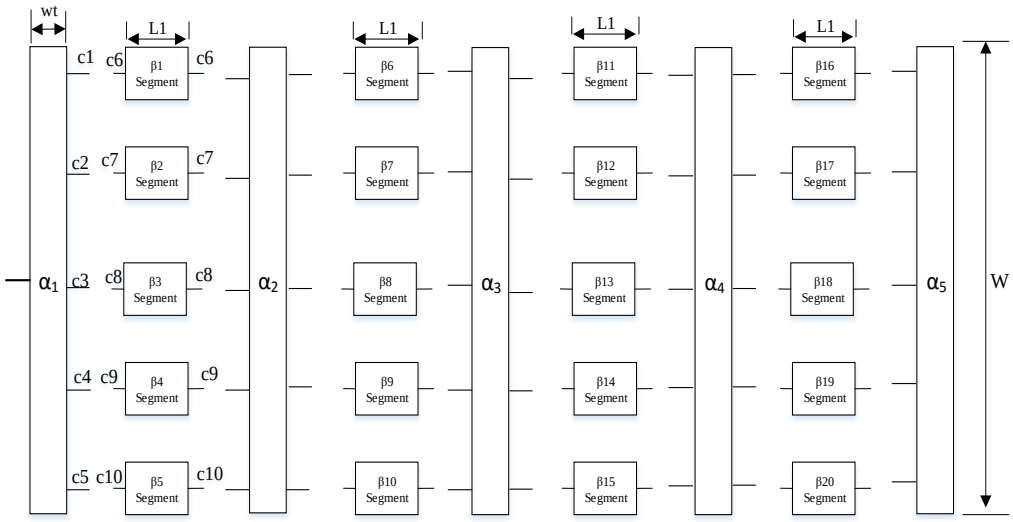

Figure 5.16: Decomposition the patch into a number of segments

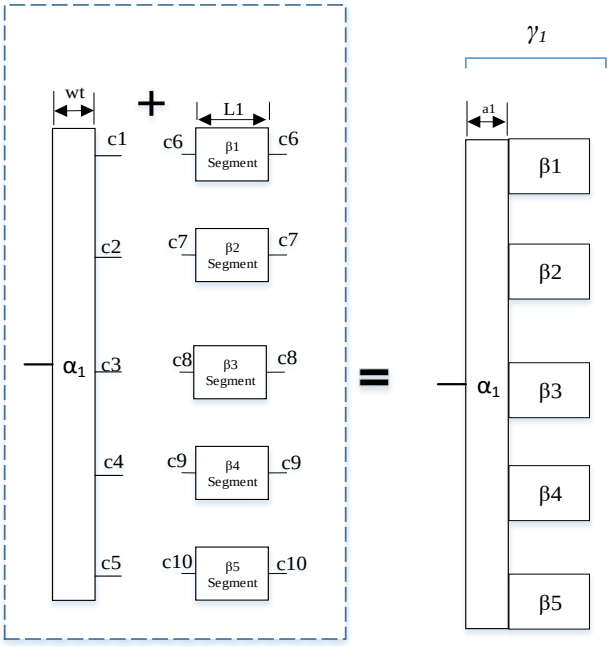

Figure 5.17: Ports of α1 and β1 segments

As can be seen in Figure 5.17 that the ports of α_1 and β_1 segments are numbered, and each side of each β segment has one interconnected port at the coupling side with determined width. This width of the port as recommended [157] must be less than or equal to the ratio relation of $\lambda g/20$, where λg is the effective wavelength of the fields in the substrate. To achieve the impedance matrices of the segment γ_1 which requires α_1 and $\beta_{1\text{-}5,}$ can be given by:

$$Z\alpha_1 = \begin{pmatrix} Z_{p1p1} & Z_{p2p1} & Z_{p3p1} & Z_{p4p1} & Z_{p5p1} & Z_{p6p1} & Z_{p7p1} & Z_{p8p1} & Z_{p9p1} & Z_{p10p1} \\ Z_{p1p2} & Z_{p2p2} & Z_{p3p2} & Z_{p4p2} & Z_{p5p2} & Z_{p6p2} & Z_{p7p2} & Z_{p8p2} & Z_{p9p2} & Z_{p10p2} \\ Z_{p1p3} & Z_{p2p3} & Z_{p3p3} & Z_{p4p3} & Z_{p5p3} & Z_{p6p3} & Z_{p7p3} & Z_{p8p3} & Z_{p9p3} & Z_{p10p3} \\ Z_{p1p4} & Z_{p2p4} & Z_{p3p4} & Z_{p4p4} & Z_{p5p4} & Z_{p6p4} & Z_{p7p4} & Z_{p8p4} & Z_{p9p4} & Z_{p10p4} \\ Z_{p1p5} & Z_{p2p5} & Z_{p3p5} & Z_{p4p5} & Z_{p5p5} & Z_{p6p5} & Z_{p7p5} & Z_{p8p5} & Z_{p9p5} & Z_{p10p5} \\ Z_{p1p6} & Z_{p2p6} & Z_{p3p6} & Z_{p4p6} & Z_{p5p6} & Z_{p6p6} & Z_{p7p6} & Z_{p8p6} & Z_{p9p6} & Z_{p10p6} \\ Z_{p1p7} & Z_{p2p7} & Z_{p3p7} & Z_{p4p7} & Z_{p5p7} & Z_{p6p7} & Z_{p7p7} & Z_{p8p7} & Z_{p9p7} & Z_{p10p7} \\ Z_{p1p8} & Z_{p2p8} & Z_{p3p8} & Z_{p4p8} & Z_{p5p8} & Z_{p6p8} & Z_{p7p8} & Z_{p8p8} & Z_{p9p8} & Z_{p10p8} \\ Z_{p1p9} & Z_{p2p9} & Z_{p3p9} & Z_{p4p9} & Z_{p5p9} & Z_{p6p9} & Z_{p7p9} & Z_{p8p9} & Z_{p9p9} & Z_{p10p9} \\ Z_{p1p10} & Z_{p2p10} & Z_{p3p10} & Z_{p4p10} & Z_{p5p10} & Z_{p6p10} & Z_{p7p10} & Z_{p8p10} & Z_{p9p10} & Z_{p10p10} \end{pmatrix} \quad (5.9)$$

$$Z\gamma_1 = \alpha_1\beta_{1\text{-}5} = \begin{pmatrix} Z_{p1\beta1} & Z_{p2\beta1} & Z_{p3\beta1} & Z_{p4\beta1} & Z_{p5\beta1} & Z_{p6\beta1} & Z_{p7\beta1} & Z_{p8\beta1} & Z_{p9\beta1} & Z_{p10\beta1} \\ Z_{p1\beta2} & Z_{p2\beta2} & Z_{p3\beta2} & Z_{p4\beta2} & Z_{p5\beta2} & Z_{p6\beta2} & Z_{p7\beta2} & Z_{p8\beta2} & Z_{p9\beta2} & Z_{p10\beta2} \\ Z_{p1\beta3} & Z_{p2\beta3} & Z_{p3\beta3} & Z_{p4\beta3} & Z_{p5\beta3} & Z_{p6\beta3} & Z_{p7\beta3} & Z_{p8\beta3} & Z_{p9\beta3} & Z_{p10\beta3} \\ Z_{p1\beta4} & Z_{p2\beta4} & Z_{p3\beta4} & Z_{p4\beta4} & Z_{p5\beta4} & Z_{p6\beta4} & Z_{p7\beta4} & Z_{p8\beta4} & Z_{p9\beta4} & Z_{p10\beta4} \\ Z_{p1\beta5} & Z_{p2\beta5} & Z_{p3\beta5} & Z_{p4\beta5} & Z_{p5\beta5} & Z_{p6\beta5} & Z_{p7\beta5} & Z_{p8\beta5} & Z_{p9\beta5} & Z_{p10\beta5} \\ Z_{p1\beta6} & Z_{p2\beta6} & Z_{p3\beta6} & Z_{p4\beta6} & Z_{p5\beta6} & Z_{p6\beta6} & Z_{p7\beta6} & Z_{p8\beta6} & Z_{p9\beta6} & Z_{p10\beta6} \\ Z_{p1\beta7} & Z_{p2\beta7} & Z_{p3\beta7} & Z_{p4\beta7} & Z_{p5\beta7} & Z_{p6\beta7} & Z_{p7\beta7} & Z_{p8\beta7} & Z_{p9\beta7} & Z_{p10\beta7} \\ Z_{p1\beta8} & Z_{p2\beta8} & Z_{p3\beta8} & Z_{p4\beta8} & Z_{p5\beta8} & Z_{p6\beta8} & Z_{p7\beta8} & Z_{p8\beta8} & Z_{p9\beta8} & Z_{p10\beta8} \\ Z_{p1\beta9} & Z_{p2\beta9} & Z_{p3\beta9} & Z_{p4\beta9} & Z_{p5\beta9} & Z_{p6\beta9} & Z_{p7\beta9} & Z_{p8\beta9} & Z_{p9\beta9} & Z_{p10\beta9} \\ Z_{p1\beta10} & Z_{p2\beta10} & Z_{p3\beta10} & Z_{p4\beta10} & Z_{p5\beta10} & Z_{p6\beta10} & Z_{p7\beta10} & Z_{p8\beta10} & Z_{p9\beta10} & Z_{p10\beta10} \end{pmatrix} \quad (5.10)$$

The next step is for determining the impedance matrix of γ_2 segment, which can be synthesised by γ_1 and α_2 segments. The same thing for γ_3 that consists of α_1, $\beta_{1\text{-}5}$ and α_3 segments.

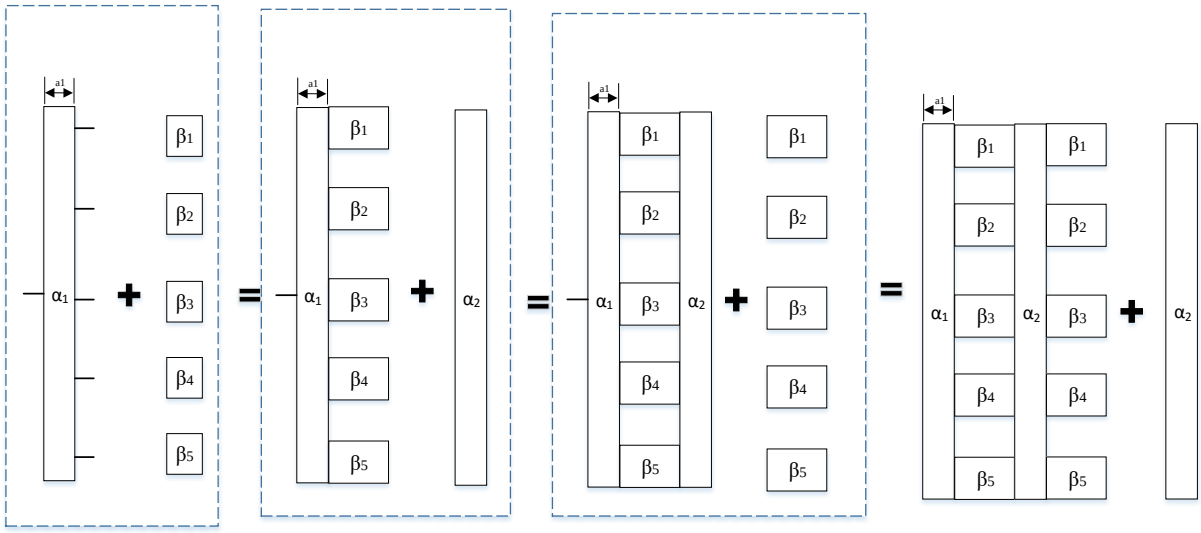

Figure 5.18: Synthesis of γ segments into final structure

By repeating the same procedures for the other similar segments, and so on until the whole patch structure be synthesised, as illustrated in Figure 5.19. Hence, the total Z-parameters of

the final patch design can be obtained where the final expression of impedance Z-matrix for the γ segment can be given by:

$$Z\gamma = Z\gamma_1 + Z\gamma_2 + Z\gamma_3 + Z\gamma_4 \quad (5.11)$$

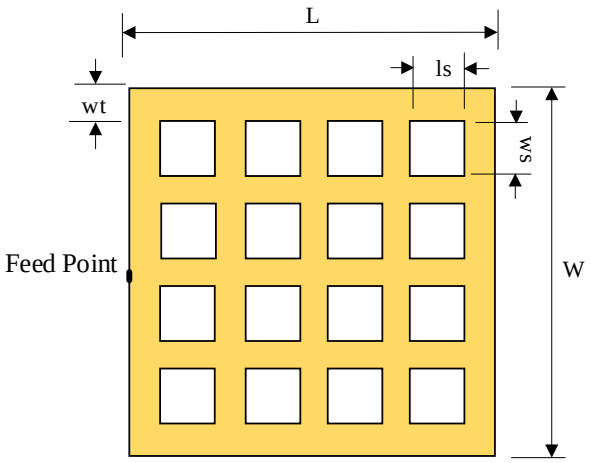

Fig. 5.19: Final γ segment of patch design

The mathematical model results will be compared, with the results of CST simulation and discussed in next Section 5.7.

5.7 Modelling of Slots loaded Patch Antennae Using CST Microwave Studio

To test the results of the mathematical model obtained above. The CST Microwave Studio was used to determine and compare the Z-impedance of the slots on microstrip patch antennae. The CST slot patch model is shown in Figure 5.20.

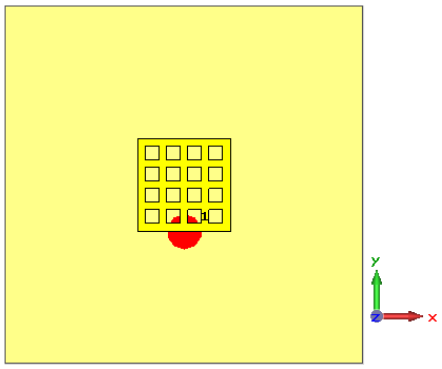

Figure 5.20. The CST slot patch model

5.8 Results and Discussion

The input impedance (Real and imaginary parts) of square patch antennae loaded with 16 slots are shown in Figure 5.21.

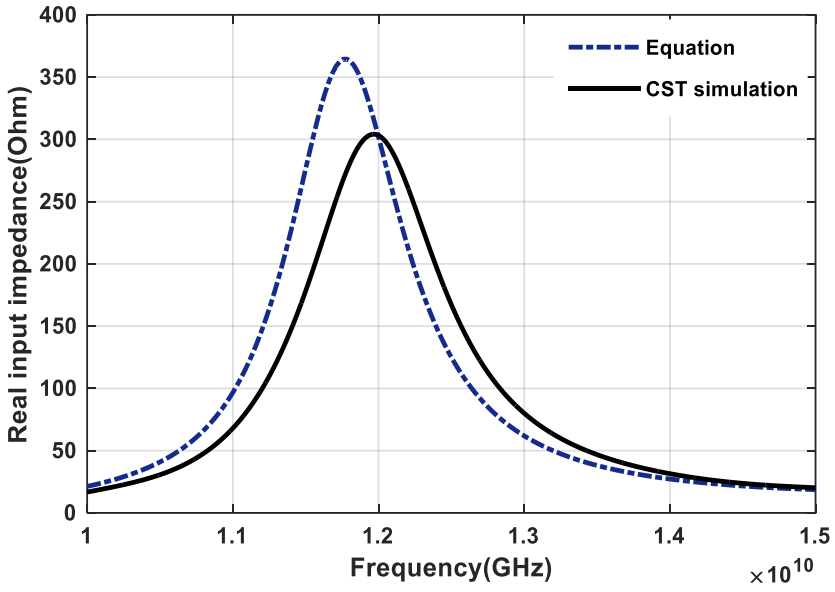

(a)

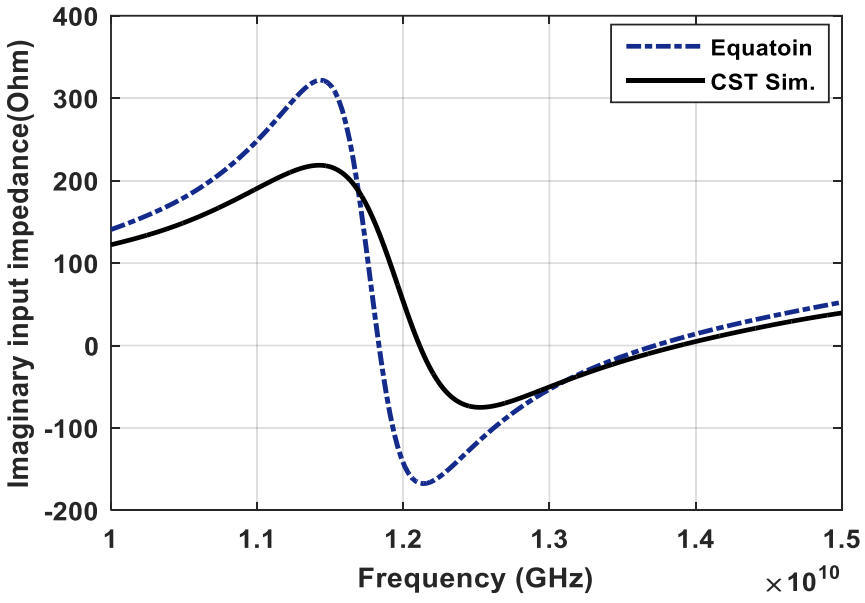

(b)

Figure 5.21: Input impedance of slots loaded square patch antennae with (a) Real parts (solid line CST, dashed line Math. Model) and (b) imaginary parts (solid line CST, dashed line Math. Model)

Table 5.3: Impedances characteristic of slots loaded square patch antennae obtained by the theoretical model and CST simulated results

Model	**Resonant Frequency (GHz)**	**Input Impedance (Ω)**
Segmentation (theoretical)	11.78	464.4
CST Simulation	11.96	304.2

From table 5.3, it can be seen that the resonance frequencies and the real parts of the input impedance for theoretical and CST Microwave are close to each other, there is small frequency difference of 35 MHz between them. The peak value of the theoretical result is slightly different comparing to the results obtained from the CST simulation results. The real part of the theoretical is slightly higher than the CST simulation with values of 464.4 Ω and 304.2Ω, respectively. It might be due to the approximate model. Although, the results are not close enough. However, this model can be used as quick estimating solution for determining of resonance frequency for such slotted patch, in addition to obtain an input impedance (real and imaginary parts) estimated values.

The full wave analysis can be employed to determine the antennae characteristics of very complex patch antennae where by this technique the complete set of Maxwell's equations can be solved without any simplifying assumptions. Thus, in the analysis, dielectric losses, conductor losses, surface wave, and in addition to coupling to external elements can be included. In this thesis, the application of a commercially available software, CST Microwave studio is employed, which provides the most accurate and efficient computational solutions for impedance and radiation characteristics, especially for very complicated structures. It will be also used in chapter 6 to analyse and optimize the performance of suspended patch antennae, integrated with solar cell, which would not be simple to model.

5.9 Summary

In this chapter the co-planar modelling technique was applied to a square patch antennae at design frequency of 3 GHz and 11.95 GHz, in order to determine the input impedance. This patch antennae was also designed and modelled using CST studio for comparison. The

segmentation modelling technique was then used in order to determine the impedance characteristic of slots loaded patch antennae, and then the results were demonstrated, analysed and compared with CST simulated results. It was found that the segmentation results were agreed to the CST full wave simulation, when the segmentation approach applied to a basic single slot design, at a relatively low frequency. Whilst, were close enough to the CST results when the approach was extended to a 4 x 4 slot patch design at high frequency of 11.95 GHz. In this case, the results of the theoretical approximation model were not accurate enough for the complex structure of a patch loaded with multi-slots. Nevertheless, quick estimating solution was performed for determination of resonance frequency and input impedance.

Chapter 6 Design and Development of ku-band Combined Solar Antennae for SatCom.

6.1 Introduction

As mentioned in Chapter 3 in the literature review, integration of the solar cell beneath the antennae elements reduces solar efficiency due to a shading problem, but can improve the RF performance of the antennae. In this case, an optimum is sought between reducing solar efficiency and improving RF performance. Therefore, in this chapter, the meshing technique has been applied to microstrip antennae elements as a compromise between RF performance and optical transparency. However, most transparent antennae studied in the literature review suffer from narrow bandwidth and operate at relatively low frequency.

In this design, in order to achieve broadband performance for the desired application whilst providing good transparency, a new technique with a suspended transparent element is proposed and implemented for the proposed antennae of the Ku-band transparent dual-band antennae integrated with a poly-Si solar cell for Fixed-Satellite-Services (FSS) in remote areas. It operates over a frequency range from 11.7 GHz to 12.22 GHz for the downlink, and 14.0 GHz to 14.5 GHz for the uplink. A comparison is also made between the proposed designs, and the simulation and practical results are discussed.

The previous chapter discussed theoretical literatures survey and

6.2 Methodology and Design Process

In this thesis, the research design process is set out, in order to describe the main procedures of the project. In addition, the research process will also be used to offer a better understanding of the overall concept of the research design idea. The research will include:

- Theoretical, mathematical modelling and simulation of antennae geometries; the theoretical aspect of the study creates a background in theory and sets design methods to investigate, analyse and model the selected antennae.
- The practical implementation, testing and measurement of solar antennae single element designs is required, in order to analyse and investigate the solar antennae to determine its performance characteristics: for instance, reflection coefficient,

resonant frequency, impedance bandwidth, gain and the radiation patterns, transparency, and solar cell efficiency.

The design process can be divided into several main stages, as be shown in Figure 6.1:

- The first stage of designing an integrated solar array antennae is to design a linear individual element unit.
- To make the solid RF radiating element out of a transparent design patch using meshing technique.
- Simulation results will be carried out for this element using full-wave modelling assistance from data analysis electromagnetic software tools such as Microwave Studio (CST).
- After that, the design will be prototyped and tested, and an RF anechoic chamber will be used for practical measurement antennae in order to simulate free-space in the RF environment.
- From single feed linear polarised unit, to design and fabricate a dual feeding, dual-polarised solar antennae element.
- In the next stage, the dual-polarised individual element need to be incorporated into sub-array integrated solar cells with dual linear polarisation, and will then be created and optimized.
- Finally, the results will be obtained, analysed and discussed.

Figure 6.1: Flow chart summarises the research design process for the proposed PV solar antennae.

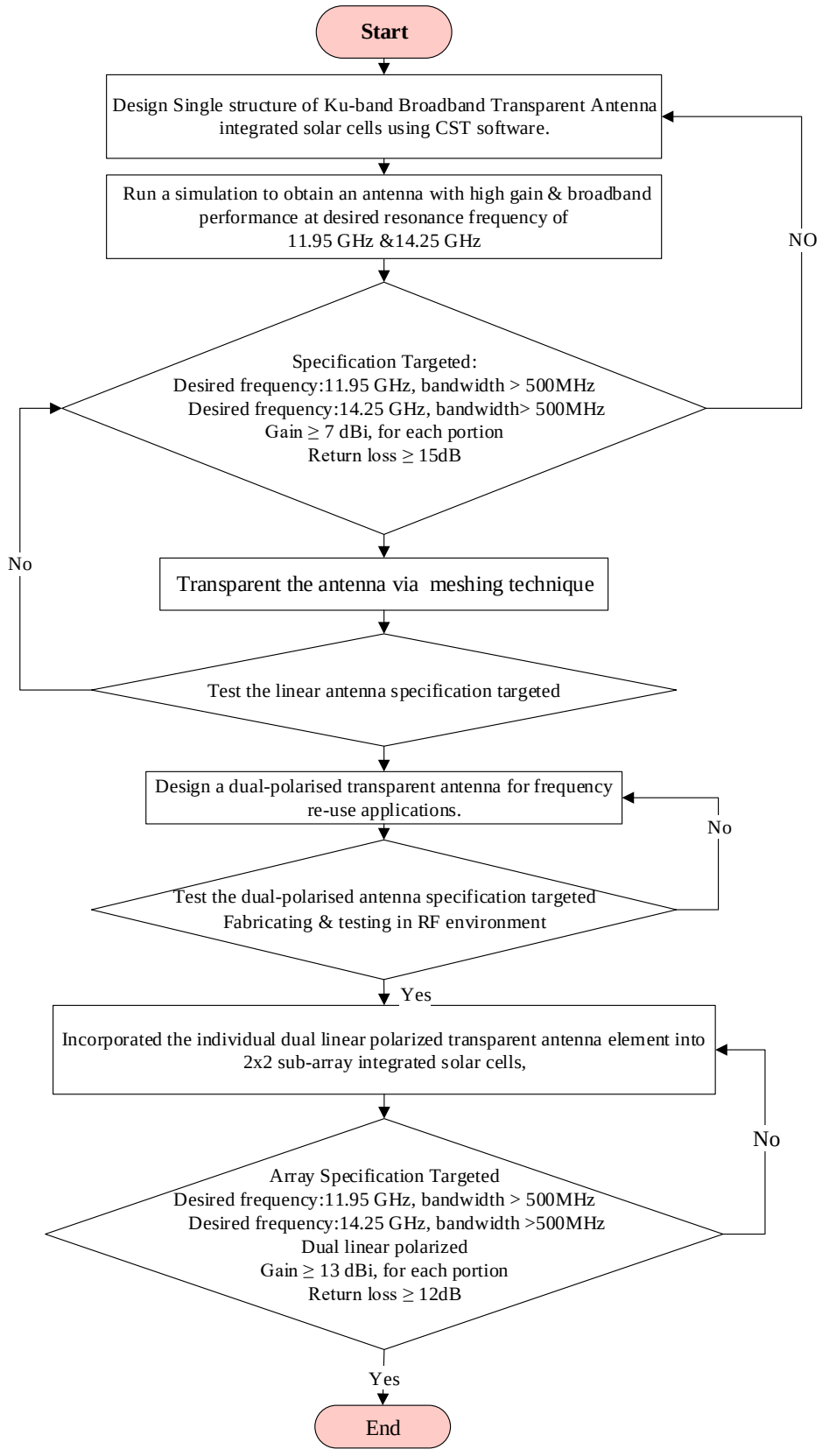

Figure 6.1: Flow chart shows the design process for the proposed sub-array antennae

6.3 Ku-band Suspended Meshed Patch Antennae Integrated with PV Solar Cell

6.3.1 Single Meshed patch antennae design

Before embarking on the design of the Ku-band suspended transparent patch antennae, a single patch element was designed at a half wavelength at resonant frequency with a quarter–wavelength interconnecting feed line, using a CST Microwave environment, as shown in Figure 6.2. The structure is designed as the square microstrip antennae element for a dual-polarised development design shown in later sections. The patch radiator with microstrip line is stuck onto an inexpensive Plexiglas substrate with a dielectric constant of εr = 2.59 and thickness h =1.5 mm. Other parameters are necessary for analysis of the transmission line. For example, the thickness of the patch conductor = 0.035 mm and loss tangent of substrate $\tan\delta$ = 0.068. In this design, the overall patch dimensions were determined based on the transmission line model, using MathCad software for designing a solid patch to operate at the desired frequency of 11.95 GHz [29]. The optimized length of the patch is 6.0 mm and the width is 6.0 mm at f_o = 11.95 GHz.

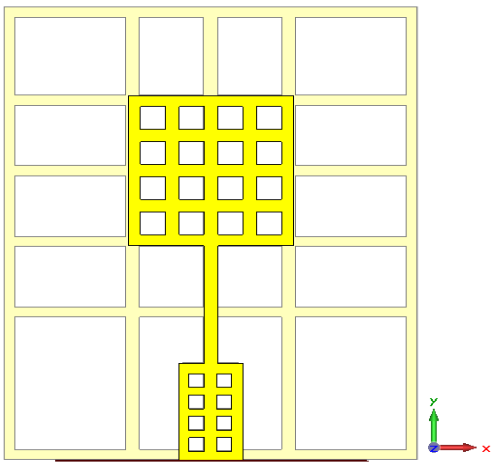

Figure 6.2: Square single meshed patch antennae excited by microstrip line at resonant frequency of 11.95 GHz (downlink).

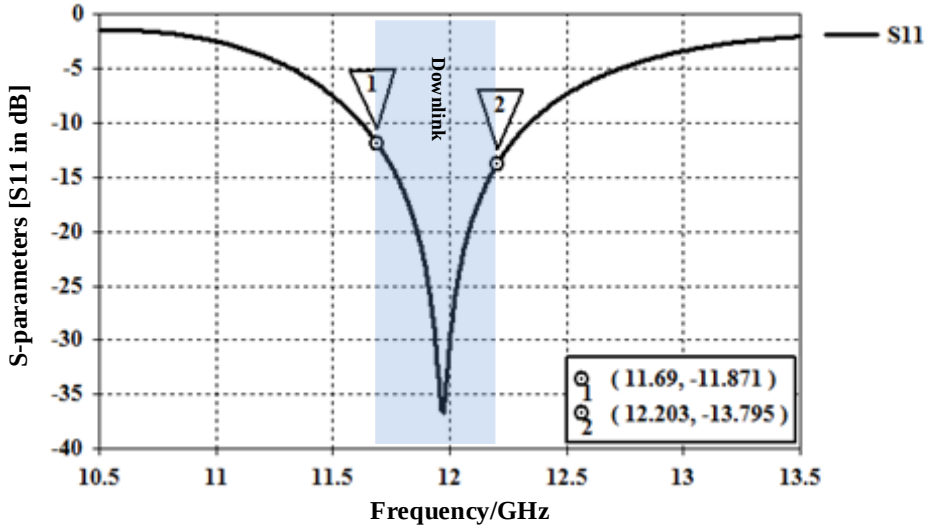

Figure 6.3: Reflection coefficient S_{11} (dB) of the single meshed square patch antennae

In Figure 6.3, it was demonstrated that the square microstrip meshed patch antennae has a narrow bandwidth, determined at -10 dB. Therefore, in the sections, which follow the bandwidth of this antennae will be broadened.

6.3.2 Selection of an appropriate Substrate Material for The Proposed Transparent Patch Antennae

There is significant parameter affect patch antennae performance, due to properties of is dielectric substrates. Normally thick substrates, which have a lower dielectric constant, are used because they provide a better efficiency and large bandwidth [166, 167]. There are different types of transparent substrates with high optical transparency to allow good illumination, which can be used in the process of designing transparent patch antennae. Such as Glass or Glass Pyrex substrates, however these have high dielectric constants (εr), which are around of εr = 3.8 (at 10 – 25 GHz). Plexiglas substrates have low dielectric constant at high frequencies. They are preferable, commercial and represent a low cost alternative, in addition, can maximize the radiation, bandwidth and gain of patch antennae, comparing to other transparent substrates. Therefore, in this design low dielectric constant Plexiglas substrate with $\varepsilon_r = 2.59$ and a loss tangent of $\delta = 0.0068$ (at 10 - 25 GHz) [168], has been selected and used in order to achieve a good meshed patch antennae RF performance and transparency. In order to demonstrate the effect of substrate properties (dielectric constant and loss tangent) on the S_{11}-response characteristics of transparent microstrip patch antennae before integrated with PV solar cell. Two types of transparent

substrates with different relative dielectric constants; Glass Pyrex, with εr = 4.3 and Plexiglas, with, εr = 2.59 are simulated using CST Microwave Studio software to operate at the same high frequency of 11.95 GHz. The S_{11}-results are shown as in Figure 6.4a and b, and compared.

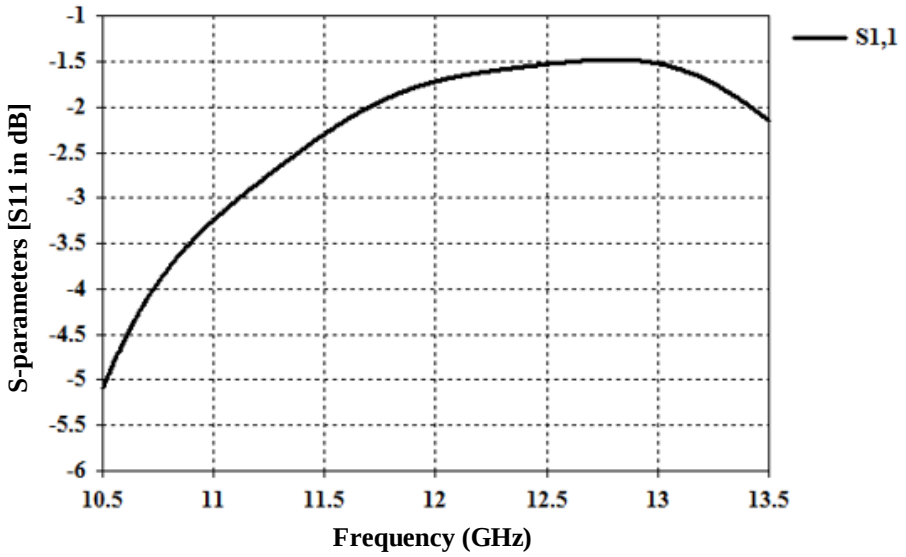

(a)

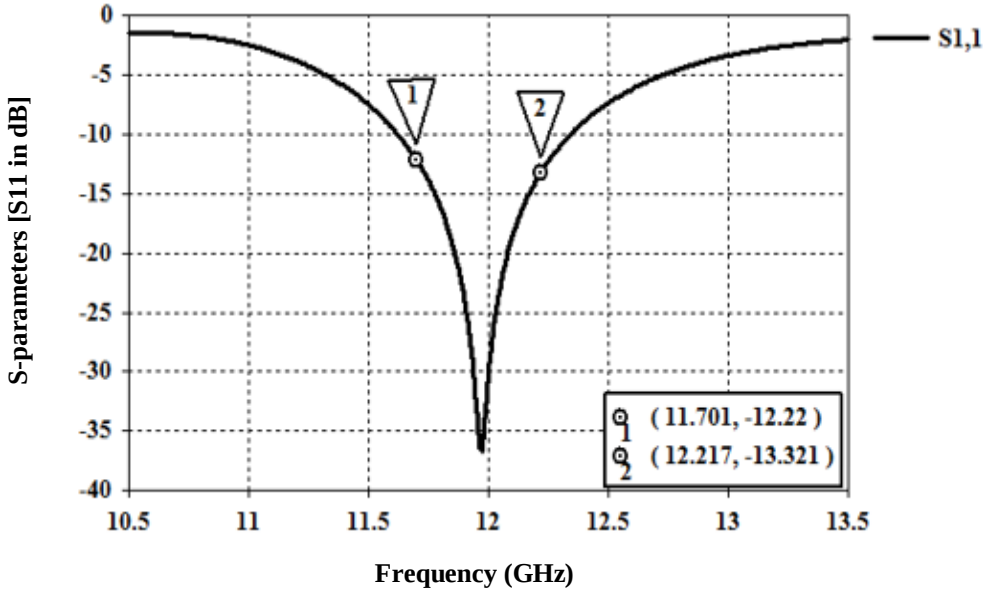

(b)

Figure 6.4: Effect of substrate properties on S_{11}-response, a) Glass Pyrex substrate ($\varepsilon r = 4.4$), b) Plexiglas substrate ($\varepsilon r = 2.59$)

It can be seen in Figure 6.4a and b that the S_{11}-response when the Glass Pyrex with higher dielectric constant was used, the S_{11}- result was significantly affected and degraded as shown in Figure 6.4a due to dielectric losses and loss tanged. Whilst, when the Plexiglas substrate was used, good S_{11}-parameter was achieved as shown in Figure 6.4b. It can be said that the main parameter in the substrate effect on the meshed patch antennae performance is a dielectric constant, since the bandwidth of the antennae has been improved at high frequency when low dielectric constant with ε_r = 2.59 and a loss tangent of 0.0068 at 11.95 GHz was used.

6.3.3 Dual-band Enhancement for the Proposed Transparent Antennae

Bandwidth limitations are associated with conventional microstrip patch antennae. Therefore, many configuration techniques have been proposed and developed to extend bandwidth [9, 102, 169-176]. The use of a transparent suspended technique in order to broaden narrowband antennae was proposed and implemented in this work. Dual-band antennae can be realized if an impedance bandwidth is achieved over a wide frequency range. In Section 6.2.4, a design for a dual resonator configuration is illustrated, consisting of a square suspended transparent microstrip patch antennae with coplanar microstrip feed-line matching.

6.3.4 Design and Fabrication of Ku-band Suspended Meshed Patch Antennae Element

In this section, the proposed suspended meshed patch antennae with dimensions of 6.0 mm x 6.0 mm x 35µm together with the coupling feeding structure is designed using CST Microwave Studio, as shown in Figure 6.5a.

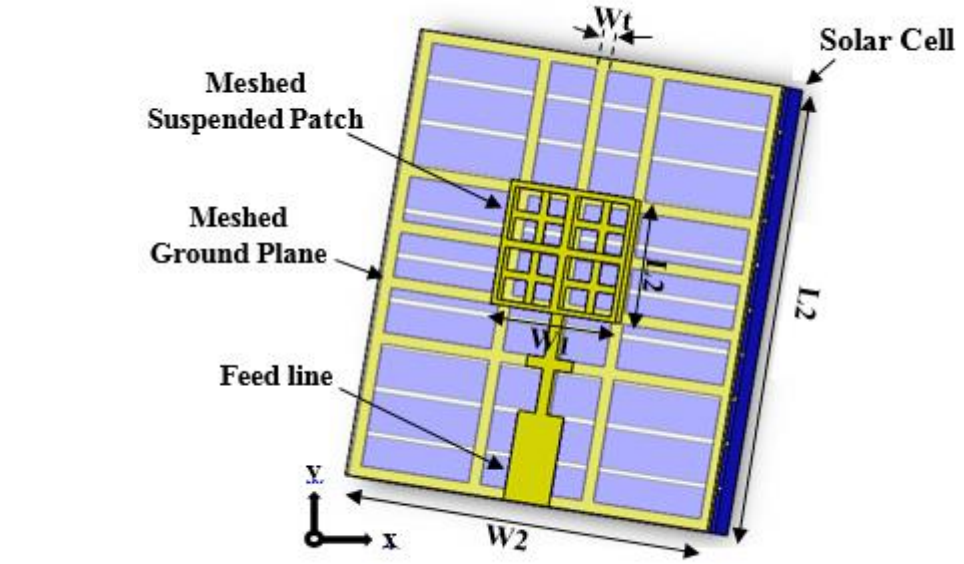

(a)

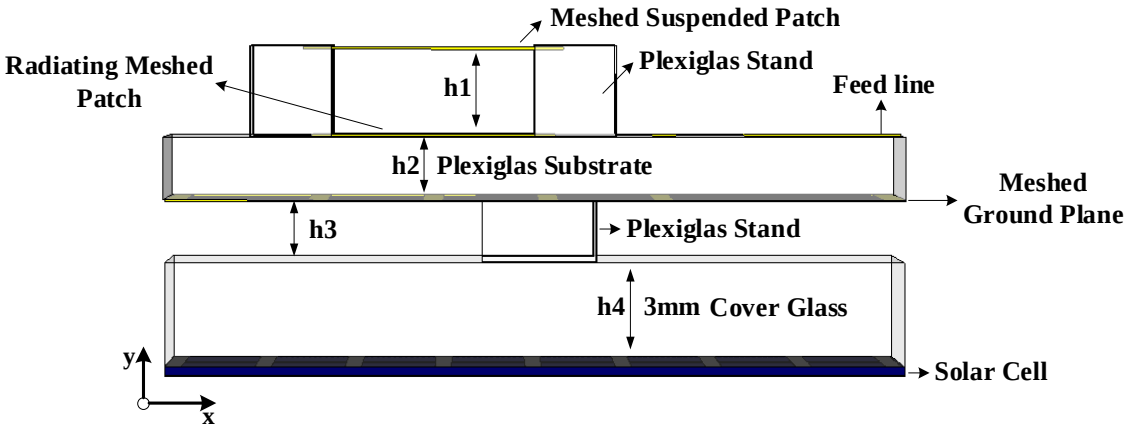

(b)

Figure 6.5: Suspended meshed patch antennae integrated with solar cell: (a) overall view in CST Microwave Studio; (b) side view. Dimensions: *W1*=6 mm, *W2*=15 mm, *wt* =0.5 mm, *L1*=6 mm, *L2*=18 mm, *h1*=2 mm, *h2*=1.5 mm, *h3*=2 mm, *h4*=3 mm.

The antennae was developed on a transparent Plexiglas substrate with a thickness of 1.5 mm and dielectric constant (εr) of 2.59, with a meshed copper ground plane on the substrate's lower side. The patch and ground plane have track widths (*wt*) of 0.5 mm. The minimum meshing line width is determined as 0.3 mm, which occurs a shift in both S_{11}-response resonance frequencies, as shown in Figure 6.12. The patch is fed by a microstrip line through a quarter-wave transformer, adding a stub to improve impedance matching. The meshed ground plane has been designed with wide dimensions slots in

order to improve the overall transparency of the antennae while maintaining the RF performance. The suspended meshed patch has four square slots and is suspended with four transparent stands in the corners above the radiating element, with an air gap of 2.0 mm, as shown in Figure 6.5b. The antennae is located above a poly-Si solar cell with a thickness of 0.2 mm. The solar cell is encapsulated between a glass layer on the top and a rear contact aluminium layer covering the back of the solar cell. It has the same dimensions as the antennae substrate with an air gap of 2.0 mm in between.

For comparison purposes, a solid suspended patch microstrip antennae integrated with a solar cell was designed and simulated in CST. In order to compare and investigate between the characteristics of the proposed combined solar patch antenna with solid patches (completely blocking light) and with the meshing (transparent) antenna elements. The structure, shown in Figure 6.6, consists of a 7.0 mm x 7.0 mm patch placed on a Plexiglas substrate with a solid copper ground plane on the lower surface. This was placed 2.0 mm above the silicon solar cell, and a suspended solid copper patch was placed above the patch element with an air of 3.0 mm and supported by four low loss dielectric posts. In this design, the substrate and ground plane are the same in dimension as the solar cell.

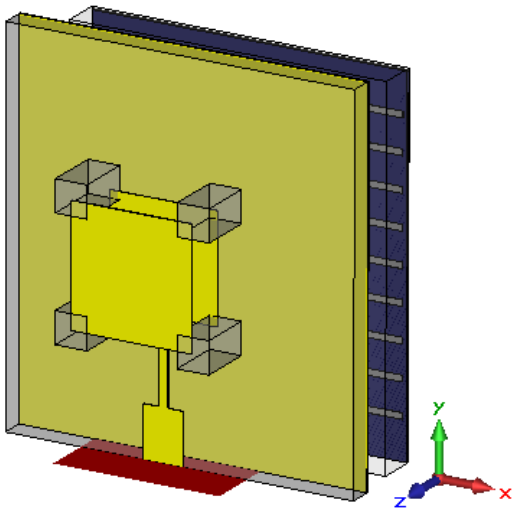

Figure 6.6: The suspended solid patch antennae integrated with solar cell

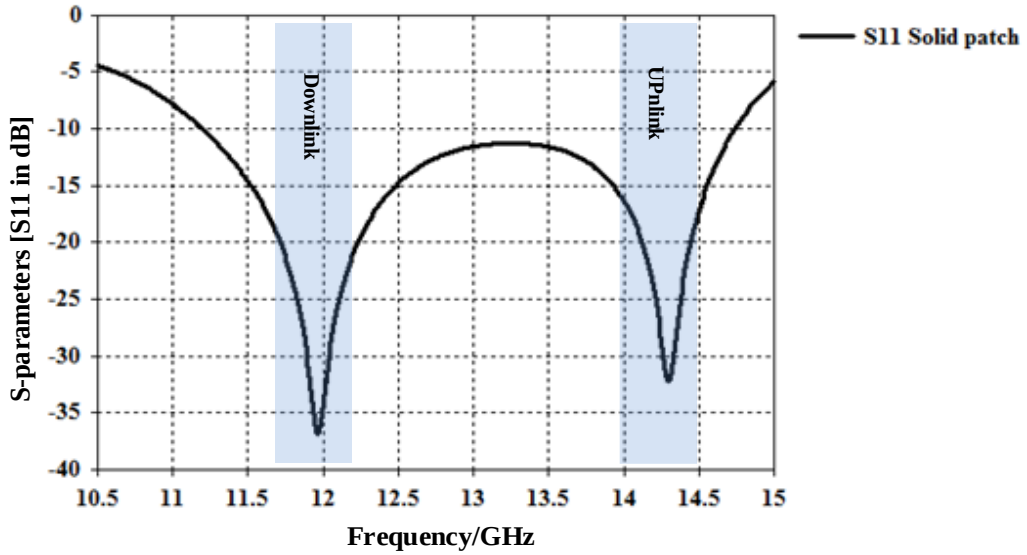

Figure 6.7: S_{11} response of the reference solid suspended patch antennae design.

Figure 6.8 below shows a comparison between the S_{11}- responses of the proposed suspended meshed antennae design and reference solid suspended patch (before and after meshing).

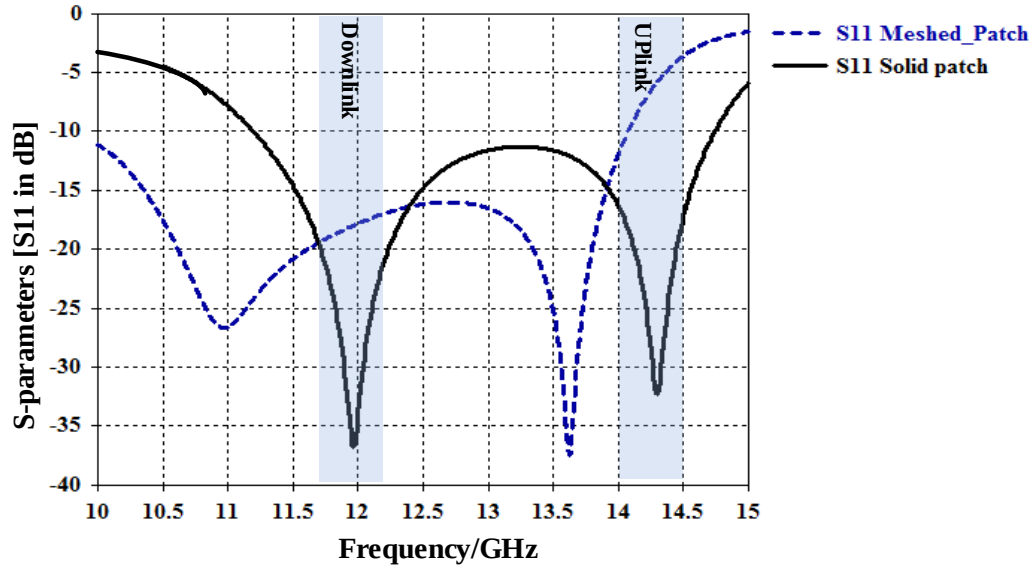

Figure 6.8: The effect of the meshing on the S_{11} simulated result of the antennae with and without meshing

As can be seen in Figure 6.8, both resonance frequencies of the proposed transparent solar patch antennae have been shifted slightly to lower frequencies. It shows that the downlink fundamental frequency has been shifted to 11.10 GHz from the design frequency of 11.95 GHz, and for uplink resonance frequency was shifted to 13.55 GHz from the design frequency of 14.25 GHz, shifted down by approximately 700 MHz or equivalent to 0.70

GHz. In other words, there was a decrease of 5 % in both bandwidths' performance for the transparent solar suspended patch antennae compared to the reference suspended solid patch antennae. In general, this shift in frequencies occurred due to the effect of the slot-loaded patch antennae element. Hence, these slots have reduced the TM modes down to the resulting resonance frequency. As discussed in Chapter 5, when slots are added to the patch, those slots act as an open circuit to the current flow and this causes the current to flow not through the slot, but round it. By sourcing the current to flow around the slots, this would cause an increase in the current travelled path. Theoretically, the length of the patch is increased slightly by this extra electric field, which enlarge the dimension of the radiating element. Due to this, the frequency is shifted downwards. Therefore, the path travelled by the current would be longer if more slots were applied on the patch antennae and this would cause the TM_n modes to shift more to a lower frequency. In addition, the grid ground plane also affects the antennae's S_{11} performance, where insertion of slots in the ground plane meanders the current path of TM modes. This results in reduced resonant frequency, and hence reduces antennae size. Moreover, meshing the patch and ground plane effectively lowers Q factor, thus increasing bandwidth.

In order to obtain suitable bandwidth responses at the desired centre frequencies, the dimensions of the meshed radiating patch and suspended patch have been reduced. In view of this, the dimensions were reduced by 5%, according to the resonance frequency shifted ratio between the design frequency and the resulting shifted resonance frequency. The S_{11} response of the transparent solar patch antennae after reduction in patch dimensions is shown in Figure 6.9.

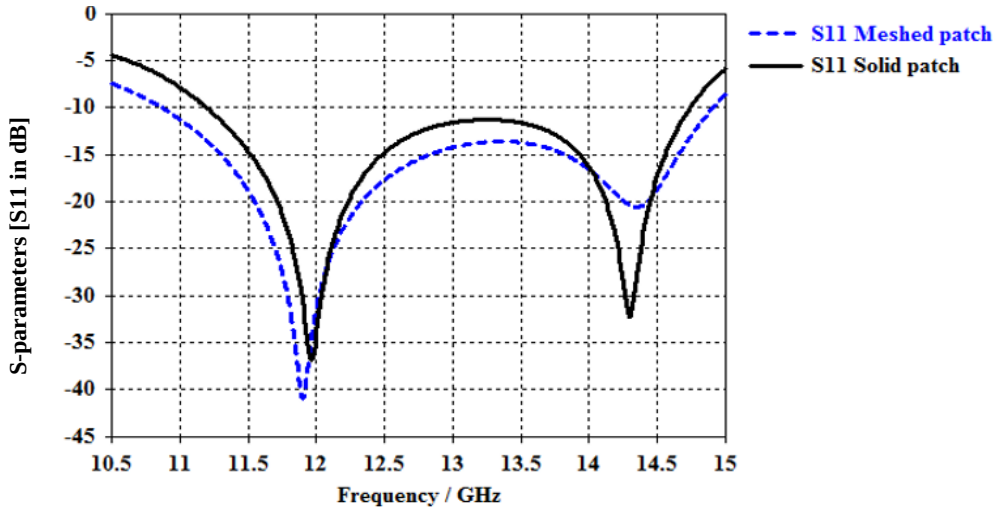

Figure 6.9: The effect of the reduction in proposed antennae dimensions on the S_{11} simulated reflection coefficient

It can be seen from the above plot that the S_{11} simulation results obtained from the proposed transparent solar patch antennae are very close to those, which were obtained from the solid suspended antennae, with only a small difference in resonance centre frequencies. In order to provide exactly the required resonance frequencies for this design, optimization by CST can be performed for the dimensions of the meshed radiating element.

The microstrip fed-line suspended meshed patch antennae was fabricated and connected to a 50 Ω-SMA connector and tested using a vector network analyser (Agilent N5230A). The photograph of the fabricated proposed design antennae integrated with solar cells is shown in Figure 6.10. In the design presented, a standard SMA connector (straight PCB mount type) was used.

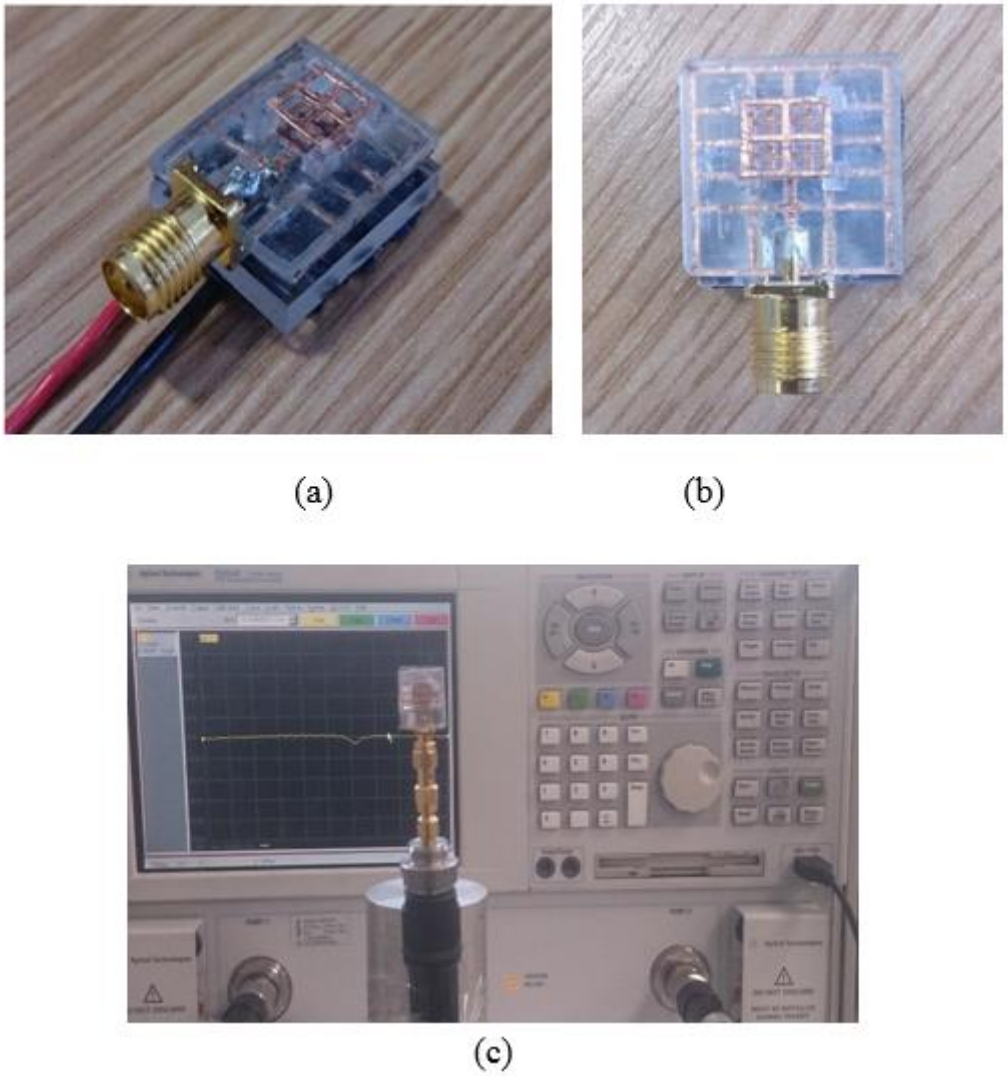

Figure 6.10: A photograph of fabricated proposed meshed patch Antennae: (a) perspective side view (b) front view, (c) fabricated antennae under measurement.

6.4 Analysing and Discussion of Simulation and Measurement Results

The simulated and measured reflection coefficient ($|S_{11}|$) patterns of the antennae is illustrated in Figure 6.11.

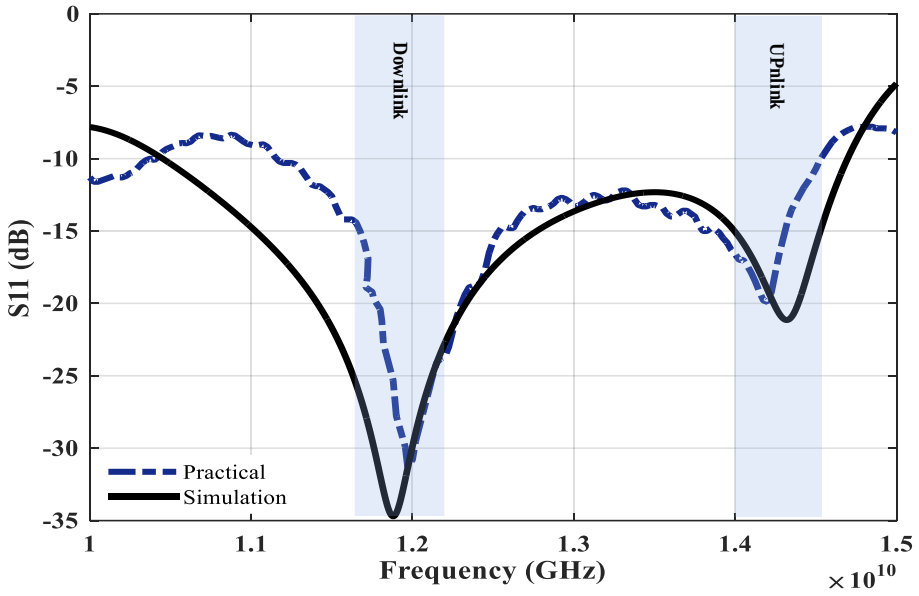

Figure 6.11: S_{11}-parameters of simulated meshed suspended patch

The simulated and measured reflection coefficient ($|S_{11}|$) patterns of the antennae are illustrated in Figure 6.11. It is evident that there are two resonances each providing broad bandwidth according to the simulation and practical results. The simulated results were carried out using CST Microwave Studio and show that S_{11} response of better than -10 dB is achievable over 500 MHz in both the downlink and uplink bands. The measured S_{11} shows that the fabricated proposed antennae resonates within both the desired frequency bands although, the practical measurements is slightly shifted, which could be due to fabrication process. However, good agreement between the simulated and measured reflection coefficient (S_{11}) responses was demonstrated.

6.4.1 Effect of variation of the grid widths and lengths on the RF S_{11} antennae performance

As mentioned earlier, the line width for the meshed patch is w_t = 0.5 mm. Following the analysis of the S_{11} response of the antennae, the effect of varying the grid line width is studied.

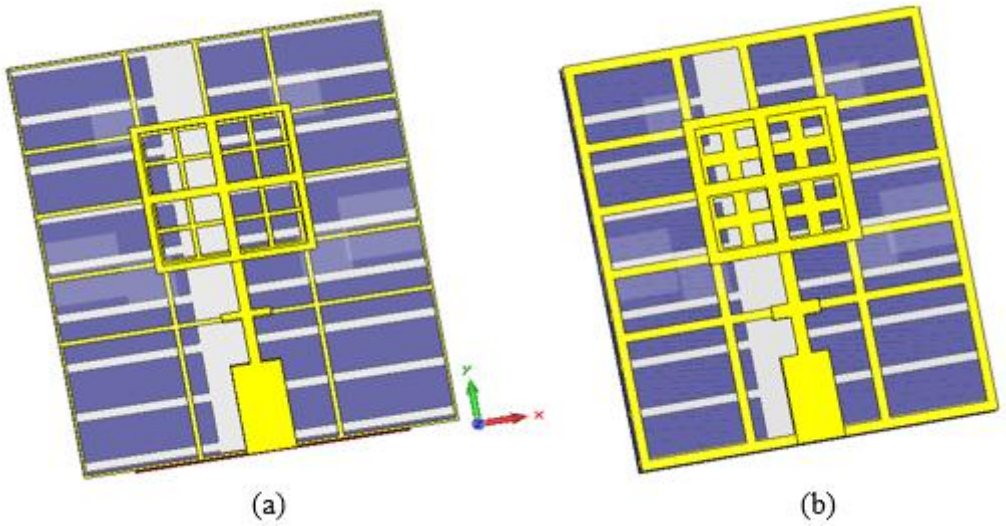

Figure 6.12: Meshed suspended solar patch antennae with varying meshing line widths (a) line width of 0.3 mm (optical transparency = 87 %), (b) line width of 0.5 mm (optical transparency = 84%)

Reducing the line width has an advantage of improving the optical transparency of the antennae, ensuring optimum photovoltaic characteristics. However, it can significantly affect the RF performance, and therefore, a careful analysis must be carried out to find the optimum line width as shown in Figure 6.13.

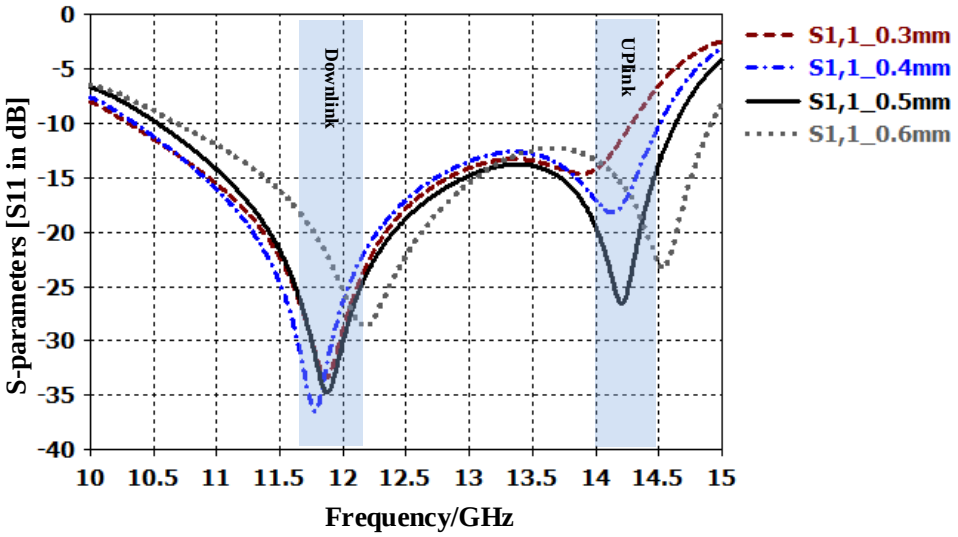

Figure 6.13: Effect of variation of the grid line width on the S_{11}-parameter

The effect of the decreasing the vertical and horizontal meshed line widths can be seen in Figure 6.13. Analysing Figure 6.13, down to 0.5 mm line width, similar RF performance is observed, while improving the optical transparency of the antennae. A significant change in

the S_{11} response and degradation in the uplink band performance is noted when the line width is reduced below 0.5 mm. It has been observed that as the transparency of the meshed patch is increased from 84 % to 87 %, due to reducing the grid line width from 0.5 mm to 0.3 mm the performance is decreased. Whilst, when the width is increased above 0.5 mm to 0.6 mm, both resonances of S_{11}-response are shifted to higher frequency. This is due to decreasing apertures dimensions, hence decreasing current path. As a result, of this study the optimum line width is for the meshed patch is found to be w_t = 0.5 mm and the antennae becomes ineffective when the line width is smaller than 0.3 mm, $w_t \leq$ 0.3 mm.

6.4.2 Impedance Characteristics

To be able to demonstrate the input impedance characteristics of the proposed antennae, the real and imaginary results with varying meshing line width (0.5 mm and 0.3 mm) are plotted, as shown in Figure 6.14 (a) and (b).

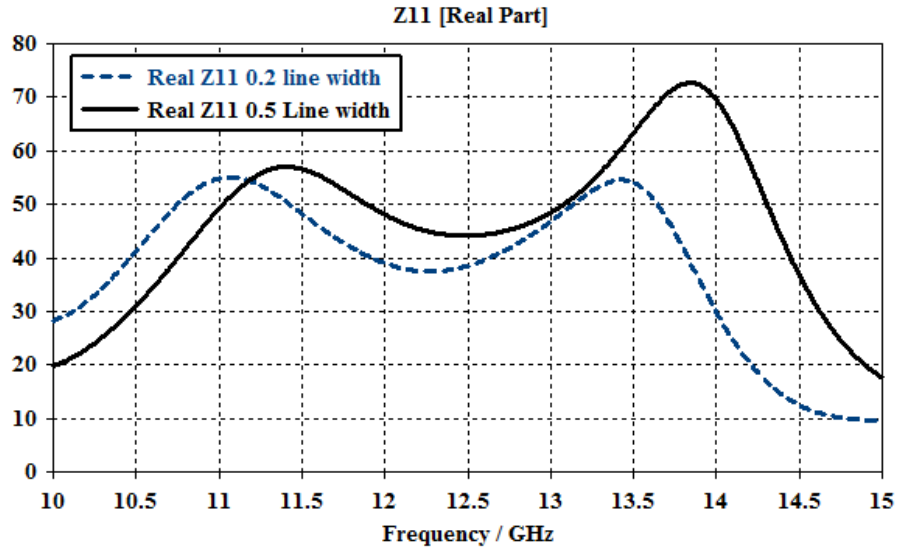

(a)

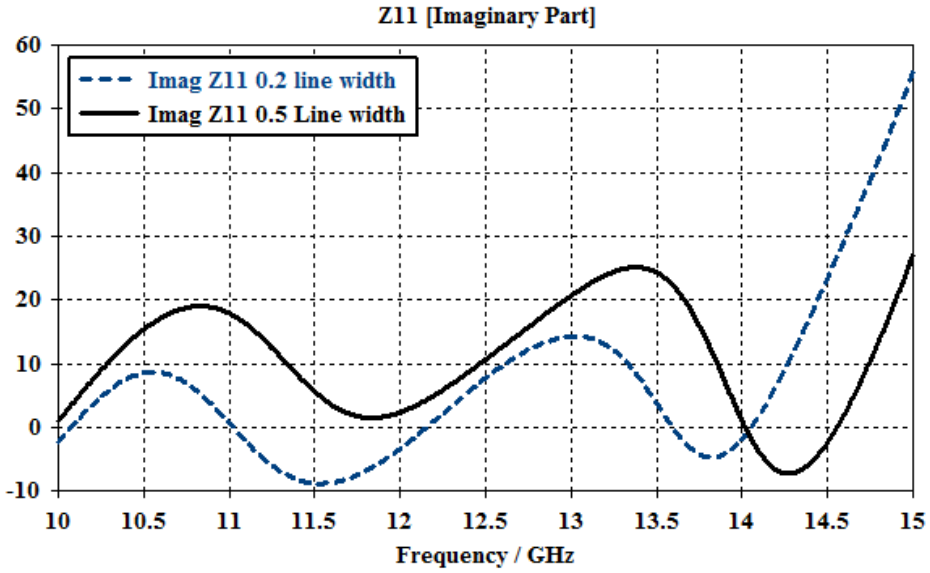

(b)

Figure 6.14: Z-parameters (a) Real, and (b) Imaginary parts of the meshed patch antennae with varying meshing line widths

It can be seen from Figure 6.14 (a) that the real and imaginary parts of the simulated input impedance patterns of the antennae are in good matching. The simulated real part for both the downlink and uplink are very close to 50 Ω source impedance when the antennae was optimized to meshed line width of 0.5 mm. The imaginary part shown in Figure 6.14 (b) is close to zero and indicating good impedance matching at both resonant frequencies. For the 0.3 mm, a significant change in the real and imaginary values is observed at the downlink and uplink bands, which are shifted to lower frequency with the difference being about of 0.5 GHz. This is due to reducing the grid line width from 0.5 mm to 0.2 mm, and thus widen the slots.

6.4.3 Current Distribution

Figure 6.15, shows the simulated surface current distribution of the proposed meshed antennae at 11.95 GHz and 14.25 GHz downlink and uplink bands respectively.

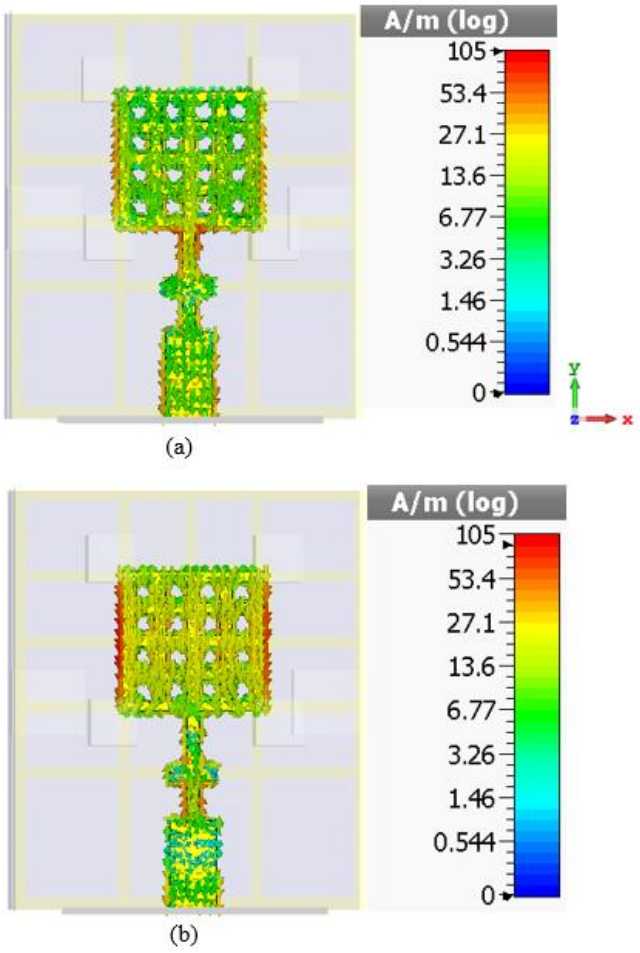

Figure 6.15: Current distribution across the suspended meshed Patch at (a) 11.95 GHz, (b) 14.25 GHz bands.

The surface current flows through the feed line towards the multi-slots radiating element and the current is distributed into the vertical (*y*-axis) and horizontal (*x*-axis) directions along the slot edges. The current density induces an E-field across the slots and therefore, contributes to radiation and creates resonance frequency modes. As can also be seen in Figure 6.15, the highest current intensity is focused on the edges towards the *x*-direction and is reduced at the centre of the patch. The loading slots effect the current flow paths and cause the current to travel a longer distance around the slots, which effectively increases the size of the patch antennae electrically and reduces the resonance of the TM_{01} mode down towards the fundamental frequency. This explains the reason that the meshed square patch is miniaturised.

6.4.4 Effect of Solar Cell on the Antennae Performance

In order to discuss the effect of solar integration on the antennae performance, the proposed microstrip meshed patch antennae design with and without integrated solar cell was

simulated using CST Microwave Studio and is illustrated in Figure 6.16. The results have been demonstrated in Figure 6.17 and Figure 6.18.

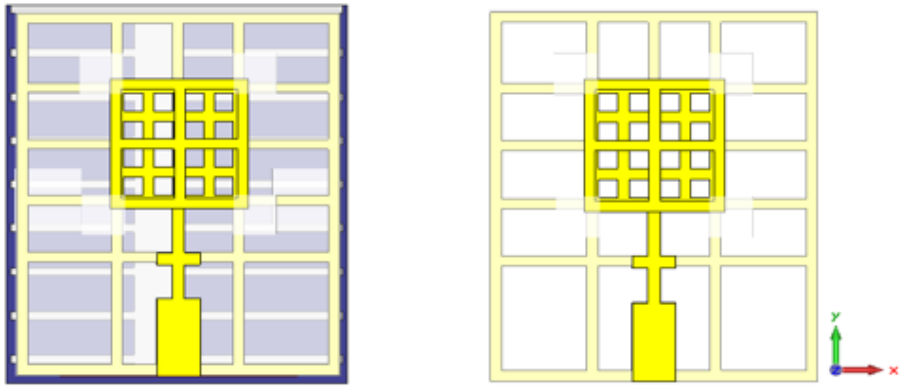

Figure 6.16: Proposed suspended meshed patch antennae (a) with solar cell (b) without solar cell and cover glass (with only meshed ground plane)

A comparison is made in Figure 6.17, between the simulated S_{11}-responses of two cases of the proposed suspended transparent solar patch antennae with and without integrated solar cell.

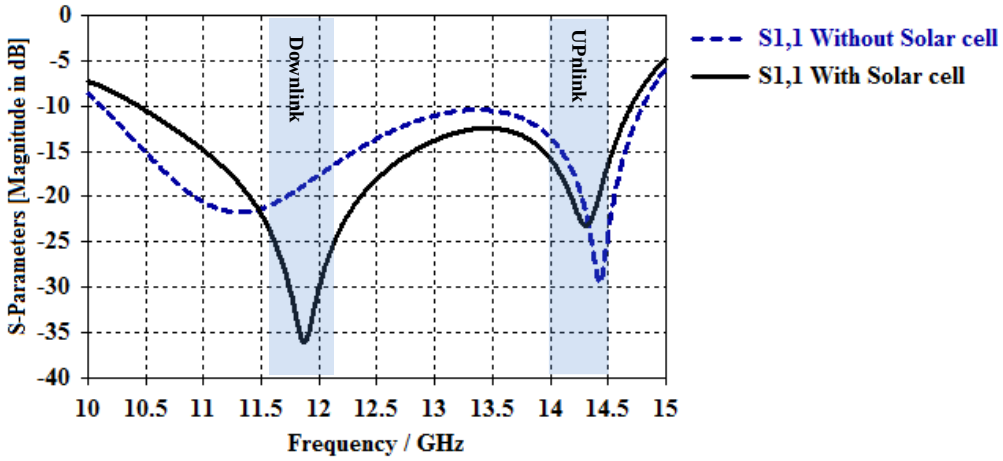

Figure 6.17: Simulated S_{11}- parameters of suspended meshed antennae with and without solar cell

Analysing Figure 6.17, it is evident that the presence of the solar cell affects the S_{11}-response of the antennae and therefore, the design parameters have been optimized in the presence of the solar cell. In Figure 6.17, the downlink resonance frequency is shifted by 650 MHz from the intended design frequency of 11.95 GHz to 11.3 GHz while the uplink resonance

frequency is shifted by 200 MHz from 14.45 GHz to 14.25 GHz. The simulated radiation patterns of the antennae with and without the solar cell are illustrated in Figure 6.18. In this simulation design, all the results of the combined solar antenna were taken at ambient room temperature. However, in previous related study in reference [81], the analysis of the performance of the PV antennas with temperature variation due to solar radiation, it showed that the antenna performance was not degraded significantly. It was slight downward shift in the resonance frequency when the temperature changes from 330.8k (55.6 ℃) to ambient temperature of 293 K (25 ℃).

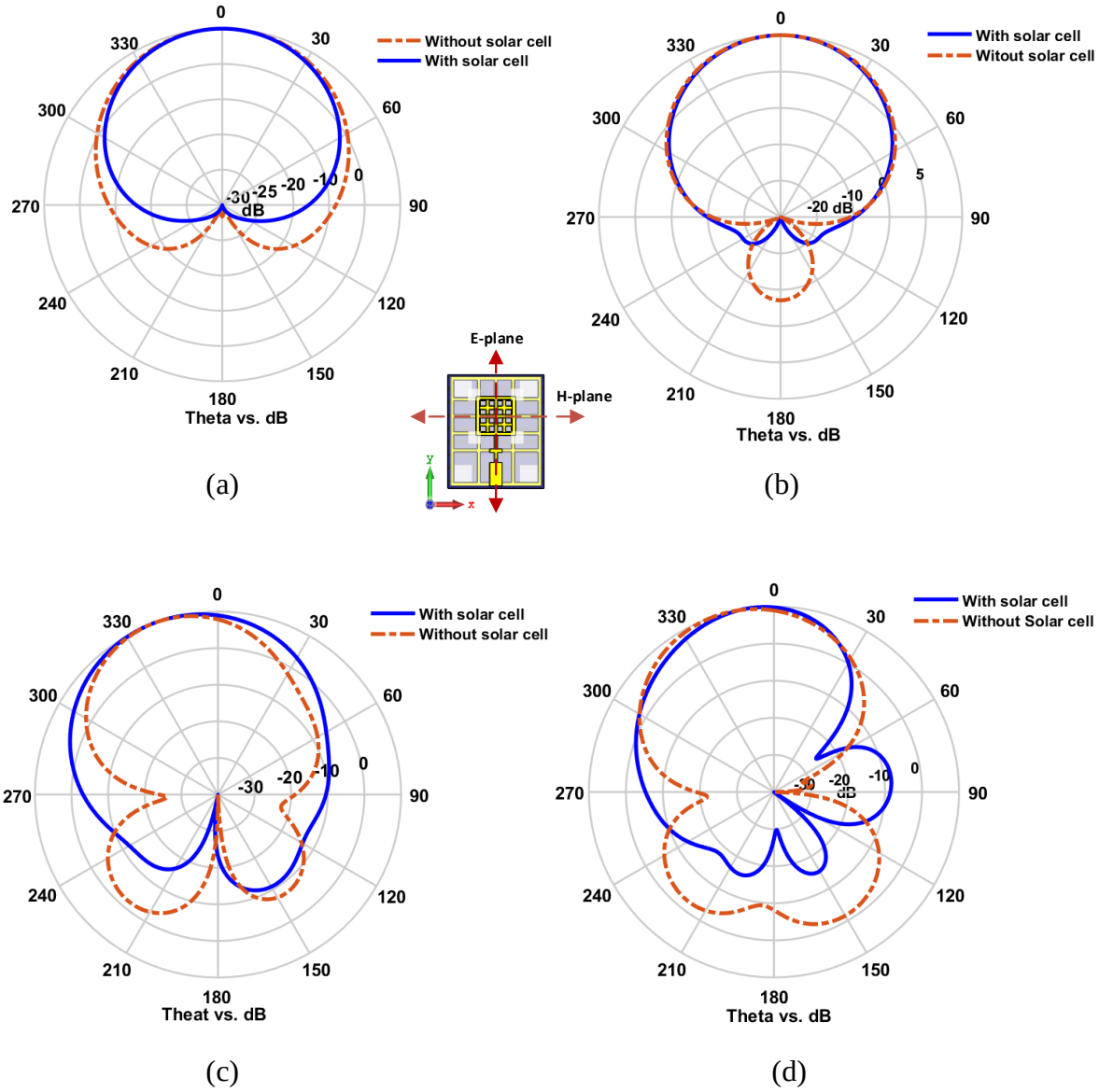

Figure 6.18: Simulated radiation patterns of the meshed antennae with and without solar cell: (a) H-plane downlink / with and without solar cells, (b) H-plane uplink / with and without the solar cells, (c) E-plane downlink / with and without solar cells, (d) E-plane uplink / with and without the solar cells

As can be seen in Figure 6.18 (a), the downlink radiation characteristics of the antennae in the H-plane with and without solar cell are nearly identical in gain and radiation patterns. In Figure 6.18, (b), (c) and (d) slight differences are observed with the antennae without the integrated solar cell exhibiting a back-lobe radiation below −10 dB. It is found that by using the meshing technique, the antennae becomes transparent and the bandwidth is increased. However, it has a degraded front to back ratio (FBR), due to the partial decline in the ground plane conductivity, thus, reducing the gain from 7.885 dBi to 6.69 dBi in the H-plane (Figure 6.18 (b), dashed line) and from 8.05 dBi to 6.79 dBi in the E-plane (Figure 6.18 (d)) at 14.25 GHz uplink (solid and dashed lines), respectively. In addition, it can be noticed in Fig. 6.18 (d), the antennae has a pattern similar to monopole radiation pattern in the uplink E-plane without solar cell (dashed line). Alternative solutions can be utilized in order to improve FBR, in case of solar antennae integration; the solar cells can play the role of an additional ground plane. Thus, kill the back-lobe radiation, which is reduced from 0 ∼ −8 dB to about −20 dB, and hence improving the directivity and the gain, as shown in Figures 6.18 (b) and 6.18 (d) (solid lines).

6.4.5 Radiation Pattern and Gain

Figure 6.19, shows the proposed meshed suspended antennae far-field measurement in the anechoic chamber.

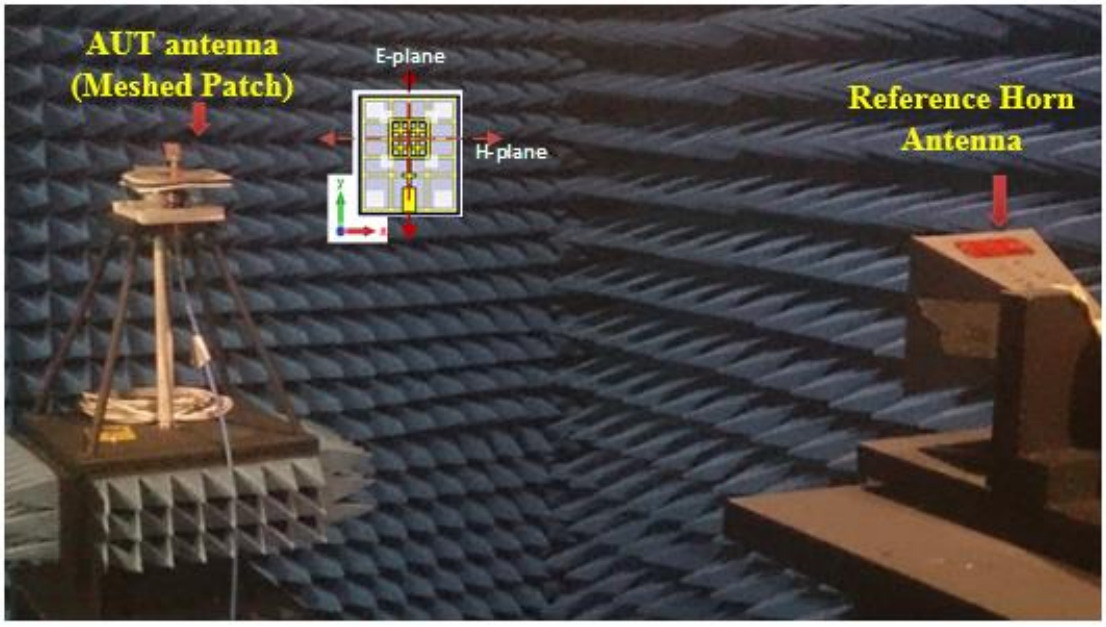

Figure 6.19: Antennae far-field measurement for the meshed suspended proposed antennae in the anechoic chamber.

The simulated and measured of H-plane and E-plane for downlink and up-link far-felid radiation patterns are shown in Figure 6.20 (a), (b), (c) and (d). They were obtained and compared at the desired operating frequencies at both bands, as shown in Figure 6.20. The performance parameters values are given in Table 6.1. The H-plane (y-z) and E-plane (x-z) far-field radiation pattern measurements were performed in a microwave anechoic chamber in order to work in free-space environment to avoid undesirable reflection waves and interference signals, as illustrated in Figure 6.19. For the measurements, a standard horn antennae with gain of 20 dBi was used as a reference antennae.

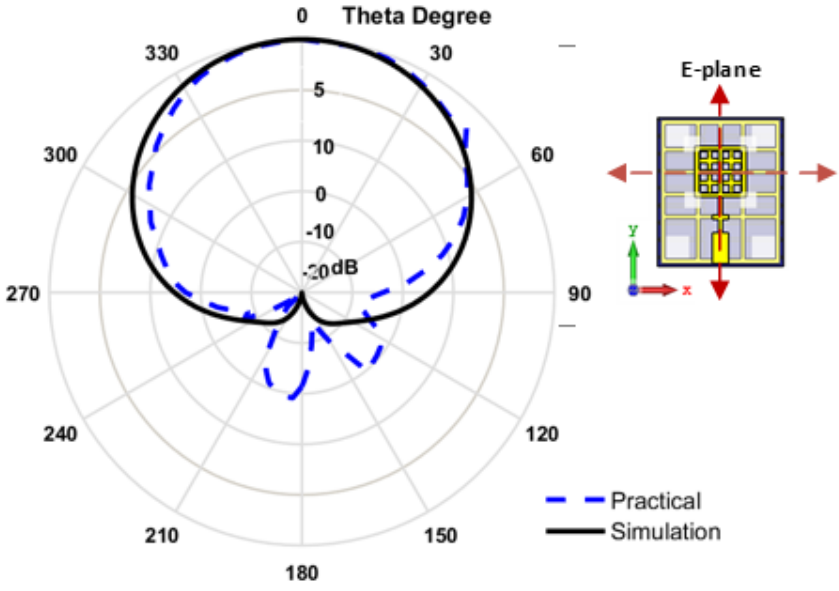

At 11.95 GHz (a)

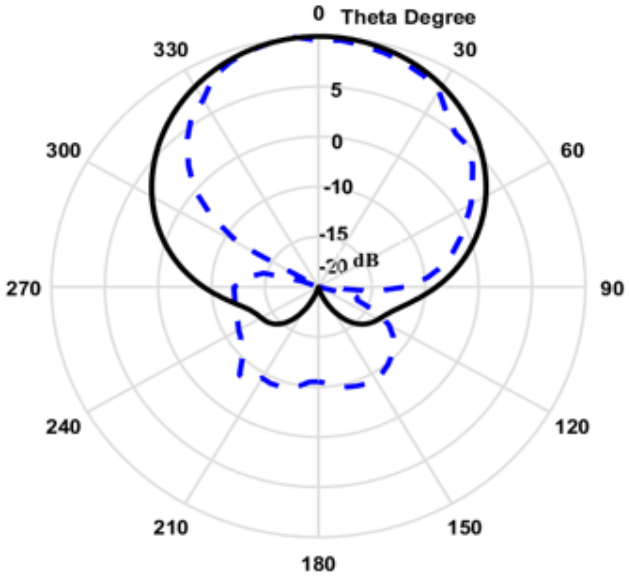

At 14.25 GHz (b)

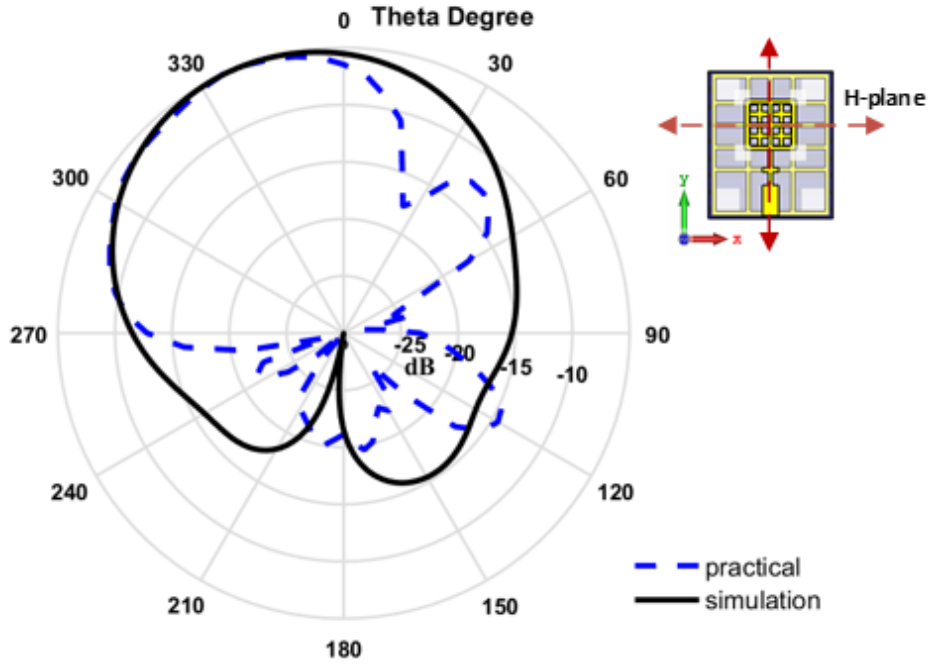

At 11.95 GHz (c)

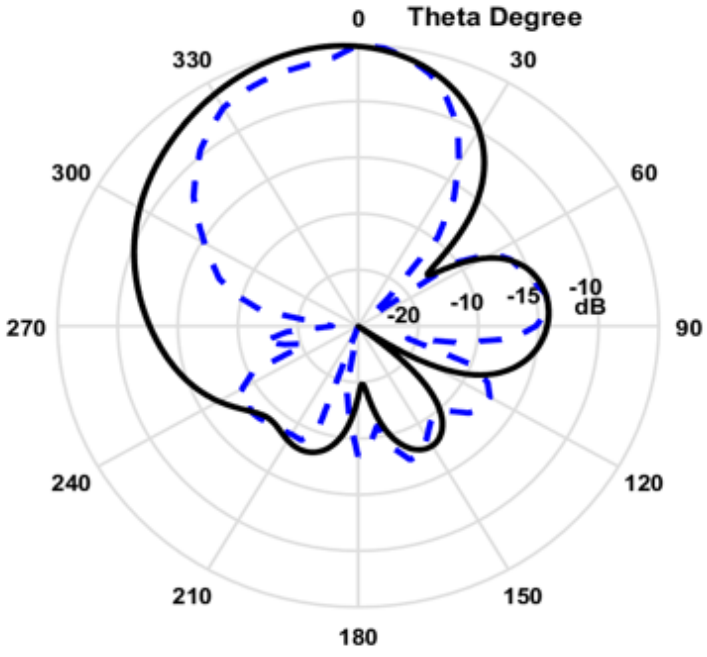

At 14.25 GHz (d)

Figure 6.20. Simulated and measured results of far-field radiation patterns: (a) *H*-plane downlink, (b) *H*-plane uplink, (c) *E*-plane downlink, (d) *E*-plane uplink for suspended transparent patch antennae.

It can be noticed in Figure 6.20 that there is good agreement between the simulated and measured far- field patterns in the H-plane (x-z plane). The discrepancy in the E-plane (y-z plane) can be attributed to a number of reasons. A very important factor can be understood by analysing the surface current distributions presented in Figure 6.15. It can be seen in Figure 6.15 that the surface current flows dominantly in the y-direction (as opposed to x-direction; that could not be seen such a big difference in the H-plane (x-z plane) because the surface current flowing in the x-direction is much less in comparison to the surface current flowing in the y-direction. This also might explain why the agreement in the H-plane is better than the agreement in the E-plane). As a result, any differences in the meshed wire configuration between the simulation and experimental models of the antennae (including the position, width and flatness of the copper tracks of the meshed patch) can cause such differences between the simulated and experimental E-plane patterns as opposed to H-plane patterns exhibiting superior agreement.

Moreover, another factor could effect on the both planes especially in practical, is the structure of the Poly-Si solar cell that consists of contact fingers on the top surface of the poly-Si layer, which separated by 2 mm from each other that might contribute to result a shift in main lobe radiation direction. In other words, from RF point of view, this means that the solar cell surface is not completely homogeneous in materials properties (partially non-conductive).

For SMA connector, it can be noticed that in the presented design, a standard SMA connector (jack straight PCB mount type), was used as shown in Figure 6.10. The simulation (SMA connector is not present) and experimental (SMA connector is present) studies carried out in Figures 6.11, and 6.20 have demonstrated that no significant effect on the antennae performance is caused due to the connector size. To put this statement into context, as an example, no shift is observed in the resonance frequency of 11.95 GHz in Figure 5.11. The simulated and measured impedance characteristics of the antennae exhibit good agreement in Figure 6.14. The simulated and measured H-plane radiation patterns in Figure 6.20 are also in good agreement. For more demonstration, the simulated 3D-far-field radiations, the 3D-dimensional antenna radiation pattern is a three-dimensional graphical indicates the three co-odinates (x, y, z), and representes spherical coordinates (r, θ, Φ). The total efficiency in 2D-contour plots are illustrated below in Figure 6.21, and Figure 6.22, respectively, for both bands 11.95 GHz downlink and 14.25 GHz uplink. The practical measurements of the fabricated suspended meshed antennae were carried out in a microwave anechoic chamber. The signal generator with amplitude power of PG = 14 dBm, was connected to a standard

horn antennae (as reference antennae) with known gain of GT = 20 dBi operating across the frequency range of 7.5-15 GHz. The power meter was connected to the Antennae under Test (AUT), in order to find out the AUT gain performance. The distance between the AUT and the reference antennae that be content with the far-field condition was calculated using 2*(R^2) /lambda and was set to R = 1.45 m. Then, the proposed antennae was rotated over 360° in the directions of both; E-plane and H-plane. Next, the received power levels at each 5° interval angle were measured and recorded.

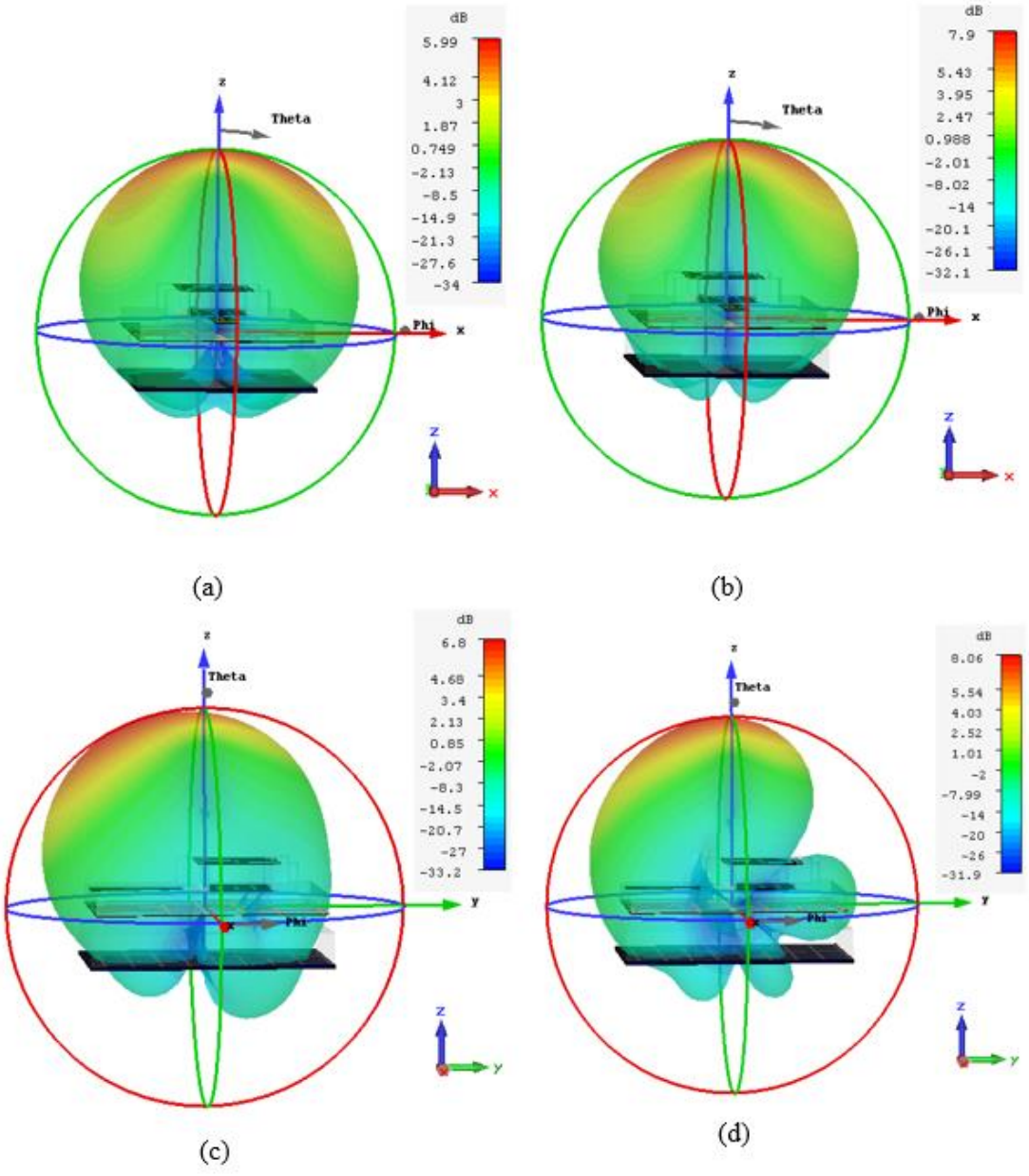

Figure 6.21: 3D-patterns: (a) H-plane downlink, (b) H-plane up link radiation patterns, (c) E-plane down-link, (d) E-plane up link

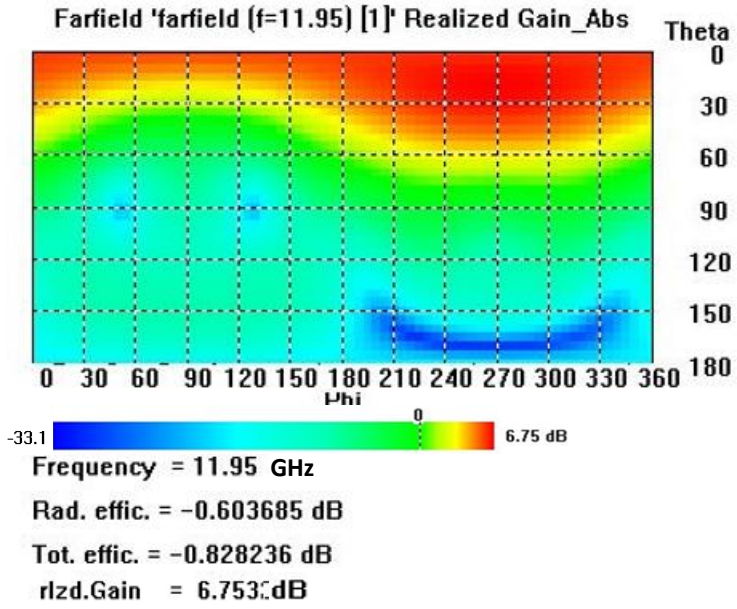

(a)

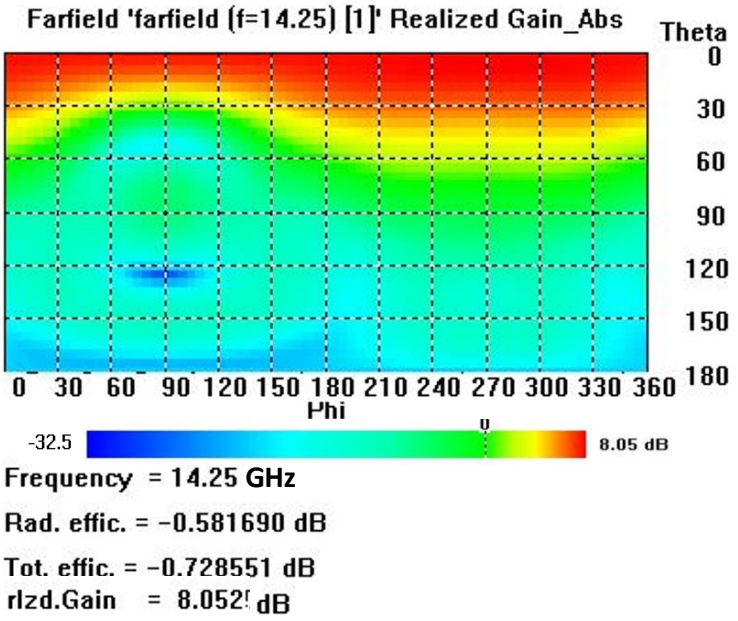

(b)

Figure 6.22: Simulated total radiation efficiency and realized gain at (a) down-link, (b) up-link resonance frequency

In the calculation of the E-plane and H-plane antennae gains for each resonance frequency; downlink at 11.95 GHz and uplink at 14.25 GHz, and Friis free space equation that expressed below was used. The direct received power is:

$$P_r = P_t G_t G_r \frac{\lambda^2}{(4\pi d)^2} \tag{6.1}$$

where, *Gt* and *Gr* are the transmit and receive antennae gains, respectively. The P_r is the received power and P_t is the transmitted power. *R* is the separation distance between the reference and tested antennae (AUT), and λ is the wavelength. The P_0 is forward power (dB) from the signal generator to the transmitter antennae that taking into account cable loss, which is given by:

$$P_0(dBm) = P_G(dBm) - L_C(dB) \tag{6.2}$$

Lc: Cable loss (dB), P_G : signal generator power. The overall performance of the proposed antennae, and the values of the main performance parameters are summarized in table 6.1. The overall opticalt transparency of the antennae can be defined by the ratio of the see-through surface area of the antennae to the total surface area of the antennae. The transparency in percentage (%) can be calculated based on Equation (6.3) given below [177].

$$Transparency\ (\%) = 100 * \frac{Antenna\ Transparent\ Area}{Antenna\ Solid\ Area} \tag{6.3}$$

Table: 6.1. Performance results for the proposed antennae over the uplink and downlink frequency bands.

Antennae Parameters		**Downlink band**	**Uplink band**
Resonance frequency (GHz)		11.95	14.25
Realized Gain (dBi) H-plane	Simulated	5.99	7.9
	measured	6.055	7.61
Realized Gain (dBi) E-plane	Simulated	6.8	8.07
	measured	6.2	7.9
Beam width (3dB)		90°.6	74.2°
Impedance Bandwidth (MHz)		> 500	> 500
Radiation Efficiency (dB)		-0.60 (87.1%)	-0.58 (87.5%)
Total Efficiency (dB)		-0.82 (82.6%)	-0.72 (84.5%)
Transmitted power P_G (dBm)		14.0	14.0
Received power P_R (dBm)		-39.77	-39.0
Cable losses (dB)		2.1	3.0
Patch Dimnsions (mm^2)		6	6
Overall optical transparency (%)		84 %	84 %

It is noted that good overall antennae efficiency and high power gains are observed at both resonance frequency bands, confirming that the proposed antennae works properly at both desired bands. The antennae exhibits simulated realized gains of 5.99 dBi for downlink and 7.9 dBi uplink bands with 3 dB beam widths of 90.7◦ and 74.0◦, respectively. The obtained radiation efficiency is −0.60 dB (87.1%) for the downlink band and −0.58 dB (87.5%). The total efficiency for the desired bands are −0.82 dB (82.6%) and −0.72 dB (84.5%) respectively while the measured downlink and uplink gains are reported to be 6.05 dBi and 7.61 dBi. The differences between the simulated and experimental results can be attributed to the imperfections in the construction process of the antennae and fabrication tolerances. It was also noticed that the uplink power gain is higher than at the downlink band. This is due to the narrower beam-width at uplink band, and at 14.25 GHz, the wavelength is smaller compared to the downlink, resulting in an electrically larger aperture size in the uplink band. The results also show the achieved impedance bandwidth in each portion was 500 MHz A VSWR of less than or equal to 1.1 was obtained at both uplink and downlink frequency bands. The overall optical transparency of the meshed radiating element has been calculated as 84.0%, based on Equation (6.3).

6.5 Solar Cell Performance Characteristics Measurement Respect to Integration with Meshing Patch Antennae

The solar cell electrical characteristics, such as the open-circuit voltage (V_{oc}) and short-circuit current (I_{sc}), were measured with and without the integrated suspended meshed patch antennae element as shown Figure 6.23. In order to compare the effect of the solar antennae integration topology on the transparency and illumination efficiency operation of the solar cell, the antennae's transparent substrate and the Poly-Si solar cell have the same dimensions, 18.0 mm × 15.0 mm. The simulation was carried out using a Flood Light Solar Simulator in an electrical power workshop, with measured light intensity of 1000 W/ m2, the light was focused on the solar cell, with the cell electrical output wires being connected to an Ampere-Volt-Ohm (AVO) meter in order to measure the generated output DC voltage and current. For the measurements were carried out to determinate the illumination intensity for the solar cell arrangements, a digital light meter model no. (MS 6612) was used as shown below in Figure 6.24. Table 6.2 summarises the solar cell performance measurements values.

(a) (b)

(c)

Figure 6.23 Polycrystalline solar cell DC characteristics measurement; (a) flood Light Solar Simulator (normal incidence) (b) from oblique angle (c) without any antennae integrated above.

Figure 5.24: light meter.

Table 6.2: solar cell performance characteristics

Performance characteristics / Configuration	V_{OC} (mV)	I_{SC} (mA)	Dc power (P) (mW)	Overall optical transparency (%)
Cell without any antennae integrated above	1.07	30.8	32.95	100
Cell with transparent antennae integrated above	1.02	24.6	25.1	84
Cell with transparent antennae (illumination from oblique side angle)	0.765	10.09	7.676	58.6
Cell with solid antennae integrated above	0.52	0.67	0.3484	0

As can be seen in Table 6.2, for non-integrated antennae element, V_{oc} and I_{sc} values were measured to be V_{oc} = 1.07 mV and I_{sc} = 30.8 mA, resulting in a DC power output of 32.95 mW. In contrast, when the meshed antennae element is placed above the solar cell the observed output values were slightly decreased to V_{oc} = 1.02 mV and I_{sc} = 24.6 mA, respectively, resulting in a DC power output of 25.1 mW. The use of the radiating meshed antennae element has yielded little decrease in output DC power of 7.85 mW at normal incidence, compared to the DC solar power without any antennae integrated above, and this is reasonable and acceptable. (It should be also noted that the values are very small in milliwatts, this is due to small of the solar cell dimensions). For practical applications, the solar illumination angle does not remain constant. To investigate the effect of changing the illumination angle on the solar cell performance, additional measurements were carried out with different tilt angles as shown in Figure 6.23 (b). It was observed that the output values of Voc and Isc are reduced to Voc = 0.765 mV and Isc = 10.09 mA, resulting in a DC power output of 7.67 mW. This is due to the impact of optical shading at oblique illumination angles caused by the non-direct photovoltaic illumination. In these experiments, the data measurements of the combined solar antenna were taken at a temperature of about 34 ± 1˚C at the Lab. However, in the previous related study in [178], the analysis of the performance of the PV antennas with temperature variation due to solar radiation, showed that the antenna performance was not degraded significantly. It was slight downward shift in the resonance frequency at 330.8k (55.6 ℃) compared to ambient room temperature of 293 K (25 ℃).

6.6 Transparency Improvement of Ku-band Suspended Transparent Patch Solar Antennae

6.6.1 Introduction

It was demonstrated in Section 6.3.4 that when the suspended meshed geometry element was used, it was possible to achieve a good optical transparency of 84 %, while maintaining the RF performance of the photovoltaic antennae. However, the antennae still retains the disadvantage from a photovoltaic point of view that some light blockage occurs at oblique angles, due to the suspended track lines affecting solar illumination intensity. In view of this, in this section, three antennae are designed and simulated for comparison purposes, in order to improve the antennae's overall optical transparency.

The first antennae, presented in Section 6.6.2, is a transparent patch antennae design consisting of an Indium Tin Oxide (ITO) radiating patch element loaded with a suspended ITO parasitic patch element. An ITO is a triplex composition of indium, tin and oxygen in varying ratios. It is transparent and conductive thin layers and commonly used due to its two main properties of: optical transparency and electrical conductivity. The second design, presented in Section 6.6.3, consists of a meshed copper radiating patch element loaded with another meshed copper patch element suspended above the radiating patch as a parasitic element. The third design, presented in Section 6.6.4, involves replacing the suspended meshed parasitic patch element of the design shown in Section 6.6.3 with an ITO patch element designed in CST Microwave Studio. This novel design of Ku-band suspended transparent patch antennae integrated with a photovoltaic (PV) solar cell for satellite communications is proposed and presented. Different from the previous section, in this antennae, an alternative approach to designing a transparent patch antennae that is unique in combining two transparent design techniques of meshing patch and transparent ITO. From potential transparent conductive materials, transparent ITO films have been selected, due to their high levels of optical transparency, acceptable conductivity and efficiency compared to other conductive film materials. The results in terms of improvement in optical transparency and acceptable RF performance are compared and discussed.

6.6.2 Ku-band Suspended Transparent ITO conductor Patch Antennae

In this section, a suspended patch antennae with ITO transparent conductive material is designed to develop an antennae is a ternary composition of indium, tin and oxygen in varying proportions which is fully optically transparent. This antennae comprises three thin ITO layers: the radiating patch, ground plane and a suspended element. The sheet resistance for the ITO layers is 8 Ω/sq. while the layer thickness is 100 nm and the optical transmission level is about 95%. The ITO patch element is 7 mm x 7 mm x 100 nm in size and is placed onto a transparent Plexiglas substrate measuring 12 mm x 12 mm x 1.5 mm, with a dielectric constant of εr = 2.59 and loss tan δ = 0.068. The lower surface of the substrate is coated with the ITO as ground plane. The suspended element glass is only coated with an ITO layer on the outer bottom surface, whilst on the top side is not coated. The suspended patch is positioned over the radiated element using four glass stands as the supporting structure placed in the corners of the patch. An air gap is present between the suspended ITO patch and the radiating ITO patch as depicted in Figure 6.25. The suspended patch creates a dual-band operation. The whole antennae is placed over a polycrystalline silicon (poly-Si) solar cell, with an air gap of 2.0 mm, which is fed through a 50 Ω-coaxial probe feed. The antennae is designed and simulated in CST Microwave Studio, as illustrated in Figure 6.25.

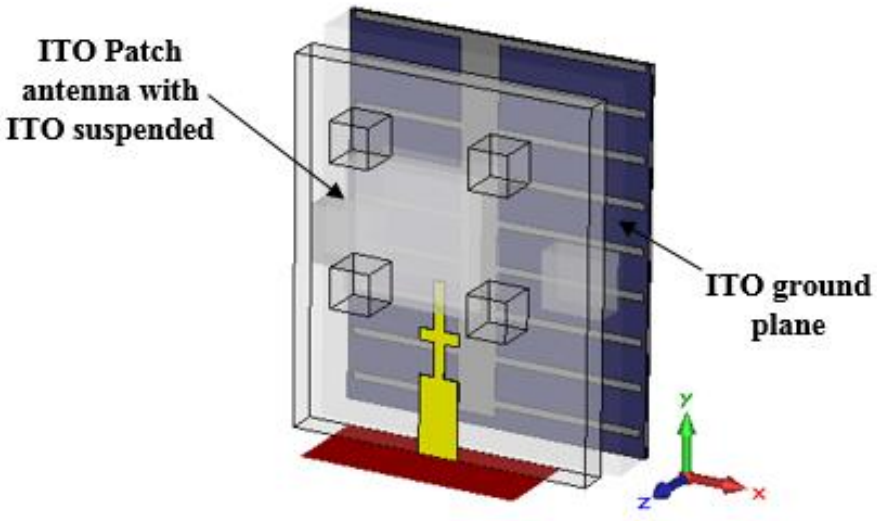

Figure 6.25: ITO suspended antennae integrated with solar cell overall view

The resultant return loss and the radiation patterns are shown in Figure 6.26 (a), (b) and (c).

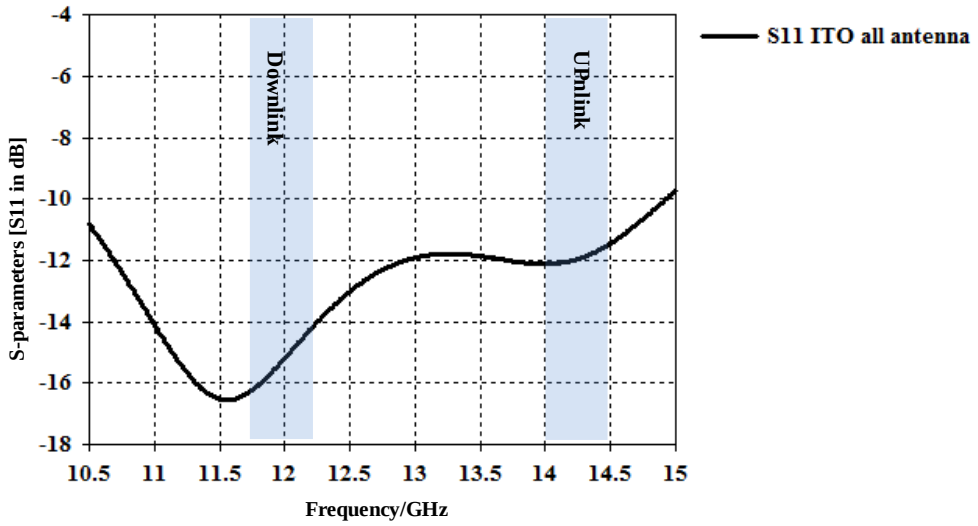

(a)

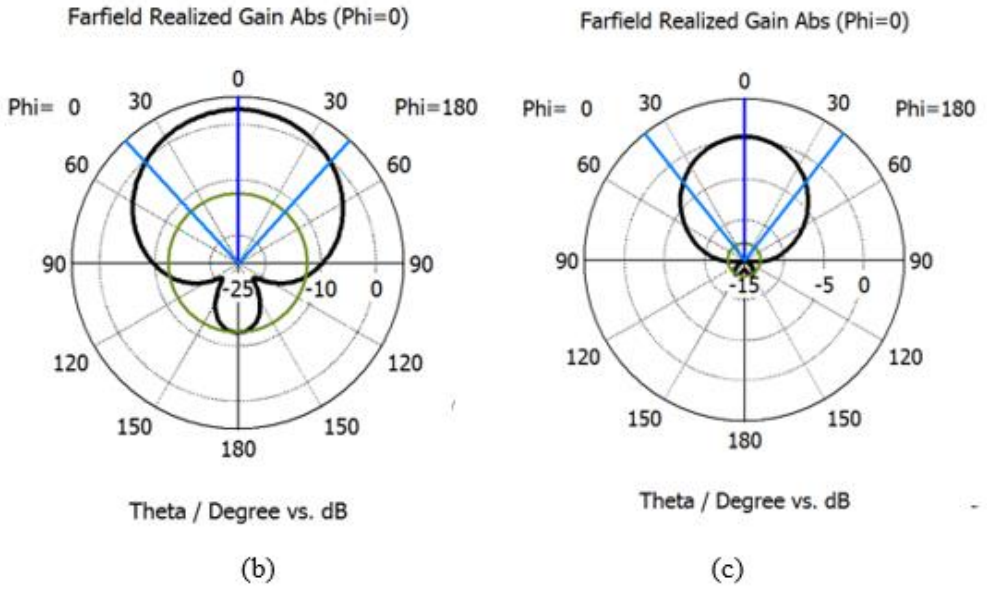

(b) (c)

Figure 6.26: Simulated results for transparent ITO patch Antennae (a) S_{11}-parameter (dB), radiation patterns; (b) down-link at11.95 GHz, and (c) uplink at14.25 GHz

From Figure 6.26 (a), (b) and (c), it can be noticed that the effect of replacing the solid copper patch and suspended patch with the ITO conductive material for the Ku-band suspended transparent antennae has been significantly degraded the antennae performance. Therefore, it can be said that using of transparent ITO conductive material, for full design broadband direct-coupling feeding transparent suspended patch antennae have disadvantage at high frequency such as Ku-band range. The results will be compared and discussed in detail in Section 6.6.6.

6.6.3 Suspended Meshed Patch Antennae Design

As demonstrated and reported earlier in the previous section 6.6.2 that has a significant degradation in performance, when full ITO antennae was used. To achieve a compromise between optical transparency and RF performance, the suspended ITO patch is replaced by a meshed copper patch element. In this design, the both the radiating patch and the suspended patch have identical meshing geometries while the ground plane has a coarser meshing structure. This design has been developed with the same overall dimensions, as in the previous ITO transparent patch element shown in Figure 6.25. The designed antennae is shown in Figure 6.27.

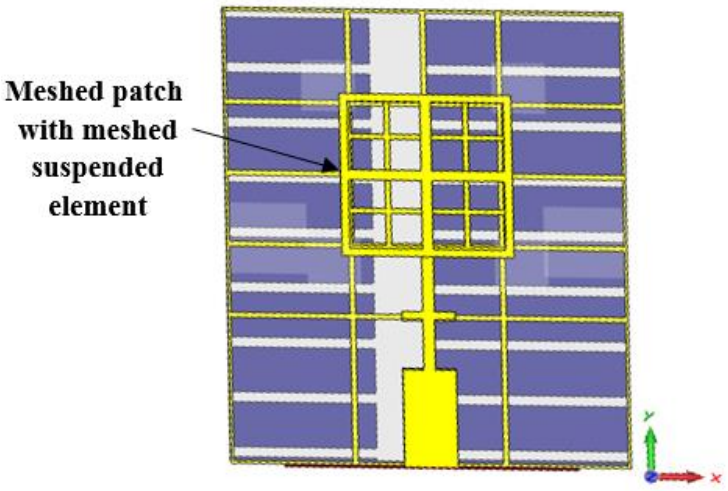

Figure 6.27: Single suspended meshed patch antennae integrated with solar cell: perspective view in CST Microwave Studio

6.6.4 Transparency Improvement Using ITO Transparent Parasitic Conductor Element

As mentioned in previous section 6.6.3, due to the relatively degradation in the overall transparency, which is presented at oblique angle. The transparency of suspended meshed patch antennae can be improved by using different techniques and constructions. In this design to provide more improvement in overall optical transparency while maintaining broadband enhancement and acceptable gain. A new technique is proposed that is combination of two previous designs in section 6.6.2 and 6.6.3, of (ITO transparent and meshed patch antennae). The meshed patch antennae in Figure 6.27, that use a suspended meshed copper conductor to a compromise between RF performance and optical transparency has been redesigned. This can be accomplished by replacing the suspended

meshed copper conductor with a transparent conductor such as Indium Tin Oxide (ITO) film coated on 1mm transparent substrate glass, as can be shown in Figure 6.28.

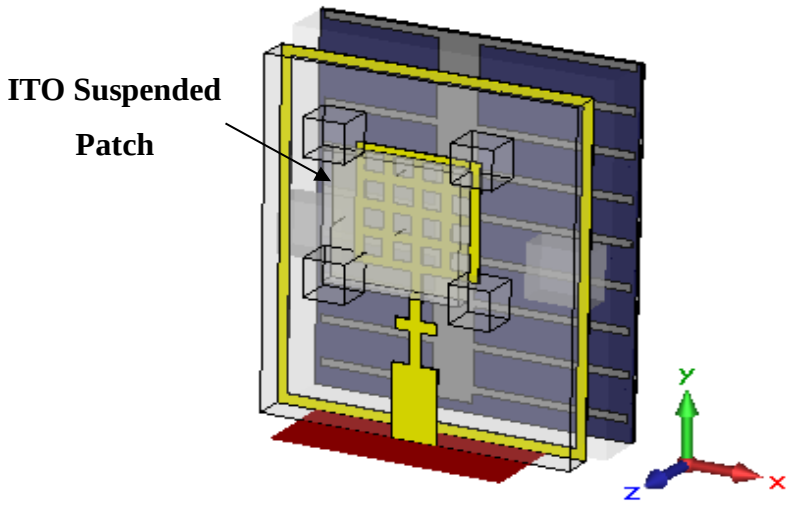

Figure 6.28: Meshed antennae with ITO suspended patch

The simulated S_{11}-response of the proposed meshed antennae with an ITO suspended patch integrated with a solar cell is illustrated in Figure 5.29 (a). Also, the downlink and up link radiation patterns are shown in Figure 5.29 (b) and (c).

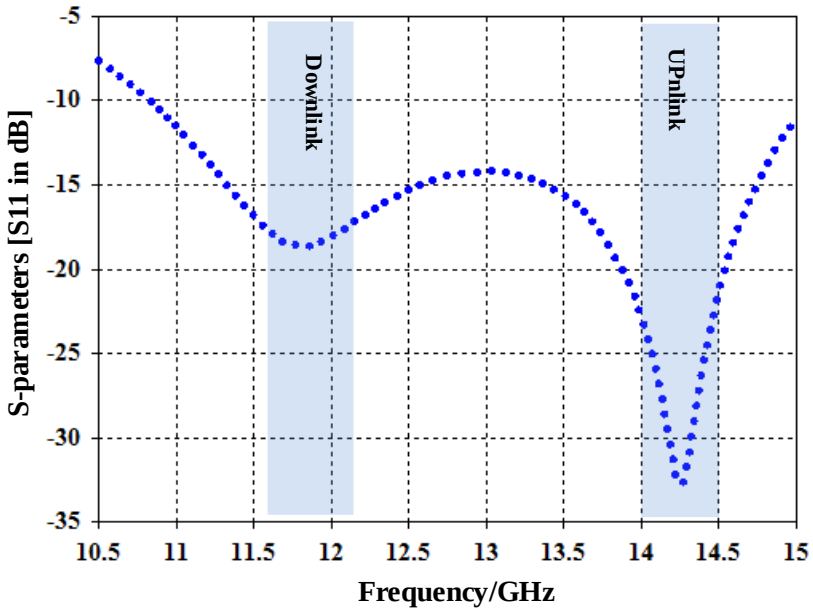

(a)

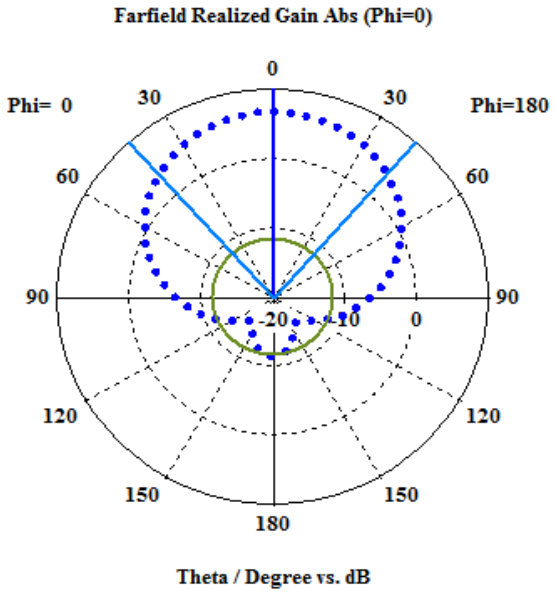

(b)

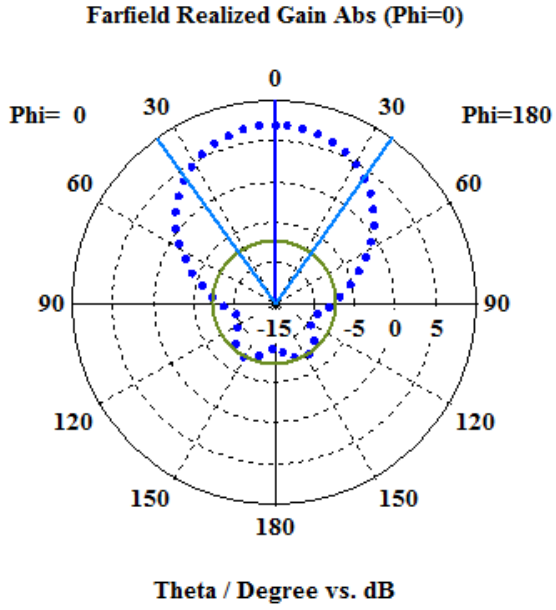

(c)

Figure 6.29: Simulated results of ITO suspended meshed antennae: (a) S_{11}- parameters, radiation patterns; (b) down-link at 11.95 GHz, and (c) uplink at 14.25 GHz.

6.6.5 Results and Discussion

In order to assess the replacement of the grid copper patch and suspended patch with meshing and transparent ITO conductive material, Figure 6.30 provides a comparison between the S_{11} patterns of the designs presented in Section 6.6.2 (all elements consisting of an Indium Tin Oxide ITO), in Section 6.6.3 (meshed suspended patch) and Section 6.6.3

(ITO suspended meshed patch), respectively. The simulated results of the three antennae are also summarized in Table 6.3 for discussion.

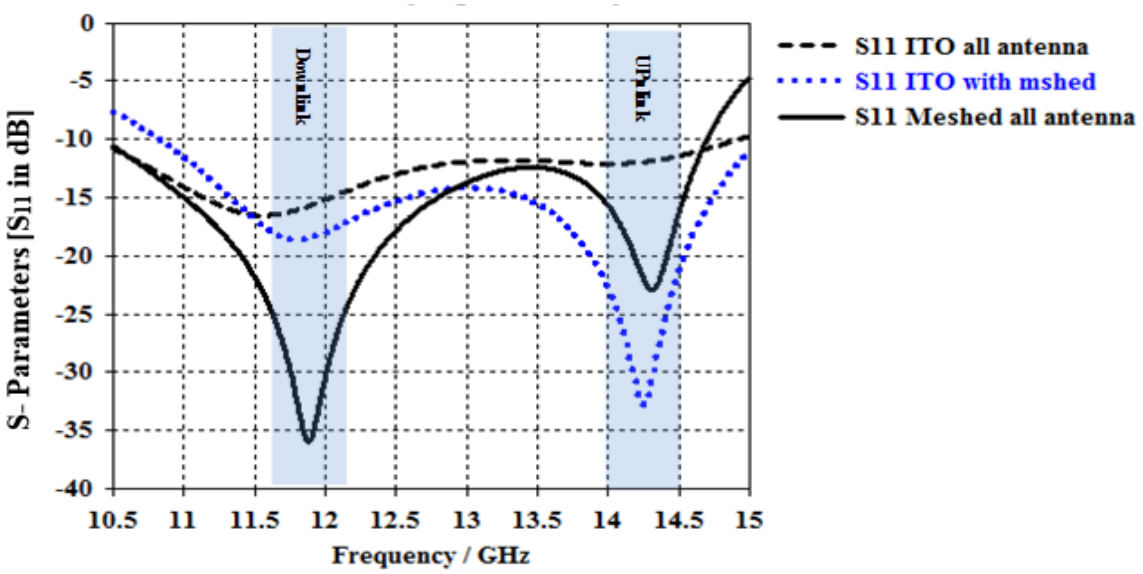

Figure 6.30: Simulated S_{11}-parameters of ITO suspended patch, suspended meshed patch, and ITO suspended meshed antennae.

Table 6.3: Summary of simulation results for three antennae over resonance frequencies bands

Antennae Types Parameters	ITO patch antennae		Suspended meshed patch antennae		ITO suspended meshed patch antennae	
Resonace frequency (GHz)	Downlink	Uplink	Downlink	Uplink	Downlink	Uplink
	11.60	N/A	11.95	14.25	11.95	14.25
Bandwidth(MHz) (RL ≥ -10 dB)	500	N/A	500	500	500	500
Realized Gain (dBi)	2.67	0.26	7.35	8.37	6.71	6.99
Beam width (3dB)	76°.7	85°.1	84°.2	72°.2	83°.3	72°.4
Patch Dimnsion (mm^2)	7		6.6		6.6	
Overall Optical Transparency (%)	95		77~ 84		90	

It can be seen in Table 6.3 that the suspended ITO patch antennae element has very low gains and bandwidths apparently not available (N/A) over both desired frequency ranges. Whilst the antennae does exhibit a resonance at the downlink band, the second resonance at the uplink band is no longer apparent. Additionally, the antennae gains have been reduced to ~2.67 dBi and 0.26 dBi respectively, due to the low electrical connectivity of the ITO (compared to copper metal) to allow highly transparency thin conductors. Therefore, it can be said however that it has very good optical transparency of approximately 95%. Use of transparent ITO conductive material as a radiating element in designing broadband suspended transparent patch antennae still suffers from degradation of RF performance, and is rather expensive.

For the suspended meshed patch antennae shown in Figure 6.27, it can be noted that RF performance has been improved compared to the ITO suspended patch antennae. As shown in table 6.1, it has a power gain of 7.35 dBi with a beam width of 84.2˚ over the downlink band and a gain of 8.37 dBi with a beam width of 72.2˚ over the uplink band. It can also be observed that a bandwidth of more than 500 MHz over each band has been achieved, determined at -10 dB bandwidth. The overall transparency was found using Equation (6.3), and the results are reasonably good at a normal incidence of approximately 84%. However, at oblique angles it was degraded to about 58 %, due to shading from suspended grid lines that affects the oblique illumination of the solar panel cells. For the meshed antennae suspended with an ITO patch, it can be seen that when an ITO suspended transparent conductor is used, the overall optical transparency of the antennae is improved to about 90 %. Meanwhile, RF performance is maintained with minimal degradation. The realized gains are measured at 6.77 dBi (downlink) and 7.01 dBi (uplink), and the results indicate a slight reduction, of only 0.58 dBi and 1.36 dBi respectively, when compared to the suspended meshed antennae. A -10 dB bandwidth of 500 MHz over the desired standard Ku-band portion has been obtained. Moreover, it is found that the antennae offers a good trade-off between overall optical transparency and RF performance. It is also noted that the proposed compact suspended transparent patch antennae has a reduced size, due to the effect of the slots, which are added to the antennae.

6.7 Chapter Summary

In this chapter, a topology technique for the integration of solar cells beneath the antennae elements was selected and used, alongside their power service. It was demonstrated that:

- Although the technique reduces solar efficiency due to shading of the RF radiating element, to address this, a meshing technique was applied. It was necessary, before placing the antennae on the solar cell, to begin by meshing a single square microstrip patch antennae that was designed to operate at an operating frequency of 11.95 GHz (downlink), and printing it upon an optically transparent Plexiglas substrate using CST Microwave Studio. A calculated overall antennae optical transparency of 84 % was achieved, and the S_{11}-response of the meshed antennae was demonstrated. However, it showed a single resonance narrow impedance bandwidth.
- The dual-band suspended transparent technique in Section 5.2.4 was implemented successfully in order to address the drawback of narrow impedance bandwidth. A dual-band suspended transparent Ku-band patch antennae integrated with PV solar cell was designed and investigated. The results were compared between the single square microstrip meshed patch antennae and the dual-band antennae. Dual-bandwidth of more than 500 MHz in each portion was demonstrated. A trade-off between RF performance and an overall transparency of 84 % was achieved.
- The effect of replacing the solid elements of a microwave suspended patch antennae with meshed elements was also examined and discussed. The simulated results were analysed and show shifting in resonance frequencies.
- In this chapter also, an investigation of the integration technique from the perspective of both the antennae and the PV solar cell was carried out.
- The effect of the integration and non-integration of the solar cell on the antennae's performance was demonstrated in Section 5.3.4. The downlink and the uplink resonance frequencies were shifted from the intended design frequency. This is due to the presence of the solar cell layer's encapsulation material at the bottom, which changes the dielectric constant of the antennae substrate, thus resulting in shifting of the resonance frequency in both bands.
- Throughout this chapter, and finally in Section 5.5, the ITO suspended meshed patch antennae for Ku-band satellite applications integrated with solar cells has been developed and designed. The overall optical transparency was improved to approximately 90% compared to the previous design in Section 5.2.4.
- It was successfully demonstrated that the proposed linear-polarised RF suspended transparent patch antennae was designed. This up-to-date work can be extended to

provide an initial work that continues with developing and assessing the relative merits of designing a Ku-band antennae element for dual-polarised operation. This will be performed in later sections within this research. It can be used for frequency re-use in Ku-band downlink and uplink communications to achieving a final design, which works well in terms of both solar efficiency and RF performance.

As a result of this, the proposed designs provide new knowledge and development in the field of photovoltaic antennas that overcome the associated problems of current PV antennas (mentioned in the literature). They confirmed that operate at high broadband (Downlink, Uplink) frequencies using proposed topology transparent techniques, with reasonable trade-off between the RF antenna performance and solar performance was achieved. In addition, the designs have the potential to service as a basic building block of a direct feeding 2D-array solar antennas of Ku-band SatCom applications.

Chapter 7 Dual-band, Dual-polarised Combined Solar Antennae for Ku-band Frequency Re-use.

7.1 Introduction

Dual-polarised and dual-frequency operations are important topics in the application of wireless communications, and this design has become very challenging when considering future demands. Dual-polarised Microstrip Patch Antennae have recently received considerable attention due to their small size and capability of being radiated at different operating frequencies from the same radiating element [178-180]. This has a variety of applications in wireless communication systems, such as in satellites and aerospace systems [181-183]. It can also be applied in mobile communication systems to obtain polarisation diversity. Today, satellite communications need lightweight antennae that can be used in different bands, and provide frequency re-use operation services, such as in Ku-band or Ka-band satellite communications. This type of dual-polarised satellite communication link must have high isolation between the two ports in order to reduce interference for good performance. These antennae can also be used for transmission and reception, or to integrate the receiving and transmitting functions into one antennae to reduce antennae size with a low profile [36]. For remote area wireless communications, PV microwave antennae are highly desirable and required due to the cost-effective system they use.

As mentioned in the literature review, the work which has been done previously on patch antennae integrated with solar cells has used linear polarisation or circularly polarised antennae, while no work has been carried out on photovoltaic dual-polarisation compact patch antennae which can be developed into two-dimensional fully PV array patch antennae. Therefore, in this chapter, single unit and 2x2 sub-array dual band-frequency and dual-polarized suspended transparent patch antennae integrated with solar cells for frequency re-use are designed and demonstrated.

7.2 Dual-Polarized Single Element Design

In this section, the proposed single structure dual polarized suspended meshed element is illustrated (see Figure 7.1). This antennae was developed from the proposed linear

polarisation antennae in Chapter 6, with similar fabricated materials and parameters (the same thickness and dielectric constant). However, the substrate area is extended to be square, with dimensions of 18 × 18 mm^2, in order to be suitable for a dual-polarised design. The antennae is excited on both adjacent sides, with two identical feed mechanisms for horizontal and vertical polarisations through two microstrip transmission lines with a quarter-wavelength transformer, and with signals of continuous phase difference and a direction of perpendicular polarisation to each other. The CST modelling and fabricated prototype for the dual-polarised suspended solar patch antennae are illustrated in Figure 7.1.

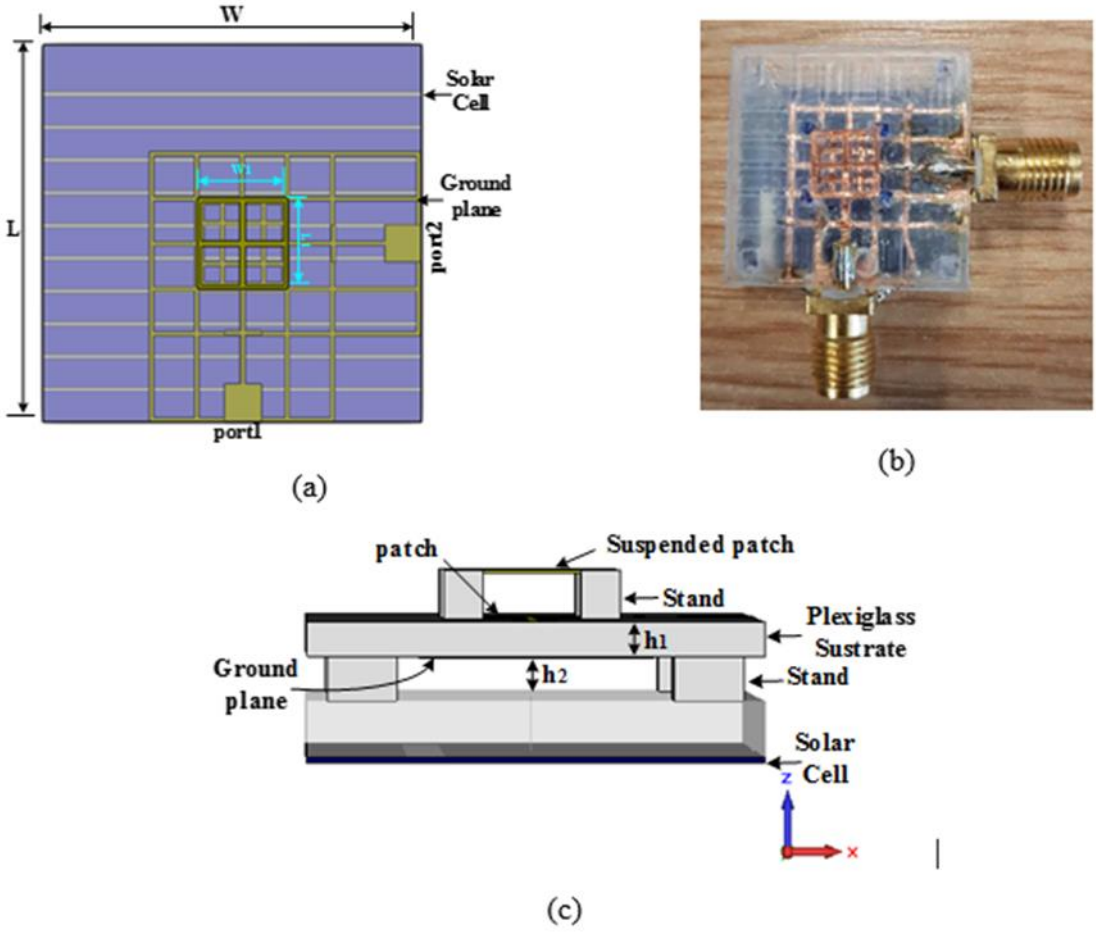

Figure 7.1: Dual-polarised suspended meshed patch antennae with a poly-Si solar cell: (a) design in CST Microwave Studio; (b) side view; (c) fabricated prototype antennae. Dimensions: $W = L = 22$ *mm*, $W_1 = L_1 = 6$ *mm*, $h_1 = 1.5$*mm*, $h_2 = 2$ *mm*.

7.2.1 Simulation and Measurement Results

The simulated and measured reflection coefficients S_{11} and S_{22} parameters (at port1 and port2) of the proposed transparent dual-polarised solar patch antennae are demonstrated in Figure 7.2. The measurements were carried out using a VNA, Agilent E8364B.

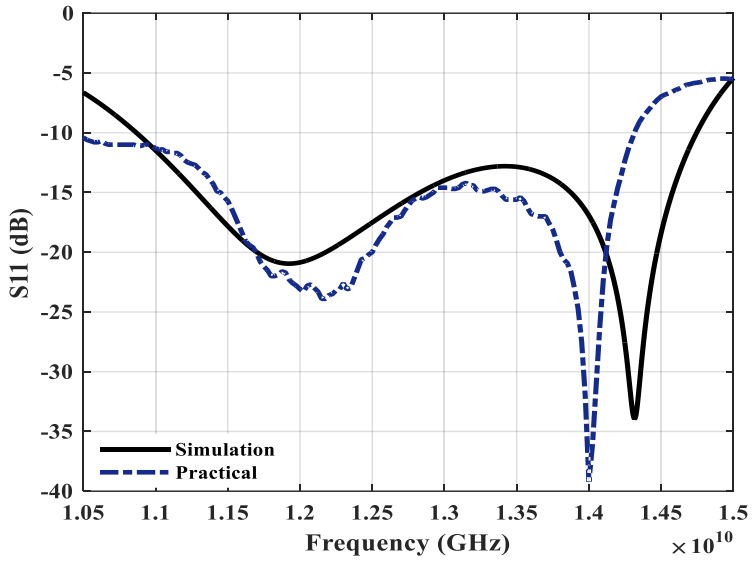

(a)

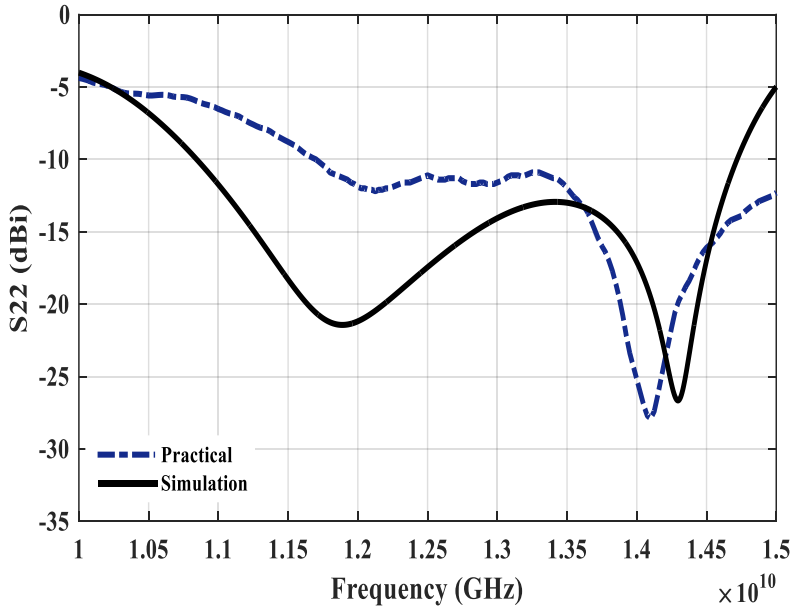

(b)

Figure 7.2: Simulated and measured reflection coefficients of the dual-polarised solar patch antennae (a) S_{11}, (b) S_{22}.

As shown in Figure 7.2, the proposed antennae offers reasonable response results for S-parameters at the two exciting ports for both S_{11} and S_{22} parameters, across both the desired dual-frequency bands (11.7-12.2 GHz downlink and 14.0 – 14.5 GHz uplink). In Figure 7.2a, the S_{11} measurement response agrees quite closely with the simulation result at the desired frequency downlink band, whilst at the uplink, the operational frequency band is shifted towards the lower end, with a frequency shift of 200 MHz from the design frequency of 14.25 GHz. However, the S_{11} response can show good matching return loss,

with a reflection coefficient level of above -12.6 dB. In Figure 7.2b for S_{22} response, the measured uplink operational resonance band is slightly shifted, to a lower resonance frequency of 14.15 GHz, and the downlink band operates across the intended operating frequency range, but poor matching has been observed, which was obtained at a relatively low level of -12.1 dB reflection coefficient. Nevertheless, this is still greater than -10 dB.

In view of this, it can be said that in both S-parameters, the small difference in the measured uplink-band resonant frequency is attributed to the hand-constructed fabrication process and the imperfections caused in the resulting dimensions. Clearly, it is extremely difficult to cut the mesh cells by hand, and if this design were manufactured using a more accurate production technique, such as chemical etching, this would improve accuracy. Otherwise, good agreement between the simulations and practical measurements has been achieved.

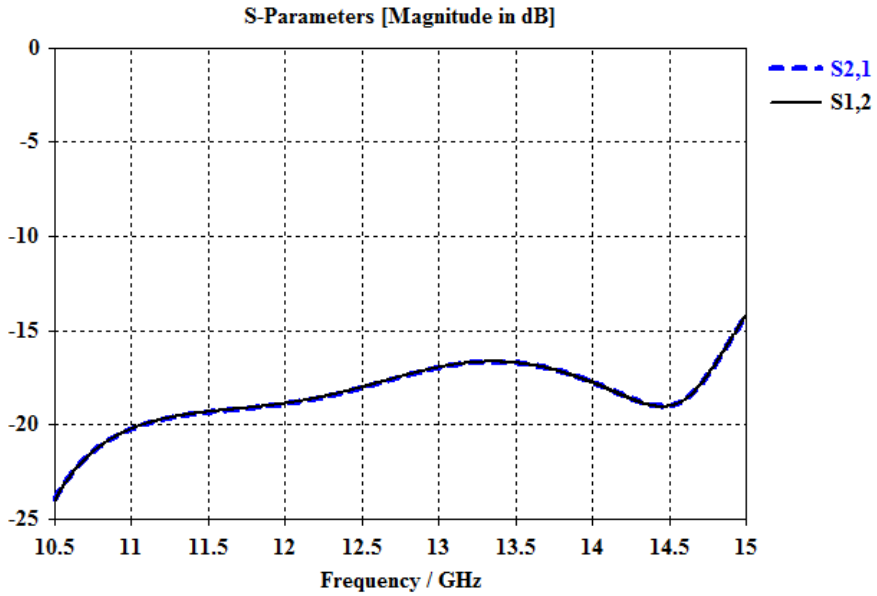

Figure 7.3: Cross-polarisation isolation level

Figure 7.3: shows that the isolation between the horizontal and vertical two feeding ports of the proposed antennae is ~ -18 dB (at both desired bands), which still presents poor isolation, and hence, a high level of cross polarisation. This might be due to several obvious reasons, such as both input feeding ports being highly coupled to each other, or due to the antennae's symmetric structure cross-polarised current components on the patch element, and / or it might be that those feeding ports are operating at a different frequency. Therefore, it is desirable to achieve an isolation of lower than -30 dB between the receiving and transmitting ports (downlink and uplink), in order to obtain separation between the excited ports.

Figure 7.4 (a) and (b) shows the simulated radiation patterns for the E-plane and H-plane far field both at 11.95 GHz and 14.25 GHz of the proposed antennae.

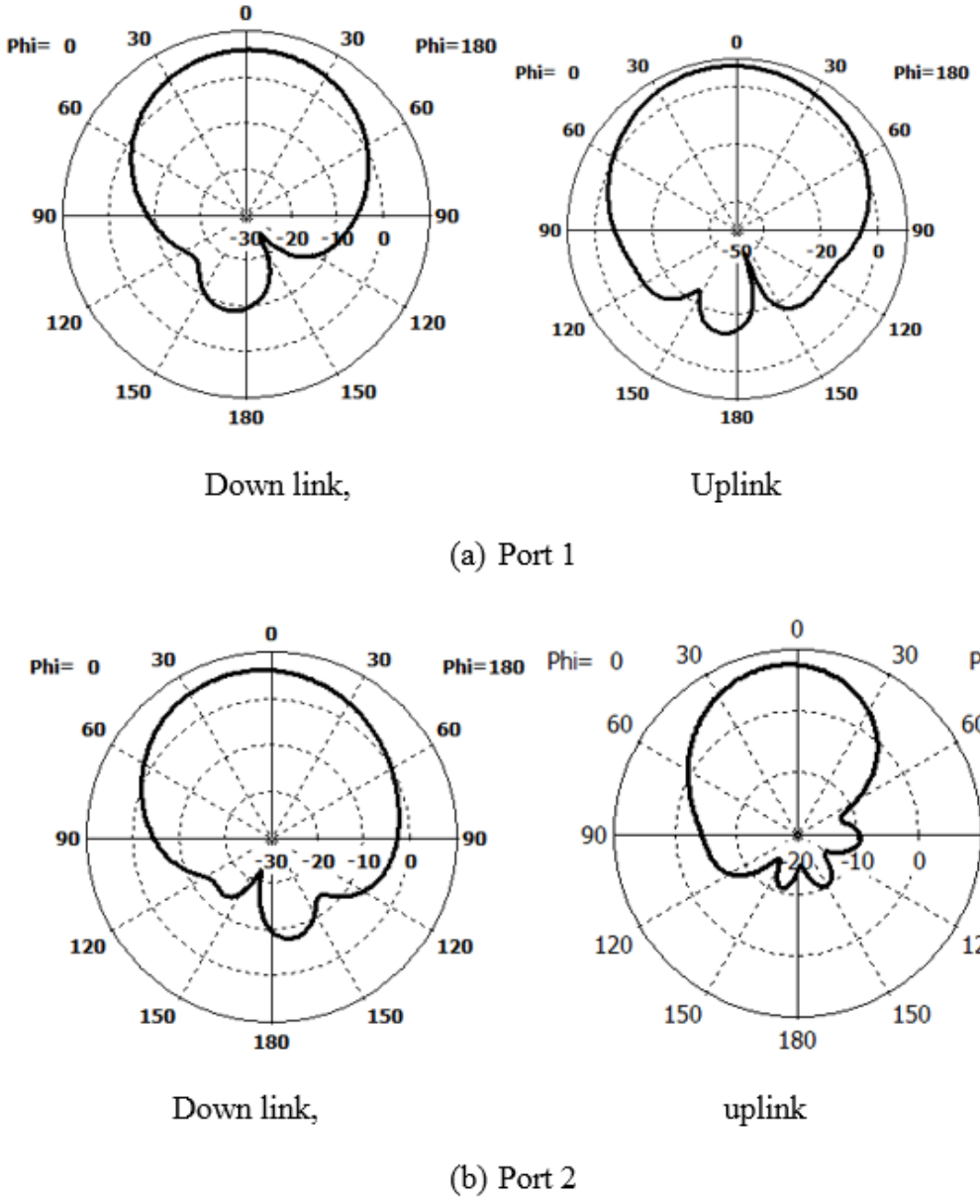

Figure 7.4: Simulated E-plane and H-plane far-field radiation patterns (a) antennae fed through port 1 (b) antennae fed through port 2.

As shown in Figure 7.4, the radiation patterns for the E- and H-planes of the proposed dual-polarised PV patch antennae were simulated at 11.95 GHz and 14.25 GHz, downlink and uplink, respectively. There is a slight difference in radiation patterns between the two feeding ports 1 and 2, due to the symmetry in the structure of the antennae. The E- plane and H-plane radiation patterns obtained at downlink operating frequency 11.95 GHz are close to the E-plane and H-plane radiation patterns at an uplink frequency of 14.25 GHz. It can also be seen

that the antennae has two maximum gains of 6.25 dBi and 7.6 dBi, achieved at the operating frequencies, respectively. However, in this single dual-polarised feeding element design, the isolation between the dual polarised ports of each element is never more than 30 dB. Hence, having acceptable low cross polarisation requires an appropriate method to be employed. Therefore, in the next section, it will be suggested that this antennae element needs to be arranged in a 2x2 sub-array with a different phase of excitation, which will achieve good cross-polar discrimination.

7.3 Design of dual-polarised Subarray Antennae to Achieve Extremely Low Cross-polar Levels

7.3.1 Introduction

The radiation pattern of a single element patch antennae has a relatively wide broadside, and therefore, normally, each element itself provides a low value of gain. However, in some applications, a high gain is required to meet demands such as long-distance communications. This can be achieved by increasing the antennae elements, through multi-elements, which are referred to as an array, due to the fact that a K-band antennae element is to be incorporated into an antennae array consisting of N elements [33, 184-187].

In this section, the design of a 2×2 element sub-array dual-polarized meshed patch antennae for dual band is presented and demonstrated, which is incorporated from the single dual-polarised photovoltaic antennae illustrated in section 6.1. This sub-array antennae has achieved a good radiation performance with gain greater than 13 dBi and port isolation more than 30 dB over the desired frequency ranges. An investigations can be carried out in order to incorporate the design of 2x2 sub-array integrated with solar cells with dual-linear polarised. In order to be applicable and provide design requirements for frequency re-use in Ku-band satellite communication array antennae for remote areas.

7.3.2 2x2 Sub-Array Dual-Polarized Antennae Model

Figure 7.5 shows the structure of a 2x2 sub-array dual-polarised patch antennae. It consists of 4-element square suspended meshed patch elements, which are identical in size and separated by equal inter-element spacing, which is determined as approximately of 0.7λ (17.5 mm). The whole dimensions of the sub-array module are 45 mm x 45 mm (4.5cm x 4.5cm).

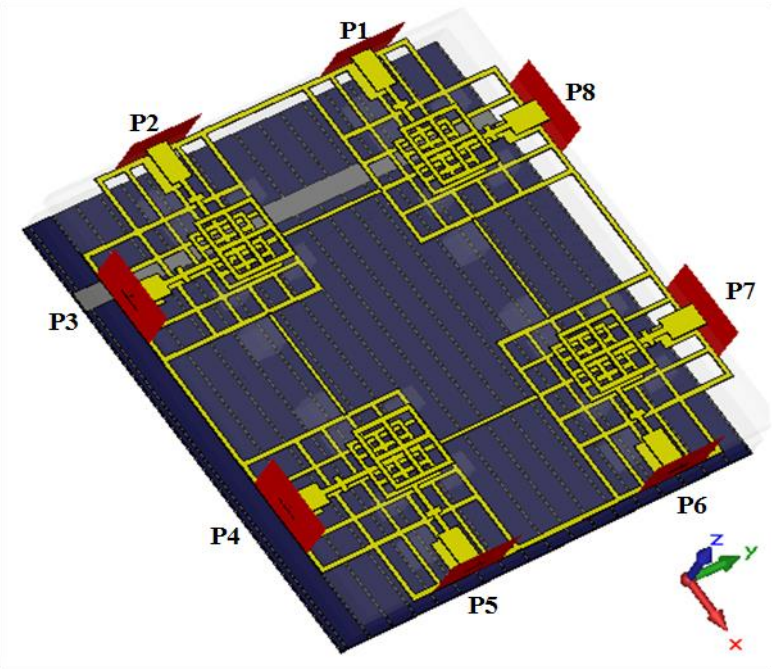

Figure 7.5: Configuration of the 2×2 sub-array dual-Polarised antennae

In this design, the aim is to achieve high isolation by creating a single dual polarised element with high isolation between exciting ports (and hence, low cross-polar level in the radiation pattern). This can be achieved by employing a typical patch element with mediocre isolation and arranging the elements as illustrated in Figure 7.5. Thus, in the vertical direction, the upper element was fed from the top and the lower element was fed from the bottom, but with a 180° phase reversal. This excitation causes the vertically polarised fields of the upper and lower element to add, but the cross-polarised fields to cancel. The same can be done for the left and right elements in the horizontal direction to cancel the cross polarisation. The input feeding ports of the elements are arranged as demonstrated in Figure 7.5, and these feeding ports on the sub-array antennae structure are named P1 to P8, in order to be arranged for phase excitation.

After running the post possessing and exciting all 4-elements with equal amplitude and 180-degree phase difference between the upper and lower ports and the left and right ports, all the elements of the array are excited in phase. Such this operation will not affect the co-polarisation radiation pattern. The resultant co- and cross-polar levels of the radiation patterns will be demonstrated in Section 6.6. It can be predicted that the cross-polar level will be more than 30 dB below the co-polar level. It can be said clearly that constructing a feeding network to provide these excitations with a meshed configuration (this cannot be achieved by simply feed connecting**)** will be challenging, as non-conventional feeding

network is required, but not impossible. The realisation of the feeding network is regarded as future work.

7.3.3 Results and Discussion

The simulation results of the element model were found using CST Microwave Studio. Figure 7.6 demonstrates the simulated reflection coefficient (S_{11} port 1 – S_{11} port 8) for the proposed 2×2 sub-array dual-polarized antennae.

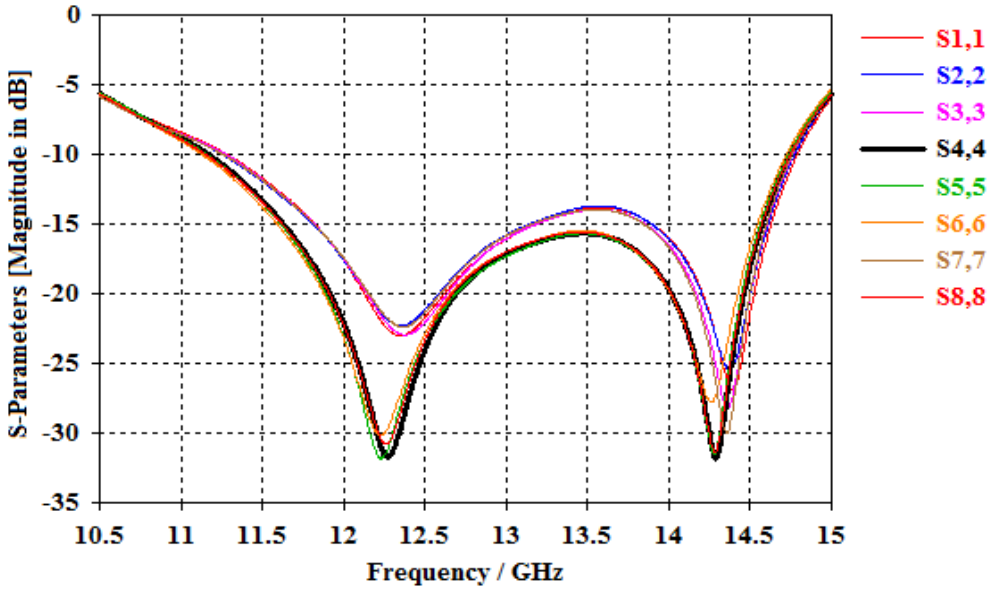

Figure 7.6: Simulated S_{11} reflection coefficients (S_{11} port 1 – S_{11} port 8)

As can been seen in Figure 7.6, convergence reflection coefficient responses for multiple-port excitation is demonstrated, when the 2×2 sub-array dual-polarized antennae is fed through port 1 to port 8. In view of the discussion in Section 7.2.2, the upper and lower elements were excited with equal amplitude, but with a 180-degree phase difference. The simulated radiation patterns of this 2×2 sub-array antennae structure are shown in Figure 7.7a, b where Figure 7.7(a) demonstrates the co-polar pattern, which is the proposed antenna's radiation in H-plane desired direction. Whereas, Figure 7.7 (b) the cross-polarisation (sometimes written as X-pol) that is the polarisation (in E-plane) orthogonal to the desired polarisation direction. Considering the cross-polar discrimination over the 3 dB beam width of the co-polarisation, the element radiation patterns after the phase difference of feeding excitation show that the level of cross-polarisation has been significantly improved.

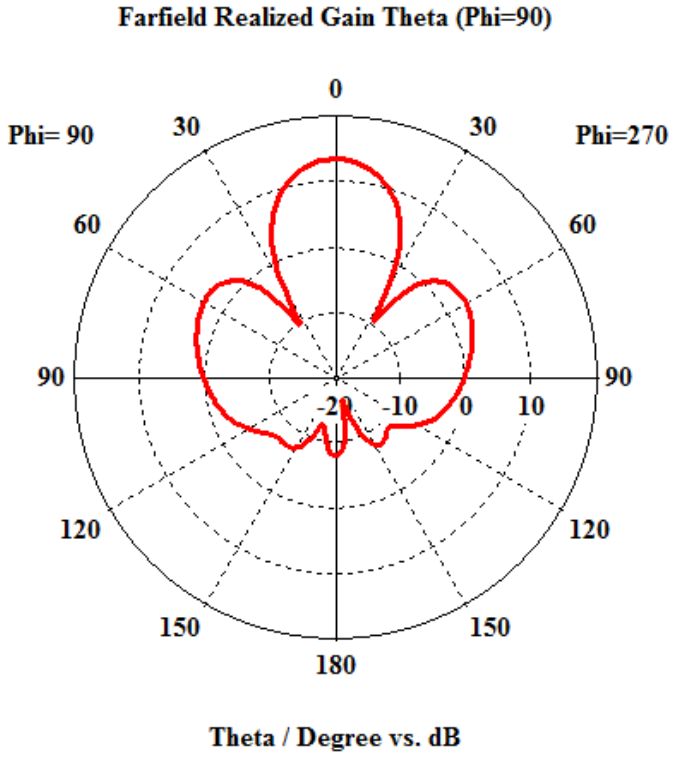
Farfield Realized Gain Theta (Phi=90)
0
30
30
Phi= 90
Phi=270
60
60
90
90
-20
-10
0
10
120
120
150
150
180
Theta / Degree vs. dB

(a)

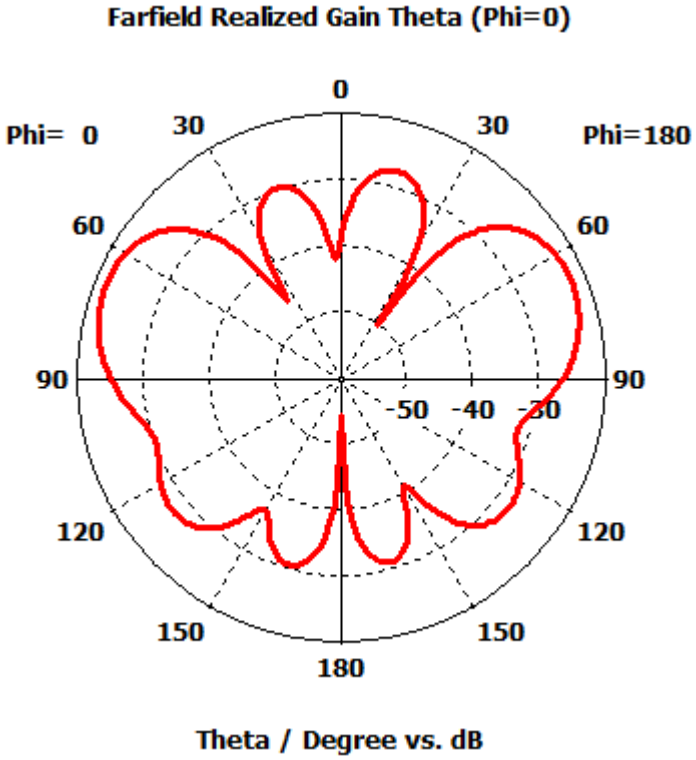
Farfield Realized Gain Theta (Phi=0)
0
30
30
Phi= 0
Phi=180
60
60
90
90
-50
-40
-30
120
120
150
150
180
Theta / Degree vs. dB

(b)

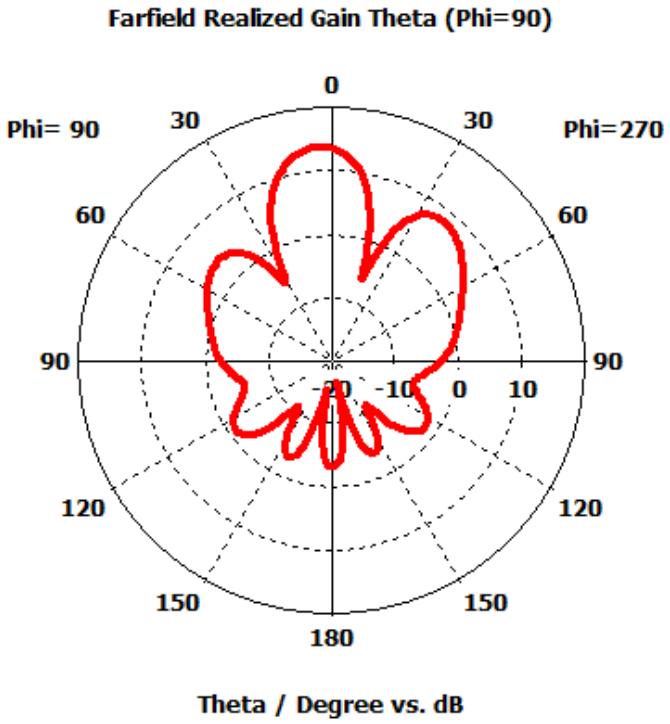

(c)

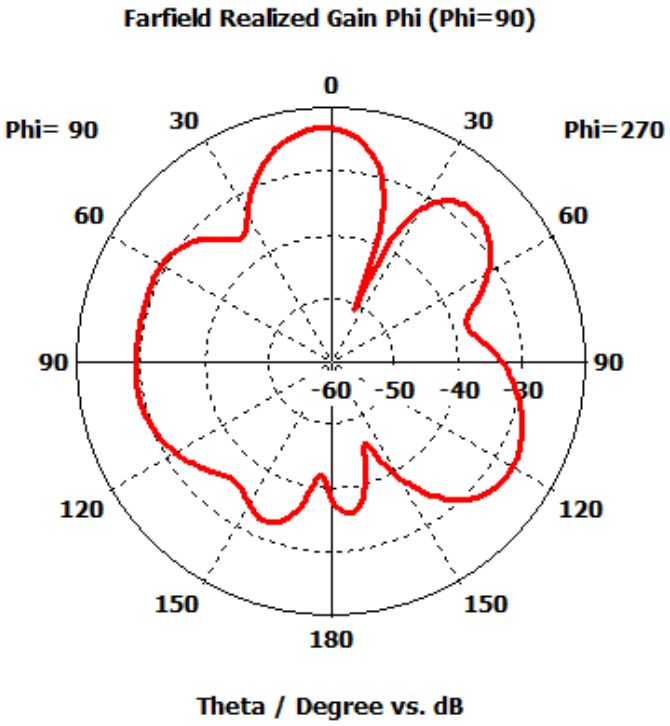

(d)

Figure 7.7: Simulated E-plane and H-plane far-field radiation of patterns 2 × 2 element sub-array (a) H-plane downlink, (b) H-plane uplink, (c) E-plane down-link, (d) E-plane up link

As shown in Figure 7.7, the radiation pattern results for the theta and phi components were as expected. The cross-polar level of the radiation pattern is extremely low, as desired (more than 30 dB lower than the co-polar level), representing good results. It can be seen that the cross-polar discrimination within the main lobe pattern at 11.95 GHz is over 50 dB (13.4 +38) on the axis (e.g. zero degrees), and at 14.25 GHz it is 38 dB (13.9 +24.1) on the axis. It can also be observed that a narrower-beam radiation pattern is exhibited compared to a wide-beam antennae before the elements are incorporated into the subarray, as demonstrated in Section 6. The proposed sub-array antennae's maximum gains are greater than 13 dBi, which has maximum simulated gains of 13.4 dBi at 11.95 GHz downlink, and 14.0 dBi at 14.25 GHz uplink operating frequencies. It is found that the -3 dB beam widths at the downlink are obtained within an angle range from 29.2˚ to -29. 2˚, and at the 3 dB uplink, the angular width is -22.6˚ to 22.6˚, respectively at the operating frequencies. It can be noticed also that the 38 dB between some ports is not relevant, as this only represents the cross polar discrimination when obtained from the difference between co and cross-polar radiation patterns. The simulated 3D far-field radiation pattern of the proposed antennae is demonstrated in Figure 7.8. The 3D-dimensional antenna radiation pattern is a three-dimensional graphical indicates the three co-ordinates (x, y, z), and representes spherical coordinates (r, θ, Φ).

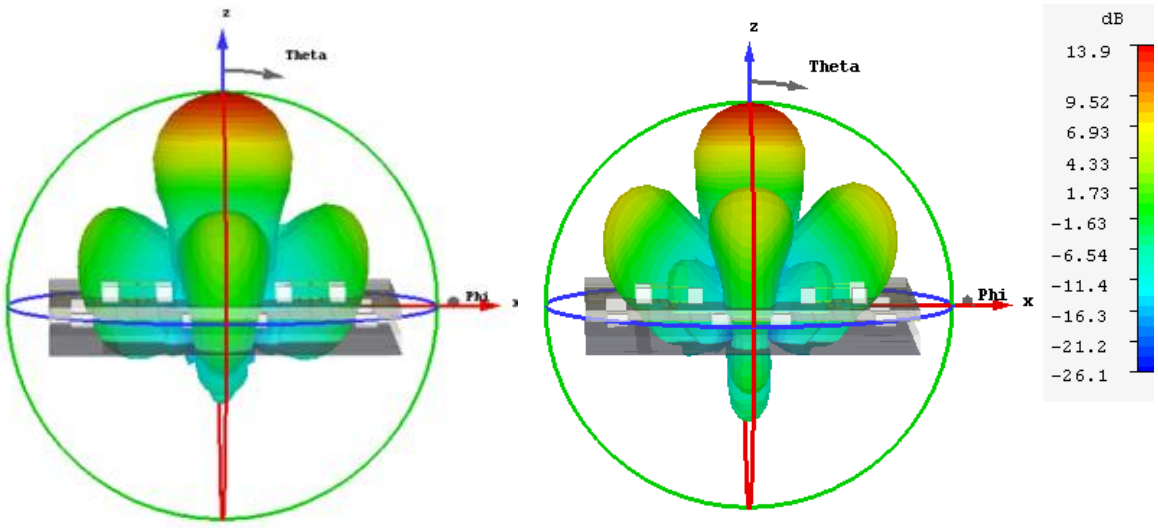

(a) (b)

Figure 7.8: Simulated 3D far-field radiation pattern of the 2 x 2 sub-array solar antennae, at

(a) 11.95 GHz downlink, (b) 14.25 GHz uplink

7.4 Summary

In this chapter, a single dual polarised suspended transparent patch antennae integrated with PV solar antennae for frequency re-use Ku-band dual-polarised communication systems was proposed and designed successfully. The results of the RF performance were demonstrated with respect to the solar antennae integration topology and dual feed excitation. It was shown that poor isolation occurred between feed ports. For the requirement to achieve a high gain dual-polarised antennae from a single element, which provides low value of gain and wide broadside, the design of a dual-polarised 2×2-element subarray was performed and investigated. The challenge of achieving input ports with high isolation was successfully addressed by suggesting a way of using the phase difference between the input ports. As a result, new knowledge and development were added to the field of PV patch antennae where such proposed integrated transparent topology direct coupling designs can be presented for frequency re-use dual-polarised at Ku-band frequencies or higher. Moreover, it can be incorporated into 2D-array solar antenna to produce a narrow beam and increased gain for long distance communications.

A twin lead new feeding line technique to match the full array elements will be suggested as future work.

Chapter 8 Conclusion and Future Work

8.1 Conclusion

The aim of this research work was to investigate, design and develop the use of dual-band, dual-polarised PV solar planar patch antennae for frequency re-use in ku-band SATCOM.

In this thesis new knowledge and development in the field of photovoltaic patch antennas communications were obtained. The proposed compact designs have provided bridge for the associated drawbacks with the current PV antennas in the literature. These developed designs have the potential and confirmed that operate at high frequencies and exhibit broadband Downlink and Uplink, by implementing new topology transparent techniques. Moreover, provide dual-polarisation simultaneously operation from the same PV patch antenna for frequency re-use, with achieved narrow beam and increased gain. In addition, it has the capability for employing and incorporated into a direct feeding Ku-band 2D-array solar antennas.

Therefore, in this research, rigorous study and investigations on current integration topology techniques of microwave antennae and solar cell were carried out. These topologies were classified, analysed in detail and various studies and proposed solutions were introduced in the literature. They were within a single unit cell or limited number of linear-array elements at low relative operating frequencies and offering narrow bandwidth. It was also observed that most proposed solar integrated antennae have linear polarisation or circular polarisation performance. Thus, these are unsuitable candidates to be developed and employed for dual-polarisation solar patch antennae systems. In view of this, in this thesis the proposed solutions to address these disadvantages were performed and demonstrated in details as follows:

- A broadband transparent suspension technique was developed by suspending a transparent element above the RF radiating meshed patch to achieve dual band RF performance with good overall optical transparency. The drawback of a narrow impedance bandwidth was successfully addressed. As a result of this work, a novel compact dual-band suspended transparent Ku-band patch antennae integrated with a PV solar cell was successfully designed, fabricated and experimentally tested. A good bandwidth enhancement (wide dual-bandwidth) was observed in comparison to the conventional single square transparent patch antennae which traditionally exhibits narrow impedance bandwidths at -10 dB. This new proposed design provides

a building block of an integrated 2D phased array antennae communication system for remote area satellite applications. The antennae has the potential to cover the frequency bands ranging from 11.7 GHz to 12.22 GHz (downlink) and 14.0 GHz to 14.5 GHz (uplink) allocated by the ITU to Regions 1 and 2. With instantaneous bandwidths of > 500 MHz obtained in each portion for broadband two-way satellite internet, and TV applications for fixed satellite service (FSS). A good compromise was achieved between the antennae RF performance and the overall transparency, which has realized element gains of 6.5 dBi and 7.61 dBi, for downlink and uplink bands, respectively. The overall optical transparency of the antennae has been found to be approximately 84% and the solar cell yielded an adequate solar efficiency about of 82.3 %, which showed that the changing of the solar illumination does not affect the RF antennae performance demonstrating the stability of the PV solar antennae. Moreover, the developed solar transparent patch antennae was successfully realised as a low profile and compact structure.

- Throughout this thesis, a design was developed which provided improvement of the overall optical transparency of the suspended meshed design due to the impact of optical shading at oblique illumination angles caused by (grid lines), i.e. the non-direct photovoltaic illumination. New RF suspended transparent antennae integration techniques were proposed and implemented in section 5, which compared two designs (ITO transparent and meshed patch antennae). The Ku-band suspended meshed patch antennae that uses a suspended patch and ground plane meshed copper conductors was modified and developed. This was accomplished by replacing the meshed copper conductors with a transparent conductor of Indium Tin Oxide (ITO) film coated on the transparent substrates glass. It was successfully shown that bandwidth enhancements and more improvements in overall optical transparency have been achieved. The overall optical transparency was improved to approximately 90% and this enhances the efficiency of the solar cell while maintaining good RF antennae performance over the same frequency bands as the suspended meshed antennae design.

- Most PV solar integrated antennae reported in the literature have linear polarisation or circular polarisation performance. Therefore, these are unsuitable to be employed for dual-polarisation operation services. Despite that, some works were proposed employing a slant dual-polarised microstrip solar patch antennae for frequency diversity communication. However, these are not suitable for solar

compact array_antennae downlink and uplink SatCom applications due to the inclusion of the dual-polarised complex DC/RF isolation circuit and presence of the stacked solar cell output connections that overlap each other. In addition, these designs operate at low frequency bands. In this thesis, to address these challenges, in chapter 6 a new proposed of dual-polarised, dual-band suspended transparent patch antennae integrated with solar cells for Ku-band frequency re-use was designed and demonstrated which can be developed and employed into two-dimensional fully PV dual-polarised array patch antennae. It was also illustrated that a lightweight suspended transparent patch antennae with dual coupling feeding was successfully performed. The obtained results showed a small difference in the measured reflection coefficients at both uplink and downlink-bands resonant frequencies was observed. This was attributed to the hand-constructed fabrication process and the caused imperfections in the resulting dimensions with a meshing line width of as small as 0.3 mm. It should be stated that it is extremely difficult to cut the mesh cells by hand and if this design was manufactured using a more accurate production technique, such as chemical etching, this would improve accuracy. Nevertheless, good practical results were achieved and these could only improve if more accurate fabrication techniques were employed. The elements realised good downlink and uplink gains, which were found to be 6.5 dBi, and 7.6 dBi, respectively. However, poor isolation of ~ 18 dB between two feeding ports was measured and hence, a high level of cross polarisation occurred for a single dual-polarised element.

A solution to this disadvantage was performed in chapter 6 where the simulation of an arrangement of a 2 x2 sub-array of dual polarised transparent antennae elements with good port isolation was demonstrated. This was achieved by feeding opposite elements on opposite sides and adding 180 degrees difference between the elements. This resulted in the co=polar radiation from opposite elements to add and the cross-polar radiation to cancel. It was demonstrated that a cross-polar discrimination of greater than 30 dB was achieved between the receiving and transmitting ports (downlink and uplink). As a result, the antennae exhibited a narrow beam and increased gain of 13 dBi, which is a requirement for frequency re-use operation. Hence, the 4-element sub-array simulated has the potential to be developed in order to meet the full requirements of a Ku-band solar 2D-phased array antennae.

8.2 Future work

Some further work and investigations can be carried out in order to integrate the a dual-polarised feeding network into a full array of broadband antennae elements integrated with solar cells in order to provide the full design requirements for Ku-band satellite communication phased array antennae.

- Due to the limitation of time and the amount of work that would be required, the full array feed network was not developed. However, it is suggested that using twin lead feeding lines realised along the grid meshed lines could be developed to feed the full proposed antennae array.
- The required phase differences could be achieved by adjusting the length of the microstrip transmission lines feeding the patch elements within the array in order to provide the desired communication direction.
- The next step suggested in a future project is to simulate and analyse a full array antennae and optimising the design in order to avoid any not desirable side lobes or grating lobes.

- Future work can be extended to deal with new satellite communication applications evolving to cover higher frequency bands such as Ka-band (30/20 GHz) or higher frequency bands which will have great importance for broadband services and also, to provide smaller communication component sizes.

References

[1] C. Peixeiro, "Microstrip patch antennas: An historical perspective of the development," in *Microwave & Optoelectronics Conference (IMOC), 2011 SBMO/IEEE MTT-S International*, 2011, pp. 684-688.

[2] R. Garg, P. Bhartia, I. J. Bahl, and A. Ittipiboon, *Microstrip antenna design handbook*: Artech house, 2001.

[3] R. Bancroft, *Microstrip and printed antenna design*: The Institution of Engineering and Technology, 2009.

[4] H. Gutton and G. Baissinot, "Flat aerial for ultra high frequencies," *French patent,* vol. 703113, 1955.

[5] L. Lewin, "Radiation from discontinuities in strip-line," *Proceedings of the IEE-Part C: Monographs,* vol. 107, pp. 163-170, 1960.

[6] E. Denlinger, "Radiation from microstrip resonators (correspondence)," *IEEE Transactions on microwave Theory and techniques,* vol. 17, pp. 235-236, 1969.

[7] J. Watkins, "Circular resonant structures in microstrip," *Electronics letters,* vol. 5, pp. 524-525, 1969.

[8] J. Kraus, "Antennas. 2nd editor," ed: McGraw Hill: New York, 1988.

[9] G. Kumar and K. Ray, *Broadband microstrip antennas*: Artech House, 2003.

[10] E. Byron, "A new flush mounted antenna element for phased array application," *Phased array antennas,* pp. 187-192, 1972.

[11] R. Munson and J. Krutsinger, "Single slot cavity antenna assembly," ed: Google Patents, 1973.

[12] J. Howell, "Microstrip antennas," *IEEE Transactions on Antennas and Propagation,* vol. 23, pp. 90-93, 1975.

[13] L. Fraas and L. Partain, "Solar Cells: A Brief History and Introduction," *Solar Cells and their Applications, John Wiley & Sons, Inc,* pp. 1-15, 2010.

[14] D. M. Chapin, C. Fuller, and G. Pearson, "A new silicon p - n junction photocell for converting solar radiation into electrical power," *Journal of Applied Physics,* vol. 25, pp. 676-677, 1954.

[15] K. Loh, "Solar Cells for Space Applications," 2013.

[16] R. Lee, E. Clark, D. Wilt, A. Pal, F. Miranda, C. Mueller, *et al.*, "Integrated solar cell array antenna for satellite and terrestrial communications," in *Antennas and Propagation Society International Symposium, 2005 IEEE*, 2005, pp. 231-234.

[17] A. Georgiadis and A. Collado, "Solar powered class-E active antenna oscillator for wireless power transmission," in *Radio and Wireless Symposium (RWS), 2013 IEEE*, 2013, pp. 40-42.

[18] A. Georgiadis, S. Kim, H. Lee, and M. M. Tentzeris, "UHF solar powered active oscillator antenna on low cost flexible substrate for wireless identification applications," in *Microwave Symposium Digest (MTT), 2012 IEEE MTT-S International*, 2012, pp. 1-3.

[19] R. Prasad and R. Mehrotra, "A solar powered telecom architecture for off-grid locations," in *Telecom World (ITU WT), 2011 Technical Symposium at ITU*, 2011, pp. 205-210.

[20] E. Palm, F. Hedén, and A. Zanma, "Solar powered mobile telephony," in *ecodesign*, 2001, p. 219.

[21] R. Morais, J. B. Cunha, M. Cordeiro, C. Serodio, P. Salgado, and C. Couto, "Solar data acquisition wireless network for agricultural applications," in *Electrical and Electronics Engineers in Israel, 1996., Nineteenth Convention of*, 1996, pp. 527-530.

[22] D. A. Baker, "Telemetry power system," ed: Google Patents, 2007.

[23] A. P. Glynn, "Solar powered mobile phone," ed: Google Patents, 2015.

[24] C. Alippi, R. Camplani, C. Galperti, and M. Roveri, "A robust, adaptive, solar-powered WSN framework for aquatic environmental monitoring," *IEEE Sensors Journal*, vol. 11, pp. 45-55, 2011.

[25] B. A. Becker, "Combining Antennas and Solar Cells for Greater Efficiency," in *Aerospace, Antennas, Design, Europe, News*, ed, 4 Dec 2013.

[26] http://www.groundcontrol.com. (2002-2018). *Satellite_Scada_Telemetry.html*. Available: http://www.groundcontrol.com/Satellite_Scada_Telemetry.htm

[27] Available: https://www.indiamart.com/proddetail/automatic-weather-station-4865666091.html

[28] S. Silver, *Microwave antenna theory and design*: Iet, 1949.

[29] C. Balanis, "Antenna Theory Analysis and Design 3rd edition, A John Wiley & Sons," *Inc., Publication,* 2005.

[30] C. A. Balanis, "Antenna theory: A review," *Proceedings of the IEEE,* vol. 80, pp. 7-23, 1992.

[31] R. E. Collin and F. J. Zucker, "Antenna theory," 1969.

[32] K. M. Parvez, S. Sinha, and S. M. Haque, "Miniaturization of Slot Antenna Using Meander Slits," in *2018 IEEE 88th Vehicular Technology Conference (VTC-Fall)*, 2018, pp. 1-5.

[33] A. B. Constantine, "Antenna theory analysis and design," *MICROSTRIP ANTENNAS, third edition, John wiley & sons,* 2005.

[34] A. Firdausi, G. P. N. Hakim, and M. Alaydrus, "Microstrip Antenna Array for Next Generation WLAN 802.11 ac Applications," in *2018 International Conference on Radar, Antenna, Microwave, Electronics, and Telecommunications (ICRAMET)*, 2019, pp. 86-89.

[35] S. Drabowitch and C. Ancona, "Antennas. Volume 2-Applications," *Paris, Masson, Editeur, 1978. 246 p. In French,* 1978.

[36] J. R. James and P. S. Hall, "Handbook of microstrip antennas. Volumes 1 & 2," *NASA STI/Recon Technical Report A,* vol. 90, p. 46005, 1989.

[37] D. M. Pozar, "Microstrip antennas," *Proceedings of the IEEE,* vol. 80, pp. 79-91, 1992.

[38] C. Balanis, "Fundamental Parameters and Definitions for Antennas," *Modern Antenna Handbook,* vol. 17, p. 1, 2008.

[39] J. D. Kraus and R. J. Marhefka, "Antennas for all applications 3rd ed," ed: McGraw-Hill, New York, 2001.

[40] T. C. Edwards and M. B. Steer, *Foundations for microstrip circuit design*: John Wiley & Sons, 2016.

[41] S. W. Ellingson, *Radio Systems Engineering*: Cambridge University Press, 2016.

[42] R. Yadava, *Antenna and wave propagation*: PHI Learning Pvt. Ltd., 2011.

[43] E. Lee, P. Hall, and P. Gardner, "Compact dual-band dual-polarisation microstrip patch antenna," *Electronics Letters,* vol. 35, pp. 1034-1036, 1999.

[44] C.-H. Tsao, Y. Hwang, F. J. Kilburg, and F. J. Dietrich, "Planar dual polarization antenna," ed: Google Patents, 1990.

[45] Z. Zhang, T. Zhang, C. Guo, X. Hou, and Z. Yan, "S-band dual circularly polarized microstrip patch antenna array for satellite communication," in *2017 Sixth Asia-Pacific Conference on Antennas and Propagation (APCAP)*, 2017, pp. 1-3.

[46] K. Carver and J. Mink, "Microstrip antenna technology," *IEEE transactions on antennas and propagation,* vol. 29, pp. 2-24, 1981.

[47] D. M. Pozar, *Microwave engineering*: John Wiley & Sons, 2009.

[48] R. Munson, "Conformal microstrip antennas and microstrip phased arrays," *IEEE Transactions on Antennas and propagation,* vol. 22, pp. 74-78, 1974.

[49] J. R. James, P. S. Hall, and C. Wood, *Microstrip antenna: Theory and design*: Iet, 1981.

[50] R. E. Collin, "Foundations for microwave engineering," 1992.

[51] R. Collier and P. White, "Surface waves in microstrip circuits," in *Microwave Conference, 1976. 6th European*, 1976, pp. 632-636.

[52] K. Carver, "A modal expansion theory for the microstrip antenna," in *Antennas and Propagation Society International Symposium, 1979*, 1979, pp. 101-104.

[53] R. W. Dearnley and A. R. Barel, "A comparison of models to determine the resonant frequencies of a rectangular microstrip antenna," *IEEE Transactions on Antennas and Propagation,* vol. 37, pp. 114-118, 1989.

[54] A. Benalla and K. C. Gupta, "Multiport network model and transmission characteristics of two-port rectangular microstrip patch antennas," *IEEE transactions on antennas and propagation,* vol. 36, pp. 1337-1342, 1988.

[55] S. Rajebi, C. Ghobadi, and J. Nooriniya, "Multiport network method and using it for accurate design of square spiral antennas," in *Proceedings of the 5th WSEAS International Conference on Software Engineering, Parallel and Distributed Systems*, 2006, pp. 180-186.

[56] E. Abaei, E. Mehrshahi, G. Amendola, E. Arnieri, and A. Shamsafar, "Two dimensional multi-port method for analysis of propagation characteristics of substrate integrated waveguide," *Progress In Electromagnetics Research,* vol. 29, pp. 261-273, 2012.

[57] J.-C. Koo, J. Shim, T.-I. Suh, J.-K. Bang, and H.-T. Kim, "Size optimization of a microstrip GPS antenna for automobile glass with a genetic algorithm," *Journal of electromagnetic waves and applications,* vol. 18, pp. 1459-1470, 2004.

[58] S. Behera and K. Vinoy, "Multi-port network approach for the analysis of dual band fractal microstrip antennas," *IEEE Transactions on Antennas and Propagation,* vol. 60, pp. 5100-5106, 2012.

[59] S. Behera and K. Vinoy, "Multi-port network modeling for fractal shape microstrip antenna," 2011.

[60] D. F. Hunter and K. Gupta, "Multiport network modeling of electro magnetically coupled microstrip patches," in *Antenna Technology and Applied Electromagnetics, 1990. ANTEM 1990. Symposium on*, 1990, pp. 32-37.

[61] T. Okoshi and T. Miyoshi, "The Planar Circuit--An Approach to Microwave Integrated Circuitry," *IEEE Transactions on Microwave Theory and Techniques,* vol. 20, pp. 245-252, 1972.

[62] T. Okoshi, *Planar circuits for microwaves and lightwaves* vol. 18: Springer Science & Business Media, 2012.

[63] W. J. Parnell, "Greens functions, integral equations and applications," ed: MATH, 2013.

[64] G. Arfken, H. Weber, and F. Harris, "Mathematical Methods for Physicists: A Comprehensive Guide (New York: Academic)," 2011.

[65] A. Holub and M. Polivka, "Multiport network modeling of a complex canonically shaped patch antenna," 2007.

[66] S. F. Ooi, S. Lee, A. Sambell, E. Korolkiewicz, and S. Scott, "A new and explicit matrix input impedance formula for the H - shaped microstrip patch antenna," *Microwave and Optical Technology Letters,* vol. 49, pp. 1756-1759, 2007.

[67] D. M. Pozar and D. H. Schaubert, *Microstrip antennas: the analysis and design of microstrip antennas and arrays*: John Wiley & Sons, 1995.

[68] P. Dreyer, M. Morales-Masis, S. Nicolay, C. Ballif, and J. Perruisseau-Carrier, "Copper and Transparent-Conductor Reflectarray Elements on Thin-Film Solar Cell Panels," *Antennas and Propagation, IEEE Transactions on,* vol. 62, pp. 3813-3818, 2014.

[69] C. Bendel, J. Kirchhof, and N. Henze, "Application of photovoltaic solar cells in planar antenna structures," in *Photovoltaic Energy Conversion, 2003. Proceedings of 3rd World Conference on*, 2003, pp. 220-223.

[70] S. Vaccaro, P. Torres, J. Mosig, A. Shah, J.-F. Zürcher, A. Skrivervik, *et al.*, "Integrated solar panel antennas," *Electronics Letters,* vol. 36, pp. 390-391, 2000.

[71] M. J. R. Ons, "Integration of Antennas and Solar Cells for Autonomous Communication Systems," 2010.

[72] M. N. Mahmoud, "Integrated solar panel antennas for cube satellites," 2010.

[73] M. Tanaka, Y. Suzuki, K. Araki, and R. Suzuki, "Microstrip antenna with solar cells for microsatellites," *Electronics Letters,* vol. 31, pp. 5-6, 1995.

[74] O. Yurduseven, "Integration of microwave antennas with solar PV for multiband and wideband mobile, WLAN and WiMAX applications," Northumbria University, 2014.

[75] T. Shahvirdi and R. Baktur, "Analysis of the effect of solar cells on the antenna integrated on top of their cover glass," in *Antennas and Propagation & USNC/URSI National Radio Science Meeting, 2015 IEEE International Symposium on*, 2015, pp. 2429-2430.

[76] S. Shynu, M. Roo Ons, M. Ammann, S. McCormack, and B. Norton, "Integration of Microstrip Patch Antennas with Polycrystalline Silicon Solar Cells," 2009.

[77] S. Shynu, M. R. Ons, M. J. Ammann, S. Gallagher, and B. Norton, "Inset-fed microstrip patch antenna with integrated polycrystalline photovoltaic solar cell," 2007.

[78] T. Yekan and R. Baktur, "An experimental study on the effect of commercial triple junction solar cells on patch antennas integrated on their cover glass," *Progress In Electromagnetics Research,* vol. 63, pp. 131-142, 2016.

[79] M. R. Ons, "Investigation on Proximity-coupled Microstrip Integrated PV Antenna," Dublin Institute of Technology, 2007.

[80] S. Shynu, M. J. R. Ons, M. J. Ammann, S. McCormack, and B. Norton, "A metal plate solar antenna for UMTS pico-cell base station," in *Antennas and Propagation Conference, 2008. LAPC 2008. Loughborough*, 2008, pp. 373-376.

[81] M. Roo-Ons, S. Shynu, M. Seredynski, M. Ammann, S. McCormack, and B. Norton, "Influence of solar heating on the performance of integrated solar cell microstrip patch antennas," *Solar Energy,* vol. 84, pp. 1619-1627, 2010.

[82] S. Shynu, M. J. R. Ons, G. Ruvio, M. J. Ammann, S. McCormack, and B. Norton, "A microstrip printed dipole solar antenna using polycrystalline silicon solar cells," in *Antennas and Propagation Society International Symposium, 2008. AP-S 2008. IEEE*, 2008, pp. 1-4.

[83] S. Shynu, M. Ammann, and B. Norton, "Quarter-wave metal plate solar antenna," *Electronics Letters,* vol. 44, pp. 570-571, 2008.

[84] T. W. Turpin and R. Baktur, "Meshed Patch Antennas Integrated on Solar Cells," *Antennas and Wireless Propagation Letters, IEEE,* vol. 8, pp. 693-696, 2009.

[85] O. Yurduseven, D. Smith, N. Pearsall, and I. Forbes, "A transparent solar patch antenna for 2.4/2.5 GHz WLAN-WiMAX applications," in *Environment Friendly Energies and Applications (EFEA), 2012 2nd International Symposium on*, 2012, pp. 614-617.

[86] O. Yurduseven, D. Smith, N. Pearsall, I. Forbes, and D. Johnston, "A meshed multiband solar patch array antenna," in *Antennas and Propagation Conference (LAPC), 2012 Loughborough*, 2012, pp. 1-5.

[87] O. Yurduseven, D. Smith, and M. Elsdon, "A transparent meshed solar monopole antenna for UWB applications," in *Antennas and Propagation (EuCAP), 2014 8th European Conference on*, 2014, pp. 2145-2149.

[88] M. Roo-Ons, S. Shynu, M. Ammann, S. McCormack, and B. Norton, "Transparent patch antenna on a-Si thin-film glass solar module," *Electronics letters,* vol. 47, pp. 85-86, 2011.

[89] T. Yasin, "Optically Transparent Multifunctional Patch Antennas Integrated with Solar Cells for Small Satellites," 2011.

[90] A. S. Kumar and S. Sundaravadivelu, "Design of solar cell antenna (SOLAN) in different AgHT-8 patch shape for reflection co-efficient, gain, power and directivity compared with existing AgHT-4 and ITO."

[91] U. Pushpa and S. Chopde, "An insight on transparent antennas," *International Journal of Modern Engineering Research,* vol. 4, pp. 35-41, 2014.

[92] N. M. Ali, N. Misran, M. Mansor, and M. Jamlos, "Transparent solar antenna of 28 GHz using transparent conductive oxides (TCO) thin film," in *Journal of Physics: Conference Series*, 2017, p. 012036.

[93] A. Rashidian, L. Shafai, and C. Shafai, "Miniaturized Transparent Metallodielectric Resonator Antennas Integrated With Amorphous Silicon Solar Cells," *IEEE Transactions on Antennas and Propagation*, vol. 65, pp. 2265-2275, 2017.

[94] S. Vaccaro, J. Mosig, and P. De Maagt, "Making planar antennas out of solar cells," *Electronics Letters*, vol. 38, pp. 945-947, 2002.

[95] C. Baccouch, D. Bouchouicha, H. Sakli, and T. Aguili, "Patch Antenna based on a Photovoltaic Cell with a Dual resonance Frequency," *Advanced Electromagnetics*, vol. 5, pp. 42-49, 2016.

[96] O. Yurduseven, D. Smith, N. Pearsall, and I. Forbes, "A triband short-circuited suspended solar patch antenna," in *Antennas, Propagation & EM Theory (ISAPE), 2012 10th International Symposium on*, 2012, pp. 294-297.

[97] C. Baccouch, H. Sakli, D. Bouchouicha, M. Latrach, and T. Aguili, "Patch Antenna based on a photovoltaic cell."

[98] O. Yurduseven, D. Smith, N. Pearsall, and I. Forbes, "Design of a highly efficient wideband suspended solar array antenna," in *Antennas and Propagation Society International Symposium (APSURSI), 2012 IEEE*, 2012, pp. 1-2.

[99] O. Yurduseven and D. Smith, "A solar cell stacked multi-slot quad-band PIFA for GSM, WLAN and WiMAX networks," *IEEE Microwave and Wireless Components Letters*, vol. 23, pp. 285-287, 2013.

[100] O. Yurduseven, D. Smith, N. Pearsall, and I. Forbes, "A Solar Cell Stacked Slot-Loaded Suspended Microstrip Patch Antenna with Multiband Resonance Characteristics for WLAN and WiMax Systems," *Progress In Electromagnetics Research*, vol. 142, pp. 321-332, 2013.

[101] O. Yurduseven, D. Smith, and N. Pearsall, "Solar cell stacked modified Z-double L-slot quad-band PIFA," in *Antennas and Propagation (EuCAP), 2013 7th European Conference on*, 2013, pp. 3721-3725.

[102] M. Elsdon, O. Yurduseven, and X. Dai, "Wideband metamaterial solar cell antenna for 5 GHZ Wi-Fi communication," *Progress In Electromagnetics Research C,* vol. 71, pp. 123-131, 2017.

[103] T. C. Pu, H. H. Lin, C. Y. Wu, and J. H. Chen, "Photovoltaic panel as metamaterial antenna radome for dual - band application," *Microwave and Optical Technology Letters*, vol. 53, pp. 2382-2388, 2011.

[104] C.-Y. Wu, H.-H. Lin, T.-C. Pu, and J.-H. Chen, "High gain dual-band antenna using photovoltaic panel as metamaterial superstrate," in *Antennas and Propagation (APSURSI), 2011 IEEE International Symposium on*, 2011, pp. 2235-2238.

[105] H.-H. Lin, T.-C. Pu, C.-Y. Wu, and J.-H. Chen, "Photovoltaic panel with reactance elements for dual-band antenna radome."

[106] O. Yurduseven, D. Smith, and M. Elsdon, "A dual-polarized solar cell stacked microstrip patch antenna with a λ/4 DC/RF isolation circuit for 5.8 GHz band WiMAX networks," in *Antennas and Propagation (EuCAP), 2014 8th European Conference on*, 2014, pp. 1382-1385.

[107] T. R. Jones, J. P. Grey, and M. Daneshmand, "Solar Panel Integrated Circular Polarized Aperture-Coupled Patch Antenna for CubeSat Applications," *IEEE Antennas and Wireless Propagation Letters,* vol. 17, pp. 1895-1899, 2018.

[108] W.-Y. Li, C.-Y. Wu, W.-J. Chen, and H.-H. Lin, "Internal LTE/WWAN handset antenna integrated with solar cells for performance improvement," in *Antennas and Propagation Society International Symposium (APSURSI), 2012 IEEE*, 2012, pp. 1-2.

[109] A. Collado and A. Georgiadis, "Conformal hybrid solar and electromagnetic (EM) energy harvesting rectenna," *IEEE Transactions on Circuits and Systems I: Regular Papers*, vol. 60, pp. 2225-2234, 2013.

[110] T. Wu, R. Li, and M. M. Tentzeris, "A scalable solar antenna for autonomous integrated wireless sensor nodes," *IEEE Antennas and Wireless Propagation Letters*, vol. 10, pp. 510-513, 2011.

[111] F. Giuppi, A. Georgiadis, S. Via, A. Collado, R. Vyas, M. M. Tentzeris, *et al.*, "A 927 MHz solar powered active antenna oscillator beacon signal generator," in *Wireless Sensors and Sensor Networks (WiSNet), 2012 IEEE Topical Conference on*, 2012, pp. 1-4.

[112] S. X. Ta, J. J. Lee, and I. Park, "Solar-Cell Metasurface-Integrated Circularly Polarized Antenna With 100% Insolation," *IEEE Antennas and Wireless Propagation Letters,* vol. 16, pp. 2675-2678, 2017.

[113] S. X. Ta and I. Park, "A circularly polarized antenna integrated with metasurface solar cells," in *Antennas and Propagation in Wireless Communications (APWC), 2017 IEEE-APS Topical Conference on*, 2017, pp. 120-122.

[114] C. Bendel, J. Kirchhof, and N. Henze, "Solar cell antennas in wireless communication and radio broadcast systems," in *Proceedings of the 19th European Photovoltaic Solar Energy Conference and Exhibition, Paris, France*, 2004.

[115] M. Danesh and J. R. Long, "Compact solar cell ultra-wideband dipole antenna," in *Antennas and Propagation Society International Symposium (APSURSI), 2010 IEEE*, 2010, pp. 1-4.

[116] A. Budianu, A. Meijerink, M. J. Bentum, J. M. Klein, and S. Engelen, "Integrated downlink antennas in the deployable solar panels of a cubesat," in *Aerospace Conference, 2014 IEEE*, 2014, pp. 1-11.

[117] F. Declercq, A. Georgiadis, and H. Rogier, "Wearable aperture-coupled shorted solar patch antenna for remote tracking and monitoring applications," in *Antennas and Propagation (EUCAP), Proceedings of the 5th European Conference on*, 2011, pp. 2992-2996.

[118] S. Lemey, F. Declercq, and H. Rogier, "Dual-band substrate integrated waveguide textile antenna with integrated solar harvester," *IEEE Antennas and wireless propagation letters,* vol. 13, pp. 269-272, 2014.

[119] S. Vaccaro, P. Torres, J. Mosig, A. Shah, A. Skrivervik, J. F. Zürcher, *et al.*, "Combination of antennas and solar cells for satellite communications," *microwave and optical technology letters,* vol. 29, pp. 11-16, 2001.

[120] S. Shynu, M. J. R. Ons, M. J. Ammann, S. McCormack, and B. Norton, "Dual band a-Si: H solar-slot antenna for 2.4/5.2 GHz WLAN applications," in *Antennas and Propagation, 2009. EuCAP 2009. 3rd European Conference on*, 2009, pp. 408-410.

[121] T. Shahvirdi and R. Baktur, "Integrated after-market solar panel antennas with multi-diversity," in *Radio Science Meeting (Joint with AP-S Symposium), 2013 USNC-URSI*, 2013, pp. 111-111.

[122] M. Maharaja and C. Kalaiselvan, "Integration of Antennas and Solar Cells for Satellite and Terrestrial Communication," *International Journal of Scientific and Research Publications,* vol. 3, 2013.

[123] S. Vaccaro, J. R. Mosig, and P. de Maagt, "Two advanced solar antenna" SOLANT" designs for satellite and terrestrial communications," *IEEE Transactions on Antennas and Propagation,* vol. 51, pp. 2028-2034, 2003.

[124] S. Vaccaro, P. Torres, J. Mosig, A. Shah, J.-F. Zurcher, A. Skrivervik, *et al.*, "Stainless steel slot antenna with integrated solar cells," *Electronics Letters,* vol. 36, pp. 2059-2060, 2000.

[125] J. Huang, "Mars rover antenna for solar-array integration," *Telecommun. Mission Oper. Prog. Rep,* vol. 42, p. 136, 1998.

[126] J. Huang and M. Zawadzki, "Antennas integrated with solar arrays for space vehicle applications," in *Antennas, Propagation and EM Theory, 2000. Proceedings. ISAPE 2000. 5th International Symposium on*, 2000, pp. 86-89.

[127] M. Zou, J. Pan, and Z. Shen, "Frequency-reconfigurable water antenna integrated with solar cell," in *Microwave and Millimeter Wave Technology (ICMMT), 2016 IEEE International Conference on*, 2016, pp. 858-860.

[128] D. D. Bohra and P. Varshney, "Solar Cell Integration in Cubesat: A New Era in SatCom."

[129] O. Fawole and R. Baktur, "Multifunction solar panel antenna for cube satellites," in *Antennas and Propagation Society International Symposium (APSURSI), 2012 IEEE,* 2012, pp. 1-2.

[130] R. Caso, A. D'Alessandro, A. Michel, and P. Nepa, "Integration of Slot Antennas in Commercial Photovoltaic Panels for Stand-Alone Communication Systems," *Antennas and Propagation, IEEE Transactions on,* vol. 61, pp. 62-69, 2013.

[131] S. X. Ta and I. Park, "A Circularly Polarized Antenna Integrated with a Solar Cell Metasurface for CubeSat," in *2018 Asia-Pacific Microwave Conference (APMC)*, 2018, pp. 696-698.

[132] T. Yekan and R. Baktur, "Conformal Integrated Solar Panel Antennas: Two effective integration methods of antennas with solar cells," *IEEE Antennas and Propagation Magazine,* vol. 59, pp. 69-78, 2017.

[133] W. Alomar, J. Degnan, S. Mancewicz, M. Sidley, J. Cutler, and B. Gilchrist, "An extendable solar array integrated Yagi-Uda UHF antenna for CubeSat platforms," in *Antennas and Propagation (APSURSI), 2011 IEEE International Symposium on*, 2011, pp. 3022-3024.

[134] O. Yurduseven, D. Smith, N. Pearsall, I. Forbes, and F. Bobor-Oyibo, "A solar parabolic reflector antenna design for digital satellite communication systems," in *Communication Systems, Networks & Digital Signal Processing (CSNDSP), 2012 8th International Symposium on*, 2012, pp. 1-3.

[135] M. Zawadzki and J. Huang, "Integrated RF antenna and solar array for spacecraft application," in *Phased Array Systems and Technology, 2000. Proceedings. 2000 IEEE International Conference on*, 2000, pp. 239-242.

[136] E. Lim, K. Leung, C. Su, and H. Wong, "Green antenna for solar energy collection," *IEEE Antennas and Wireless Propagation Letters,* vol. 9, pp. 689-692, 2010.

[137] C. Kocia and S. V. Hum, "Design of an optically transparent reflectarray for solar applications using indium tin oxide," *IEEE Transactions on Antennas and Propagation,* vol. 64, pp. 2884-2893, 2016.

[138] P. Dreyer, M. Morales-Masis, S. Nicolay, C. Ballif, and J. Perruisseau-Carrier, "Copper and transparent-conductor reflectarray elements on thin-film solar cell panels," *IEEE Transactions on Antennas and Propagation,* vol. 62, pp. 3813-3818, 2014.

[139] P. Dreyer, J. S. G. Diaz, and J. Perruisseau-Carrier, "Design of a reflectarray element integrated in a solar cell panel," in *Antennas and Propagation Society International Symposium (APSURSI), 2013 IEEE*, 2013, pp. 1558-1559.

[140] N. A. Al-Shalaby and S. M. Gaber, "Parametric study on effect of solar-cell position on the performance of transparent DRA transmitarray," *AEU-International Journal of Electronics and Communications,* vol. 70, pp. 436-441, 2016.

[141] M. A. Moharram and A. A. Kishk, "A Ka Band Optically Transparent Reflectarray Design Integrated with Solar Cells," in *Ubiquitous Wireless Broadband (ICUWB), 2015 IEEE International Conference on*, 2015, pp. 1-4.

[142] M. A. Moharram and A. A. Kishk, "Optically Transparent Reflectarray Antenna Design Integrated With Solar Cells," *IEEE Transactions on Antennas and Propagation,* vol. 64, pp. 1700-1712, 2016.

[143] W. An, L. Xiong, S. Xu, F. Yang, H.-P. Fu, and J.-G. Ma, "A Ka-Band High-Efficiency Transparent Reflectarray Antenna Integrated With Solar Cells," *IEEE Access,* vol. 6, pp. 60843-60851, 2018.

[144] Y. Liu, H. Wang, G. Liu, and X. Dong, "Design of a transparent reflectarray integrated with solar cells using quad-key element," in *2017 Sixth Asia-Pacific Conference on Antennas and Propagation (APCAP)*, 2017, pp. 1-3.

[145] P. Hersch and K. Zweibel, "Basic photovoltaic principles and methods," Solar Energy Research Inst., Golden, CO (USA)1982.

[146] H. Häberlin, *Photovoltaics: system design and practice*: John Wiley & Sons, 2012.

[147] P. J. Reddy, *Science technology of photovoltaics*: BS publications, 2010.

[148] A. Luque and S. Hegedus, *Handbook of photovoltaic science and engineering*: John Wiley & Sons, 2011.

[149] I. Fusegawa and M. Sato, "Single-crystal silicon wafer," ed: Google Patents, 2002.

[150] J. Nelson, *The physics of solar cells*: World Scientific Publishing Company, 2003.

[151] A. Fahrenbruch and R. Bube, *Fundamentals of solar cells: photovoltaic solar energy conversion*: Elsevier, 2012.

[152] M. A. Green, Y. Hishikawa, E. D. Dunlop, D. H. Levi, J. Hohl - Ebinger, and A. W. Ho - Baillie, "Solar cell efficiency tables (version 52)," *Progress in Photovoltaics: Research and Applications,* vol. 26, pp. 427-436, 2018.

[153] A. Ingle, D. Sangotra, R. Chadge, and P. Thorat, "Module configurations in photovoltaic system: A review," *Materials Today: Proceedings,* vol. 4, pp. 12625-12629, 2017.

[154] W.-S. Chen, "Single-feed dual-frequency rectangular microstrip antenna with square slot," *Electronics Letters,* vol. 34, pp. 231-232, 1998.

[155] S. Maci, G. B. Gentili, P. Piazzesi, and C. Salvador, "Dual-band slot-loaded patch antenna," *IEE Proceedings-Microwaves, Antennas and Propagation,* vol. 142, pp. 225-232, 1995.

[156] W.-S. Chen, C.-K. Wu, and K.-L. Wong, "Single-feed square-ring microstrip antenna with truncated corners for compact circular polarisation operation," *Electronics Letters,* vol. 34, pp. 1045-1047, 1998.

[157] V. Palanisamy and R. Garg, "Analysis of arbitrarily shaped microstrip patch antennas using segmentation technique and cavity model," *IEEE Transactions on Antennas and Propagation,* vol. 34, pp. 1208-1213, 1986.

[158] A. Benalla and K. Gupta, "Faster computation of Z-matrices for rectangular segments in planar microstrip circuits (short paper)," *IEEE Transactions on Microwave Theory and Techniques,* vol. 34, pp. 733-736, 1986.

[159] R. Sorrentino, "Planar circuits, waveguide models, and segmentation method," *IEEE Transactions on Microwave Theory and Techniques,* vol. 33, pp. 1057-1066, 1985.

[160] R. Chadha and K. Gupta, "Segmentation method using impedance matrices for analysis of planar microwave circuits," *IEEE Transactions on Microwave Theory and Techniques,* vol. 29, pp. 71-74, 1981.

[161] T. Okoshi and T. Takeuchi, "Analysis of planar circuits by segmentation method," *Electronics Communications of Japan,* vol. 58, pp. 71-79, 1975.

[162] P. Sharma and K. Gupta, "An alternative procedure for implementing the desegmentation method," *IEEE transactions on microwave theory and techniques,* vol. 32, pp. 1-4, 1984.

[163] P. Sharma and K. Gupta, "Desegmentation method for analysis of two-dimensional microwave circuits," *IEEE Transactions on Microwave Theory and Techniques,* vol. 29, pp. 1094-1098, 1981.

[164] E. Abaei and E. Mehrshahi, "Efficient desegmentation technique for analysis of planar circuits," in *Microwave Conference (GeMIC), 2011 German*, 2011, pp. 1-4.

[165] E. Abaei, E. Mehrshahi, and H. Sadreazami, "Modified desegmentation technique in analysis of arbitrary shaped planar circuit," in *Applied Electromagnetics (APACE), 2010 IEEE Asia-Pacific Conference on*, 2010, pp. 1-4.

[166] A. Thakur, M. Chauhan, and M. Kumar, "Effect of Substrate relative dielectric constant on Bandwidth characteristics of Line feed Rectangular Patch Antenna."

[167] M. R. Hasan and A. Al Suman, "Substrate height and dielectric constant dependent performance of circular micro strip patch array antennas for broadband wireless access," *J. Emerg. Trends Comput. Inf. Sci.,* vol. 3, pp. 1392-1397, 2012.

[168] K. L. Kaiser, *Electromagnetic shielding*: Crc Press, 2005.

[169] C.-K. Wu, K.-L. Wong, and W. S. Chen, "Slot-coupled meandered microstrip antenna for compact dual-frequency operation," *Electronics letters*, vol. 34, pp. 1047-1047, 1998.

[170] M. Ali, N. Nordin, N. Ya'acob, and M. M. Tan, "Design of wideband microstrip patch antenna using L-probe fed at 2.6 GHz," in *Computer and Communication Engineering (ICCCE), 2012 International Conference on*, 2012, pp. 961-965.

[171] H. Griguer, E. Marzolf, H. Lalj, F. Riouch, and M. H. Drissi, "Patch antenna bandwidth enhancement through the use of metamaterials," in *Telecommunications, 2009. ICT'09. International Conference on*, 2009, pp. 323-327.

[172] M. Rani, S. Rahim, A. Tharek, T. Peter, and S. Cheung, "Dual-band transparent antenna for ISM band applications," *PIERS Proceedings, T aipei*, 2013.

[173] N. Wang, H. Tian, Z. Guo, D. Yang, J. Zhou, and Y. Ji, "Bandwidth and gain enhancement of optically transparent 60-GHz CPW-fed antenna by using BSIS-UC-EBG structure," *Photonics and Nanostructures-Fundamentals and Applications*, vol. 15, pp. 99-108, 2015.

[174] M. Stanley, Y. Huang, H. Wang, H. Zhou, A. Alieldin, and S. Joseph, "A Transparent Dual-Polarized Antenna Array for 5G Smartphone Applications."

[175] A. Desai and T. Upadhyaya, "Transparent dual band antenna with μ - negative material loading for smart devices," *Microwave and Optical Technology Letters*, 2018.

[176] A. Desai, T. Upadhyaya, and M. Palandoken, "Dual band slotted transparent resonator for wireless local area network applications," *Microwave and Optical Technology Letters*, 2018.

[177] A. Genc, T. Turpin, T. Yasin, and R. Baktur, "Active integrated meshed patch antennas for small satellites," *Microwave and Optical Technology Letters*, vol. 54, pp. 1593-1595, 2012.

[178] J.-J. Xie, Y.-Z. Yin, J. Ren, and T. Wang, "A wideband dual-polarized patch antenna with electric probe and magnetic loop feeds," *Progress In Electromagnetics Research*, vol. 132, pp. 499-515, 2012.

[179] N. Misran, M. T. Islam, L. L. San, and R. Azim, "Dual-polarized patch antenna for wireless communication," in *Electrical Engineering and Informatics, 2009. ICEEI'09. International Conference on*, 2009, pp. 703-706.

[180] J.-J. Xie, X.-S. Ren, Y.-Z. Yin, and J. Ren, "Dual-polarised patch antenna with wide bandwidth using electromagnetic feeds," *Electronics letters*, vol. 48, pp. 1385-1386, 2012.

[181] S. O. Kundukulam, M. Paulson, C. Aanandan, and P. Mohanan, "Dual - port dual - polarized microstrip antenna," *Microwave and Optical Technology Letters*, vol. 34, pp. 459-460, 2002.

[182] M. Paulson, S. O. Kundukulam, C. Aanandan, and P. Mohanan, "Analysis and design of a dual - port compact microstrip antenna," *Microwave and Optical Technology Letters*, vol. 32, pp. 125-127, 2002.

[183] H. Saeidi - Manesh, S. Karimkashi, G. Zhang, and R. J. Doviak, "High - Isolation Low Cross - Polarization Phased - Array Antenna for MPAR Application," *Radio Science*, vol. 52, pp. 1544-1557, 2017.

[184] M. T. Ali, T. A. Rahman, M. R. Kamarudin, M. N. Md Tan, and R. Sauleau, "A planar antenna array with separated feed line for higher gain and sidelobe reduction," *Progress In Electromagnetics Research*, vol. 8, pp. 69-82, 2009.

[185] S. Gao and S. Zhong, "Dual - polarized microstrip antenna array with high isolation fed by coplanar network," *Microwave and optical technology letters*, vol. 19, pp. 214-216, 1998.

[186] R. Gardelli, G. La Cono, and M. Albani, "A low-cost suspended patch antenna for WLAN access points and point-to-point links," *IEEE Antennas and Wireless Propagation Letters*, vol. 3, pp. 90-93, 2004.

[187] Y. M. Madany, D. A. Mohamed, and M. H. Elbanna, "Design and Analysis of 2× 2 Smart Distributed Subarray Microstrip Antenna System for Communication and Radar Applications," in *European Wireless 2014; 20th European Wireless Conference; Proceedings of*, 2014, pp. 1-6.

List of Publications

The research papers and journal have been published or accepted:

- **journal**
  - F. Nashad, Foti S, David Smith, Elsdon M, Okan Yurduseven[2] "Ku-band suspended meshed patch antennae integrated with solar cells for remote area applications" Progress in Electromagnetics Research (PIERC), Vol. 83, page 245-254, 2018.

- **Conferences**
  - Nashad F, Foti S, Smith D, Elsdon M, Yurduseven O. "Development of transparent patch antennae element integrated with solar cells for Ku-band satellite applications". *In Antennae & Propagation Conference (LAPC), 2016 Loughborough 2016 Nov 14 (pp. 1-5). IEEE.*
  - Nashad F, Foti S, Smith D, Elsdon M. "Compact dual-band transparent patch antennae integrated with solar cells for Ku-band Satcom". *In EE PGR Conference 2017 Northumbria, 15th June in City Campus East Building.*
  - Nashad F, Foti S, Smith D, Elsdon M, Yurduseven[2] O. "Transparency improvement of Ku-band transparent patch antennae integrated with solar cells for Ku-band satellite applications". *The International Conference on Antennae Measurement and Applications – 2018 CAMA- in Västerås, Sweden, from 03 to 06 September 2018.*
  - Ahmed Al-Karakchi, Farhat Nashad, Ghanim Putrus, Foti S, Smith D, Elsdon M " Cost-effective Integration System of Solar Cell Powered Remote Small-size Wireless Communications". *2nd International Conference on Electrical, Communication, Computer, Power and Control Engineering ICECCPCE19, 13-14 February, 2019 | Mosul, Iraq.*

APPENDIX 3A

Calculations for Q factor of Patch: (by Mathcad).

For chapter 3, Mutli-port Network and Segmentation

$fr := 3\cdot10^{9}$ $\mu o := 4\pi\cdot10^{-7}$ $\varepsilon r := 2.33$ $\varepsilon o := 8.854\cdot10^{-12}$ $c := 3\cdot10^{8}$ $\sigma(xx) := (2 - \delta(0,xx))$

$h := 1.57\cdot10^{-3}$ $\sigma c := 5.95\cdot10^{7}$ $t := 35\cdot(10)^{-6}$ $\lambda o := \frac{c}{fr}$ $\lambda o = 0.1$

$\tan\delta := 0.0012$ $f := 2.8\cdot10^{9}, 2.801\cdot10^{9} .. 3.3\cdot10^{9}$ $ko := \frac{2\pi}{\lambda o}$ $ko = 62.832$

$$\varepsilon reff := \frac{\varepsilon r + 1}{2} + \frac{\varepsilon r - 1}{2}\cdot\left(1 + 12\cdot\frac{t}{W}\right)^{\frac{-1}{2}} \qquad \varepsilon reff = 2.325$$

$$\Delta L := h\cdot(0.412)\cdot\frac{(\varepsilon reff + 0.3)\cdot\left(\frac{W}{h} + 0.264\right)}{(\varepsilon reff - 0.258)\cdot\left(\frac{W}{h} + 0.8\right)}$$

$\Delta L = 7.993\times10^{-4}$

$Leff := L + 2\cdot\Delta L$ $\qquad Leff = 31.599\times10^{-3}$

We the effective conductor width

$$We := W + \frac{t}{\pi}\cdot\left(1 + \ln\left(\frac{2h}{t}\right)\right) \qquad We = 30.061\times10^{-3}$$

The characterstic impedance of the transmission line Zo:

$$Zo := \frac{\frac{120\cdot\pi}{\sqrt{\varepsilon reff}}}{\frac{We}{h} + 1.39 + 0.666\cdot\ln\left(\frac{We}{h} + 1.444\right)} \qquad Zo = 10.962$$

- **To find the conductance G1** :

$$Prad := \frac{|V^2|}{2\cdot\pi\cdot(\mu o)}\cdot\left[\int_0^{\pi}\left[\frac{\sin\left(\left(\frac{ko\cdot We}{2}\cdot\cos(\theta)\right)\right)}{\cos(\theta)}\right]^2\cdot\sin(\theta)^3\,d\theta\right]$$

$$I := \int_0^{\pi}\left[\frac{\sin\left(\left(\frac{ko\cdot We}{2}\cdot\cos(\theta)\right)\right)}{\cos(\theta)}\right]^2\cdot\left(\sin(\theta)^3\right)d\theta$$

$$G1 := \frac{I}{120\pi^2} \qquad G1 = 9.473\times10^{-4}$$

$$R1 := \frac{1}{G1} = 1.056\times10^{3}$$

- **the mutual conductance G12**

$$G12 := \frac{1}{120\cdot\pi^2}\cdot\int_0^{\pi}\left[\frac{\sin\left(\left(\frac{ko\cdot W}{2}\cdot\cos(\theta)\right)\right)}{\cos(\theta)}\right]^2\cdot\left(J0(ko\cdot L\cdot\sin(\theta))\cdot\sin(\theta)^3\right)d\theta$$

$$G12 = 3.8194\times10^{-4}$$

$$Gin := G1 + G12 = 1.329\times10^{-3} \qquad RT := \frac{1}{2Gin} = 376.149$$

Q Factor :

$$Qd := \frac{1}{\tan\delta} \qquad Qd = 833.333$$

$$Qc := h\sqrt{(\mu o)\cdot fr\cdot\sigma c} \qquad Qc = 743.573$$

$$Qr := \frac{\pi}{4(Gin\cdot Zo)} \qquad Qr = 53.899$$

$$Qt := \left(\frac{1}{Qd}+\frac{1}{Qc}+\frac{1}{Qr}\right)^{-1} \qquad Qt = 47.398$$

Q factor for a square Patch (6x6 mm) at 11.95GHz (by Mathcad)

$fr := 11.95\cdot10^{9}$ $\mu o := 4\pi\cdot10^{-7}$ $\varepsilon r := 2.59$ $\varepsilon o := 8.854\cdot10^{-12}$ $c := 3\cdot10^{8}$ $\sigma(xx) := (2-\delta(0,xx))$

$h := 1.5\cdot10^{-3}$ $\sigma c := 5.95\cdot10^{7}$ $t := 35\cdot(10)^{-6}$ $\lambda o := \frac{c}{fr}$

$\tan\delta := 0.068$ $f := 10.8\cdot10^{9}, 10.801\cdot10^{9}\ldots 15\cdot10^{9}$ $ko := \frac{2\pi}{\lambda o}$

$\lambda o = 0.025$

Q Factor:

$$Qd := \frac{1}{\tan\delta} \qquad Qd = 14.706$$

$$Qc := h\sqrt{(\mu o)\cdot fr\cdot \sigma c} \qquad Qc = 1.418\times 10^{3}$$

$$Qr := \frac{\pi}{4(Gin\cdot Zo)} \qquad Qr = 19.931$$

$$Qt := \left(\frac{1}{Qd} + \frac{1}{Qc} + 0\right)^{-1} \qquad Qt = 14.555$$

APPENDIX: 3B

Eigenvalues and Eigen functions of Square Patch

Wave equation with second order P.D.E: The wave equation with P.D.E have two characteristics: which is called the two-dimensional wave equation as follows:

$$\frac{\partial^2\phi}{\partial x^2} + \frac{\partial^2\phi}{\partial y^2} - \frac{1}{C^2}\frac{\partial^2\phi}{\partial t} \qquad \text{No sources} \qquad (3B.1)$$

Here *c* is a constant speed, if we assume that ϕ (*x*, y) (T) can be written as the product of the form *X*(*x*, *y*) *T* (*t*), in the two-dimensional scalar can be solved by the general formula of Ansatz equation:

$$\phi = \phi\ (x, y)\ T(t) \qquad (3B.2)$$

Inserting Eq. (B.2) into Eq. (B.1) leads to:

$$\frac{\partial^2\phi}{\partial x^2}(T) + \frac{\partial^2\phi}{\partial y^2}(T) = \frac{1}{C^2}\frac{\partial^2\phi}{\partial t}(T) \qquad (3B.3)$$

Divided by (ϕT), we see that:

$$\frac{1}{\phi}\left(\partial^2{}_X\phi + \partial^2{}_Y\phi\right) = \frac{\partial^2}{C^2T(t)}T(t) \qquad (3B.4)$$

Changing Eq. (B.4) to total derivative, the left hand side only depends on (*x*, y) and the right

hand side depends only on time (t). Linear operators acting as differential operators on the space (C) so, consider the derivative operator with eigenvalue equation that becomes:

$$\frac{1}{\phi}\left(\partial^2{}_X\phi+\partial^2{}_Y\phi\right)=\frac{\partial^2}{C^2T(t)}\frac{d^2T}{dt^2}=-\lambda^{-2} \tag{3B.5}$$

By re-arranging Eq. (B.5) right hand side:

$$\frac{1}{T(t)}\frac{d^2T}{dt^2}=\frac{C^2}{\lambda^2} \tag{3B.6}$$

That means the left hand side, becomes:

$$\frac{1}{\phi}\left(\partial^2{}_X\phi+\partial^2{}_Y\phi\right)=-\frac{2\pi^2}{\lambda^2} \tag{3B.7}$$

Where: k = 2π/λ and is called wave number, c =ω/k,

By returning to the partial differential equation (P.D.E) of the spatial dependence in Eq. (B.1). The two wave equation can be rewritten as follows:

$$\frac{\partial^2\phi}{\partial x^2}+\frac{\partial^2\phi}{\partial y^2}+k^2\phi=0 \tag{3B.6}$$

APPENDIX: 3C

<u>Review and derivation of Z -Parameters for Multiport Network Model.</u>

Z_{ij} with Both Ports at same points on x axis

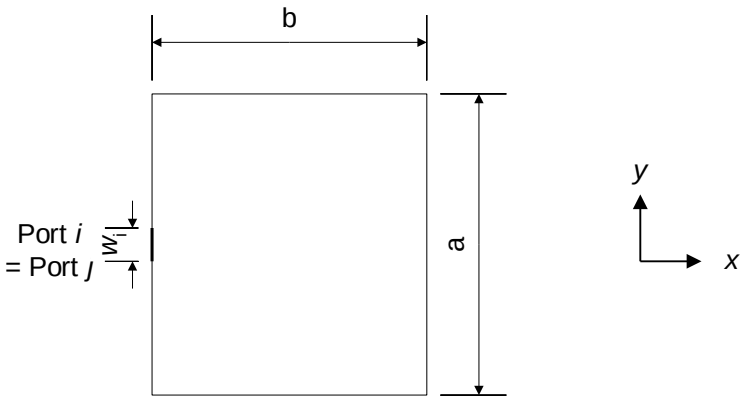

Figure B.1: port *i* and port *j* at same point on *x* axis

Considering Z_{ii}, ports *i* and *j* are located at the same point.

Two-dimensional Green's Functions in terms of Eigen function expansions

$$G(x,y;x_0,y_0)=\sum_{m=1}^{\infty}\sum_{n=1}^{\infty}A_{mn}\phi_{mn}(x,y) \tag{3C.1}$$

Substituting the Eq. (16) into Eq. (14), this gives:

$$\sum_{m=1}^{\infty}\sum_{n=1}^{\infty}A_{mn}\phi_{mn}(x,y)=-j\varpi\mu_0 h\delta(x,y-x_0,y_0) \tag{3C.2}$$

For equation (3c.2) to be orthonormalised, the left hand side must be multiplied by $\phi_{mn}*$, and thus:

$$\sum_{m=1}^{\infty}\sum_{n=1}^{\infty}A_{mn}\phi_{mn}(x,y)\phi_{mn}*(x_0,y_0)=-j\varpi\mu_0 h\delta(x,y-x_0,y_0)\phi_{mn} \tag{3C.3}$$

By taking the integration for both sides and by using the following orthonormal relationship:

$$\int_a^b\phi_Z(x)\phi_Z*(x)dz=1 \tag{3C.4}$$

Together with the delta function.

where an equation for Green's function in terms of the delta function δ, considering δ as function that has unit integral, can be written by:

$$\int_{-\infty}^{\infty}\delta(x)dx=1,\qquad \text{hence,}\qquad \int_{-\infty}^{\infty}\delta(z-z_0)dz=1, \tag{3C.5}$$

Yields the following:

$$A_{mn}(k_m{}^2+k_n{}^2-k^2)=-j\omega\mu_0\phi_{mn}*(x_0,y_0) \tag{3C.4}$$

Thus:

$$A_{mn}=\frac{-j\omega\mu_0 h\phi_{mn}*(x_0,y_0)}{k_m{}^2+k_n{}^2-k^2} \tag{3C.5}$$

Inserting (C.5) into (C.1) this gives:

$$G(x,y;x_0,y_0)=-j\omega\mu_0 h\frac{\phi_{mn}*(x_0,y_0)\phi_{mn}(x,y)}{k_m{}^2+k_n{}^2-k^2} \tag{3C.6}$$

Since, ϕ_{mn} relate to the Eigen-functions of the patch, and was derived as in Appendix (A), by:

$$G(x,y;x_0,y_0)=-j\omega\mu_0 h\frac{\phi_{mn}*(x_0,y_0)\phi_{mn}(x,y)}{k_m{}^2+k_n{}^2-k^2} \tag{3C.7}$$

$$\phi_{m,n}(x,y) = k_{m,n}\cos\left(\frac{m\pi x}{a}\right)\cos\left(\frac{n\pi y}{b}\right) \quad (3C.8)$$

Rectangular patch loaded with n-ports

A voltage for two-dimensional patch can be defined as:

$$V(x,y) = -hE_Z(x,y) \quad (3C.9)$$

The voltage at any point (x,y) due to a current source at (x_0,y_0) is given by:

$$V(x,y) = \iint_{D_p} G(x,y;x_0,y_0).Js(x_0,y_0)dx_0dy_0 \quad (3C.10)$$

where D_p is the region inside the planar circuit, and G is the 2-dimensional Green's Function of the rectangular patch.

If the source and observation points are on the periphery of the patch, then the voltage is given by:

$$V = -\int_{C_p} G(x,y;x_0,y_0)J_S(x_0,y_0)dt \quad (3C.11)$$

the line integral round the boundary can be replaced by a line integral over the port width:

$$V = -\sum_j \int_{W_j} G(x,y;x_0,y_0)J_S(x_0,y_0)dW_j \quad (3C.12)$$

The average voltage at port i due to current source at port j is given by:

$$Vi = -\frac{1}{Wi}\sum_j \int_{Wi}\int_{Wj} G(x,y;x_0,y_0)J_S(x_0,y_0)dW_idW_j \quad (3C.13)$$

where:

$$I_j = -\int_{Wi} J_S(x_0,y_0)dW_j \quad (3C.14)$$

Thus:

$$J_S = -\frac{I_j}{W_j} \quad (C.15)$$

Therefore:

$$V_i = \frac{1}{W_i}\sum_j \frac{I_j}{W_j}\int_{Wi}\int_{Wj} G(x,y;x_0,y_0)dW_idW_j \quad (3C.16)$$

The Z - parameters of a 2 port network can be given by:

$$Z_{ij} = \frac{V_i}{I_j}\Big|_{Ii=0} \tag{3C.17}$$

$$Z_{ij} = \frac{V_i}{I_j}\Big|_{I_i=0} = \frac{1}{W_i W_j}\int_{Wi}\int_{Wj} G(x,y;x_0,y_0)dW_i dW_j = Z_{ji} \quad , \tag{3C.18}$$

$$Z_{ii} = \frac{j\omega\mu_0 h}{abW_iW_j}\sum_{m-0}^{\infty}\sum_{n=0}^{\infty}\sigma_m\sigma_n\left\{\left[\frac{\cos(k_{xm}x_i)\sin(k_{yn}y_i)}{k_{yn}}\right]_{yi-wi/2}^{yi+wi/2}\right\}^2 \frac{1}{k_{xm}{}^2 + k_{yn}{}^2 - k^2} \tag{3C.18}$$

From equation (3C.18), the mathematical solution for the formula becomes as follows:

$$Z(f) := \left(\frac{i\cdot 2\cdot\pi\cdot f\cdot\mu_0\cdot h}{a\cdot b\cdot w\cdot w}\right)\cdot\left[\sum_{m=0}^{\infty}\left[\sum_{n=0}^{\infty}\left[\sigma(m)\,\sigma(n)\left(\frac{2\sin\left(ky_n\cdot\frac{w}{2}\right)}{ky_n}\right)^2\cdot\frac{\cos(k(m)\cdot x1)\cdot\cos(k(m)\cdot x2)\cdot\cos\left(ky_n\cdot y1\right)\cdot\cos\left(ky_n\cdot y2\right)}{\left[\left(kx_m\right)^2+\left(ky_n\right)^2-(k(f))^2\right]}\right]+\sigma(m)\,w^2\cdot\left[\frac{\cos(k(m)\cdot x1)\cdot\cos\left(kx_m\cdot x2\right)}{\left[\left(kx_m\right)^2-(k(f))^2\right]}\right]\right]\right]$$

… (3C.18)

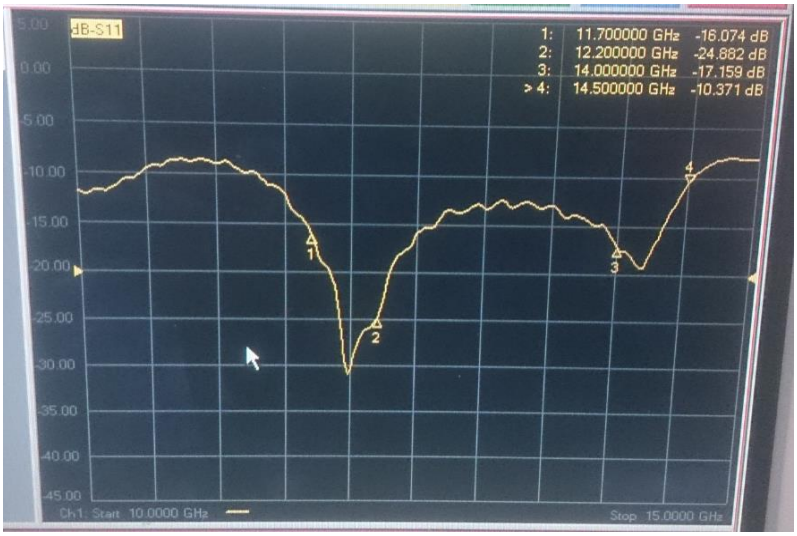

S11-parameters of practical meshed suspended patch